THE EFFECTS OF LOW-ENERGY HEAVY CHARGED PARTICLES ON THE OPTICALLY STIMULATED LUMINESCENCE AND THERMOLUMINESCENCE OF ALUMINUM OXIDE AND BERYLLIUM OXIDE

by

Joel Pogue

June 2021

Director of Dissertation: Dr. Regina DeWitt

Major Department: Physics

Optically Stimulated Luminescence (OSL) and Thermoluminescence (TL) are methods utilized to evaluate the energy absorbed by crystalline insulators. It is necessary to test luminescent materials in a controlled environment to elucidate the underlying luminescence processes involved and improve dosimeter properties. The goal of this work is to investigate the effects of low-energy heavy ion bombardment on the OSL and TL signals from Al_2O_3:C and BeO, which are two of the most prolific OSL dosimeters currently utilized. This dis-sertation describes the design and application of the particle accelerator luminescence beam constructed as part of this research, gives an overview of the two dosimeter materials studied, and discusses luminescence characteristics resulting from exposure to heavy charged particles (HCP), as well as β and α emitting sources.

Experimental irradiation parameters, such as ion type, energy per ion, total absorbed energy, and current, were systematically varied to better understand the fundamental TL and OSL mechanisms of Al_2O_3:C and BeO responsible for signal shape and magnitude. The shape change of OSL curves induced by increasing absorbed energy from HCPs is investigated for both materials. Lastly, a robust methodology for calculating luminescence efficiency is outlined, and resulting values are presented. The BeO OSL proton efficiencies calculated in this work are compared to previous results.

THE EFFECTS OF LOW-ENERGY HEAVY CHARGED PARTICLES ON THE OPTICALLY STIMULATED LUMINESCENCE AND THERMOLUMINESCENCE OF ALUMINUM OXIDE AND BERYLLIUM OXIDE

A Dissertation

Presented to the Faculty of the Department of Physics

East Carolina University

In Partial Fulfillment of the Requirements for the Degree

Doctor of Philosophy in Biomedical Physics

by

Joel Pogue

June, 2021

THE EFFECTS OF LOW-ENERGY HEAVY CHARGED PARTICLES ON THE OPTICALLY STIMULATED LUMINESCENCE AND THERMOLUMINESCENCE OF ALUMINUM OXIDE AND BERYLLIUM OXIDE

by

Joel Pogue

APPROVED BY:

DIRECTOR OF
DISSERTATION: _____
Regina DeWitt, PhD

COMMITTEE MEMBER: _____
Jefferson Shinpaugh, PhD

COMMITTEE MEMBER: _____
Michael Dingfelder, PhD

COMMITTEE MEMBER: _____
Jae Won Jung, PhD

COMMITTEE MEMBER: _____
Adriana Heimann, PhD

CHAIR OF THE
DEPARTMENT OF PHYSICS: _____
Jefferson Shinpaugh, PhD

DEAN OF THE
GRADUATE SCHOOL: _____
Paul J. Gemperline, PhD

ACKNOWLEDGEMENTS

First and foremost, I would like to sincerely thank my advisor, Dr. Regina DeWitt, for all of the time and energy she has invested in me these past four years. Her guidance, expertise, and patience were integral to my scientific growth. She is exceptionally kind, humble, respectful, and dependable. It is hard to overstate the impact her efforts have made on this research, and I could not be more thankful for the extensive time she spent helping me refine this dissertation.

Next, I would like to thank my committee members for agreeing to advise me concerning this research: Dr. Jefferson Shinpaugh, Dr. Michael Dingfelder, Dr. Jae Won Jung, and Dr. Adriana Heimann. I have enjoyed the many fruitful discussions about physics, as well as the conversations about life in general.

My sincerest thanks go to the Physics department staff: Chris Bonnerup, Gene Oakley, and William Holland. I have spent many hours building, laughing, brainstorming and troubleshooting with each of these men. The beamline, and my experience in the accelerator lab, would not be what it is without their significant contributions.

Next I would like to thank Wilson Hawkins for being a great friend; this includes frequent training sessions and advice about anything and everything to do with the particle accelerator. The time freely given has not gone unnoticed. I would also like to thank Emmanuel Osunkwor for his friendship, encouragement, laughter, and much appreciated collaboration.

I am very grateful to Dr. Mark Akselrod for providing the Al_2O_3:C single crystal dosimeters utilized in this dissertation; this research would not be possible without his contribution.

I would like to thank Dr. Nathan Carlson and Mark Strausbauch for assisting in the β source calibration process; their time and collaboration efforts are very appreciated.

A special thanks goes to my parents, Steve Pogue and Wendy Latham, for their unwavering love and support. Their contribution to my current success is immeasurable.

Most importantly, I would like to thank my beautiful wife, Mikeala, for being my source of stability these past 5 years. Life has been exceedingly rewarding with her by my side. I

am grateful for the numerous times she has encouraged me, eased my frustrations, offered sound advice, and offered a helping hand. I am especially thankful that she so graciously, and without complaint, accepted additional parenting and home duties towards the end of this dissertation; this is a testament to her character.

Table of Contents

List of Tables

List of Figures

Chapter 1

Introduction

1.1 Historical Luminescence Overview

OSL and TL are phenomena in which light or heat stimulate a substance that has previously received energy from an external source, typically through ionizing radiation. The material emits light, the so-called luminescence, which can be utilized to derive information about the material's absorbed energy.

Identifying the first observance of OSL is difficult since the term *Optically Stimulated Luminescence* was not used until the mid-twentieth century. Beforehand, this phenomenon was typically referred to as photostimulated luminescence or phosphorescence. In 1843, Edmond Becquerel noted that the phosphorescence was quenched from several materials if they were exposed to infrared after exposure to ionizing radiation [1], which was later also observed by famous scientist Henri Becquerel in 1883 [2]. In 1912, Nichols and Merritt discovered that infrared stimulation causes increased luminescence output and quicker quenching [3]. Although many scientists observed phenomena relating to luminescence in the early twentieth century and before, a robust description of luminescence dosimetry requires use of Quantum Mechanics. For this reason, research of OSL and TL did not begin to gain momentum until the 1950's.

A more comprehensive picture of luminescence phenomena emerged as the scientific commmunity learned about band structure, quantization of energy levels, and electron/hole movements. In 1949, H. W. Leverenz first described the full process of TL and OSL when he stated the following,"When the energy storage of phosphors consists of trapped excited electrons or metastable states, for then additional activation energy must be supplied to release the trapped electrons. This activation energy may be supplied by heat... or it may be supplied by additional photons."[4] Two key luminescence components are described here: energy that is deposited into a substance is then stored inside via trapped, excited electrons, and these electrons are released from their excited states when the substance is thermally or optically stimulated.

In 1959, Wallack received a US patent for what he termed an OSL gamma radiation dosimeter [5] and in 1963 Fowler was the first to coin the phrase Optically Stimulated Luminescence in his paper titled *Solid State Dosimetry* [6]. Even so, it would be many years before OSL proved itself as a reliable method/means of dosimetry, primarily because the materials being used at this time were sulfides. Sulfides contain traps at shallow energy levels, allowing thermal energy from the environment to cause signal fading between irradiation and infrared stimulation. Between the 1970's and 1990's, great strides were made as scientists began to study wide-band-gap insulating materials, enabling the use of traps that are deep enough to be thermally stable. This presented a more reliable means of dosimetry by ensuring the majority of electron traps are not activated until stimulated by a higher energy source. Such materials include BeO [7, 8], CaF_2 [9], $CaSO_4$ [10, 11], and, most notably, Al_2O_3 [12].

OSL and TL have cemented themselves as effective dating tools in geology and archaeology since the 1980's. Because the half-lifes of naturally occurring radionuclides such as Uranium and Thorium are so long and the radiation from space is relatively constant, Huntley et al. determined the relative age of geologic samples by simply measuring the dose stored in the sample and dividing by the environmental dose rate [13]. This discovery peaked new scientific interest in luminescence dosimetry, such that Aitken coined the term *optical dating*

in 1998 [14]. Over the past few decades, luminescence dating has become a well-established and robust method of determining the age of sedimentary deposits [15].

There are many other current luminescence applications; these include personal dosimetry, space dosimetry, medical dosimetry, and the potential for dosimetry after a radiation disaster and evaluating security threats [16]. Space radiation is complex enough such that one type of dosimeter is not sufficient to determine the weighted dose, which considers the relative biological effectiveness (RBE) and the absorbed dose. A combination of TL detectors, OSL detectors, and Plastic Nuclear Track (PNT) detectors is believed to be the best way of evaluating the ionizing radiation induced health risk of astronauts [17]. OSL has promising medical prospect for two reasons: high sensitivity and an all-optical measurement. High sensitivity leads to high spatial resolution, making it a useful technique in situations with high dose variance. Because of OSL's inherent nature, optical fibers allow dose measurements in hard to reach or small places. These advantages are self-evident in the medical field. OSL has the potential to become an effective tool for determining if a radiological or nuclear device was previously in a location in an effort to increase security and track down nuclear weapons [16]. This is because many items in an everyday setting can act as OSL dosimeters [15]. Thus a nuclear device's previous presence can be measured even if the device has since moved. This research front is in its early stage, however. It is also believed that OSL has the potential for dosimetry of a large population after a nuclear disaster to determine the radiation dose recieved by the public. Fortunately, there have not been enough catastrophic instances to validate this claim.

1.2 Motivation for this Dissertation

While luminescence dosimeters are intended to measure low linear energy transfer (LET) radiation, they can be used for heavy ion dosimetry if the material's response to high LET radiation is well-described. This would allow the true absorbed dose to be calculated, and

could potentially provide information necessary to obtain the quality factor required to calculate weighted dose.

The international Commission on Radiation Protection (ICRP) defines the quality Q of radiation as a function of unrestricted LET in water [18]. Thermoluminescent detectors (TLDs) and optically stimulated luminescence detectors (OSLDs) are efficient for $LET < 10\ keV/\mu m$ where Q has a constant value of 1 [19]. However, luminescence signals exhibit strong dependence on $LET > 10\ keV/\mu m$ as Q increases, leading to fundamental differences in luminescence characteristics when measuring signal from low-LET radiation (γ rays, β particles, and X-rays) and high-LET radiation (α particles, other HCPs, and neutrons). This can be problematic, since the radiation that does the most biological damage can be difficult to detect and quantify with luminescence. For this reason, a combination of OSLDs and PNTDs are ideal for the complex fields in space dosimetry because PNTDs are efficient when exposed to high-LET radiation [17].

In spite of these inherent limitations, there are several benefits to obtaining a greater understanding of effects of HCPs on luminescence signals. First, a greater understanding of high-LET dependencies will always be welcomed while OSLDs are utilized for manned space exploration in mixed-LET fields [20, 21]. Second, there has been a significant and recent increase in proton, and even Carbon, cancer therapy. OSLDs are already used for medical purposes, such as in-vivo Brachytherapy quality assurance and secondary monitoring of linac dose depth distributions. The advantage of being able to use OSLDs to reliably monitor high energy cyclotron beams is self-evident. Lastly, a general understanding of high-LET luminescence effects is relevant to dating; there are many naturally occurring high-LET alpha emitters such as Uranium and Thorium [22]. Dating precision is dependent on the signal precision, and therefore the ability to calculate signal from a mixed-LET field. It is important to note that the ions used in this work are much lower energy, and thus slower than those observed in space or utilized for radiotherapy. However, this leads to a relatively higher LET along the particle track, which will be discussed later in depth. For this reason

the LET effects of HCPs are more pronounced at lower ion energies. The energy range of the ECU particle accelerator corresponds to natural α emitters, which are on the order of a few MeV.

The two materials used in this work, Al_2O_3:C and BeO, are among the most relevant current luminescence dosimeters. Akselrod and Kortov found that doping Al_2O_3 with Carbon vastly increases its' TL sensitivity [23]. Researchers at Oklahoma State University decided to test this new, high-sensitivity Al_2O_3:C using OSL instead of TL, yielding remarkable results [24]. To date, Al_2O_3 has been the most effective OSL and TL dosimetry material, and has even seen commercial success. Both, the effectiveness of using OSL to date crystalline structures and the success of Al_2O_3:C as a dosimeter, have led to significant surges in OSL research since the turn of the 21st century. Another material that has found increased research interest in the past 15 years is BeO. Although first luminescence properties were recorded in 1969, advances in material preparation and radiation therapy have rekindled what Bulur et al. refer to as "New observations from an old material" [25]. BeO is characterized by a very bright OSL signal and sensitivity to low doses. Possibly the most promising characteristic of BeO is that its effective Z is near tissue-equivalent, and thus may provide a future alternative to Al_2O_3:C [26]. This is the reason Santos et al. have developed a fiber-optic coupled BeO dosimetry system and tested it on many types of radiation fields within the past few years [27, 28, 29, 30].

1.3 Outline of Experimental Work

This dissertation consists of 9 chapters.

Background information necessary to understand optically stimulated luminescence and thermoluminesence is compiled in Chapter 2. This includes a discussion of the energy band model, a brief description of crystals and their differences compared to conductors and semiconductors, an overview of luminescence phenomena and their associated mathematical

descriptions, and an introduction to heavy charged particle tracks.

The experimental methods used to irradiate samples with a calculable quantity of absorbed energy, then measure their luminescence is described in Chapter 3. The accelerator irradiation process can be broken into 3 general components: the ion source, the particle accelerator, and the luminescence beamline/sample chamber. The workings of these components are described, as well as the calculations required to obtain selected ions in the back of the chamber. The Risø OSL/TL reader irradiation and measurement capabilities utilized in this research are described. Lastly, beam specific parameters and their relevance to this work are discussed.

Chapter 4 gives an in-depth description of Al2O3:C and BeO, the materials used in this research. This includes dosimeter characteristics, as well as an overview of the previous HCP research conducted with each dosimeter and how this previous work led to the questions investigated in this dissertation.

Preliminary findings using the Risø's β and α sources are presented and discussed in Chapter 5. Material attributes tested include dosimeter non-uniformity, effect of repeated measurements on signal, and dose response and supralinearity.

Chapter 6 investigates the effects of various parameters on the signal induced by HCPs created in the ECU particle accelerator lab. Experimental parameters were varied during irradiation to better understand fundamental luminescence processes. Specific parameters investigated in this work include material exposed, ion type, ion energy, total absorbed energy, and fluence rate. Experimental results are shown, and the resulting luminescence signal characteristics are discussed.

An in-depth analysis of OSL curve shape is completed in Chapter 7. This entails determining the number of components that contribute to a given OSL signal, then iteratively fitting many OSL curves simultaneously. Component growth and linearity curves can then be constructed. Lastly, these findings can be used to explain the shape change of normalized OSL curves as well as response characteristics.

The procedure for obtaining luminescence efficiencies is detailed in chapter 8. This process entails creating β-dose calibration curves, fitting HCP signals using these curves, and calculating efficiencies utilizing two distinct methods.

Chapter 9 summarizes the main results and conclusions of all original work presented in this research. The current experimental processes are critiqued so that improvements can be made. Lastly, future research directions are proposed.

Chapter 2

Luminescence Background

As mentioned in the introduction chapter, heavy charged particles have dense ionization tracks that lead to different signal magnitude effects compared to low LET radiation. This chapter constructs the framework necessary to understand why HCPs induce these effects. This is accomplished by explaining the origin and nature of solid state energy bands, how charges move through crystals, and the fundamental components of OSL and TL processes. I then describe the key components of luminescence dosimtery and give a mathematical overview of rate equations and other pertinent mathematical relationships important in luminescence studies. Lastly, HCP tracks and charged particle interactions are discussed in relation to this work.

2.1 Energy Band Theory

Solid-state physics dictates that, in a given electronic band structure, there are ranges of energy levels that an electron can occupy and energy ranges in between that it may not occupy. These allowed energies are referred to as energy bands while the ranges in between are forbidden bands (also called band gaps). Band structure is derived from the Pauli exclusion principle, which states that two or more identical fermions in the same quantum mechanical system cannot occupy the same quantum state. An electron of a single atom can

occupy a single discrete energy level. However, the Pauli exclusion principle says that when two atoms combine to form a molecule, each atomic orbital is forced to split into $(2\ell+1)$N molecular orbitals of different energy, where N is the number of atoms and $(2\ell+1)$ is the orbital degeneracy pertaining to each energy level. Now extrapolate this phenomenon to a macroscopic solid on the order of N $\sim 10^{22}$ atoms. There must be N $\sim 10^{22}$ molecular orbitals, each with their own energy, bunched into an energy range on the eV scale. This means that the gaps in between the discrete orbital energies are $\sim 10^{-22}$ eV. As Figure 2.1Adapted from Chetvorno [1]. shows, this allows the conduction and valence bands to be treated as continuous energy spectra rather than many discrete energy levels.

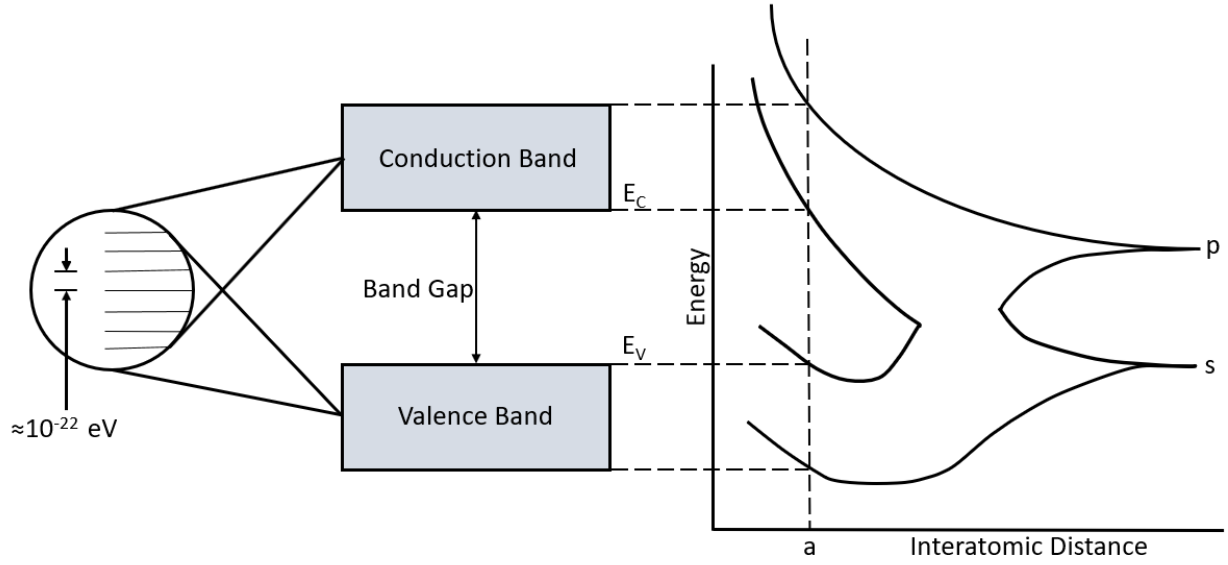

Figure 2.1: Diagram of the quasi-continuous nature of energy bands. While they are not technically continuous, their energy gaps are small enough to be considered continuous. Adapted from Chetvorno.

Determining the energy band and band gap values associated with such materials requires an intrinsic understanding of the way charges move throughout a solid structure. An electron inside of a solid is subject to a periodic potential, which derives its electric field from the ionic composition of the solid. Schrödinger's time-independent equation gives us the capability of

[1] https://en.wikipedia.org/wiki/Band_gap#/media/File:Solid_state_electronic_band_structure.svg, last accessed on May 22, 2021.

describing the motion of this charged non-relativistic particle [31]:

$$E\Psi(\mathbf{r}) = \left[\frac{\hbar^2}{2m}\nabla^2 + V(\mathbf{r})\right]\Psi(\mathbf{r}) \tag{2.1}$$

E is the energy of the given state, $\Psi(\mathbf{r})$ is the wave function of the position vector, $\hbar = \frac{h}{2\pi}$ is the reduced Planck's constant, m is the mass of the charged particle, ∇^2 is the Laplacian, and $V(\mathbf{r})$ is the potential of the position vector. Although not in its traditional form, the equation above simply states that the total energy of the system is equal to the sum of the kinetic and potential energies of the system.

Bloch's Theorem proves that Schrödinger's time-independent equation must have solutions of the form

$$\Psi(\mathbf{r}) = \Psi(\mathbf{r} + \mathbf{R}) \cdot e^{i\mathbf{k}\cdot\mathbf{r}} \tag{2.2}$$

in a periodic crystal lattice [32, 33]. $e^{i\mathbf{k}\cdot\mathbf{r}}$ is the equation of a plane wave, $\mathbf{R}$ is the Bravais lattice translation vector, and $\Psi(\mathbf{r}) = \Psi(\mathbf{r} + \mathbf{R})$ is the Bloch function which contains the periodicity of the lattice. This means that the wave equation eigenstates of a periodic crystal lattice structure are the product of a plane wave and a function containing the periodicity of the crystal lattice. Because the wave equations of a Bravais lattice have to be periodic, the Born-Von Karman boundary condition imposes that

$$\Psi(\mathbf{r}) = \Psi(\mathbf{r} + N_i\mathbf{a}_i), \quad i = 1, 2, 3 \tag{2.3}$$

where $\mathbf{a}_i$ are the primitive lattice vectors and N_i are all integers of order $N^{1/3}$ (i.e., $N = N_1N_2N_3 \equiv$ the total number of primitive cells in the crystal)[34].

Using this condition, Kronig and Penney created a quantum-mechanical model to solve the simplest case. That is, a one dimensional lattice of positive ions where the distance between two neighboring ions equals a, V is the potential around the ions, and b is the distance between potential wells. This problem can be visualized as an infinite array of

rectangular potential wells of height V separated by a distance of b. The final solution of this model is found to be

$$\cos(ka) = cos(a\alpha) + P\frac{sin(a\alpha)}{(a\alpha)}, \tag{2.4}$$

where $\alpha^2 = \frac{|E|2m}{\hbar^2}$ and $P = \frac{mVba}{\hbar^2}$ [35, 33]. It is worth noting that the only parameters not stipulated by the physical system are the crystal lattice momentum, k, and the energy of the system, E. The left hand side of equation (2.4) is limited to values between -1 and 1,inclusive. However, the right hand side of equation (2.4) sometimes has values greater than 1 or less than -1. In these cases no value of k allows for the equation to be true, translating to the existence of select energy ranges that have no eigenfunctions of the Schrödinger equation. These energy ranges are what constitute band gaps, or forbidden regions.

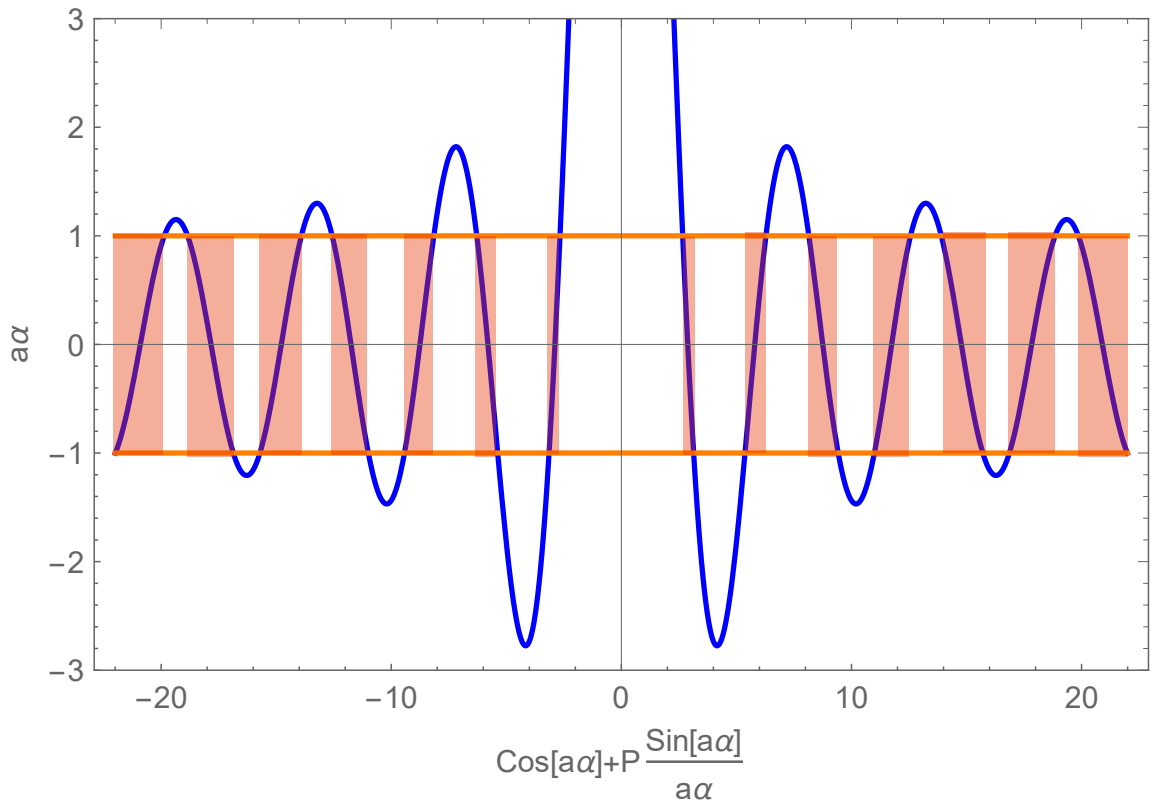

Figure 2.2: Solution to Kronig-Penney Model: Plot of $cos(a\alpha) + P\frac{sin(a\alpha)}{(a\alpha)}$ vs. $a\alpha$ for $-7\pi \leq a\alpha \leq 7\pi$ and $P=\frac{7\pi}{2}$. The shaded regions constitute allowed energies while the unshaded regions constitute band gaps. Adapted from Kittel [33].

Figure 2.2 shows $cos(a\alpha) + P\frac{sin(a\alpha)}{(a\alpha)}$ plotted against $a\alpha$ for values of $a\alpha$ between -7π and 7π. P was chosen to be $\frac{7\pi}{2}$ and the horizontal lines at -1 and 1 dictate the domains in which there are real solutions to the Schrödinger equation. The shaded regions represent energy bands while the unshaded regions represent band gaps. Notice that as the value of $|a\alpha|$ gets larger, the size of the energy bands increases and vice versa. Another consequence to consider is that without the presence of P (i.e., V→0) there would be no band gaps, corresponding to a continuous energy band in which all energies are allowed (free electrons). The opposite case occurs as P→∞, corresponding to an atom that is completely isolated and thus constrained to a single energy state [36].

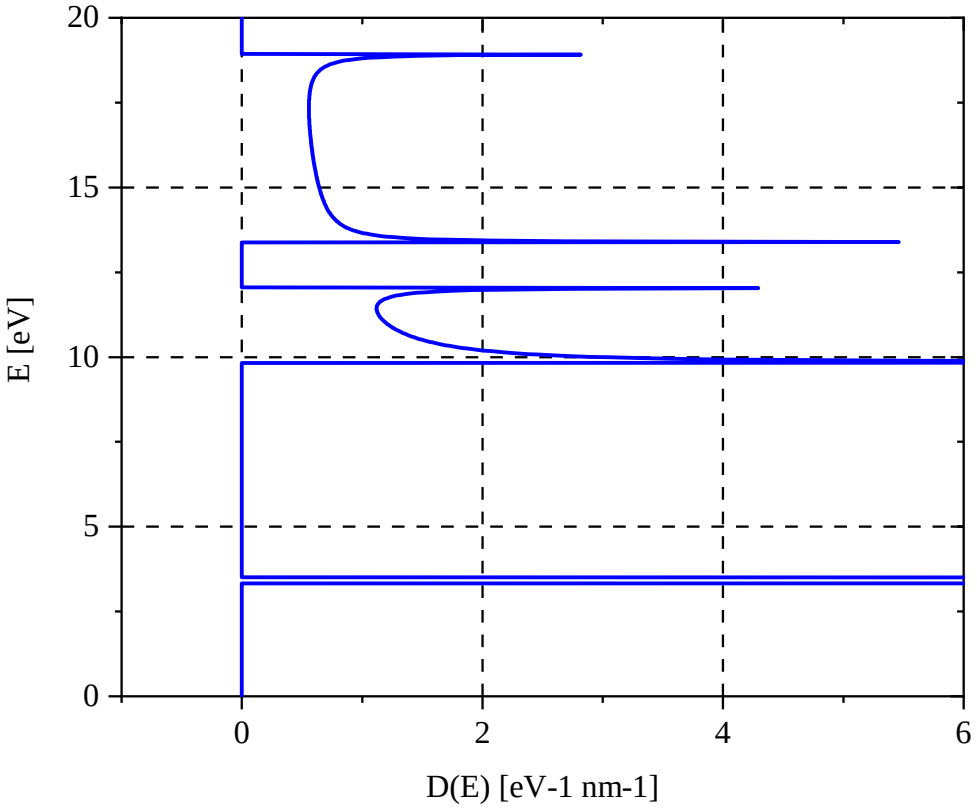

Figure 2.3: Density of electron states (eV^{-1} nm^{-1}) plotted against energy (eV) for V = 10 eV, m = 9.11E-31 kg, a = 5E-10 m, and b = 2E-10 m.

Rearranging the right side of equation (2.4) yields the relationship between k and E

($k_0^2 = \frac{2m|E|}{\hbar^2}$), allowing the dispersion relation to be found, followed by the electron density of states. Because the density of states in the k space is $D(k) = 2/\pi$, the energy density of states is found to be

$$y = \begin{cases} \frac{2}{\pi}\frac{dk}{dE} = \frac{2}{\pi}\frac{dk}{d\alpha}\frac{d\alpha}{dE}, & |\alpha| < 2, \\ 0, & |\alpha| > 2, \end{cases} \tag{2.5}$$

where $\frac{dk}{d\alpha}$ and $\frac{d\alpha}{dE}$ are rather non-trivial relations analytically solved by Kollmitzer and Hadley [37]. Plotting this function for $V = 10$ eV, $m = 9.11$E-31 kg, $a = 5$E-10 m, and $b = 2$E-10 m yields the electron density of states (figure 2.3[2]). The energy bands are comprised of all energy values where $D(E) \neq 0$, whereas $D(E) = 0$ constitutes the band gap.

To better understand how energy band structure affects crystals, it is necessary to define the Fermi-Dirac distribution [33].

$$f(E) = \frac{1}{e^{(E-\mu)/kT} + 1} \tag{2.6}$$

f(E) is the probability that an electron's state has an energy of E when at thermodynamic equilibrium. k is the boltzmann constant, T is the absolute temperature of the system, and μ is the electron electrochemical potential. When the state energy equals the electrochemical energy, Equation (2.6) reduces to $\frac{1}{2}$. This corresponds to the state having a 50 percent chance of occupation, otherwise known as the Fermi level.

Figure 2.4 depicts how the Fermi level is used to classify solid state materials. The Fermi-Dirac distribution is represented by the hue of the rectangles. The Fermi level lies within the conduction band for conductors, which explains their high electrical conductivity. The Fermi level lies within the band gap for semiconductors and insulators. However, the conduction and valence bands of semiconductors are close enough to the Fermi level for it to become thermally populated with electrons or holes if energy is applied to the material.

[2] http://lampx.tugraz.at/~hadley/ss1/KronigPenney/KronigPenney.php, last accessed on May 22, 2021.

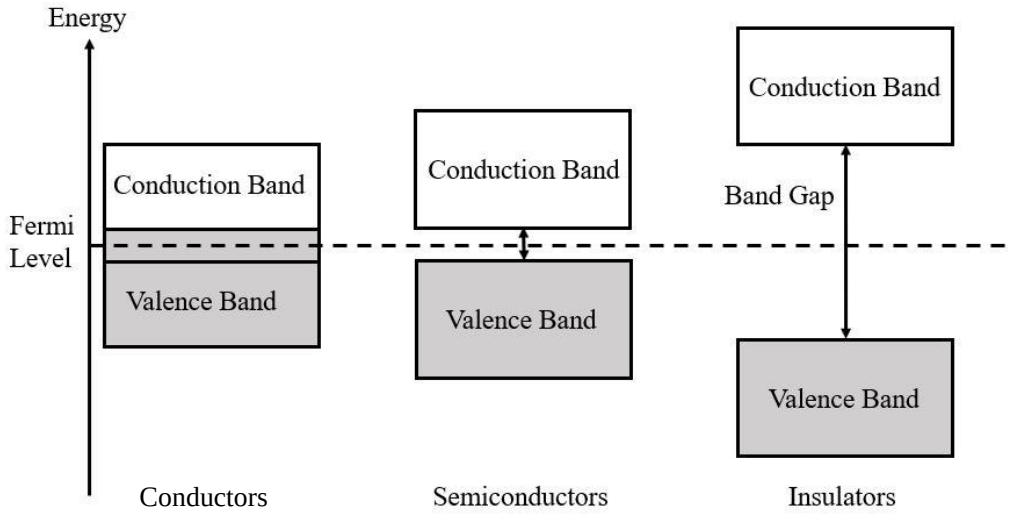

Figure 2.4: Depiction of the Fermi level for Conductors, Semiconductors, and Insulators. The height correlates to energy while hue indicates whether electron states are filled or empty. Notice that the valence and conduction bands overlap for metals, allowing the electrons to freely migrate through the material, and hence the material is electrically conductive.

2.2 Crystal Structure

The smallest unit of solid state structures, specifically crystals, is the primitive cell. Identically linked primitive cells create the periodicity of the crystal lattice structure. Thus, an ideal crystal is treated as an infinite crystal lattice [38]. Crystals can behave as conductors, semiconductors, or insulators, depending on the capacity and distance between bands. However, the crystals used in this work are insulators. Semiconductors can receive energy to overcome their band gap when they are thermally stimulated, whereas the insulator band gap is too large to overcome [33]. This explains why the conductivity of semiconductors is thermally dependent. Whenever electrons migrate from the conduction band to the valence band, they leave behind holes. A hole is exactly what it sounds like: not a particle itself, but rather the absence of an electron. For this reason, holes are often called quasi-particles and behave like mobile, positively charged particles [39].

An ideal crystal behaves as an ideal semiconductor, displaying the behavior shown in

Figure 2.5. When at thermal equilibrium, all of the electrons fill the valence band E_V. When the crystal is thermally stimulated, some electrons migrate from the valence band to the conduction band E_C, leaving behind holes. The difference in energies between the valence and conduction band equals the band gap. Notice that the Fermi level dissects the band gap exactly [40]. The size of the band gap and the magnitude of stimulation the crystal receives determine the likelihood that an electron migrates from the valence band to the conduction

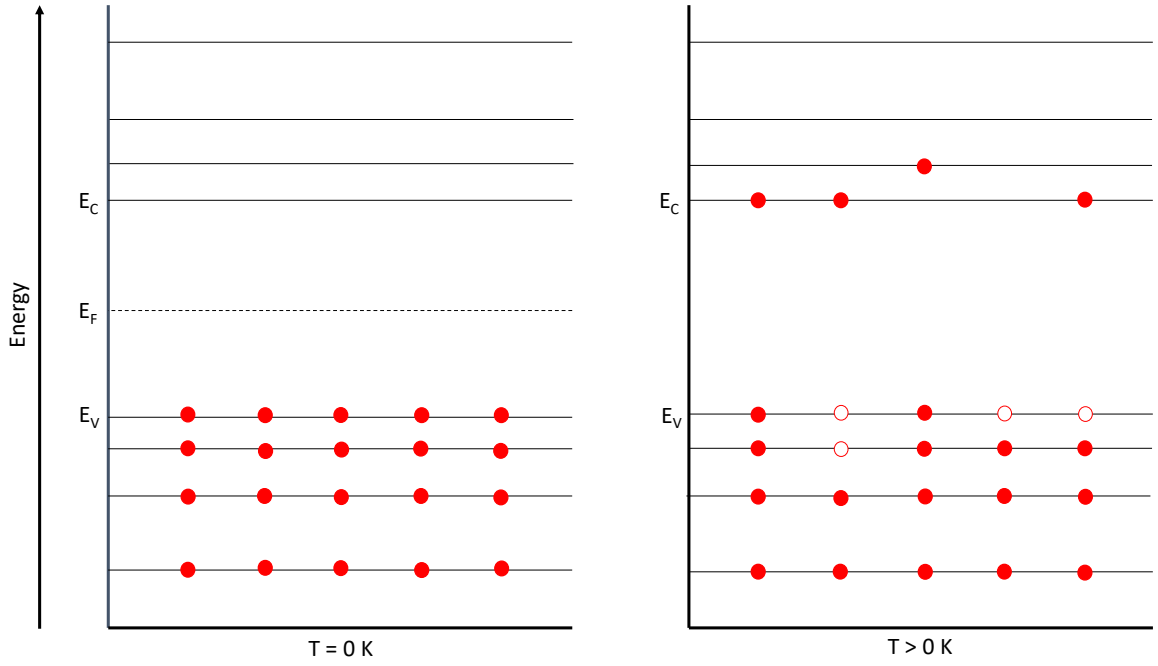

Figure 2.5: Diagram of an ideal semiconductor at thermal equilibrium and thermal non-equilibrium. There are no electrons in the conduction bands at T = 0 K. However, electrons receive the energy to transition and leave behind holes at T > 0 K. E_F: Fermi level, E_C: conduction band, E_V: valence band, filled circles: electrons, and open circles: holes.

band.

Up until this point, only the overly simplistic case for crystals has been considered. We have assumed no lattice structure deformity and a completely homogeneous ionic composition (i.e., no external dopants). None of these assumptions hold true in nature and because of this, important consequences must be considered. Whenever a crystal lattice contains trace ionic impurities the Fermi levels of the crystal appear to shift because the intrinsic potential

of the system at the location of these impurities changes. The potential energy associated with Equation (2.1) is no longer $V(\mathbf{r})$, but instead $V(\mathbf{r}) + V'(\mathbf{r})$. Understanding why the new potential has two components rather than just an entirely new potential is crucial. At locations near an impurity, the potential of the ideal crystal and the potential of the impurity need to be accounted for, leading to new energy band structures. $V'(\mathbf{r}) \to 0$ at locations far from impurities, corresponding to an unaltered ideal crystal structure.

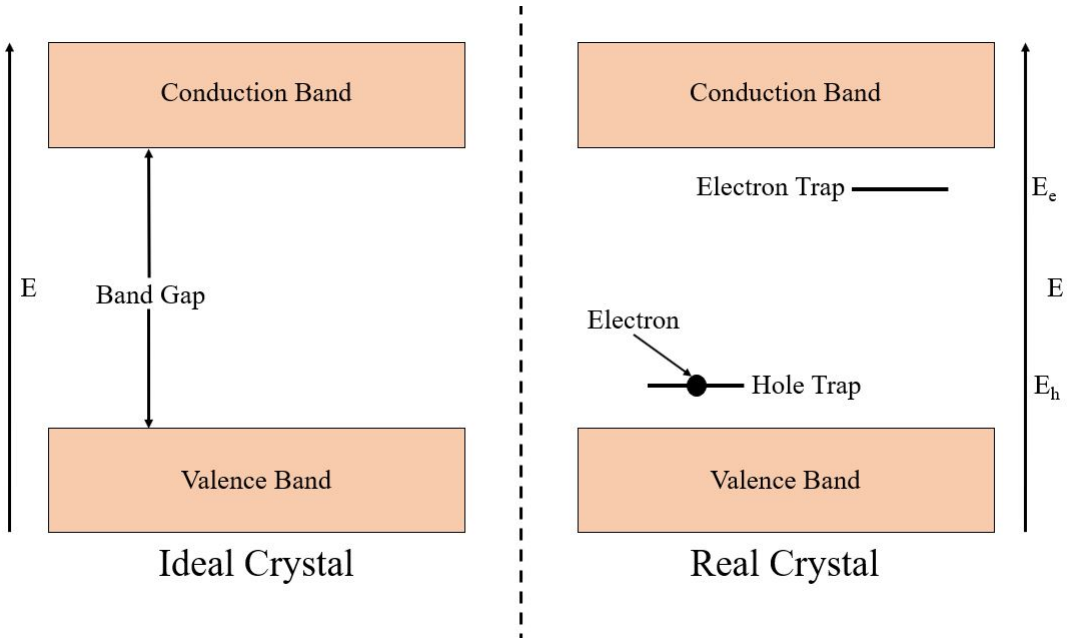

Figure 2.6: Diagram of ideal crystals versus natural crystals.

Crystals containing impurities have new electron states in their band gap, known as defects. This is due to a change in the local electric potential near these defects, which occur naturally in substances such as quartz due to their growth from chemically complex melts [41]. However, some materials such as Al_2O_3:C and BeO are artificially doped with impurities to enhance their luminescence properties. These defects fall into two categories and are shown in Figure 2.6. Electron traps, E_e, have energy states just below the conduction band and arise when a defect attracts and interacts with electrons. Hole traps, E_h, have energy states just above the valence band and can easily release an electron (trap a hole). Grasping these concepts is required to understand fundamental luminescence processes.

2.3 Luminescence Phenomena

2.3.1 Overview

OSL and TL are methods used to measure the absorbed energy or dose delivered to a crystalline insulator or semiconductor by ionizing radiation. OSL utilizes light, whereas TL utilizes heat, to stimulate a sample after the sample has been irradiated. The four steps of this process (ground state, irradiation, storage, and stimulation) can be seen clearly in Figure 2.7.

To begin, a crystal is in its ground state (a). When irradiated, a sample is excited and enters into a metastable state, meaning the sample has transitioned from equilibrium to a non-equilibrium, steady state. Physically, this metastable state can be perceived and characterized as a system of electrons and holes that collect in the impurities of the crystalline material. The energy from radiation lifts electrons from the valence band to the conduction band, allowing the electrons to freely migrate through the conduction band until they are trapped. These electron vacancies leave behind holes, which are then free to migrate through the valence band to the hole trap (b). The charge carriers (i.e., electrons) remain trapped in the material until they receive enough energy to overcome their potential barrier, E_e (c). Optical or Thermal stimulation excites these holes and electrons with enough energy to escape their traps and recombine at the hole trap, creating excited luminescence centers in the lattice. As these luminescence centers relax to ground state, they emit photons with energy proportional to the energy difference between their excited and ground states, E_h (d).

The electron and hole transition shown in step (b) above is just one possible example of charge migration. Further possible electronic transitions in doped semiconductors and insulators are depicted in Figure 2.8. If electrons receive energy from ionizing radiation greater in magnitude than the band gap, they are excited to the conduction band where they can migrate freely (i). Once in the conduction band, electrons can dissipate their excess energy via non-radiative and radiative processes. The energy can be transferred via

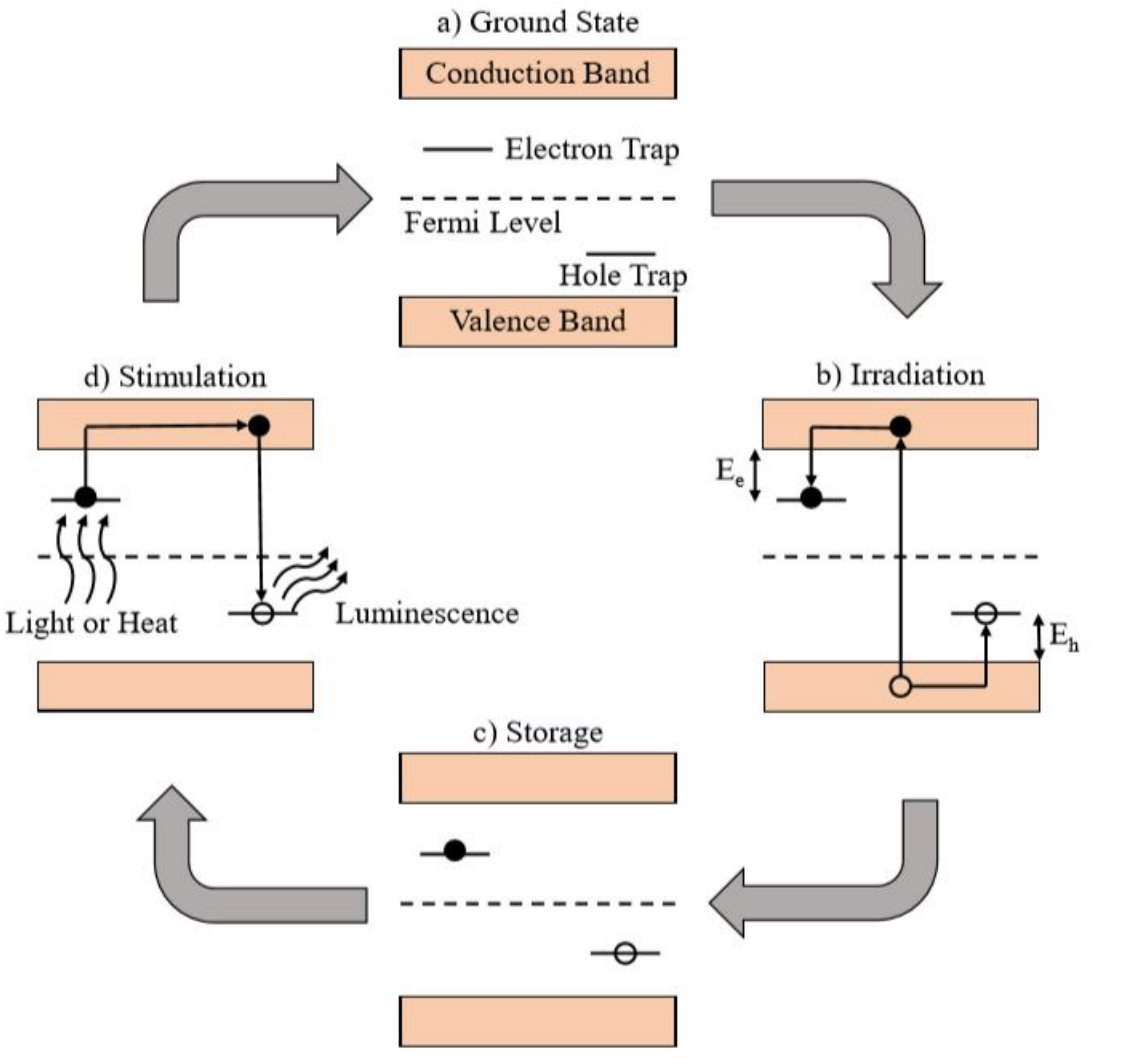

Figure 2.7: Four steps of the OSL and TL processes: ground state, irradiation, storage, and stimulation.

lattice vibrations (phonons) non-radiatively. The electrons can become trapped by radiative recombination centers (iii), and at least a fraction of their excess energy will be emitted as light. Electrons can undergo either direct recombinations (ii) or indirect recombinations (v, vi) once in the conduction band. Direct recombinations only involve the valence and conduction bands (band-to-band transition) while indirect recombinations involve the localized traps as well (band-to-center and center-to center transitions).

As mentioned before, the probability of direct recombination decreases, and thus requires more stimulation, as the material band gap increases. Band-to-center transitions occur when

free electrons are trapped (iii), before release and returning to the conduction band (iv), and finally recombining at recombination centers with holes (v). Electrons can alternatively undergo center-to-center transition via quantum tunneling (vi), which occurs stochastically between neighboring lattice defects (i.e., no migration allowed through the conduction band) [42].

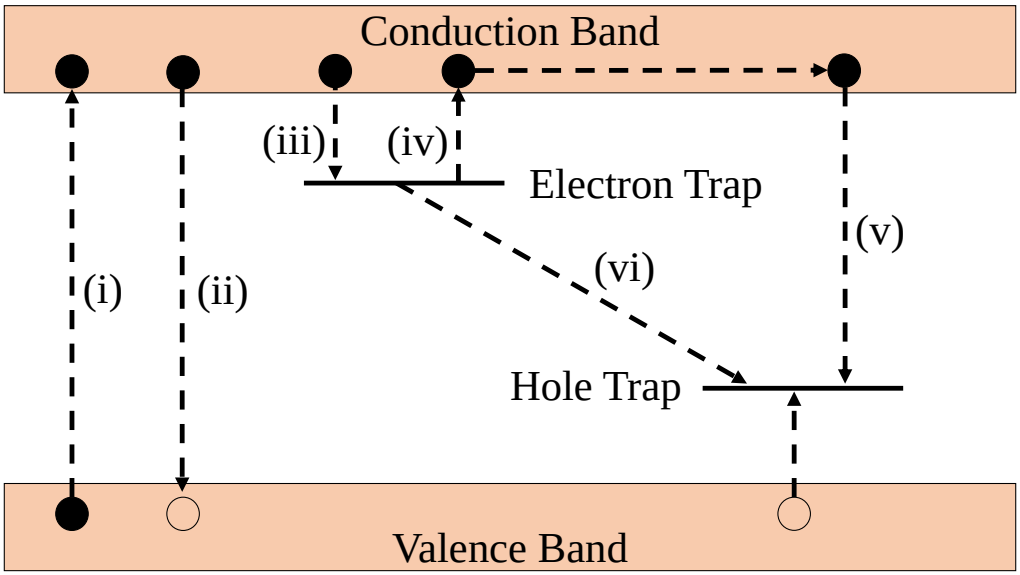

Figure 2.8: Possible electronic transitions of a doped semiconductor or insulator. Adapted from Gaza [43].

2.3.2 Mathematical Description

The usual method of mathematically describing OSL phenomena is through the use of rate equations. It makes sense to consider the simplest luminescence model to start, known as the one-trap-one-recombination (OTOR) model (figure 2.9) [44, 45, 16]. As the name suggests, an energy band containing just one trap and one recombination center in its band gap is considered. It is necessary to address a couple of assumptions that must be made in this model before continuing to the equations themselves. First, the delocalized energy bands are the means by which charge is transported and recombined. Second, this is a quasi-static process or a process that is in quasi-equilibrium. At any instant, the charges must transition slow enough such that the charge concentration in the valence and conduction bands is

relatively small, ensuring the system is near equilibrium. It is also worth noting that in this quasi-equilibrium, holes and electrons are assumed to be immediately captured by their prospective recombination centers. The mathematical interpretations of these assumptions can be found in equation (2.7).

$$\frac{\mathrm{d}n_c(t)}{\mathrm{d}t} \ll \frac{\mathrm{d}n(t)}{\mathrm{d}t} \quad , \quad n_c(t) \ll n(t) \quad , \quad \frac{\mathrm{d}n_c(t)}{\mathrm{d}t} \cong \frac{\mathrm{d}n_v(t)}{\mathrm{d}t} \cong 0 \tag{2.7}$$

N (M) is the total concentration of traps (recombination centers), $n(t)$ $(m(t))$ is the time dependent trapped electron (hole) concentration, $n_c(t)$ is the concentration of electrons in the conduction band, and $n_v(t)$ is the concentration of holes in the valence band. Conduction band electrons have a probability P_c of capture by empty traps and a probability P_r of recombining with trapped holes. Valence band holes have a probability P_h of getting trapped in the recombination center and P_s is the probability of thermal or optical stimulation. The rate of transition due to ionizing radiation is represented by r. Translated, r is the electron-hole pair creation rate per unit volume. Now that these assumptions have been accounted for, a total of four coupled, non-linear differential equations adequately model the system and are shown below.

$$\frac{\mathrm{d}n(t)}{\mathrm{d}t} = [N - n(t)]P_c n_c(t) - n(t)P_s \tag{2.8}$$

$$\frac{\mathrm{d}m(t)}{\mathrm{d}t} = [M - m(t)]P_h n_v(t) - m(t)P_r n_c(t) \tag{2.9}$$

$$\frac{\mathrm{d}n_c(t)}{\mathrm{d}t} = r - \frac{\mathrm{d}n(t)}{\mathrm{d}t} - m(t)P_r n_c(t) \tag{2.10}$$

$$\frac{\mathrm{d}n_v(t)}{\mathrm{d}t} = r - [M - m(t)]P_h n_v(t) \tag{2.11}$$

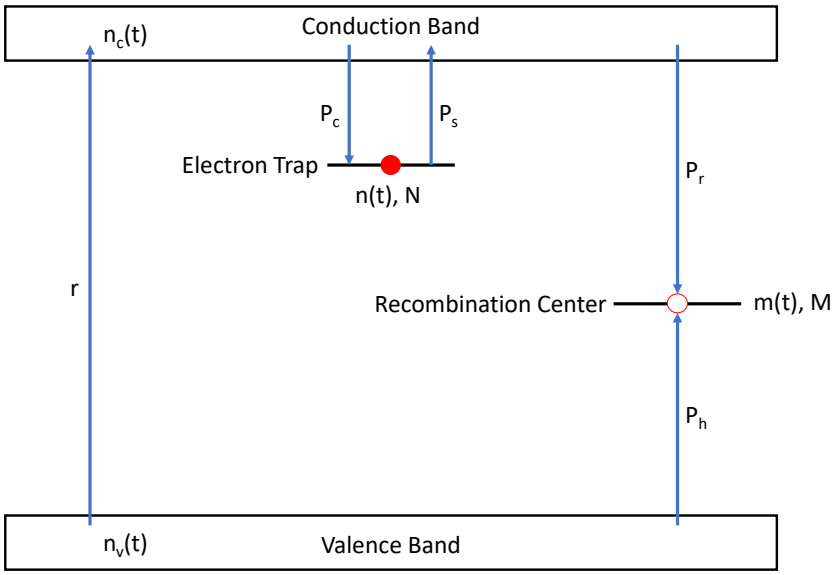

Figure 2.9: Simple one-trap-one-recombination center (OTOR) model.

Equation (2.8) states that subtracting the electron escape rate, $n(t)P_s$, from the electron capture rate, $[N-n(t)]P_c n_c(t)$, gives the time rate of change of the trapped electron concentration, $\mathrm{d}n(t)/\mathrm{d}t$. Equation (2.9) is analogous to equation (2.8), except the concentration of holes is considered rather than electrons. The rate of change in the concentration of holes in the recombination center is equal to the concentration of holes captured from the valence band minus the concentration of electrons captured from the conduction band. Equations (2.10) and (2.11) are similar in nature to equations (2.8) and (2.9) and describe the rate of change of electrons or holes into the conduction band (or valence band). It should be noted that an irradiation factor, r, makes its way into equations (2.10) and (2.11). $r \neq 0$ anytime the crystal is being exposed to radiation, otherwise, $r = 0$. Equations (2.9) and (2.10) can be simplified to the following respective forms based on the initial assumptions.

$$\frac{\mathrm{d}m(t)}{\mathrm{d}t} = r - m(t)P_r n_c(t) \tag{2.12}$$

$$n_c(t) = \frac{r + n(t)P_s}{[N-n(t)]P_c + m(t)P_r} \tag{2.13}$$

Solutions to the OTOR model vary based on whether or not retrapping (stimulated charges return to their intital defects rather than recombining) is considered. First-order kinetic theory dictates that electrons that are trapped once never retrap. Equation (2.8) now reduces to:

$$\frac{\mathrm{d}n(t)}{\mathrm{d}t} = -n(t)P_s. \tag{2.14}$$

From this rate equation, the trapped electron concentration is easily solved.

$$n(t) = n_0 e^{-P_s t} \tag{2.15}$$

Keep in mind that the OSL light intensity is proportional to the rate of change of trapped electrons, meaning equations (2.14) and (2.15) yield:

$$I_{OSL}(t) \propto \left|\frac{\mathrm{d}n(t)}{\mathrm{d}t}\right| = n_0 P_s e^{-P_s t}. \tag{2.16}$$

While this process is simple and easy to solve, it is often not representative of reality because electrons have a non-zero likelihood of retrapping. Because it is assumed that recombination centers immediately recapture all holes (i.e. $\frac{\mathrm{d}n_v(t)}{\mathrm{d}t} \cong 0$), equations (2.8) and (2.9) reduce to equations (2.17) and (2.18) if retrapping is accounted for.

$$\frac{\mathrm{d}n(t)}{\mathrm{d}t} = [N - n(t)]P_c n_c(t) - n(t)\sigma\phi \tag{2.17}$$

$$\frac{\mathrm{d}m(t)}{\mathrm{d}t} = -m(t)P_r n_c(t) \tag{2.18}$$

When specifically referring to OSL, P_s can be substituted for $\sigma\phi$. This states that the probability of optical stimulation P_s is equal to the photon flux ϕ times the photoionization cross-section σ. Using the quasi-equilibrium assumptions from equation (2.7) and assuming that stimulation occurs without irradiation, equation (2.13) simplifies to the following:

$$n_c(t) = \frac{n(t)\sigma\phi}{[N - n(t)]P_c + m(t)P_r}. \tag{2.19}$$

Plugging (2.19) into (2.18) with assumption (2.7) yields

$$\frac{\mathrm{d}n(t)}{\mathrm{d}t} = -n(t)\sigma\phi\left[\frac{m(t)P_r}{[N - n(t)]P_c + m(t)P_r}\right], \tag{2.20}$$

where $dn(t)/dt \approx dm(t)/dt$ when the system is in quasi-equilibrium.

Notice that when retrapping is very slow ($[N - n(t)]P_c \ll m(t)P_r$), the equation above reduces to our original first-order rate equation. However, when retrapping is significant ($P_c = P_r$ and $n(t) = m(t)$) equation (2.20) reduces to a second-order rate equation, allowing the OSL intensity for rapid retrapping to be derived.

$$\frac{\mathrm{d}n(t)}{\mathrm{d}t} = -n(t)^2\frac{\sigma\phi}{N} \tag{2.21}$$

$$I_{OSL}(t) \propto \frac{n_0^2\sigma\phi}{N}\left[1 + \frac{n_0\sigma\phi t}{N}\right]^{-2} \tag{2.22}$$

By analyzing the outcomes of the extreme cases discussed (1st-order (no-retrapping) and 2nd-order (very rapid retrapping)), general-order rate and intensity equations can be found.

$$\frac{\mathrm{d}n(t)}{\mathrm{d}t} = -\sigma\phi\frac{n(t)^y}{N^{y-1}} \tag{2.23}$$

$$I_{OSL}(t) = \frac{n_0^y\sigma\phi}{N^{y-1}}\left[1 + (y-1)\left(\frac{n_0}{N}\right)^{y-1}\sigma\phi t\right]^{-\frac{y}{y-1}} \tag{2.24}$$

These equations enable us to show analytic solutions of systems that vary greatly in retrapping rates. As y$\rightarrow$1 the above equation reduces to our first-order model and when y$\rightarrow$2 the above equation reduces to our second-order model. Figure 2.10 shows relative OSL intensity plotted against time for four different values of y. The higher the retrapping rate,

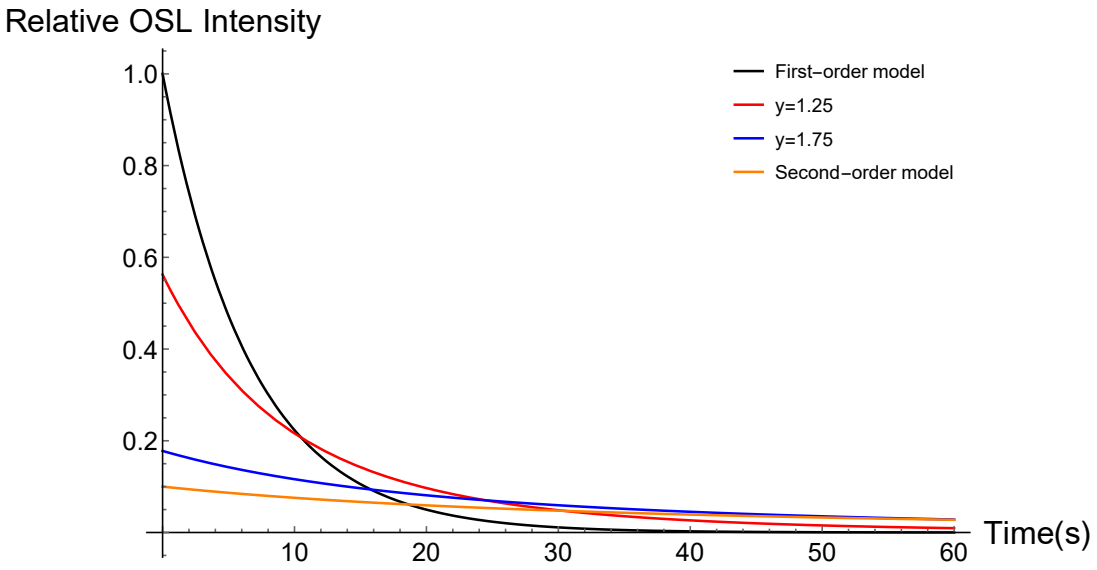

Figure 2.10: OSL curves of the general-order model with y values of 1 (first-order model), 1.25, 1.75, and 2 (second-order model). The parameters used to plot are n_0=10^{15} cm^{-3}, N=10^{16} cm^{-3}, and $\sigma\phi$=.15 s^{-1}. Plotted using equation (2.24).

the lower the initial intensity and the longer it takes the intensity to exponentially decrease.

Let us consider the same one-trap-one-recombination center model, but the trapped electrons are stimulated with heat instead of light. Thermoluminescence (TL) is different from OSL because the temperature is increased at a linear rate, $\beta = \frac{dT}{dt}$ [46]. The procedure for determining TL intensity is the same as before, except P_s (probability of thermal stimulation) is now defined by the following.

$$P_s = se^{-\frac{\Delta E}{kT}} \tag{2.25}$$

This states that the probability of thermal stimulation is equal to the attempt-to-escape frequency (s) times the Boltzmann factor ($e^{\frac{-\Delta E}{kT}}$). ΔE is the thermal depth of the electron trap, k is Boltzmann's constant, and s is a material constant that describes the attempts to escape per per second (usually between 10^{10} and 10^{16} s^{-1}). Based on the assumptions considered before and the new thermal stimulation probability, the time and temperature dependent form of TL intensity can be found.

$$I_{TL}(t,T) = -\frac{\mathrm{d}n(t)}{\mathrm{d}t} = n(t)se^{-\frac{\Delta E}{kT}} \tag{2.26}$$

Integrating by time and remembering that temperature increases linearly with time yields the 1945 Randall-Wilkins equation for first-order kinetics ($I_{TL} \propto n_0$) [47, 48]:

$$I_{TL}(T) = n_0 se^{-\frac{\Delta E}{kT}} \exp\left[-\frac{s}{\beta}\int_{T_0}^{T} \exp(-\frac{\Delta E}{kT'})dT' \right] \tag{2.27}$$

Garlick and Gibson modified this equation to second-order mechanics ($I_{TL} \propto n_0^2$) by allowing for retrapping in 1948 [49].

$$I_{TL}(T) = \frac{n_0^2 se^{-\frac{\Delta E}{kT}}}{N\left[1 + \frac{n_0 s}{\beta N}\int_{T_0}^{T} \exp(-\frac{\Delta E}{kT'})dT'\right]^2} \tag{2.28}$$

This led to the empirical general-order kinetics solution by May and Partridge in 1964 [50, 51].

$$I_{TL}(T) = \frac{n_0 s(\frac{n_0}{N})^{b-1} e^{-\frac{\Delta E}{kT}}}{\left[1 + \frac{s(\frac{n_0}{N})^{b-1}(b-1)}{\beta}\int_{T_0}^{T} \exp(-\frac{\Delta E}{kT'})dT'\right]^{\frac{b}{b-1}}} \tag{2.29}$$

Note that this solution is valid for all values except b = 1. As b→1 the above general-order solution reduces to our first-order model. When b→2 the above solution reduces to our second-order model. The retrapping rate, b, is usually assumed to be between 1 (no retrapping, first-order) and 2 (strong retrapping, second-order). Figure 2.11 shows equations (2.27), (2.28), and (28) plotted for temperatures between 270 and 400 K. The TL general-order model behaves the same as OSL general-order model: the signal decays more slowly as the retrapping rate increases. It is important to note the qualitative distinction between OSL and TL curves. OSL curves are comprised of one or more exponential decays, whereas TL curves are comprised of competing exponential functions.

The general-order model is convenient because it can be analytically derived. However, the entire solution is based on the premise of the OTOR model. That is, there is one trap

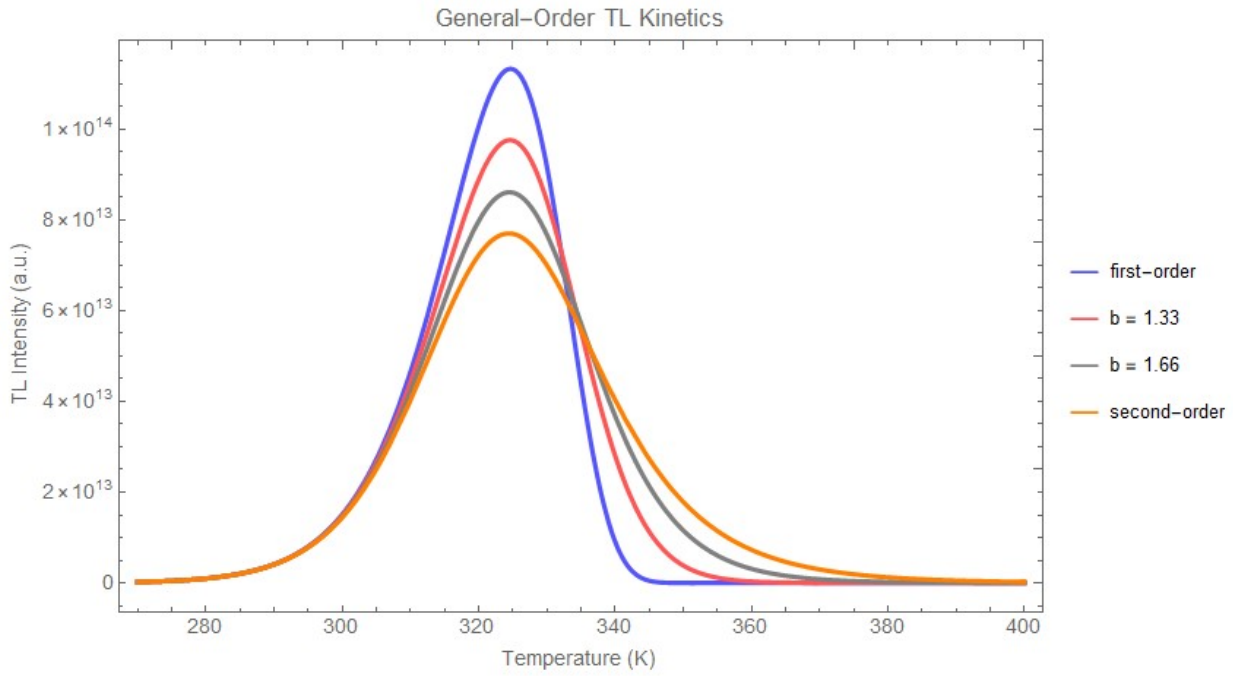

Figure 2.11: Comparison of differing kinetic orders of the general-order TL intensity solution. Constants used are $\Delta E = 1$ eV, $\beta = 1$ K/s, $s = 10^{13}$ s^{-1}, n_0=$N = 10^{17}$ cm^{-3}, and $k =$ 8.617x10^{-5} eV/K. The first-order solution (equation (26)) corresponds to b $\rightarrow$ 1 and the second-order solution (equation (27)) corresponds to b $\rightarrow$ 2.

and one recombination center. In reality, crystals contain traps at a variety of depths, each containing a different likelihood of electron migration back to the conduction band. Because this realistic system is much more complex than the simple OTOR model, numerical methods must be used to solve the system. Figure 2.12 displays a diagram of this more complex and realistic model containing multiple traps.

With this figure in mind, new rate equations can be written for a system with q traps and f recombination centers. In addition, the possibility of simultaneous thermal and optical stimulation can be considered. By comparing this new system to the rate equations for the OTOR model, the rate equation of the ith trap and the jth recombination center can be determined.

$$\frac{\mathrm{d}n_i(t)}{\mathrm{d}t} = [N_i - n_i(t)]P_{c,i}n_c(t) - n_i(t)\sigma\phi_i - n_i(t)s_i e^{-\frac{\Delta E_i}{kT}} \tag{2.30}$$

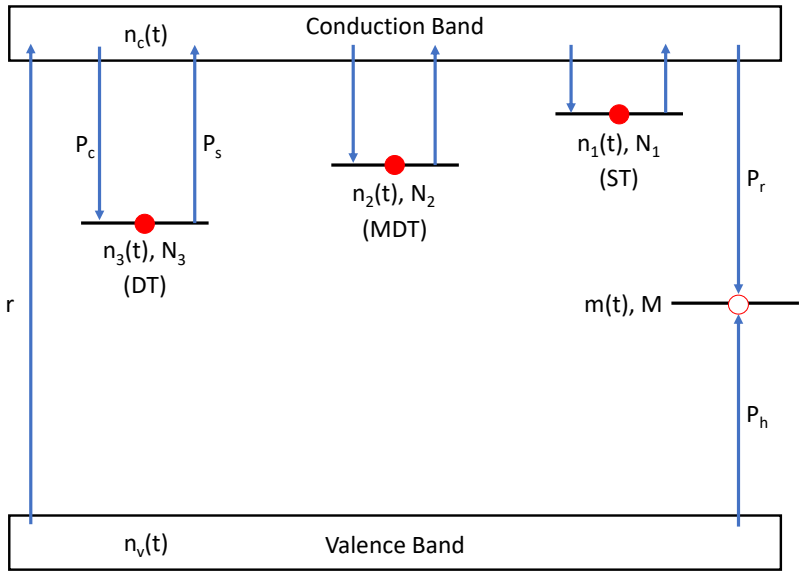

Figure 2.12: An OSL model that contains multiple electron traps, which occur at different depths. A realistic OSL process contains shallow traps (ST), deep traps (DT), and main dosimetric traps (MDT). Adapted from Yukihara and McKeever [16].

$$\frac{\mathrm{d}m_j(t)}{\mathrm{d}t} = [M_j - m_j(t)]P_{h,j}n_v(t) - m_j(t)P_{r,j}n_c(t) - m_j(t)s_j e^{-\frac{\Delta E_j}{kT}} \tag{2.31}$$

The rate equations for the conduction and valence bands can be constructed in the same fashion.

$$\frac{\mathrm{d}n_c(t)}{\mathrm{d}t} = r - \sum_{i=1}^{q}\frac{\mathrm{d}n_i(t)}{\mathrm{d}t} - \sum_{j=1}^{f} m_j(t)P_{r,j}n_c(t) \tag{2.32}$$

$$\frac{\mathrm{d}n_v(t)}{\mathrm{d}t} = r - \sum_{j=1}^{f}[M_j - m_j(t)]P_{h,j}n_v(t) - \sum_{j=1}^{f} m_j(t)s_j e^{\frac{-\Delta E_j}{kT}} \tag{2.33}$$

There are some electron-hole recombinations that do not contribute to the luminescence signal due to the presence of radiative and non-radiative recombination transitions (Γ_R and Γ_{NR}, respectively). This leads to the following radiative efficiency:

$$\eta = \frac{\Gamma_R}{\Gamma_R + \Gamma_{NR}}, \tag{2.34}$$

where the radiative transition rates can be defined in terms of radiative lifetime ($\Gamma_R = \tau_R^{-1}$ and $\Gamma_{NR} = \tau_{NR}^{-1}$) [52]. Translated, the radiative efficiency is defined as the probability of radiative transition over the total transition probability [16]. Gurney and Mott discovered that luminescence signals are strongly influenced by temperature, leading to what is now known as *thermal quenching* [53, 54]. Thus, the efficiency modifies to the following temperature dependent form:

$$\eta(T) = \Big(1 + K \cdot exp\Big(-\frac{W}{kT}\Big)\Big)^{-1}. \tag{2.35}$$

K is a constant without units and W is the activation energy, both of which depend on the luminescence center and therefore the emission band.

The astute reader will notice that luminescence has been described mathematically, but emission, absorption, and thermal quenching have not been explained. The configurational coordinate diagram (figure 2.13) shows the ground state and excited potential energy curves of a luminescence center as a function of the distance from the nucleus to the equilibrium position [55, 56, 57, 16]. The defect of interest is assumed to be r_0 distance away from its neighboring ions, and the crystal vibrations are assumed to oscillate harmonically. Thus, $m, n = 0, 1, 2$ represent the vibrational states of the oscillating crystal. The absorption and emission transitions (E_A and E_E, respectively) are shown by vertical arrows because they occur much faster than the crystal's relaxation (Franck-Condon principle, [55]).

Let us assume an electron is trapped in an excited recombination center state, $m = 2$ for example. This electron can undergo a non-radiative transition into the $m = 0$ state of the excited luminescence center via phonon emission. From this location in the diagram the electron can radiatively transition into a high vibrational state of the ground state ($n = 2$) by photon emission (E_E), before relaxing to the bottom of the ground state ($n = 0$) by phonon emission. From here the electron can be excited from the lowest vibrational ground state to a higher vibrational excited state via absorption (E_A). The configurational coordinate diagram accounts for the difference in emission and absorption energies of the luminescence

center. The absorbed photons are higher in energy than the emitted photons. This gives rise to the Stokes shift, which states that the emission band shifts to longer wavelengths than the absorption band. The magnitude of this shift depends on how strongly coupled the electrons are to their vibrating environment [16].

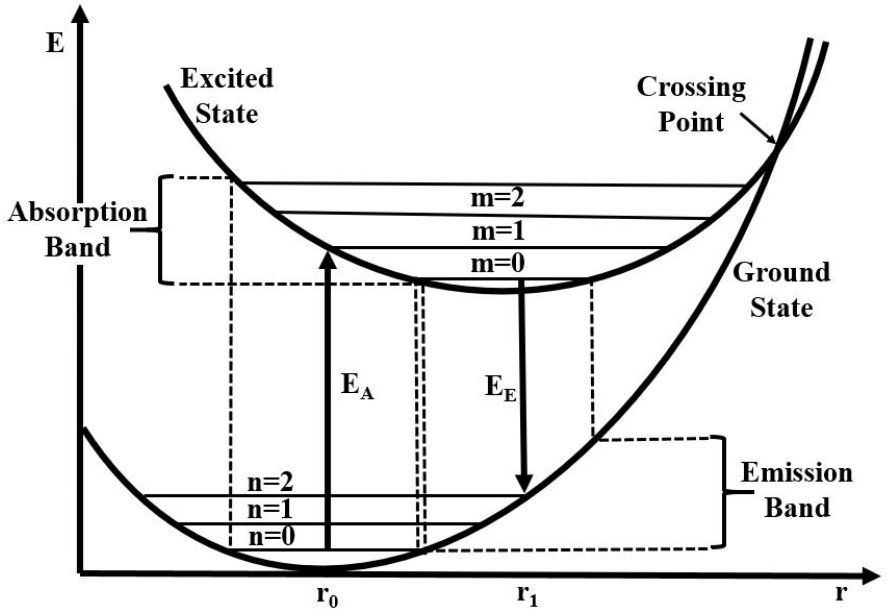

Figure 2.13: Configurational coordinate diagram showing the potential energy curves of the excited and ground states of a luminescence center versus r, the distance from nucleus to the equilibrium position. E_A is the absorption energy, E_E is the emission energy, r_0 is the equilibrium radius when the luminescence center is in ground state, and r_1 is the equilibrium radius when the luminescence center is in the excited state. The absorption band arises when the lowest vibrational ground state transitions to a higher vibrational excited state. The emission band arises when the lowest vibrational excited state transitions to a higher vibrational ground state. Adapted from Blasse and Grabmaier [56] and Nasdala et al. [57].

An important consequence of the configurational coordinate diagram materializes when ground and excited state parabolas cross. There is a likelihood that the luminescence center gains sufficient energy to reach vibrational levels at the crossing point solely through phonon interactions. The system can then relax to ground state by phonon emission through the ground state vibrational states when this occurs. Because the probability that the system has higher vibrational states increases with temperature, the probability of a non-radiative transition increases with temperature. Thus, the likelihood that luminescence centers recombine

and signal is lost increases with temperature (i.e. thermal quenching).

With this figure in mind, the non-radiative transition probability is stated as:

$$\Gamma_{NR} = \Gamma_0 \cdot exp\Big(- \frac{W}{kT}\Big), \tag{2.36}$$

where the activation energy, W, can now properly be defined as the energy required for the system to reach the crossing point. Plugging this equality into equation (2.34) yields equation (2.35), where $K = \Gamma_0/\Gamma_R$.

$$\eta(T) = \frac{\Gamma_R}{\Gamma_R + \Gamma_0 \cdot exp\Big(- \frac{W}{kT}\Big)} = \frac{1}{\Big(1 + K \cdot exp\Big(- \frac{W}{kT}\Big)\Big)} \tag{2.37}$$

Accordingly, the emission band, absorption band, and thermal quenching can all be explained via the configurational coordinate diagram.

2.4 Luminescence Dosimetry

The traditional method of characterizing a luminescence dosimeter's response to ionizing radiation is by constructing a dose response (figure 2.14a). Simply put, a dose response plots the magnitude of the luminescence signal versus exposure or dose. An ideal dosimeter's signal remains perfectly proportional to dose, up to very high doses. This is not realistic however, even when considering professionally manufactured materials. As dose increases, more and more traps are filled. Electrons in the conduction band have a decreased likelihood of encountering an empty trap and undergo direct recombination. Only trapped electrons contribute to the luminescence signal, so that the signal no longer increases with dose. This effect is called saturation. As such, it is necessary to investigate a given materials' response to different types of radiation.

The supralinearity function will be shown in conjunction with the dose response throughout this work because it aids in visualizing the linearity of a dosimeter and the magnitude

of its error by normalizing the signal response to linearity. It is defined as the signal-to-dose ratio along the response to the initial signal-to-dose ratio [58].

$$f(D) = \frac{S/D}{S_0/D_0} \tag{2.38}$$

A material's response can be described as supralinear (above linear) when $f(D) > 1$, linear when $f(D) \approx 1$, sublinear (below linear) when $f(D) < 1$, and saturated when signal no longer increases with dose. Figures 2.14a and 2.14b show the OSL response and supralinearity of BeO exposed to an ^{241}Am α source along nearly 5 orders of magnitude. The dose response is linear until 250 s, then supralinear until 20,000 s, followed by a sublinear response until saturation.

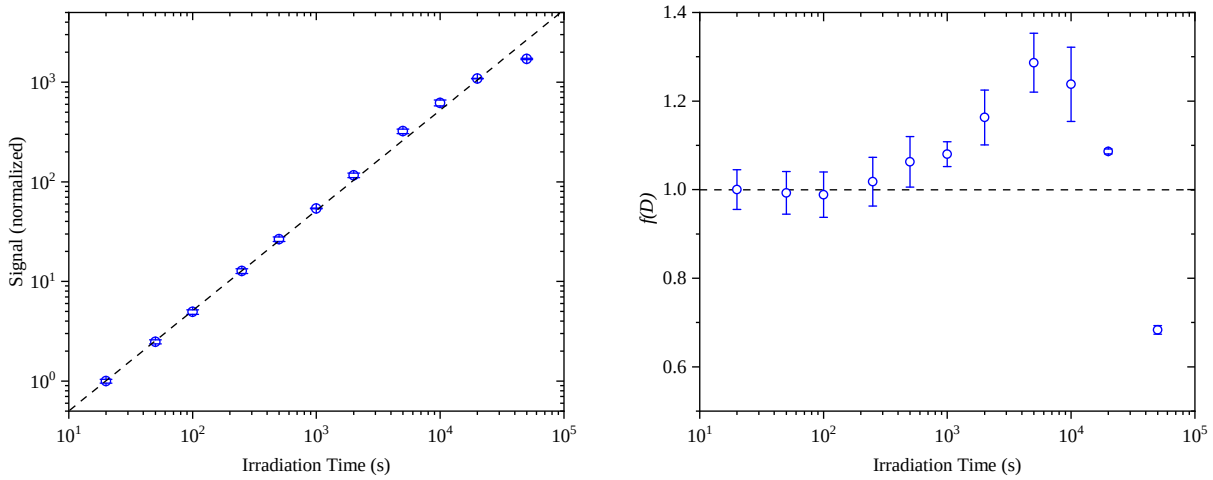

(a) (b)

Figure 2.14: OSL response (a) and supralinearity $f(D)$ (b) of BeO exposed to ^{241}Am α irradiation. The dashed line indicates a perfectly linear signal response. Points show the mean and standard deviation of multiple dosimeters.

This is a rather common 'linear-supralinear-saturation' response shared among many dosimeters. To the contrary, some materials have signals that saturate exponentially, and as such follow the 'linear-sublinear-saturation' model. The type of signal response is dictated by the material's intrinsic trapping mechanisms, which will be discussed in greater depth

later.

As a closing remark, is important to ensure that the signal measurement devices are operating within their respective proportional response ranges. Otherwise it cannot be ensured that signal response non-linearity is due to the dosimeter. For example, the PMT can become saturated and emit a lower electrical signal per unit of collected light if it exposed to a light intensity that is too great.

2.5 Heavy Charged Particle Tracks

It is important to consider not only the amount of energy deposited via radiation, but also the type of ionizing radiation that occurs. Low LET ionizing radiation (γ, β) impart dose in a near isotropic fashion. This strongly contrasts heavy charged particles (HCPs), which cause an inhomogeneous dose distribution due to a high ionization density near their particle tracks.

X-rays and photons are stochastic in nature and undergo three primary types of interactions as they pass through matter: the photoelectric effect, Compton scattering, and pair production. The energy of the incoming particle is transferred to orbital electrons in all three cases. These electrons undergo what is known as the tortuous path, where they deliver all of their energy via subsequent Coulombic interactions, resulting in a nearly uniform dose distribution.

Charged particle (electron or HCP) interactions are deterministic as they lose their energy over the course of many subsequent interactions, classified as either primary or secondary energy deposition events, according to the friction-like Continuously Slowing Down Approximation (CSDA). Energy is transferred from the charged particle to proximal electrons in a primary event, whereas electrons lose their energy in excitation and ionization further from the particle track in secondary events. There are 3 classifications of charged particle interactions with matter within the scope of this research, and their distinction is based

on the distance between the charged particle and atom of interest [59]. For the purpose of this research, nuclear interactions are not considered. They occur at energies well above the scope of this research and they are ignored in luminescence studies [43].

1)Soft collisions: When the charged particle is far from an atom it can energize the atom as a whole, occasionally creating ionizations in the form of ejected valence shell electrons. These interactions are easily the most probable charged particle interaction, and each interaction transfers a few eV to the absorbing atom.

2)Hard collisions: When the CP passes by approximately an atomic radius away, the likelihood that the CP interacts with in an individual electron increases, leading to the creation of δ rays. Additionally, Auger electrons and or X-rays will be emitted when an HCP interacts with inner shell electrons, similar to a photon interaction.

3)Coulombic interactions with external nuclear field: When the charged particle is well within the atomic radius, the nucleus is primarily responsible for CP interactions. Most ($\approx$ 98%) of these events are elastic and result in insignificant particle energy loss to the surrounding media. While this mechanism is not responsible for energy transfer, it is responsible for electron deflection (*tortuous path*). Inelastic radiative collisions are responsible for the other 2% of interactions, resulting in the emission of a photon from an electron via *bremsstralung*, or braking radiation.

When two HCP tracks overlap, the trail of interactions that each HCP leaves behind further interact, increasing the local dose deposition. This can be seen in figure 2.15, which shows the radial dose distribution of three overlapping HCP tracks as a function of d, separation between tracks [60]. Notice that the dose deposition, $D(r)$, is higher at radius r when the tracks overlap versus when they do not overlap. When fluence is low, particle tracks are far from each other, decreasing the radial dose distribution in the overlapping track region. As fluence increases, the tracks become closer in proximity until they finally interact, as seen in the figure below. At a certain fluence, the particle tracks are in such close proximity that overlap begins to effect the OSL signal by oversaturating the sample.

There are two primary areas of interest: directly along the track where the ionization density is very high, and further out where the ionization density is minimal. Signals directly along the track are approaching saturation, leading to a smaller signal-to-dose ratio than in areas with larger r.

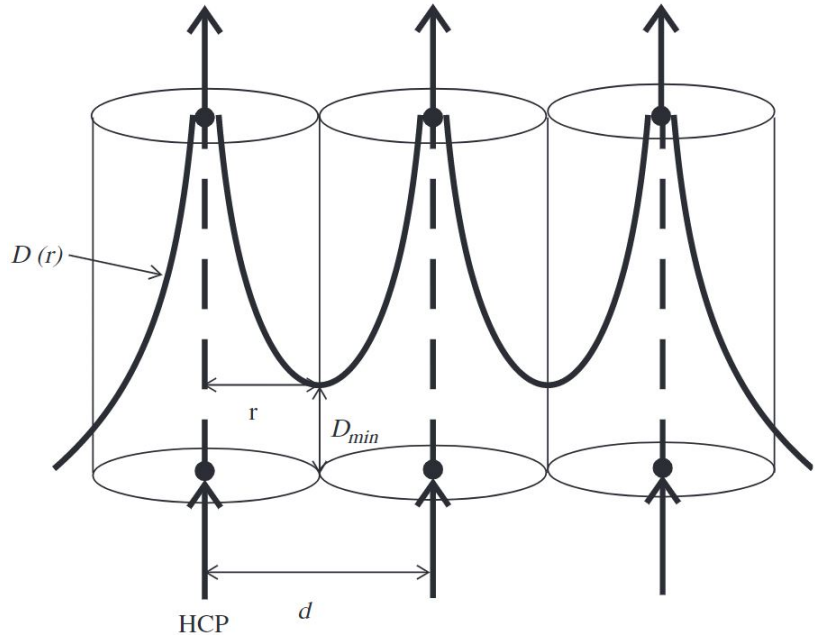

Figure 2.15: Illustration of three overlapping, parallel heavy charged particle tracks that are randomly distributed. *D(r)* is the radial dose distribution, d is the average seperation between tracks, and *d/2* is the point of intersection between two tracks which corresponds to the minimum *D(r)* value, reproduced from Sawakuchi et al. with permission [60].

A useful method of characterizing the interaction of HCPs with matter is by linear energy transfer (LET), or the mean energy deposited by ionizing radiation per unit path length. For heavy charged particles, the LET L can be found using the Bethe-Bloch formula:

$$\frac{L}{\rho} = 4\pi \frac{e^4}{m_0 c^2} \frac{N_A Z z^2}{A\beta^2} \left[\ln \frac{2m_0 c^2 \beta^2}{I(1-\beta^2)} - \beta^2 - \frac{C}{Z} - \frac{\delta}{2} \right] \tag{2.39}$$

where ρ is the physical density, N_A is Avogadro's number, β is particle velocity relative to light speed (v/c), m_0 is the electron rest mass, $N_A Z/A$ is the number of electrons per gram, z is the charge state, I is the mean excitation potential of the absorbing medium, and C and δ are correction factors [61, 59, 16]. It is evident that L varies with z^2/β^2, thus increasing

with particle size and decreasing with particle velocity and resulting in a drastic increase of LET near the end of the HCP path as the particle slows down. This behaviour describes the Bragg peak, which is defined by a low dose region at the beginning of the path followed by a sharp dose peak before the particle terminates. The Bragg peak is one of the major differences concerning the absorbed energy in a medium from HCP irradiation compared to γ or β, which have an exponentially decaying dose profile.

In conclusion, signal efficiency (i.e. the signal-to-dose ratio) decreases for two reasons: increasing the fluence until overlapping traps cause trap saturation, or increasing particle LET so that the individual tracks deposit enough energy locally to saturate available traps along the track.

Chapter 3

Experimental Methods

The previous chapter discussed the origin of luminescence signal and the impact of ionization density on trapping of charges. It was shown that the high ionization density of particle tracks can lead to saturation of the signal on the microscopic scale. The goal of this dissertation is to investigate the impact of ion-irradiation parameters, such as ion type and energy, on luminescence properties of dosimetric materials. A beamline was designed, constructed, and tested for this purpose. In this chapter I present the accelerator facility, describe the beamline, and discuss properties of the ion beams utilized in the proceeding experiments. I also describe the instrumentation utilized for luminescence measurements.

3.1 Heavy Charged Particle Irradiation

The East Carolina University physics department accelerator laboratory is equipped with a 2 MV tandem particle accelerator, which is utilized by many research groups. The research conducted in this lab is cross-disciplinary, with an emphasis in biology and medicine, as well as particle physics. Generally speaking, there are three primary experimental components in the accelerator lab: the ion source, the particle accelerator, and the beamline and target chamber. Figure 3.1 gives an overview of the accelerator lab components utilized for luminescence studies. The ions are created in the Cesium ion sputter source, which are then

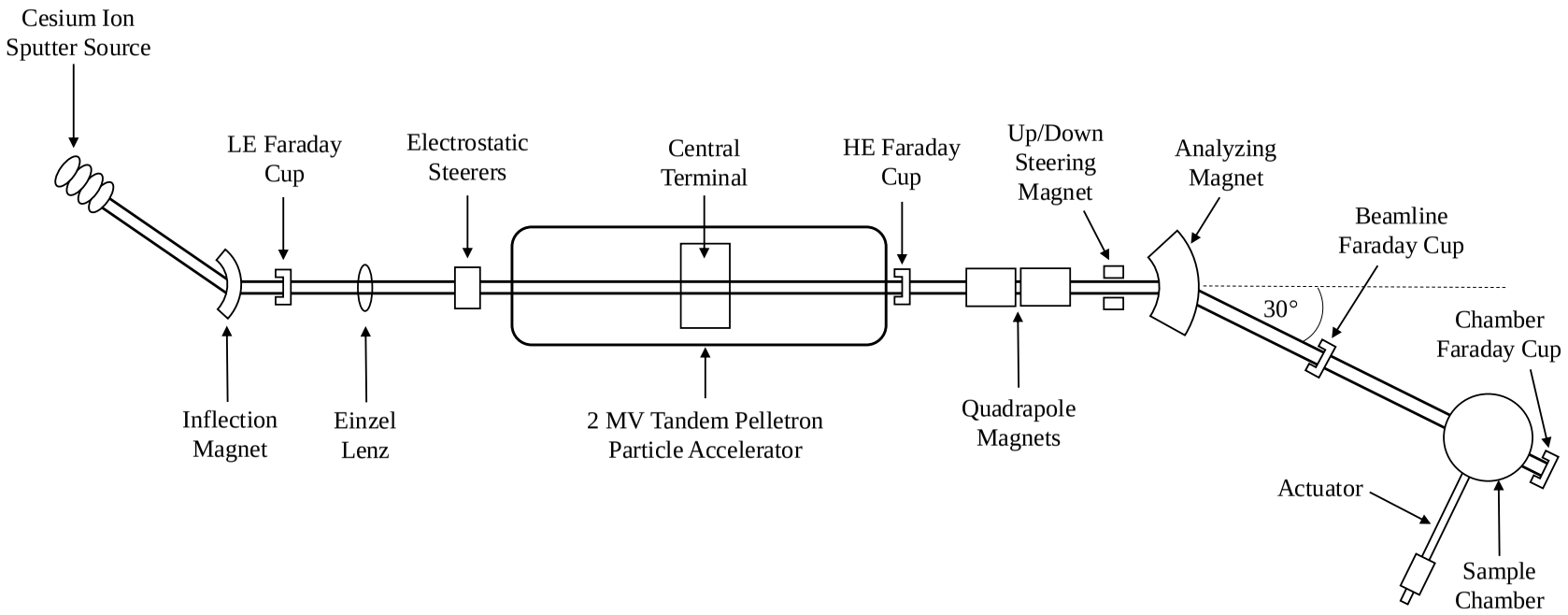

Figure 3.1: Simplified aerial schematic of the ECU accelerator lab, consisting of the ion source, particle accelerator, beamline, and sample chamber.

ejected into the particle accelerator, where they are sped up. These accelerated ions are then steered into a selected beamline by the analyzing magnet before reaching the target chamber.

3.1.1 Ion Source

In 1982 Roy Middleton designed a high-intensity sputter source, a variation of which is currently used in the accelerator lab. The design is quite prolific, allowing creation of almost all ions except noble gases. Beam current is highly variable up to values of hundreds of μA, depending on the source settings and ion type. By contrast, very low source output may be desirable and is made possible by lowering the oven temperature.

First, a solid Cesium reservoir is baked via an insulated heater to approximately 60°C. This temperature turns some Cesium to vapor, which is then injected into the tantalum ionizer (essentially a heated coil). At about 1100 °C the Cesium phase changes into plasma. The now positively charged Cs^+ nuclei are accelerated towards the negatively charged target cathode, which emits ions upon collision (*sputtering*).

The type of powder loaded into the cathode shell dictates the variety of ion species created. For example, a cathode shell packed tightly with TiH_2 powder will produce H^- ions. The ions undergo an acceleration of approximately 6 kV via the combined cathode and source voltages. A subsequent 30 kV linear accelerator increases the potential of exiting particles to approximately 36 keV.

Most cathode powders loaded into the source result in a smattering of sub-molecular species. Thus, the inflection magnet and electrostatic steerers (see figure 3.1) are calibrated to discriminate for the desired ion type by means of the charge state and also to center the beam, respectively. The electrostatic Einzel lens ensures that a focused negative ion beam enters the low energy portion of the accelerator after particles are inflected.

3.1.2 Particle Accelerator

Figure 3.2 is a basic schematic of the 2-MV tandem NEC 6SDH-2 Pelletron model accelerator found in the ECU physics accelerator lab. The accelerator behaves similar to a Van der Graaf generator in the way the charging chain picks up and deposits charge in the central terminal. The chain is comprised of alternating conducting and insulating links, or *pellets*. As this chain rotates it creates a positive bias in the central terminal, which can reach values up to +2 MV. 20 Equally spaced insulator rings connected to a resistor chain make up the accelerator columns, or gradient rings, and ensure that a constant electric field is created along the path of the ions.

For example, an H^- ion will experience a 200 KeV acceleration between each gradient ring if the central terminal is set to 2 MeV. Negative ions enter the accelerator from the left and are attracted to the positively charged central terminal. Once the ions reach the terminal, the N_2 stripper gas removes two or more electrons from the the negative ions. These now positive ions undergo a second acceleration when they are repelled away from the positive central terminal to the grounded high energy side of the accelerator, hence the name *tandem*.

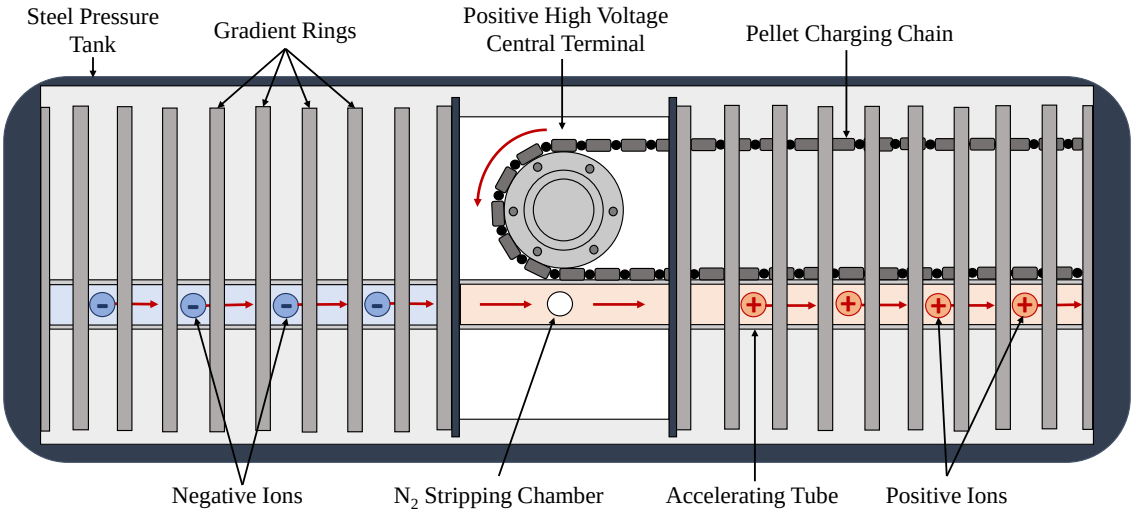

Figure 3.2: Basic schematic of the ECU 2 MV tandem pelletron National Electrostatics Corp. particle accelerator.

When the accelerator is operating at maximum voltage, particles will gain a maximum of 2 MeV for every negative elementary charge entering the central terminal and a maximum of 2 MeV for every positive elementary charge exiting the central terminal. For instance, C^- ions that are stripped to C^{2+} ions at the central terminal will produce a monoenergetic 6 MV Carbon beam (2 MeV·1 + 2 MeV·2). Sulfur hexafluoride (SF_6) is injected around the vacuum sealed drift tube to prevent electrical discharge from the high voltage central terminal. Finally, the analyzing magnet (see figure 3.1) is used to steer the previously selected specie of ions into the R30 luminescence beamline.

3.1.3 Inflection and Analyzing Magnet Calculations

Because particle energy is a multiple of the central terminal voltage and the sum of the charge magnitude entering and exiting the accelerator, a thorough investigation of parameter space is necessary to ensure that the correct ions entering and exiting the accelerator are selected. This entails determination of the inflection and switching magnet currents required to select specific ions via their charge-to-mass ratio.

A cathode loaded with titanium hydride will produce prolific H^- beam with negligible molecular contribution [62]. These negative ions can only be stripped to H^+ via the N_2 stripper gas, resulting in a single, intense peak downstream of the accelerator. In this way, Hydrogen beam presents a unique case where particle charge state is known a priori. This enables calculation of parameters necessary for describing more complex cathodes containing many atomic and molecular species.

To understand the calculation of the parameters let's start with the Lorentz force F_L, which supplies the centripetal force F_c for a charged particle with velocity v and charge q moving inside of a magnetic field B.

$$F_L = F_c \tag{3.1}$$

$$q(\mathbf{E} + \mathbf{v} \times \mathbf{B}) = \frac{mv^2}{r} \tag{3.2}$$

It can be assumed that the magnetic field dominates the Lorentz force near vacuum conditions and in the presence of a magnet (i.e. $\mathbf{B} \gg \mathbf{E}$). If we also assume that the magnetic field is uniform inside the region of interest and perpendicular to particle motion, the magnitude of the magnetic field can be solved.

$$B = \frac{mv}{qr} \tag{3.3}$$

Here, $v = (2E/m)^{1/2}$ and is the particle velocity in m/s, m is particle mass in amu,r is the radius of curvature in m, and q is the number of elementary charges. It is important to note that B is assumed to be linear with respect to magnet current i, thus $B \propto i$. From here we get the famous relation; the current required to select a certain atomic specie depends on the charge-to-mass ratio.

$$i \propto \frac{mv}{q} \tag{3.4}$$

This relation can be solved for the inflection and analyzing magnets without knowing B or r, because it is known that q equals -1 and +1, respectively. Once this proportionality is solved for protons, the current values required to obtain species of more complex cathode can be easily obtained via charge-to-mass ratios.

A cathode packed with graphite produces a plethora of poly-atomic, negative Carbon-based ions [62]. Therefore it is necessary to justify that the peak selected is the desired ion. Tables 3.1 and 3.2 show the parameters and expected currents required to select various Carbon based ions in the inflection and analyzing magnets, respectively. These tables were used to identify which ions constitute beam for a given magnet current. It is important to mention that these are only a selection of the most prolific ions, which does not include the numerous molecular species for the sake of brevity. An inflection magnet setting of 6.86 A

was required to obtain the C^- peak, resulting in a difference of 0.436% between the expected and experimental current values. An analyzing magnet setting of 93.30 A was required to obtain C^+ in the chamber, resulting in a difference of 0.423% between the expected and experimental values.

Molecule	C^-	C^{2-}	C^{3-}	C^{4-}	C_2^-	C_2^{2-}
charge (electron)	1	2	3	4	1	2
mass (amu)	12	12	12	12	24	24
velocity (m/s)	7.70E5	1.09E6	1.33E6	1.54E6	5.45E5	7.70E5
current (A)	6.89	4.87	3.98	3.44	9.74	6.89

Table 3.1: Expected inflection magnet currents for various Carbon based ions. The sum of the cathode, source, and linear accelerator voltages at the source equals approximately 38 kV.

Molecule	C^{5+}	C^{4+}	C^{3+}	C^{2+}	C^+
charge (electron)	5	4	3	2	1
mass (amu)	12	12	12	12	12
velocity (m/s)	1.39E7	1.27E7	1.13E7	9.82E6	8.03E6
current (A)	32.3	36.9	44.1	57.3	93.7

Table 3.2: Expected analyzing magnet currents for various Carbon based ions. These values assume a 1.99 MV central terminal setting and 38 kV combined source voltage.

3.1.4 Beamline and Sample Chamber

Figure 3.3 shows an aerial schematic of the luminescence beamline and its primary components. This beamline was designed and constructed as part of this dissertation. There are two manual gate valves: one between the analyzing magnet and beamline, and one between the second set of bellows and the sample chamber. The first gate valve is necessary to isolate the beamline from the accelerator when the line is not in use. The sample chamber and actuator need to be brought up to air and back down to vacuum every time new samples are loaded into the sample transfer port. The second gate valve allows the primary beamline to stay at vacuum when samples are switched, which greatly reduces the time required to

evacuate the chamber between sample irradiations. Two sets of bellows are spread out along the beamline. They allow slight beamline movement, enabling proper alignment and easing maintenance and repair.

There are two pressure gauges, one behind the chamber and one centralized in the line. Both gauges are located near their respective rough and turbo pumps, which cannot be seen in the figure because they are located underneath the line and chamber. The accelerator and beamline pressures should both be monitored when the gate valve near the analyzing magnet is opened. The pressure in the chamber needs to be critically monitored every time the chamber is brought down to vacuum. The rough pump alone is used to get the pressure to about 10^{-3} Torr, at which point the turbo pump can be turned on. Pressures should be in the 10^{-6} Torr range before opening the beamline gate valve.

A beam profile monitor located before the beamline Faraday cup provides spatial information about the beam. The monitor is essentially an oscilloscope containing a wire that rotates at 45 degrees. Graphs of the beam in the x and y directions can be visualized at the accelerator control booth utilizing the information obtained by the monitor. There are two Faraday cups used to measure current in the luminescence line: one before the slits and one after the chamber. The first cup is used as a preliminary current measure, and ensures that that the quad, analyzing, and up/down magnets are correctly calibrated. The chamber Faraday cup is wired to a variable gain amplifier and low noise cable to measure current accurately and precisely, as the values from this cup are used for absorbed energy calculations. The last beamline elements before the chamber are the collimation slits, which enable controlled and measurable shaping of the beam into any square or rectangular area up to 35 mm x 35 mm, approximately.

The back of the chamber is equipped with a YAG scintillator and camera, which are used for beam monitoring and will be discussed in great detail later. A sample transfer port is mounted between the chamber and the actuator motor, enabling the attachment of the sample holder to a motorized actuator. This labVIEW programmed actuator extends

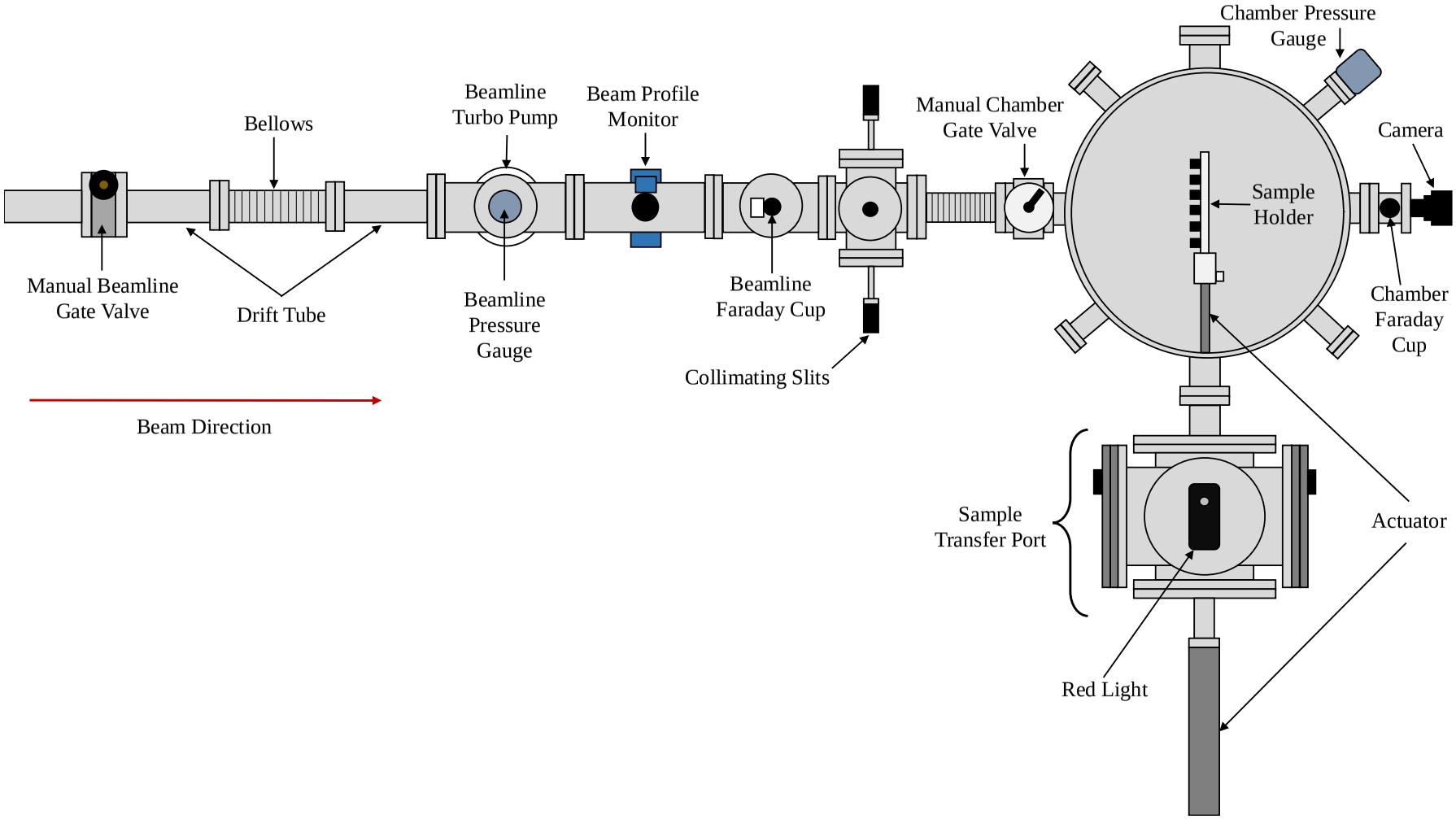

Figure 3.3: Aerial schematic of the ECU luminescence beamline, sample chamber, and actuator.

various samples into the center of the beam path at quarter mm precision. The sample port is equipped with two vacuum-tight doors and a red light for visibility. The doors are necessary to expedite the evacuation process after the samples have been loaded. It should be noted that a light-tight infrastructure surrounds the entire actuator and sample port so that the samples are not ruined post-irradiation by fluorescent light exposure.

The luminescence beamline (Figure 3.4) took about two and a half years to build, test, and make fully operational. See Appendix B for more photos and information.

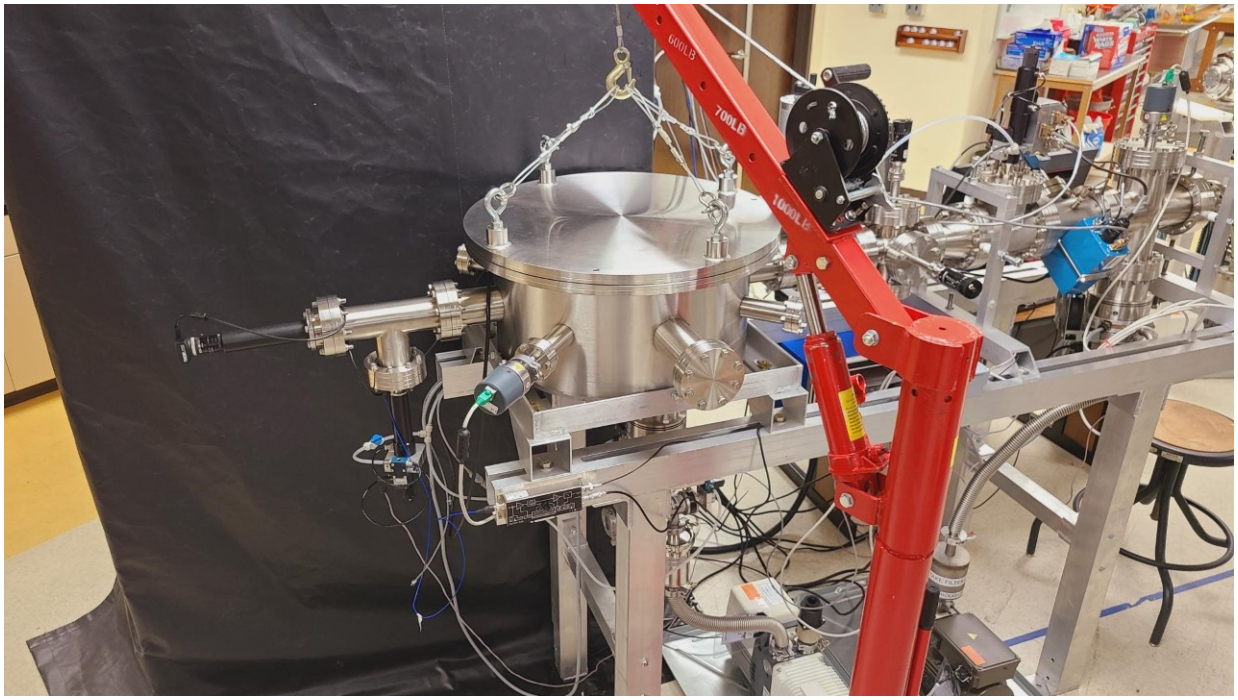

Figure 3.4: Fully operational ECU luminescence beamline.

3.2 Beam Specific Parameters

3.2.1 Energy Calculation

When investigating the luminescence properties of various materials, it is necessary to assign an absorbed dose or energy value to all measured signals. Absorbed dose D is directly connected to absorbed energy [59].

$$D = \frac{\mathrm{d}\bar{\epsilon}}{\mathrm{d}m} \tag{3.5}$$

Here, $\bar{\epsilon}$ is the absorbed energy (the sum of all energy entering the volume minus the sum of all energy departing the volume) and m is the mass. Quantifying the denominator in the equation above is quite trivial ($m = \rho V$), meaning the primary task becomes calculating absorbed energy.

It is necessary to discuss a critical caveat concerning dose calculations. Projected range increases drastically with increasing ion energy, and the "range" for a certain ion energy is an average of a penetration depth distribution. The proton energies used in this research result in penetration depths considerably smaller than the dosimeter thickness (Figure 3.5). As a consequence, the concept of energy absorbed per unit mass is misleading, since the mass penetrated by particles varies with energy. For this reason, HCP results are reported in absorbed energy instead of absorbed dose.

There are a couple of assumptions that must be addressed for absorbed energy calculation. First, it is assumed that the beam is completely attenuated by the sample (i.e, the stopping range is less than the sample thickness). This assumption is verified using the SRIM-2008 (The Stopping and Range of Ions in Matter)[1] software for all ion, energy, and sample choices [63]. Secondly, it is assumed that the fluence-rate inside of the collimated area is uniform, which will also be discussed in greater depth below.

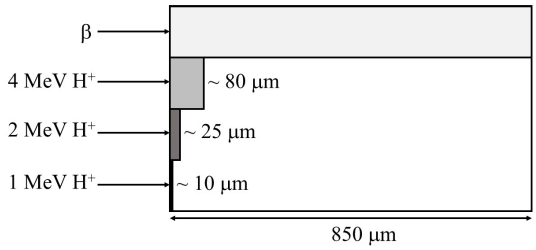

Figure 3.5: Graphic displaying SRIM ranges of various proton energies versus that of β in Al_2O_3:C [63].

[1] http://srim.org, last accessed on May 2, 2021.

Absorbed energy $\bar{\epsilon}$ was calculated by multiplying the energy per particle E times the number of incident particles N. i is the current of the beam measured in the chamber Faraday cup, t is the exposure time, n is the particle charge state, and (A_s/A_b) is the ratio of sample area to incident beam area. A correction factor of 10^6 is required to get particle fluence from current and obtain units of J (i.e. $\left(\frac{6.241 \cdot 10^{18} \mathrm{e}^-}{\mathrm{C}}\right)\left(\frac{1\mathrm{J}}{6.241 \cdot 10^{12} \mathrm{MeV}}\right)$). Absorbed energy errors were calculated using the relative uncertainty of all variables above.

$$\bar{\epsilon} = EN = 10^6 \frac{EitA_s}{nA_b} \tag{3.6}$$

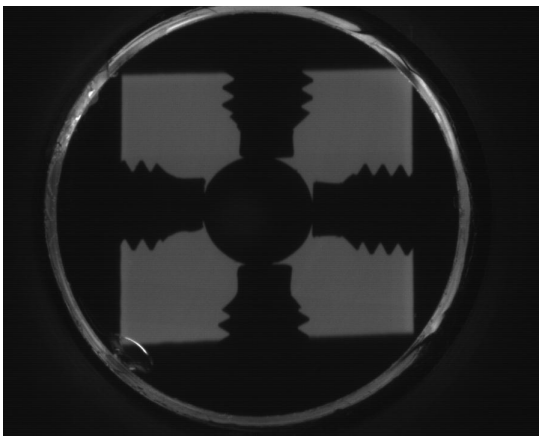

Figure 3.6: Camera view of 5 mm diameter Al_2O_3:C chip centered inside of a rectangular collimated beam. This image is meant to give an approximate ratio of the sample surface area to the beam surface area measured by the chamber Faraday cup.

3.2.2 Beam Uniformity

The beam created by the Cesium sputter source is Gaussian in nature, with a peak at its center that rapidly falls off to each side. However, the quad magnet strength and balance can be adjusted to centralize and spread out the beam, resulting in uniform beam over the monitored surface area. The key to obtaining a uniform beam lies in the ability to monitor flatness and symmetry as the current in the magnets are adjusted. A YAG (Yttrium Aluminium Garnet) scintillating crystal glued to a viewing window is attached to a high frame rate-camera in the back of the chamber. This camera allows for real time monitoring

of the light intensity output of the scintillator using ThorCam[2] imaging software. The light intensity of the YAG crystal is proportional to incident current. The intensity profile can therefore be used to obtain a uniform fluence-rate beam via quad, up/down, and switching magnet modulation.

The 3D surface plot of a typical uniform beam can be seen in figure 3.7. The variability in the color scale indicates spread in light intensity values. The beam is nearly uniform across its surface, with some small instantaneous statistical fluctuations. The associated histogram and uniformity statistics can be found in figure 3.8. The beam histogram is visibly sharp, unimodal, and symmetric, with noise equal to 3.3% of the mean signal. As mentioned before, this intensity standard deviation is instantaneous only, such that the current can be considered uniform given sufficient time. The instantaneous noise is a function of the sputter source itself and the current magnitude utilized. As current is increased, the signal-to-noise ratio (SNR) increases.

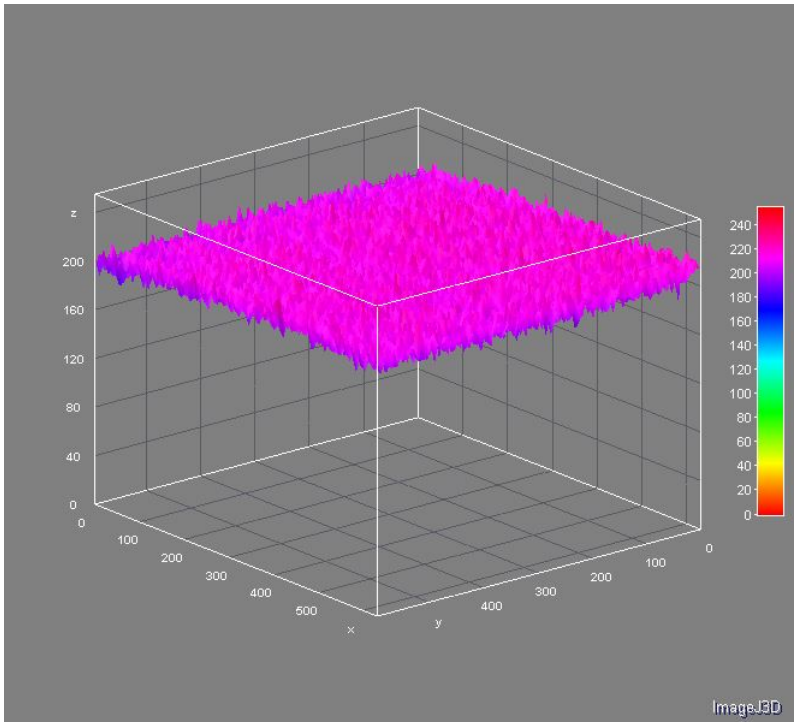

Figure 3.7: 4 MeV/u H^+ beam 3D surface plot using ImageJ software.

[2] https://www.thorlabs.us/software_pages/ViewSoftwarePage.cfm?Code=ThorCam, last accessed on May 2, 2021.

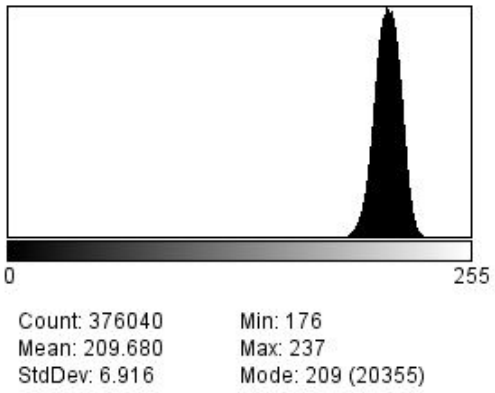

Figure 3.8: 4 MeV H^+ beam light intensity pixel histogram.

Because the YAG crystal is a very critical component in measuring and ensuring beam uniformity, steps were taken to investigate the spatial resolution and lateral light intensity spread through the YAG crystal. The scintillator is disc shaped with a diameter of 20 mm and a thickness of 2 mm. A visible green laser in combination with a 30 dB optical filter were used to measure the light effects of the scintillator via ThorCam light intensity analysis software. Initially, the YAG scintillator was frosty/unpolished on one side, causing extreme scatter in the departing light signal, as can be seen in figure 3.9. This level of scatter rendered the YAG crystal useless, therefore it was professionally polished to add clarity and obtain desirable luminescence properties. Figures 3.10a and 3.10b show the raw (no scintillator) 2D and 3D light intensity plots of the green laser. The scale in the 2D plot is in units of μmeters, indicating the laser has a diameter of approximately 1 mm. The polished YAG 2D and 3D light intensity plots can be seen in figures 3.10c and 3.10d.

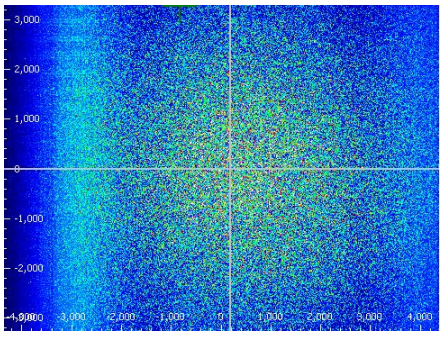

Figure 3.9: 2D light intensity plot of a green laser through an unpolished YAG scintillator.

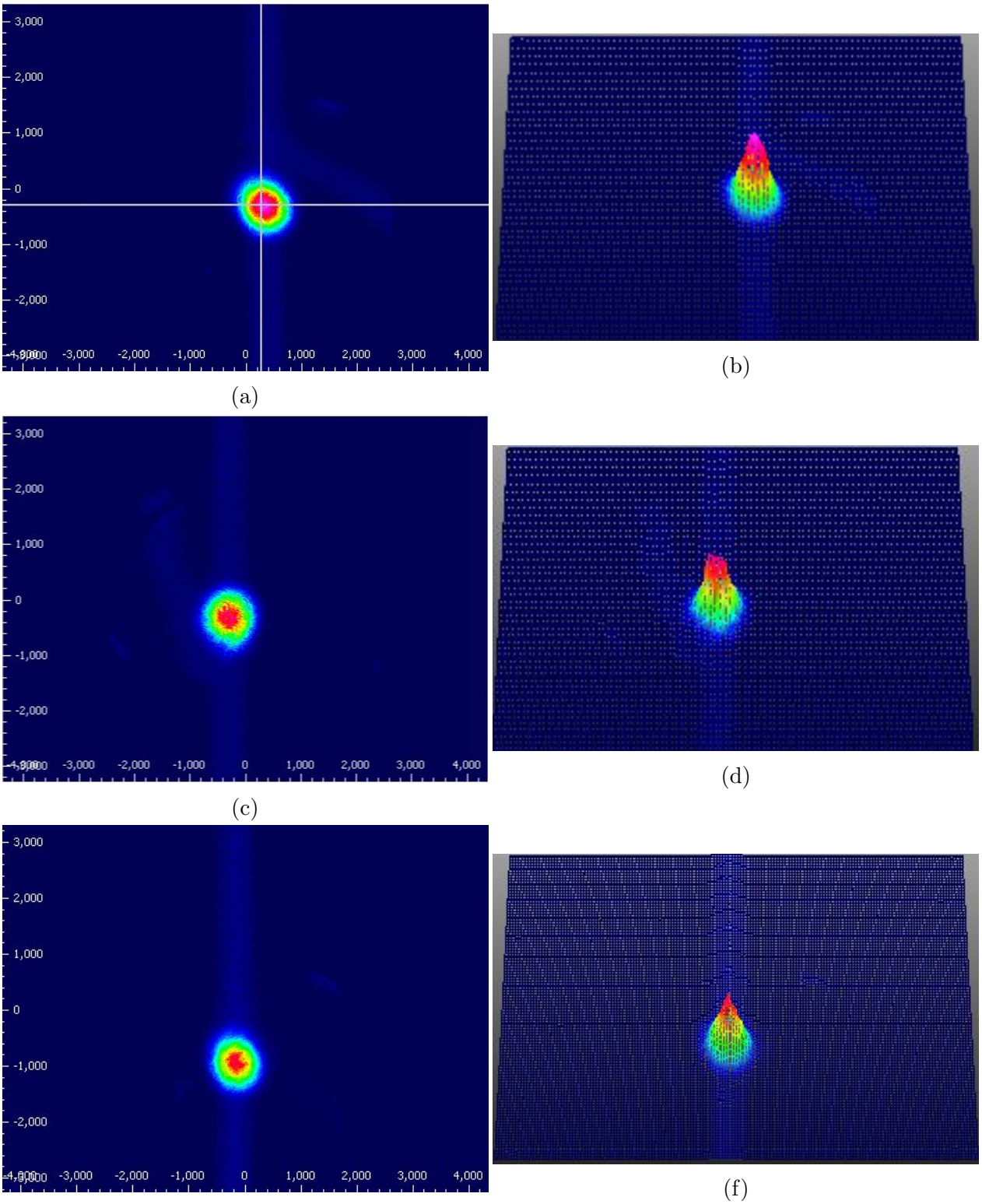

(a) (b) (c) (d) (e) (f)

Figure 3.10: 2D and 3D light intensity plots of a green laser through a 30 dB optical filter ((a) and (b)), a 30 dB optical filter and YAG scintillator ((c) and (d)), and a 30 dB optical filter and YAG scintillator glued to a viewing window ((e) and (f)).

While the symmetry and shape are well preserved when the polished YAG crystal filtered the laser, there was some peak intensity loss due to lateral scattering of the light along the 2 mm crystal thickness. This can be seen as a slight loss of the pink area/volume in figures 3.10c and 3.10d compared to figures 3.10a and 3.10b. Since the entire beamline must be kept at very low pressures, optically clear superglue was used to attach the polished YAG scintillator to a vacuum tight viewing window. Minimal blurring occurs with the addition of the viewing window and superglue (Figures 3.10e and 3.10f). However this was inevitable because the YAG crystal needed to be attached somehow.

In conclusion, the current experimental set-up conserves signal shape, spread, and symmetry while some clarity and peak signal intensity is lost. However, this loss of spatial resolution occurs on a scale that does not impede experimentation. The blurring occurs on the micrometer scale while the beam has dimensions of approximately 13 mm x 13 mm and the samples have areas of approximately 16 mm^2 and 22 mm^2. This ensures the YAG crystal is sufficient to measure beam surface area. Additionally, the slight loss in signal intensity is not detrimental, as quantifying signal intensity is not necessary.

3.2.3 Beam Surface Area

The ImageJ software[3] allows for precise measurements of irregular shapes by finding the area in $pixels^2$. By scanning an object of known size, such as the 20 mm diameter YAG crystal seen below (figure 3.11), pixel can be converted to length. The settings required to get beam on target and uniform are slightly different every time samples are irradiated, resulting in differing beam area, hot spots, cold spots, and artifacts such as the missing surface area seen in figure 3.11. The collimators may require slight adjustment each time a new beam is obtained to ensure that there are no hot or cold spots along the beam edges.

The ImageJ software is needed to obtain a new A_b value and associated uncertainty every time a new beam is on target. It is clear that the YAG crystal spatial resolution loss

[3] https://imagej.net/ImageJ, last accessed on May 2, 2021.

discussed in the previous section does not introduce significant error when calculating A_b.

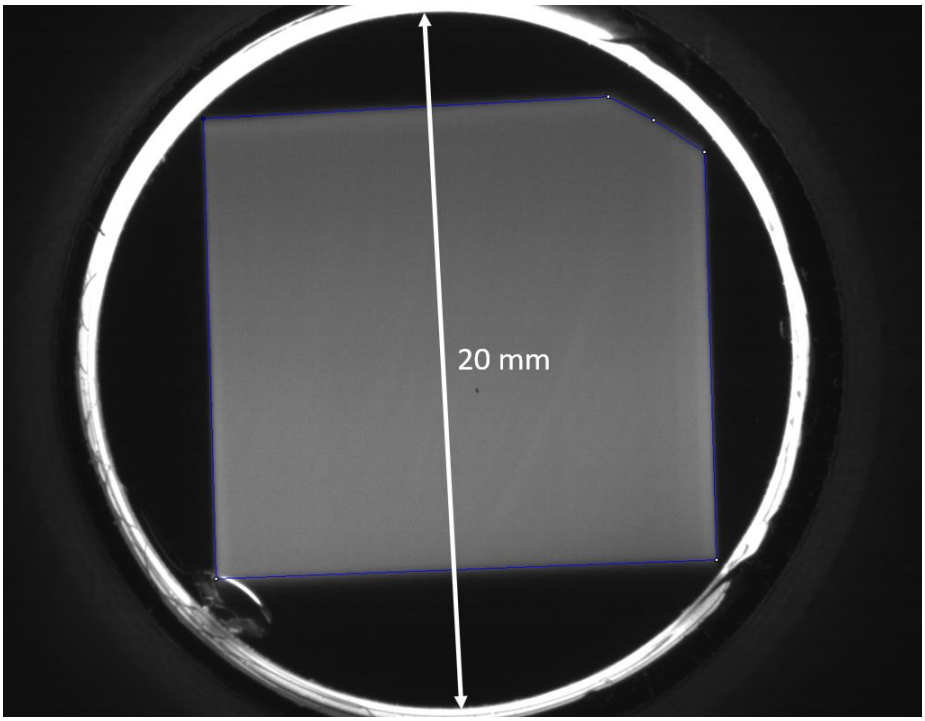

Figure 3.11: Surface area of an irregular Hydrogen beam using ImageJ software.

3.2.4 Exposure Time

The cup in the primary beamline acts as a shutter controlled by a LabVIEW program, allowing for exposure time input with sufficient precision. Once data is ready to be collected, the beamline cup is placed in position so that it absorbs the entire beam. Rearranging equation (2.32), with a specific absorbed energy in mind, will yield the required exposure time. When activated, the pneumatic Faraday cup will quickly move to the "out" position so that the sample is exposed for the desired time, followed by quickly moving back "in".

3.2.5 Sources of Error

Experimental sources of error when calculating absorbed energy include particle energy (E), current (i), shutter time (t), collimated beam area(A_b), and sample surface area (A_s). The traditional forms of mean, standard deviation, and standard error were used, when

pertinent.

While some of the errors listed above are significant, some are very small. Beam energy is almost perfectly monoenergetic once the beam is given adequate time to calibrate to its parameter settings. For instance, a central terminal voltage setting of 1.000 MeV will yield actual energy values that fluctuate between 0.998 MeV and 1.002 MeV, meaning E has an uncertainty significantly below half of a percent. The relative uncertainty varies with the central terminal voltage setting.

Both sample types are professionally manufactured and cut, but are not perfectly consistent in size. 10 Al_2O_3:C dosimeters and 10 BeO dosimeters were measured using a high precision caliper. The Al_2O_3:C samples have a mean surface area of 16.0 mm^2 and a relative surface area standard deviation of 0.4 %, while the BeO dosimeters have a mean surface area of 22.1 mm^2 and a relative surface area standard deviation of 0.4 %.

The beam surface area uncertainty arises from collimator penumbras and YAG/camera resolution limitations. Beam surface area values are found for the inner and outer edges of the penumbra, then A_b is assumed to be the average of the two values. The error is taken to be one half the difference between the outer and inner penumbra areas. Beam surface area uncertainty is typically less than 1%.

Since samples absorb the entire beam, there is a very rapid build up of absorbed energy. Thus, very low currents are sought to increase exposure time. The desired current is around 100 pA. A modular gain amplifier is used to magnify the current, before measurement, to mitigate the effect of noise and ensure precise current measurement. Beam current standard deviation typically fluctuates from below 1.5% in the pA range to significantly less than 0.5% in the nA range.

The pneumatic beamline Faraday cup is the biggest source of error, especially for very quick irradiations ($\sim$ 1s). After using Super Sound software to analyze 10 different shutter times, ranging from 1 seconds to 25 seconds, the standard deviation between input time and actual exposure time was found to be 0.10 seconds.

Variable	Typical Values	Typical Uncertainty
E	1-8 MeV	0.1%-0.4%
i	∼100 pA	0.1 %-1.5%
t	0.5s-500s	0.1%-20.0%
A_b	165 mm^2-175 mm^2	0.5%-1.0%
A_s	16.0 mm^2, 22.1 mm^2	0.4%

Table 3.3: Typical values and relative uncertainties for variables used to calculate absorbed energy.

3.3 Risø OSL/TL Reader Modalities

All luminescence measurements were performed with a Risø TL/OSL DA-20 reader (aka "The Risø") in the luminescence laboratory at ECU [64]. The reader is also equipped with radioactive β and α sources that were used for calibration measurements and comparisons with ion-irradiations.

3.3.1 β and α Source Irradiation

The Risø TL/OSL DA-20 reader used in this study is equipped with a ^{90}Sr/^{90}Y β-source and a ^{241}Am α-source. These were used for calibration and comparison purposes to irradiate samples before measurement, instead of exposing samples to the ion beam in the accelerator lab. The β and α sources are useful in testing a variety of sample characteristics such as uniformity, repeatability, and fading. Additionally, dose response curves using β and α irradiation provide baseline saturation values. Signal differences between β particles, α particles and HCPs can be compared to determine if effects specific to HCPs are occurring.

Radioactive $^{90}_{38}$Sr undergoes two β^- decays, first into $^{90}_{39}$Y, and then into $^{90}_{40}$Zr.

$$^{90}_{38}\mathrm{Sr} \rightarrow ^{90}_{39}\mathrm{Y} + ^{0}_{-1}\beta + \overline{\nu_e} \rightarrow ^{90}_{40}\mathrm{Zr} + ^{0}_{-1}\beta + \overline{\nu_e} \tag{3.7}$$

Each decay creates an energy spectrum with the release of an electron and neutrino. The

associated decay scheme and energy spectra can be seen in Figures 3.12a [65] and 3.12b [66]. The $^{90}_{38}$Sr transition has a peak energy of 546 KeV and the $^{90}_{39}$Y transition has a peak energy of 2.28 Mev. ^{90}Sr has a half-life of 28.8 years, while ^{90}Y has a half-life of 64.6 hours. Thus the source is considered a two-nuclide source. There is also no associated γ decay, making the required shielding minimal. The β dose rates for both materials used in this work were calculated using the experimental procedure shown in Appendix A. $\dot{D}_{Al_2O_3:C} = (57.1 \pm 2.3)$ mGy/s and $\dot{D}_{BeO} = (75.0 \pm 1.8)$ mGy/s.

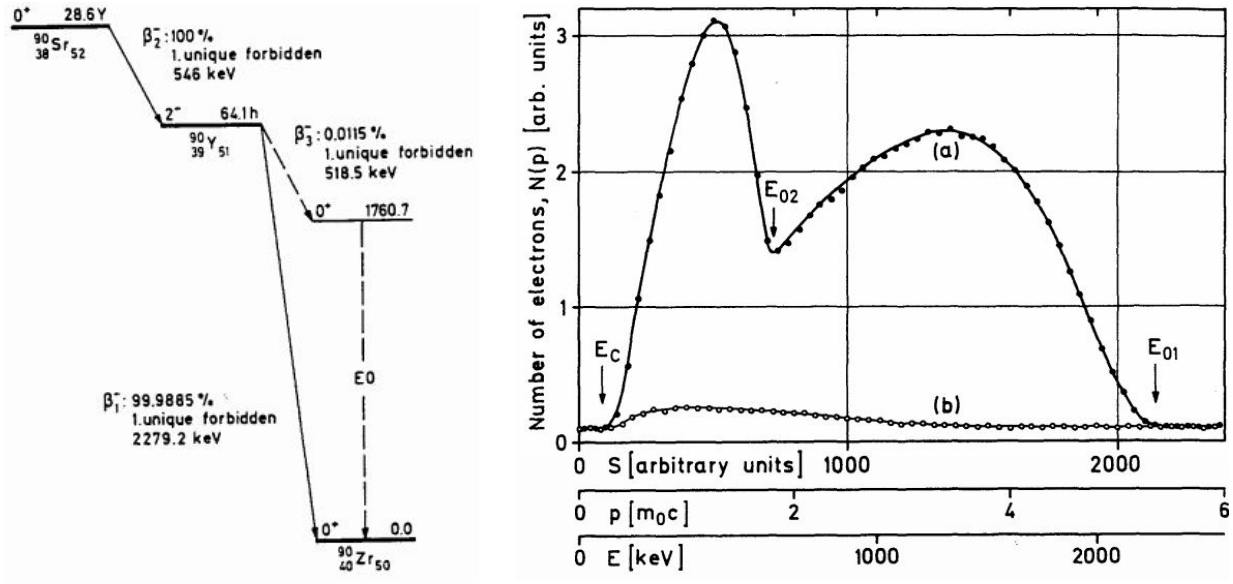

(a) (b)

Figure 3.12: $^{90}_{38}$Sr decay scheme (a) and emission spectra (b). Spectrum (a) corresponds to a raw measurement while spectrum (b) was measured using a copper filter. E_{01} and E_{02} are the ^{90}Y and ^{90}Sr spectra endpoint energies, respectively. Reproduced from Hansen with permission [65].

Radioactive $^{241}_{95}$Am undergoes decay into $^{237}_{95}$Np via the release of an α particle and a gamma ray. The discrete α particle energies (likelihood) associated with this decay are 5.486 MeV (0.852), 5.443 MeV (0.128), and 5.338 MeV (0.014). The corresponding gamma ray energies and likelihoods are low enough for the source to be considered a pure α-emitter.

$$^{241}_{95}\text{Am} \rightarrow ^{237}_{95}\text{Np} + ^{4}_{2}\alpha + \gamma \tag{3.8}$$

Calibrating the internal α source presents significant problems to the luminescence and dating communities. The Risø comes with a calibrated dose rate value to quartz, but the α particles emitted are so superficial that essentially any material will absorb all of the energy, regardless of thickness. Thus the dose rate prescribed loses relevance if different geometry samples are irradiated. Additionally, the luminescence efficiency is not equal to 1, and will vary by material. For these reasons, a nominal absorbed energy rate was calculated using geometry and material properties, according to the following procedure:

(i) a half-life decay was applied to the activity measured at calibration;

(ii) the resulting value from step (i) was divided by 2 because the source is a thin foil (i.e. to find the radiation exiting one side) ;

(iii) the energy attenuated by the N_2 gas was calculated and found to be negligible;

(iv) the ratio of the surface area of the sample to the exposed surface area of the source on one side was used to calculate the number of α particles bombarding the source per second, since the distance from sample to source is smaller than the source size.

$\dot{E}_{Al_2O_3:C} = 4.6 \cdot 10^{-7}$ J/s and $\dot{E}_{BeO} = 3.3 \cdot 10^{-7}$ J/s. Again, it should be reiterated that this is at best a nominal estimation. A more precise calibration of this source presents future research opportunities.

3.3.2 Luminescence Signal Measurement

After the samples are irradiated in the accelerator lab (or with the alpha or beta source), their signal will be measured using the the Risø (schematic and picture[4] shown in figure 3.13 [64]).The instrument itself consists of a light-tight housing to prevent unwanted exposure and resetting of the samples. The samples are loaded into a 48 sample carousel inside the reader. There are three different ways to stimulate the sample post-irradiation: light, heat, or both. The selected sample is elevated onto a heating plate and is heated and/or exposed to a previously selected LED. The color of the LED (blue, green or IR) is chosen based

[4] https://www.fysik.dtu.dk/english/research/radphys/research/radiation-instruments/tl_osl_reader, last accessed on May 3, 2021.

on the stimulation efficiency and emission spectrum of the material being analyzed (quartz, feldspar, Al_2O3:C, BeO, etc.). Each LED has a separate long pass emission filter to attenuate high energy photons, which are responsible for the majority of scattered light. While the sample is exposed to light or heat, it will luminesce.

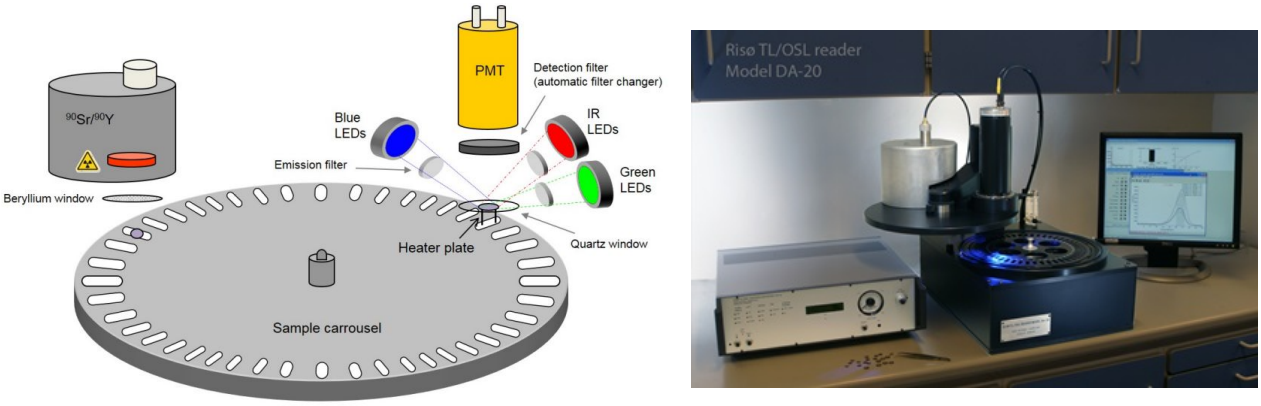

(a) (b)

Figure 3.13: (a) Schematic and (b) picture of the Risø OSL/TL reader. Schematic reproduced with permission [64].

Because the stimulation light intensity is about 18 orders of magnitude greater than the luminescent light intensity, a detection filter must be used to block out all high intensity light from LEDs, effectively seperating the stimulation and emission "windows" [64]. A photomultiplier tube (type 9235QA; ET Enterprises) is then used to translate photons into electrons, which are then multiplied via dynodes to generate a measurable current. This current is proportional to the signal output in counts/time. Due to the optical properties of Al_2O_3:C and BeO, which are the materials used in this research, the entirety of this research is performed using blue LEDs (470 ± 20 nm, 74 mW/cm2 , combined with a GG420 long pass filter) and Hoya U-340 detection filter (centered at 340 nm, FWHM 80 nm). Samples were heated at a rate of 5°C/s, except for BeO TL measurements, when a heating rate of 2 °C/s was utilized.

Figure 3.14 shows the 420 nm and 326 nm emissions of Al_2O_3:C as well as the UV detection filter and blue LED long pass filter used in this work. Both Al_2O_3:C emissions

overlap with the UV filter detection wavelengths, meaning the signal will be comprised of both components. It can also be seen that the long pass filter, which reduces the tail intensity of the LED emission, does not overlap with the UV detection filters. This ensures that the photons detected by the PMT originate in the sample, not the LEDs.

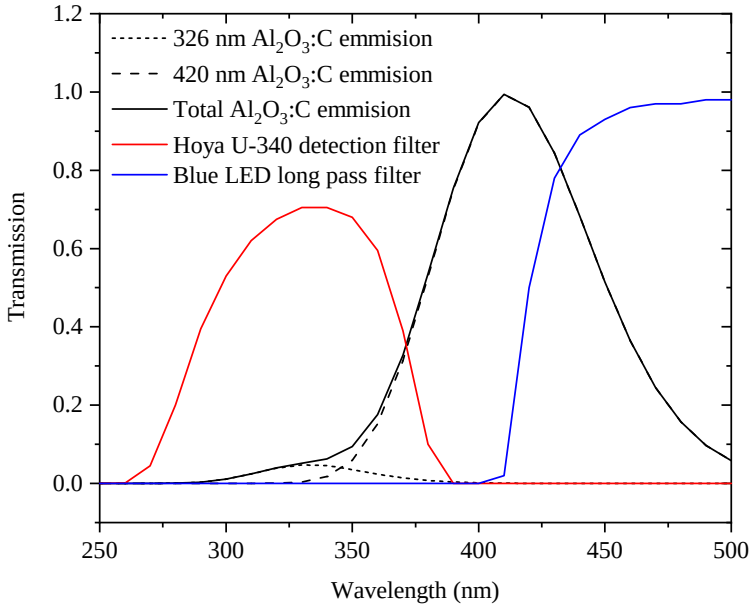

Figure 3.14: Differing emissions of Al_2O_3:C shown with the transmission of the UV detection filters and the GG420 blue LED long pass filter.

The Risø and other automated readers are manufactured to measure signals from natural minerals that have received very small amounts of background radiation. Because we are bombarding samples with high levels of ionizing radiation, it is necessary to reduce the number of photons detected during stimulation so that the PMT does not saturate. On the other hand, signals that are too weak are very noisy, making it difficult to compare signals and draw meaningful insights. Because obtaining a good signal is of highest importance, apertures, filters, and test doses were varied to keep signals in the range of $\sim 10^3$ counts to $\sim 10^6$ counts per PMT measurement. Table 3.4 shows the filters used for this purpose.

Material	Ion Type	Aperture/Filter	Test Dose	Test Dose Aperture/filter
Al_2O_3:C	β	2 mm aperture	-	-
Al_2O_3:C	α	10 mm aperture	-	-
Al_2O_3:C	Hydrogen	2.0 OD filter	10 s β	2.0 OD filter
Al_2O_3:C	Carbon	-	2 s β	2.0 OD filter
BeO	β	2 mm aperture	-	-
BeO	α	10 mm aperture	-	-
BeO	Hydrogen	3.5 OD filter	50 s β	3.5 OD filter
BeO	Carbon	2.0 OD filter	5 s β	2.0 OD filter

Table 3.4: Neutral density filters and apertures required for every material and ion combination used in this work.

The PMT measures an intensity value for present time intervals. If the time value is set to 1 s, for example, a 300s OSL curve will consist of 300 intensity values I_i. The number of TL curve values depends on max temperature and heating rate. The raw OSL signal intensity is graphed for the entirety of this work. However, the signal is background subtracted before integration using the following formula:

$$S = \sum_{i=1}^{n} I_i - n\Big(\frac{1}{p}\sum_{i=n-p+1}^{n} I_i\Big). \tag{3.9}$$

This equation simply states that the signal S equals sum of all the individual intensities I minus a background constant, which is the average intensity of the last p data points. The last 10 points were averaged to estimate background throughout this experimentation. While the background subtraction makes little difference in the Al_2O_3:C signal, it is necessary for BeO and other dosimeters that have a slowly decaying OSL signal. Optical signal is calculated using two methods in this work: the total integrated OSL area, or the initial OSL intensity integrated over the first 1% of time (l_0, see figure 3.15a).

All TL signals are background subtracted by taking a secondary TL measurement and subtracting it from the initial measurement. Contrary to OSL, the background subtracted TL intensity curves are graphed because the sample luminesces at very high temperatures due to thermal radiation, not stored ionizing radiation. Thus thermal effects are negated before

graphing. Al_2O_3:C and BeO TL signals are integrated at 100 °C and above to avoid traps that are thermally unstable, but the entire background subtracted TL curves are plotted. The TL signal can either be calculated using the total integrated TL area beyond 100 °C, or the primary TL peak height (see figure 3.15b). When the two thermal or optical methods differ from one another, it indicates the necessity to report both values.

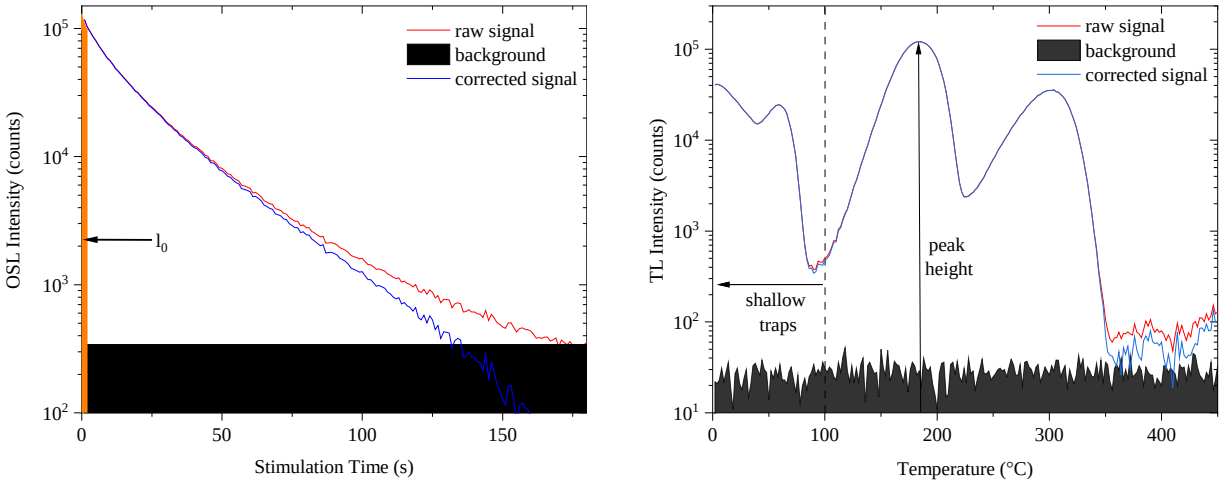

(a) (b)

Figure 3.15: Illustration of the background subtraction and signal calculation methods for typical BeO (a) OSL and (b) TL curves.

Chapter 4

Dosimetric Materials

The purpose of this chapter is twofold: to give an overview of solid state and luminescence material properties and to describe previous research relevant to the scope of this work. The previous chapter described the accelerator and beamline used to irradiate samples, while this chapter presents samples and elucidates their properties. The two materials used in this work, Al_2O_3:C and BeO, are among the most commonly used OSL dosimeters. Here their luminescence properties are described and previous HCP results are elucidated, as these results provide the basis for the investigations carried out in this work.

4.1 Al_2O_3:C

4.1.1 Crystal Structure

Aluminum Oxide, also referred to as alumina and sapphire, is a compound that has a polymorphic crystalline phase, known as α-Al_2O_3. It has been widely researched over the years due to prospect in many fields, including dosimetry. Although TL was initially used to measure the absorbed dose to Al_2O_3:C [67], research eventually showed that OSL offered much more prospect [68, 24]. The dose response curve is linear along several orders of magnitude from the μGy range up until approximately 10 Gy, ensuring that Al_2O_3:C can be

used to accurately measure a large range of absorbed doses. These are the primary reasons Al_2O_3:C is utilized for personal dosimetry, as well as the measurement of background and space radiation, and is one of the few OSL materials to have been successfully commercialized to date.

α-Al_2O_3 has a density of 3.98 g/cm^3 and a 9 eV band gap [69]. The diatomic oxygen form into a close packed sublattice and Al^{3+} ions occupy 2 of every three octahedral interstices. Thus, six nearest-neighbor octahedral O^{2-} ions surround each Al^{3+} ion [70]. Oxygen vacancies are the most prevalent Al_2O_3 defects, leading to F^+- and F-centers (one and two electron trapping centers arising from oxygen vacancies, respectively [71]). It was discovered in 1990 by Akselrod et al. that doping α-Al_2O_3 with Carbon greatly increases thermoluminescent properties [67]. Two-valent ions of Carbon impurity replace three-valent Aluminum cations in the crystal lattice, leading to the formation of new hole trapping centers (figure 4.1) [70]. This results in dosimeters that are highly sensitive along a large dose range compared to their non-doped counterparts, and have thus become the most widely utilized dosimeters in the field of OSL.

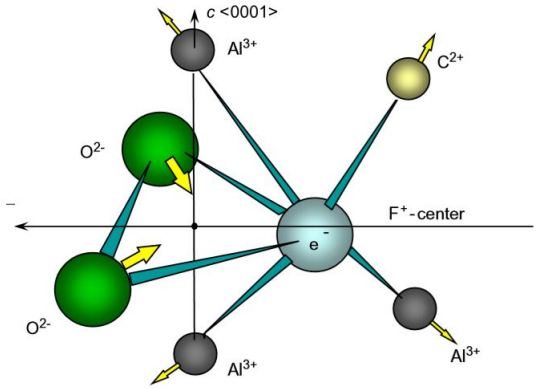

Figure 4.1: One possible configuration of the defect created by doping Al_2O_3 with Carbon, reproduced from Akselrod et al. with permission [70].

Lee and Crawford Jr. defined the F and F^+-center excitation and emission spectra of Al_2O_3 via its optical properties at room temperature (Figures 4.2a and 4.2b) [72]. It can easily be seen that F-centers create an absorption band at 6.1 eV ($\sim$ 205 nm) and an emission

band at 3.0 eV ($\sim$ 415 nm). F^+-centers create two overlapping absorption bands at 4.8 eV ($\sim$ 230 nm) and 5.4 eV ($\sim$ 255 nm) and an emission band at 3.8 eV ($\sim$ 330 nm).

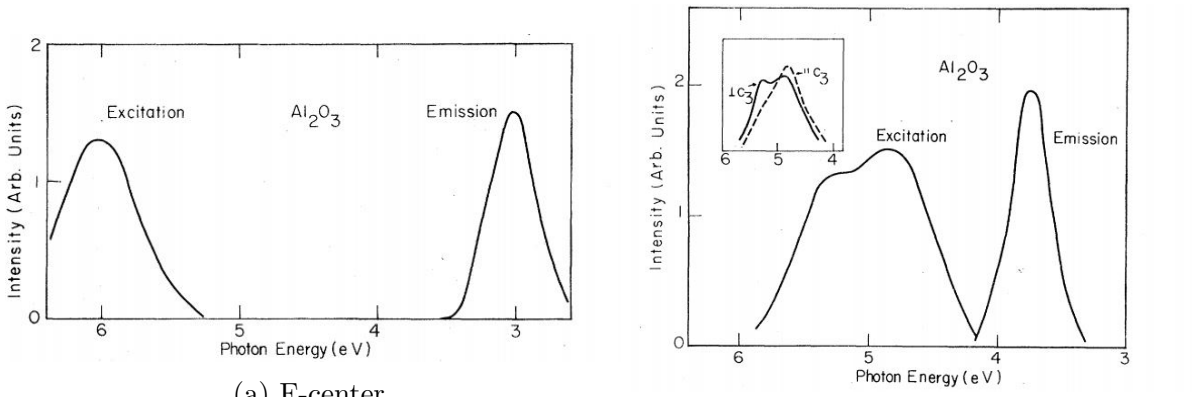

(a) F-center

(b) F^+-center

Figure 4.2: Excitation and emission of the F and F^+-centers from Al_2O_3 at 300 K, reproduced from Lee and Crawford Jr. with permission [72].

4.1.2 Luminescence Mechanism

The spectra of OSL and TL are dominated by a broad F-center emssion ($\sim$ 420 nm) [67, 73] as well as a weak F^+-center emission ($\sim$ 330 nm) [74]. Yukihara et al. [75] developed a simplified Al2O3:C band diagram to explain luminescence processes in the material. Radiative relaxation of F-centers are responsible for the main luminescence band, which occurs at $\sim$ 420 nm [72, 67]. This is critical because there are typically abundant F^+ and F-centers that pre-exist in Al_2O_3:C [76, 67]. Although it is not definitive, the main dosimetric trap (MDT) is assumed to be an electron trap [77, 78]. The model also assumes the existence of deep electron traps (DET) and deep hole traps (DHT). Although they do not contribute to signal directly, their mechanisms cause dosimeter sensitization and desensitization.

Ionizing radiation creates free electrons and holes in the conduction and valence bands, respectively (transition 1). Some of these electrons are trapped in the MDT (transition 4) and DET (transition 5), while others recombine with F^+-centers to form excited F-centers (transition 2). During optical or thermal stimulation, electrons escape the MDT to recombine with the F^+-centers, creating luminescence at 420 nm. This stimulation resets the F- and

F^+-centers to their concentration from before irradiation.

It is probable that Al_2O_3:C contains deep electron traps (DET) and deep hole traps (DHT) in addition to the MDT discussed above. Al_2O_3:C crystals were irradiated and illuminated with ultraviolet (UV) to study the F^+-center optical absorption band [79, 80, 81]. It was observed that the F^+-center absorption band increased once the samples were heated to $\sim$ 500-600 °C, which points toward an increase in concentration of F^+- centers. This phenomenon is likely due to a release of holes from DHTs that only become unstable once this temperature is reached ($F + h^+ \rightarrow F^+$). It was also observed that the F^+-center optical absorption band decreased once temperatures of $\sim$ 700-1000 °C were reached, suggesting the existence of DETs.. The released electrons destroy F^+ centers. It is critical to note that changing the concentration of F and F^+-centers via irradiation will change the sensitivity of the material. Thus, all Al_2O_3:C should be annealed to 900 °C after stimulation to empty the DETs and DHTs, and restore samples to their initial sensitivity [80, 82].

$$F^+ + e^- \rightarrow F^* \rightarrow F + h\nu_{420\,nm} \tag{4.1}$$

Notice that without the presence of traps (MDT, DET, and DHT), steady state relationship would exist between the F and F^+-centers ($F \leftrightarrow F_+$). In other words, one hole would be captured by the F-center ($F + h^+ \rightarrow F^+$) for every electron captured by the F^+-center ($F^+ + e^- \rightarrow F$). Thus, the concentration of hole and electron traps greatly effects the oxygen vacancy defect equilibrium. Electron traps capture electrons that would otherwise destroy F^+-centers and create F-centers ($F^+ + e^- \rightarrow F$). Thus, electron traps increase F^+-center concentration. Alternatively, the addition of hole traps will capture holes that would otherwise destroy F-centers and create F^+-centers ($F + h^+ \rightarrow F^+$), meaning the concentration of F^+-centers decreases as hole trap concentration increases [80].

The model above fails to describe reality in two ways; it ignores the presence of shallow traps and does not address the weaker emission at $\sim$ 330 nm. In addition to annealing samples, it is critical to discriminate between signals that derive from different traps, as

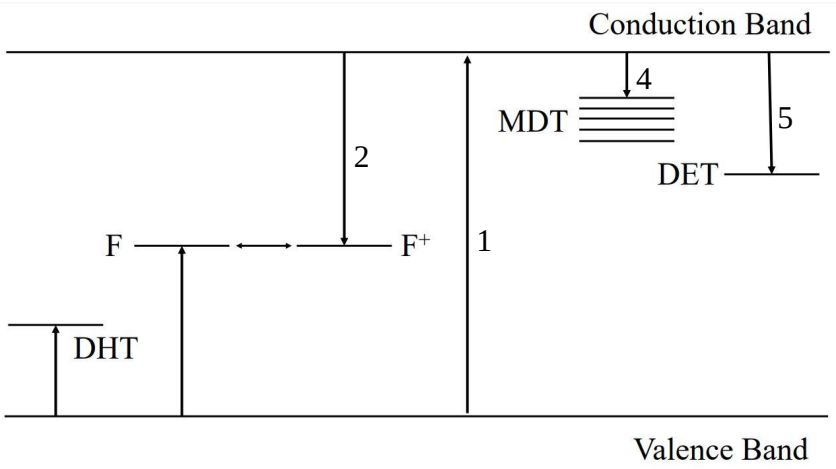

Figure 4.3: Al_2O_3:C band diagram model, which includes the defects primarily responsible for production of OSL and TL signal [81, 75, 83, 84]. These include the main dosimetric trap (MDT), deep electron trap (DET), deep hole trap (DHT), and oxygen vacancy defects (F and F^+-centers). Adapted from Yukihara and McKeever [75].

some shallow traps are thermally unstable. Additionally it is evident that there are indeed two MDT peaks, as both emissions described above are within the Hoya U-340 detection filter's absorption window (centered at 340 nm, FWHM 80 nm).

Blue (470 nm) and green (525 nm) LEDs can be used to stimulate Al_2O_3:C; each have their own benefits and disadvantages. Blue stimulation increases initial OSL intensity and decreases measurement time, while green stimulation offers an increased gap between stimulation and emission wavelengths [85]. Blue light also has sufficient energy to activate deep traps corresponding to TL signal beyond 500 °C, while green light does not. For this reason and because 470 nm is sufficiently far from UV filter's range, blue LEDs were used for all OSL measurements.

4.1.3 Previous HCP Irradiation Results

The use of OSL dosimeters in space, in particular the use of Al_2O_3:C in astronaut dosimeters, has been a topic of great interest in the luminescence community . However, radiation in space is significantly heavier and more energetic than background radiation here on earth. Because of this, the relationship between Al_2O_3:C and HCPs has been thoroughly investi-

gated to ascertain the effectiveness of Al_2O_3:C as a space dosimeter [60, 81, 86, 82, 87]. OSL is very reliable in measuring gamma and beta radiation; therefore, to determine how effective OSL is in determining absorbed dose from HCPs, the HCP efficiency is defined relative to gamma radiation. Sensitivity is the measured signal per unit absorbed energy, or the mass normalized signal divided by dose S/D. This allows us to define the relative OSL efficiency $\eta_{HCP,\gamma}$ [82].

$$\eta_{HCP,\gamma} = \frac{S_{HCP}/D_{HCP}}{S_{\gamma}/D_{\gamma}} \tag{4.2}$$

The relative efficiency is the signal per dose from HCP radiation divided by the signal per dose from low LET gamma radiation. Efficiencies close to 1 indicate that the OSL signal accurately represents the absorbed dose from HCP radiation. Figure 4.4 shows results from Gaza et al., who irradiated several Al_2O_3:C samples with different HCPs at different energies [82, 86]. Two types of detectors were used and two different readout methods were utilized for each detector. OSL was calculated using the integrated signal (OSL) and initial intensity (l_0). The peak height was used to measure TL, although the authors state that there is no difference between TL area and peak height for the purpose of characterizing HCP efficiency.

There are several conclusions that can be drawn from Figure 4.4c and from similar data other research groups have compiled. While the efficiency ratio of different readout techniques is defined to be 1 for β irradiation, different readout techniques and signal choices lead to varying dose responses when Al_2O_3:C is irradiated with HCPs [81, 86, 82, 87]. Using the initial OSL signal leads to a much greater efficiency than using the integrated OSL signal or TL signal. More importantly, the data supports the claim that the efficiency of luminescence methods in measuring dose response is LET dependent. As the LET increases, the efficiency of the chosen readout technique decreases, regardless of the technique being utilized [81, 86, 82, 87]. HCP ionization tracks have a much higher energy density than lower LET beta or gamma irradiation. These high energy density particles create regions along their ionization tracks where the local energy deposition exceeds trap density. All energy

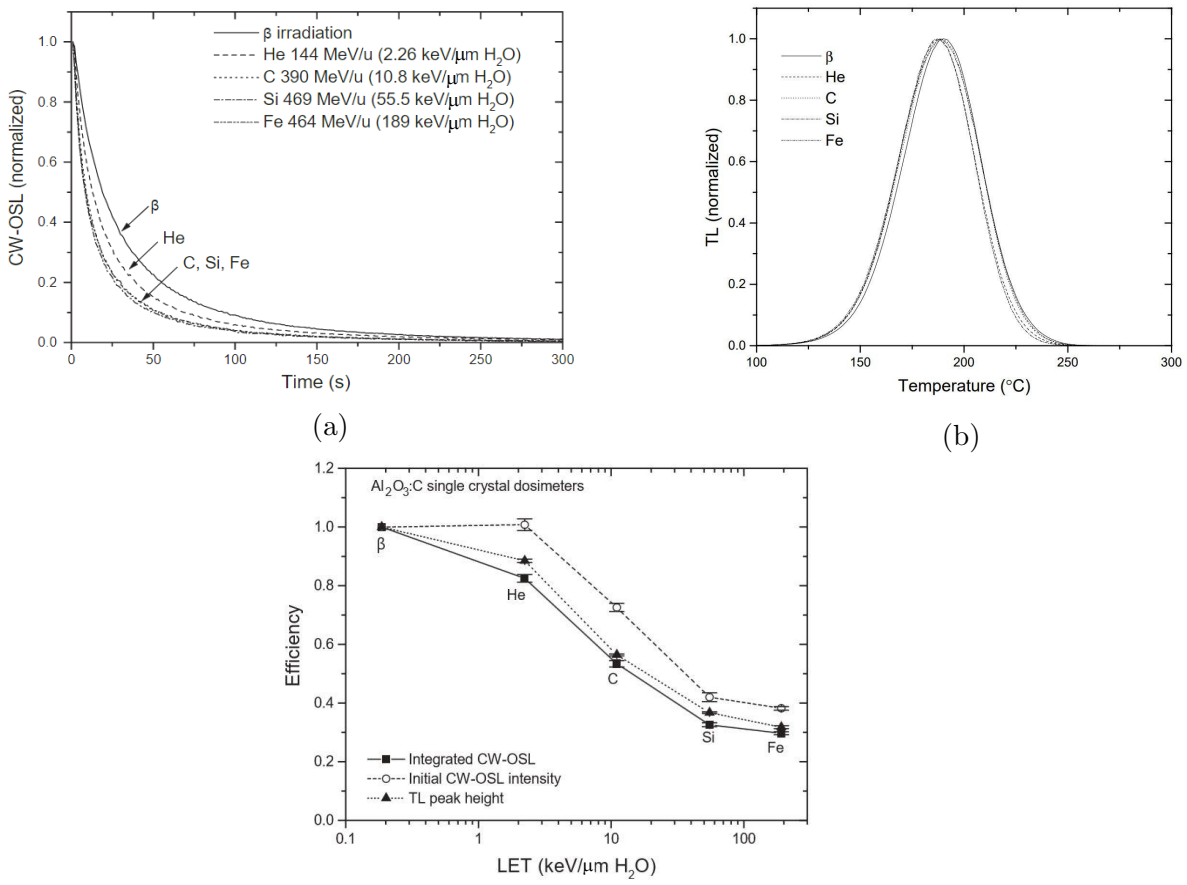

Figure 4.4: Results after irradiation with a dose of 100 mGy from β, He, C, Si, and Fe: (a) Normalized OSL curves of Luxel^{TM} dosimeters, (b) normalized TL curves of single crystal dosimeters, (c) relative efficiencies of single crystal dosimeters. Reproduced from Gaza et al. with permission [86].

that is deposited in a region where the OSL or TL signal is saturated will not contribute to the signal, leading to a decrease in relative efficiency (Figure 4.4c) [88]. These LET effects also manifest themselves when observing the normalized shapes of OSL and TL curves (figures 4.4a and 4.4b).

Gaza investigated the effects of low energy protons and 13 MeV carbon on the OSL and TL properties of Al_2O_3:C single crystal dosimeters [43]. Variables investigated include fluence, particle energy, and particle size.

The research above is not comprehensive of all Al_2O_3:C HCP data. Rather, it is an indication of the types of results possible.

4.2 BeO

4.2.1 Material Properties

Documentation of BeO ceramic luminescence properties dates back to the late 1950's [89, 7, 8, 90]. BeO was seen as an enticing TLD candidate due to its affordability and because its effective atomic number ($Z_{eff,BeO}$=7.2) is near tissue and water equivalent (Z_{eff}=7.5) [91, 26, 92]. Thus, it was investigated for its uses as a TL personnel dosimeter [93, 94], then later as a TL medical dosimeter [25]. However, it was determined that the TL signal is highly sensitive to light [95]. BeO OSL dosimeter properties were investigated starting in the late 90's, and the interest has only grown since [25]. BeO OSL has linear dose response along 6 orders of magnitude from less than 5 μGy to 5 Gy [25, 96, 97, 98].

Although they will not be utilized in this research, there are several other BeO frontiers being investigated. Linearly modulated (LM) OSL can distinguish between differing BeO traps by varying stimulation light intensity [99, 100, 101]. Also, 2 dimensional dosimetry of BeO has been made possible via point by point signal measurement techniques [98, 102, 103]. Because of the multi-faceted promise BeO offers as a material (specifically near water equivalence), significant research has been conducted towards a real time OSL (rtOSL) fiber optic dosimetry system for use in MV energy photon therapy, HDR Brachytherapy, and superficial x-ray therapy [27, 28, 29, 30].

BeO has a density of 2.85 g/cm^3 [104] and a 7.7 eV band gap [105].

4.2.2 Luminescence Properties

The luminescence mechanisms of BeO are only partially understood due to a large number of dopants and the complex phototransfer effects. As eloquently stated by Bulur, "the richness of BeO ceramics in terms of trapping states makes it difficult to generate a phenomenological model and analyse the charge traffic between the traps using numerical solutions of rate equations" [106]. However, this same complexity offers many research prospects

and leaves many questions unanswered.

BeO typically displays three TL peaks centered at ∼70 C, ∼190 °C, and ∼330 °C, dependent on heating rate. In 1998, Bulur and Göksu performed step annealing that indicated the OSL signal is derived from traps that become unstable at about ∼330 °C (figure 4.5 [25]). Figure 4.6 shows a BeO TL curve after a 200 mGy dose, before and after OSL readout [107]. The first two peaks are emptied after the dosimeter is irradiated and illuminated. However, the trapping centers responsible for the third peak are not significantly optically stimulated. These results appear contradictory: one set of experiments show that the third TL peak contains the traps responsible for the OSL signal while the other experiment shows that the first two TL peaks constitute the OSL signal. An explanation for these contrary findings was not offered until recently.

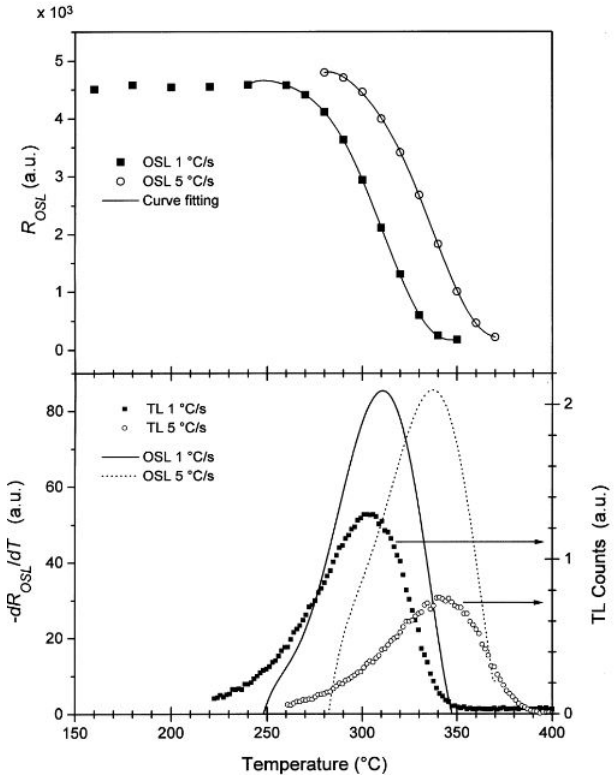

Figure 4.5: Residual OSL (R_{OSL}) and dR_{OSL}/dT versus preheat temperature, for two heating rates, compared to the TL curves. It can be seen that the OSL signal is stable until the sample is preheated to the ∼330 °C trap, indicating deep traps constitute the OSL signal. There is also a strong residual OSL signal heating rate dependence. Reproduced from Bulur and Göksu with permission [25].

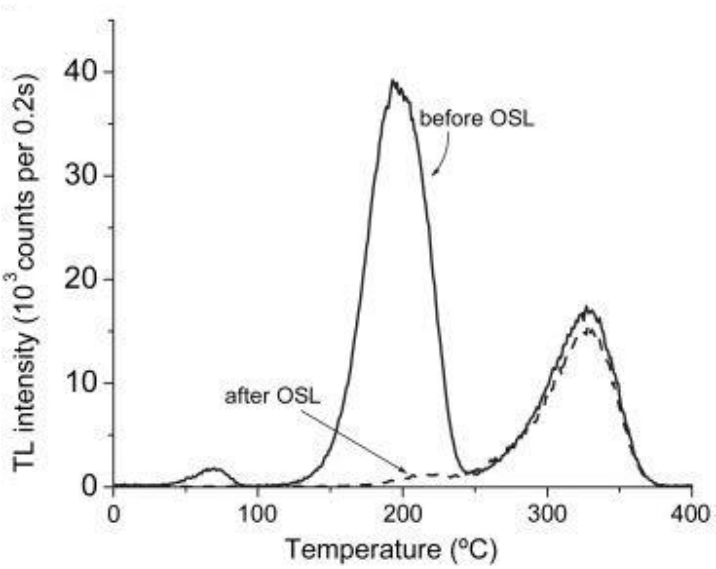

Figure 4.6: TL curve of BeO after a 200 mGy dose, before and after OSL readout, reproduced from Yukihara with permission [107].

Yukihara (2020) recently proposed a more complex framework that accounts for the discrepancy described above (figure 4.7): there are two traps that comprise the high temperature peak, optically active traps (OATs) and hard-to-bleach traps (HBTs) [108]. The HBTs cannot be easily emptied via light exposure but can be thermally transferred to the OATs, after which optical exposure will result in a thermally transferred OSL signal (TT-OSL). However, this more nuanced model does not elucidate the difference in component decay speed or assign traps to specific defects.

Although it was initially assumed that OSL and TL emission spectra were the same, it has been shown that the OSL spectrum of BeO has two broad bands at 310 and 370 nm [107], while the TL is dominated by a 335 nm emission band [95]. BeO spectral analysis has been performed, and two emission bands have been characterized [109]. F-centers (oxygen vacancies with two trapped electrons) have a 365 nm (3.4 eV) emission while F^+-centers (oxygen vacancies with one trapped electron) have a 320 nm (3.9 eV) emission. Watanabe et al. used electron spin resonance to attribute the 190 °C primary TL peak to hole centers (O^- ion) and electron/recombination centers (Al^{2+}). They also attributed the high temperature TL peak (320 °C) to the O^- ion, which they speculated to be the source of OSL kinetics

[110]. It was initially assumed that there is a broad stimulation spectrum ranging from 420 nm to 550 nm, independent of temperature [25]. However, it was more recently determined that OSL intensity increases with decreasing stimulation wavelength [107, 111].

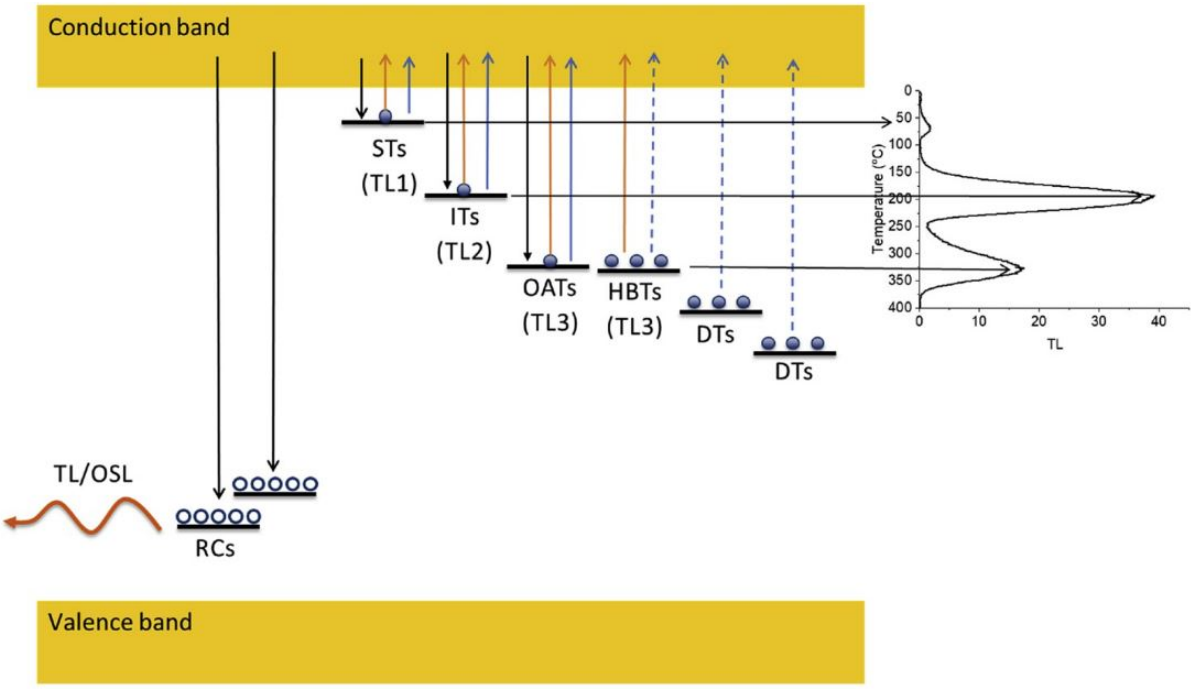

Figure 4.7: BeO trap model with shallow traps (STs), intermediate traps (ITs), optically active traps (OATs), hard-to-bleach traps (HBTs), deep traps (DTs), and recombination centers (RCs). Orange lines (blue lines) indicate thermal (optical) charge transfer. The dashed lines indicate low recombination probability, reproduced from Yukihara with permission [108].

4.2.3 Previous HCP Irradiation Results

The effects of HCPs on the luminescence signals of BeO are sparsely characterized, especially when compared to Al_2O_3:C. In 1970 it was first determined that TL peak location and peak height ratio are LET dependent in BeO citeBecker1970. The high temperature peak signal is drastically smaller in high LET radiation (α, ~5 MeV) versus low LET radiation (γ, ~0.6 MeV). The low LET radiation low temperature peak is centered at a higher temperature than the high LET radiation low temperature peak as well. However, an important caveat must be stated, as it pertains to this research. It is known that BeO samples

with differing physical and chemical preparation exhibit different TL behavior. Therefore the Thermolox® 995 BeO used in this research is assumed to have luminescence differences compared to the Coors Porcelain BeO used by Becker et al. [112].

Yasuda et al. measured the TL signals of 50 mGy and 100 mGy doses to 99.9% pure BeO sheets from a ^{137}Cs γ-ray source and He, C, Ne, Ar, and Fe heavy ions [113]. They then normalized these signals to the signal from low LET ^{137}Cs (figure 4.8a). The low temperature TL peak intensity is greater for He, C, and Ne than ^{137}Cs, and does not drop below unity until the LET is close to 86 KeV/μm (Ar). The high temperature TL peak intensity is greatest for ^{137}Cs and decreases exponentially with increasing LET. Most interestingly, the ratio of high to low TL intensity peak heights decreases until about 80 KeV/μm, then the ratio increases with increasing LET (figure 4.8b). The author postulated that these TL peak height characteristics can be utilized to evaluate mixed LET fields, such as are encountered in space.

The previously mentioned BeO research concerning HCPs focused solely on TL signals. This is because little research was conducted on the OSL response of BeO to HCPs compared to TL, until the last twenty years. Voss et al. determined that Thermolox® 995 BeO dosimeters have a linear OSL signal response from Carbon of energies between 88 and 430 MeV/u, for doses of 0 - 10 Gy [114]. In 2001, the effects of high LET particles on BeO dosimeters heavily doped with Na were investigated to determine the viability of space dosimetry [115]. 6.5, 27, and 58.7 MeV protons were utilized to determine OSL efficiencies compared to gamma [116]. Negligible OSL curve shape dependence on LET was observed. BeO OSL signals were compared to an ionization chamber and Monte Carlo simulations for a 190 MeV clinical proton beam [117].

This literature review did not discuss or even mention all research pertaining to BeO, but a sample of the most pertinent research suggesting possible results.

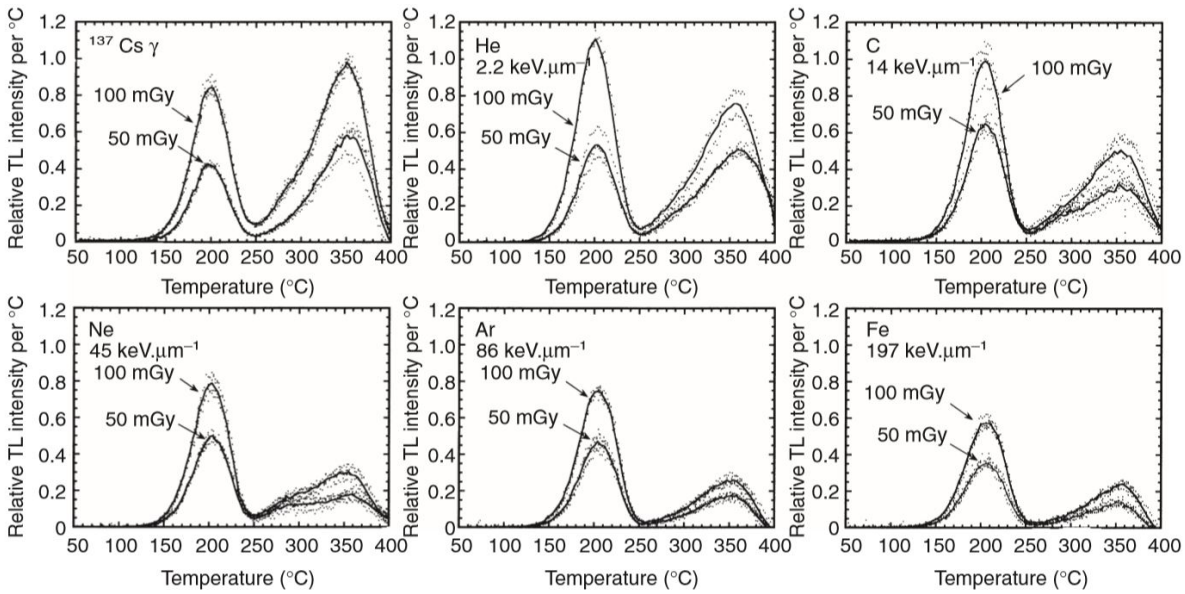

(a) TL curves for doses of 50 mGy and 100 mGy from a ^{137}Cs γ-ray source and He, C, Ne, Ar, and Fe heavy ions. The peaks are normalized to the signal intensity from ^{137}Cs, as dose from β or γ radiation is assumed to be unity. Respective HCP energies are 150, 290, 230, 550, and 500 MeV/u.

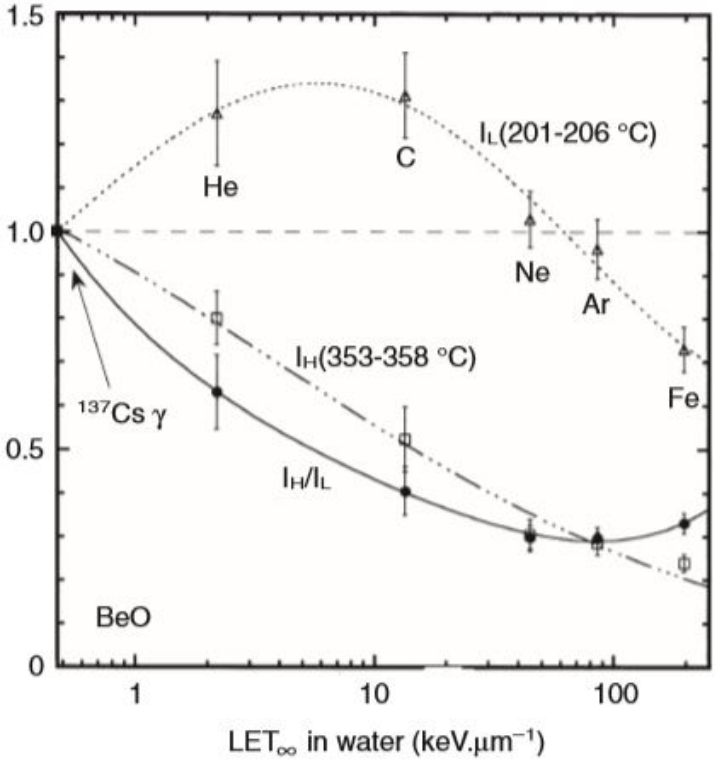

(b) Plots of the high (I_H) temperature peak heights, low (I_L) temperature peak heights, and I_H/I_L ratios normalized by ^{137}Cs γ-ray peak heights, plotted against LET_∞ in water (KeV/μm). Standard error bars of the two dose values (50 mGy and 100 mGy) are shown.

Figure 4.8: Reproduced from Yasuda et al. with permission [113].

4.3 Gaps In Research

It must first be reiterated that materials vary greatly when they are synthesized differently, or different dopants are added. Thus, materials with the same atomic make-up can have drastically different properties and must be investigated independently. The Al_2O_3:C samples used to complete this research are single crystal Al_2O_3:C square dosimeters manufactured by Landauer in Stillwater, Oklahoma. Their dimensions are approximately 4.00 mm x 4.00 mm x 0.85 mm. They are grown using different synthesis techniques than the commonly used single-crystal TLD-500s (EFG synthesis, instead of Czochralski). According to the manufacturer, there is no published research using this specific material. So while there is an abundant amount of HCP research concerning other Al_2O_3:C single crystal dosimeters (TLD-500, for example) and Luxel dosimeters, none exists for this material.

The BeO samples utilized in this research are Thermolox® 995 single crystal square dosimeters manufactured by Materion. Their dimensions are approximately 4.70 mm x 4.70 mm x 0.50 mm. Aşlar et al. investigated the Thermolox® 995 dosimeter atomic make-up (other than Be) using energy-dispersive X-ray spectroscopy (EDX), and found a smattering of dopants. These dopants, by weight, include Oxygen (97.64 %), Carbon (0.19 %), Silicon (0.22 %), Aluminum (0.18 %), Boron (0.75 %), Magnesium (0.26 %), Calcium (0.09 %), Sodium (0.56 %), and Manganese (0.11 %) [118]. Standard TLD synthesis indicates that Na concentration is among the most important dopants listed above [95, 118]. While there is a large amount of research concerning β and γ, little low-energy HCP research exists using this exact dosimeter. The only work found by the author relevant to this material has already been mentioned; Sadel et al. determined the OSL efficiencies of 6.5, 27, and 58.7 MeV protons, and found negligible curve shape difference [116]. The ECU accelerator can only create 4 MeV protons, so even these results are outside of the scope of this research.

Because both materials offer an essentially wide-open research landscape, a comprehensive approach has been taken to investigate their properties. This entails running preliminary tests using the β and α sources in the Risø, as the process is very time-efficient and repro-

ducible. Then the response of both materials described above to low-energy protons and Carbon will be investigated in a systematic manner. This includes analyzing the shape of curves and the signal response with increasing absorbed energy. Additionally, the effects of current and LET on signal shape and magnitude will be investigated.

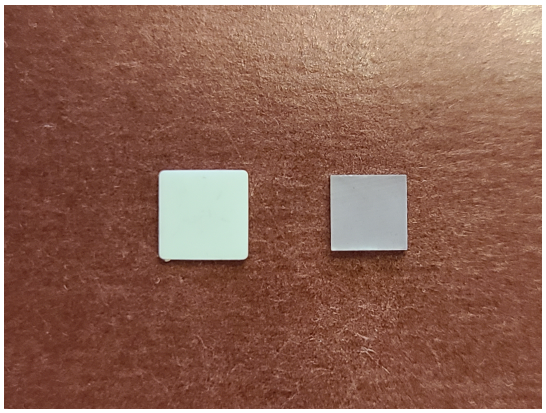

Figure 4.9: 4.7mm x 4.7mm Materion Thermalox 995 BeO sample (left) and 4mm x 4mm Al_2O_3:C sample manufactured by Landauer (right).

Chapter 5

Luminescence Characteristics after irradiation with β and α Sources

As discussed in previous chapters, β irradiation has a luminescence efficiency of 1, and is therefore an ideal candidate for comparison to HCP measurements. The available α-source emits energies close to that of ions produced by the accelerator, and it is easily accessible in the Riso. Thus, the measurements here are meant to provide an easily reproducible baseline to test material characteristics. Additionally, these results inform the experimental procedures utilized in the following chapters.

A comprehensive and systematic approach was taken to test certain attributes of Al_2O_3:C and BeO dosimeters, including uniformity, repeatability, and dose response.

By giving different dosimeters the same dose, non-uniformity among sample signals can be measured. The higher the signal variance, the greater the necessity to normalize signals by means of a test dose, or by measuring the signal from multiple dosimeters per dose.

Repeatability tests measure the reliability of a sample by giving the same sample repeatedly the same dose, and comparing signal differences. Ideally the signal variance is as low as possible, however nothing can be done to offset high repeatability differences. It should be noted whether repeatability signal differences seem to be random or systematic, which can

often be deduced by qualitative and quantitative means.

The relationship between signal and dose, i.e. the dose response, can be measured by testing the dosimeter's response to different doses and particle types. The integrated signal is plotted versus the dose and the dosimeter can be qualified as linear, supralinear, or sub-linear/saturated for a given dose value. Dose responses can be compared by many variables including, but not limited to, particle type, ion type, sample type, and readout method.

As a reminder, the following β dose rates were obtained using the formalism in Appendix A: $\dot{D}_{Al_2O_3:C} = (57.1 \pm 2.3)$ mGy/s and $\dot{D}_{BeO} = (75.0 \pm 1.8)$ mGy/s. The following α absorbed energy rates were calculated using the assumptions found in Chapter 3.2.1: $\dot{E}_{Al_2O_3:C} = 4.6 \cdot 10^{-7}$ J/s and $\dot{E}_{BeO} = 3.3 \cdot 10^{-7}$ J/s. The x-axes are listed in units of time throughout this chapter because the Risø can only deliver integer time exposures.

5.1 Al_2O_3:C

5.1.1 β Source (^{90}Sr/^{90}Y) Irradiation

OSL Uniformity

The OSL uniformity characteristics of Al_2O_3:C dosimeters were probed using the procedure summarized in the following sequence:

(i) annealing at 900 °C (15 minutes)

(ii) beta dose equivalent to 20s irradiation

(iii) OSL readout (blue LEDs, 90% power, 300 seconds, record one point every 1.5 seconds)

(iv) heating to 450 °C (at 5 °C/s)

(v) repeat steps (i)-(iv) for 9 other samples.

After annealing 10 dosimeters in an external muffle furnace, the samples were transferred to the Riso and steps ii-v were performed. The heating step iv was intended to remove

residual charges from the main dosimetric traps. All OSL and TL uniformity results use total integrated signal in this work. Results are shown in Figure 5.1.

It can be seen that there is moderate signal variance in the OSL curves of 10 separate Al_2O_3:C dosimeters, with a relative signal response standard deviation (σ_s) of 8.3%. There are significant differences in initial intensity values and slight decay-rate differences (figure 5.1a), which translate to shape differences once the curves are normalized to their respective maxima (figure 5.1b). Notice that sample 3 has the lowest initial intensity and sample 2 has the slowest signal, resulting in noticeable shape differences once the curves are normalized. The signal differences listed above are due to inconsistency between sample mass and sensitivity. While samples are professionally manufactured, they vary slightly in size and material synthesis. Additionally, apertures present geometric complications, as the luminescence signal measurement will depend on how centered the sample is inside the cup.

OSL repeatability

OSL repeatability characteristics of Al_2O_3:C dosimeters were investigated using the procedure outlined in the following sequence:

(i) annealing at 900 °C (15 minutes)

(ii) beta dose equivalent to 20s irradiation

(iii) OSL readout (blue LEDs, 90% power, 300 seconds, record one point every 1.5 seconds)

(iv) heating to 450 °C (at 5 °C/s)

(v) repeat steps (ii)-(iv) 9 times for each sample

(vi) repeat steps (i)-(v) for 3 more samples.

The initial annealing is sufficient to empty all dosimeter traps whereas heating to 450 °C leaves deep traps intact and only empties traps associated with the main dosimetric peak. This results in a cumulative filling of deep traps and an apparent increase in dose known as sensitization (figure 5.2a) [81]. The inset of the repeatability graph provides evidence that

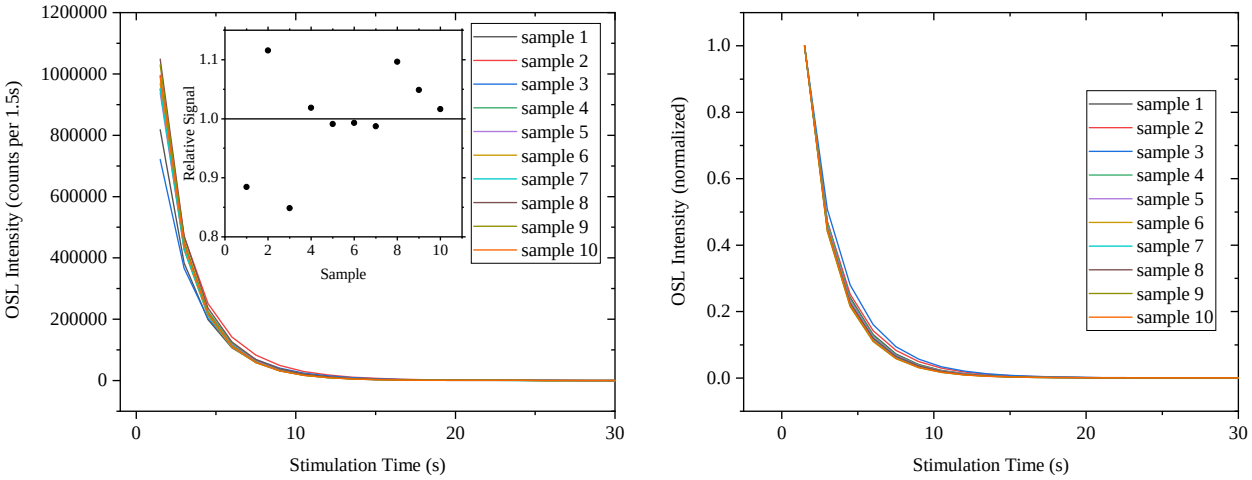

(a) (b)

Figure 5.1: Signal uniformity for 10 different Al_2O_3:C samples. a) OSL curves. The inset shows the integrated signal relative to the mean value of the 10 dosimeters. b) OSL curves normalized to their initial values. Each sample was exposed to 20 seconds of β irradiation.

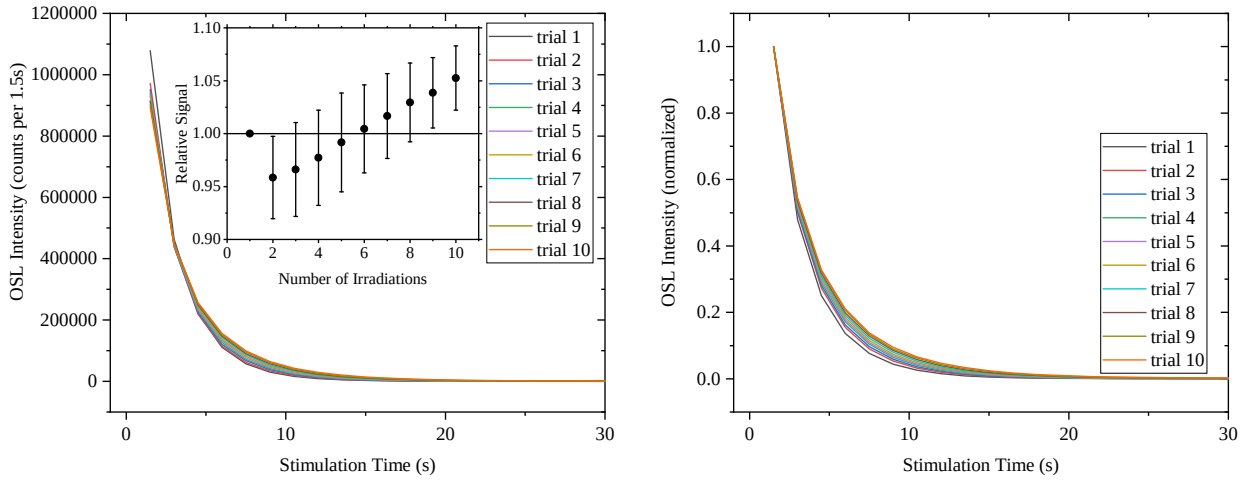

(a) (b)

Figure 5.2: Signal repeatability for 4 different Al_2O_3:C samples during 10 cycles of exposure to 20 seconds of β irradiation and measurement. a) OSL curves for one dosimeter. The inset shows the average signal of the 4 dosimeters relative to the signal measured in the first cycle as a function of number of irradiations. Error bars represent standard deviations. b) OSL curves normalized to their initial values.

curve changes are not random, but rather systematic. The dosimeter gives off a higher signal every time it is re-irradiated, even though the dose remains constant. The more the deep traps are filled, the more electrons are cycled to the main dosimetric traps, constituting a higher signal due to decreased electron competition between MDTs and DETs. The first measurement of all repeatability measurements was approximately 5% higher than successive measurements, regardless of the overall sensitization trend. This could be a systematic calibration effect of the heating mechanism since OSL is measured at 50 °C, however the exact reason has not been identified. The signal of each of the four dosimeters tested increased by approximately 1% every time they were re-irradiated.

There was some difference in the shape of the curves after normalization compared to before due to the systematic response of Al_2O_3:C chips after repeated irradiation (figure 5.2b).

TL uniformity and repeatability

The Al_2O_3:C TL uniformity and repeatability tests were completed using the same sequences as for OSL, with the exception that the OSL measurement in step (iii) is was replaced with a 90 second TL readout (0-450 °C at 5°C/s). All OSL and TL repeatability results use total integrated signal in this work. Results are shown in Figures 5.3 and 5.4.

A high variance in TL signals was observed among the 10 dosimeters, with σ_s equaling 13.54% (figure 5.3a). One explanation for the peak intensity differences and the peak temperature differences seen in figure 5.3a is inconsistent thermal contact between the sample cup and the sample. Unlike OSL, the sample is heated by a cup, which in turn is heated by a plate. Temperature scales provided by the Risø reader are temperatures of the heating plate, not sample temperature, which is always expected to be slightly lower due to thermal lag. Intensity and peak location variance occurs if the sample is not flush against the cup, or the cups are not perfectly flat. It is not possible to determine what portion of the signal variance is due to sample variation and what portion is due to inconsistent thermal contact.

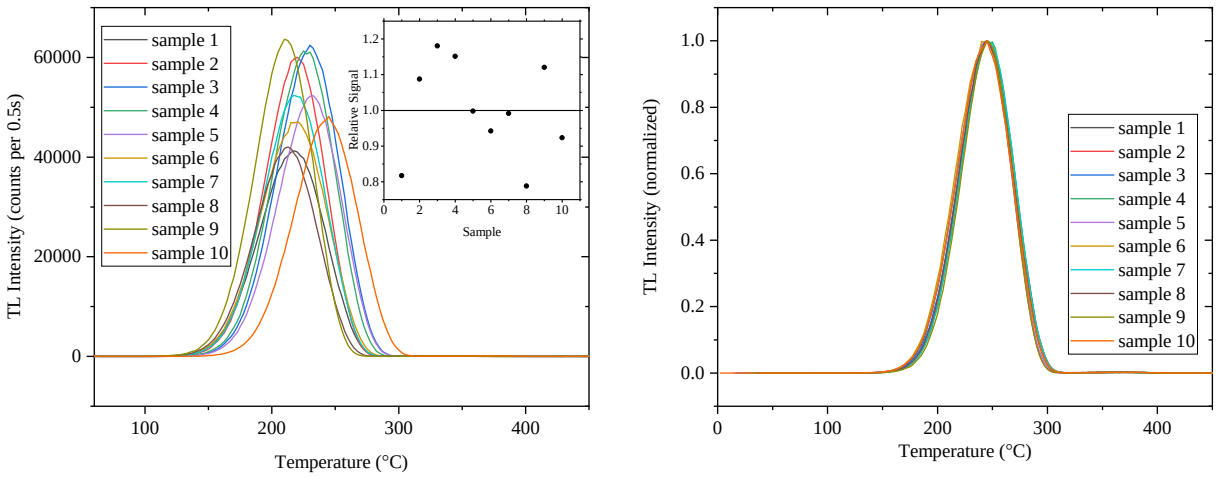

(a) (b)

Figure 5.3: Signal uniformity for 10 different Al_2O_3:C samples. a) TL curves. The inset shows the area under the main dosimetric peak signal relative to the mean value of the 10 dosimeters. b) TL curves normalized to their peak values and shifted so that peak values occur at the same temperature. Each sample was exposed to 20 seconds of β irradiation, then the luminescence was measured.

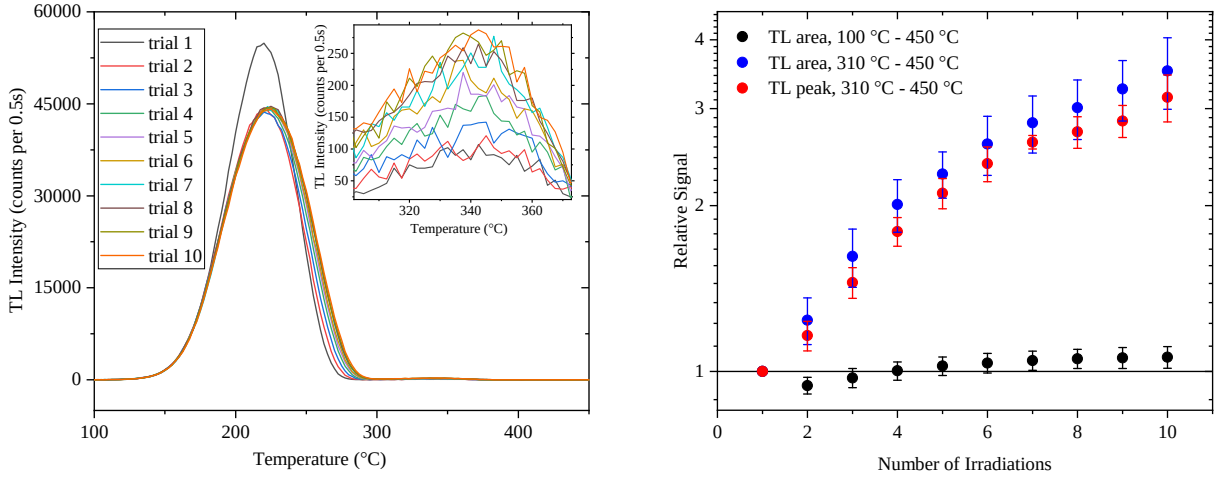

(a) (b)

Figure 5.4: TL repeatability. 4 dosimeters were exposed to repeated cycles of 20 seconds of β irradiation followed by measurement.(a) TL curves for a single Al_2O_3:C. The inset shows the high temperature peak. (b) Average values for 4 dosimeters as a function of cycle number for the entire TL signal (black), as well as the TL area and peak of the high temperature peak (red and blue, respectively). Error bars represent the standard deviation.

TL curve shape from different dosimeters is fairly consistent when the normalized peaks are artificially aligned to negate the effects of thermal lag due to contact variance (figure 5.3b). This highlights the fact that the temperature axes of normalized TL graphs are nominal and should be understood more as approximations than as exact values.

All four dosimeters that were tested for TL repeatability showed the strange behaviour seen in trail 1 of figure 5.4a. The associated TL curve has a higher peak with a more rapidly decaying tail. TL signals followed the same signal trend as OSL; there is an initial drop of $\approx 5\%$ signal after the first measurement, followed by a steady increase of about 1% signal per irradiation caused by successive filing of DETs. The low temperature and high temperature side of the TL peaks move to higher temperatures with each irradiation. However it is apparent from figure 5.3a that this change is more drastic for the high temperature side. The much smaller high temperature peak shown in the inset centers around 340 °C and displays the same behaviour as the primary peak. It can be seen in figure 5.4b that the high temperature TL peak area and height roughly triple even though the total signal only increases by approximately 10% from trial 1 to trial 10. It is important to emphasize that simple integration was utilized to quantify the signal associated with each temperature domain shown in figure 5.4b. It is not possible to determine whether the observed trend is due to "bleeding" of the main peak into the high temperature peak, or another cause altogether without deconvoluting the curves.

Dose response

The Al_2O_3:C OSL dose response was investigated using the procedure outlined below:

(i) annealing at 900 °C (15 minutes) in an external furnace

(ii) beta dose #1

(iii) OSL readout (40 seconds, record one point every 0.2 seconds)

(iv) heating to 450 °C (at 5 °C/s)

(v) repeat steps (ii)-(iv) for beta doses #2-6.

(vi) repeat steps (i)-(v) for 3 more samples.

All following Al_2O_3:C OSL signals are collected every 0.2s for 40s rather than every 1.5s for 300s. It was initially thought this dosimeter would have a slowly decaying OSL signal, since other Al_2O_3:C single crystals do. The uniformity and repeatability curves provide evidence to the contrary, however. The initial intensity of the OSL curves increases with irradiation time (figure 5.5a), resulting in significant curve shape differences. As the dose increases, the normalized signal decays more rapidly (figure 5.5b). A useful way to quantify OSL curve shape changes is shown in the inset of the figure, where the area under the normalized curves is plotted as a function of irradiation time. This is a documented method used to quantify change in normalized curve shape as a function of dose [60, 119]. It is clear that the normalized curve area decreases with increasing dose, signifying quicker OSL decay. The area under the normalized OSL curve slowly decreases for low doses followed by significant decrease beyond 20s β.

TL responses were measured with the same sequence as for OSL, with the exception that the OSL measurement in step (iii) was replaced with a TL readout (0-450 °C at 5°C/s). TL curves are shown in figure 5.6. A rather striking trend is observed when looking at the TL curves of 2-100s β. Dose increase causes an increase in both peak intensities (figure 5.6a) as well as a shift in peak temperature (figure 5.6b). The peak temperatures decrease as dose increases, with values ranging from 252.5 °C (100s β) to 282.5 °C (2s β). Normalized curves highlight this trend as curves for low doses have a flatter rising flank and a steep falling flank, while the opposite is the case in curves for high-dose irradiations. The inset, which shows the area of the normalized TL curves, clearly indicates that increasing dose not only increases signal in the high temperature peak, but changes TL curve shape. This has previously been observed [120, 80].

Dose responses are shown on the logarithmic scale throughout the entirety of this work, rather than the linear scale, because it is easier to visualize data that span many orders of magnitude. For visual aid, a dashed black line indicating a perfectly linear dose response

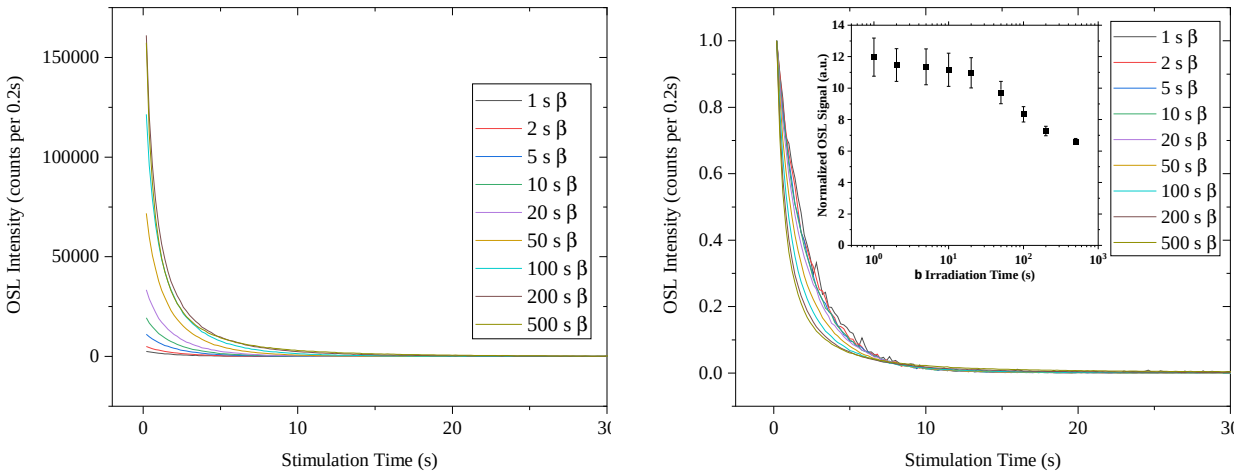

(a) (b)

Figure 5.5: OSL curves for a Al_2O_3:C dosimeter after irradiation with increasing beta doses (a) OSL curves as measured and (b) OSL curves normalized to their initial values. The inset shows the area under the normalized curves. Data points are mean values of four dosimeters, error bars indicate the standard deviation.

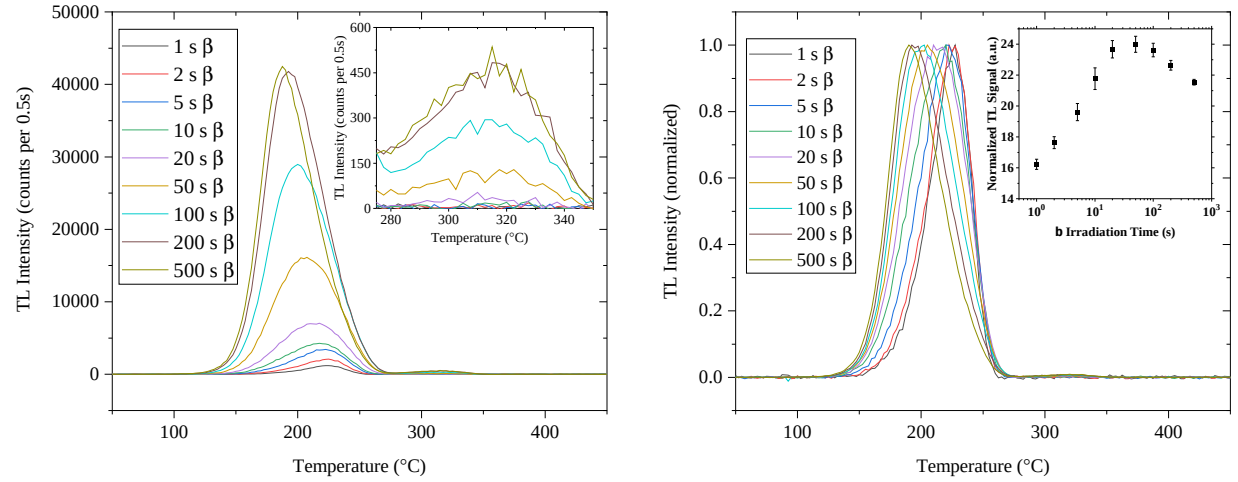

(a) (b)

Figure 5.6: (a) TL curves for an Al_2O_3:C dosimeter after irradiation with increasing beta doses. The inset shows the high temperature peak. (b) TL curves normalized to their peak values. The inset shows the area under the normalized curves. Data points are mean values of four dosimeters, error bars indicate the standard deviation.

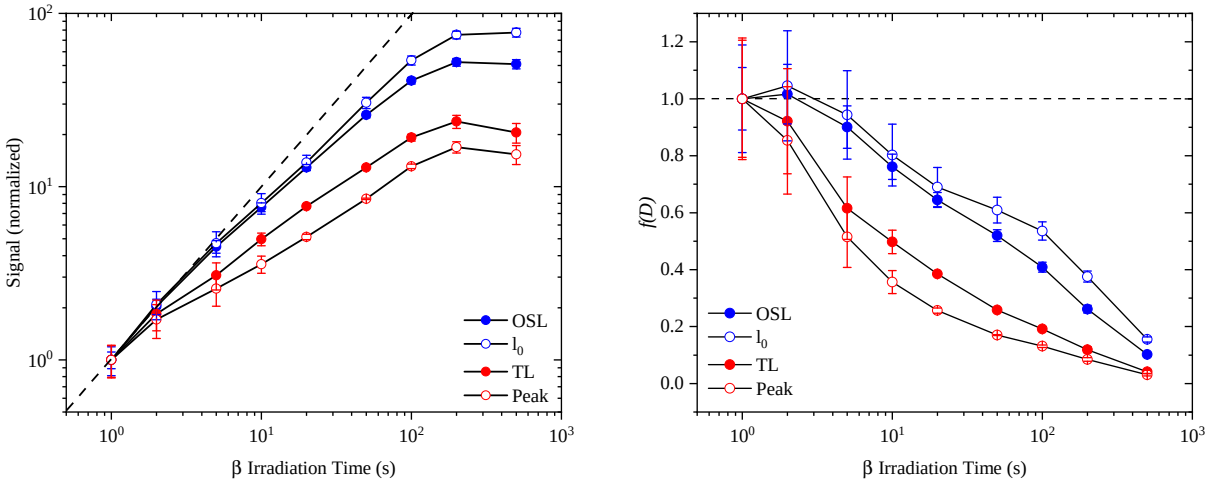

(a) (b)

Figure 5.7: (a) Al_2O_3:C dose responses from 1-500s . Signals were calculated with the 4 methods indicated in the legend. Signals were normalized to the values obtained for the lowest dose point. The dashed line indicates a linear relationship. Each point indicates the mean and standard deviation of three unique dosimeters. (b) Supralinearity for the 4 dose responses. The dashed line at 1 indicates linearity.

has been added to all dose response graphs.

The integrated OSL and l_0 dose responses are nearly linear between 1 and 5s, after which the response quickly becomes sublinear and saturates (figure 5.7a). Both thermal methods present responses that are sublinear from the beginning and have lower signals than either optical method for all doses measured.

Figure 5.7b illustrates that the TL and peak methods are significantly more sublinear than the optical methods. For instance, the peak method has a supralinearity value of about 0.5 at 5 s, whereas the l_0 method does not drop below 0.5 until between 100 and 200 s. The relative errors are not preserved since the y axis is on the linear scale. However, it is apparent that the OSL and l_0 signal standard deviations are smaller than those of TL and peak height. This is likely because thermal readouts have inconsistent cup contact, in addition to dosimeter mass and sensitivity differences that affect all measurement techniques. Additionally, it is clear that the non-uniformity among dosimeters changes magnitude based

on dose. Thus the OSL and TL σ_s values listed are dose-specific and should be treated with care.

5.1.2 α Source (^{241}Am) Irradiation

To test the properties of Al2O3:C after alpha irradiation, the same sequences were used as for beta irradiation with only slight modifications allowing for differences in signal intensities.

Uniformity and repeatability

The 10 dosimeters exposed to 500 seconds of α have drastically different initial OSL intensities (figure 5.8a) and moderate decay-rate variation (figure 5.8b), resulting in considerable curve shape variance. TL signals exhibit significant peak location and intensity differences when different samples are exposed to the same α dose (figure 5.8a). Additionally the normalized primary peak signal width is rather non-uniform (figure 5.8b). The integrated OSL and TL σ_s from 500s of α are 11.0% and 11.6%, respectively (figure 5.12a).

OSL curves do not change shape much when repeatedly exposed to α, then measured (figure 5.10). This differs from the significant curve shape changes observed for β (figure 5.2a). Contrary to the β results, TL peak height magnitude observably shrinks (figure 5.11a) even though the normalized curves do not appear to change (figure 5.11b). Upon repeated irradiation and OSL measurement, the dosimeters show an initial sensitization after which they reach a signal plateau (figure 5.12b). The increase in sensitivity is less than when exposed to β. TL signal desensitizes when exposed to α, whereas it increased in sensitivity with subsequent irradiations when exposed to β. This is very difficult to explain beyond elucidating the possibility that saturation effects may be present in higher LET/lower range radiation.

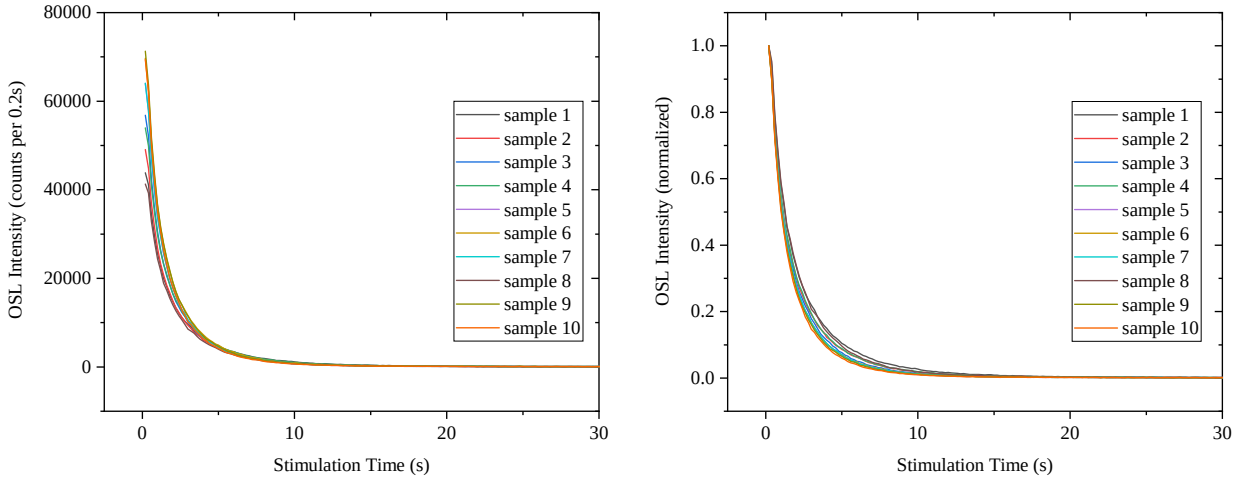

(a) (b)

Figure 5.8: Signal uniformity for 10 different Al_2O_3:C samples. a) OSL curves. b) OSL curves normalized to their initial values. Each sample was exposed to 500 seconds of α irradiation.

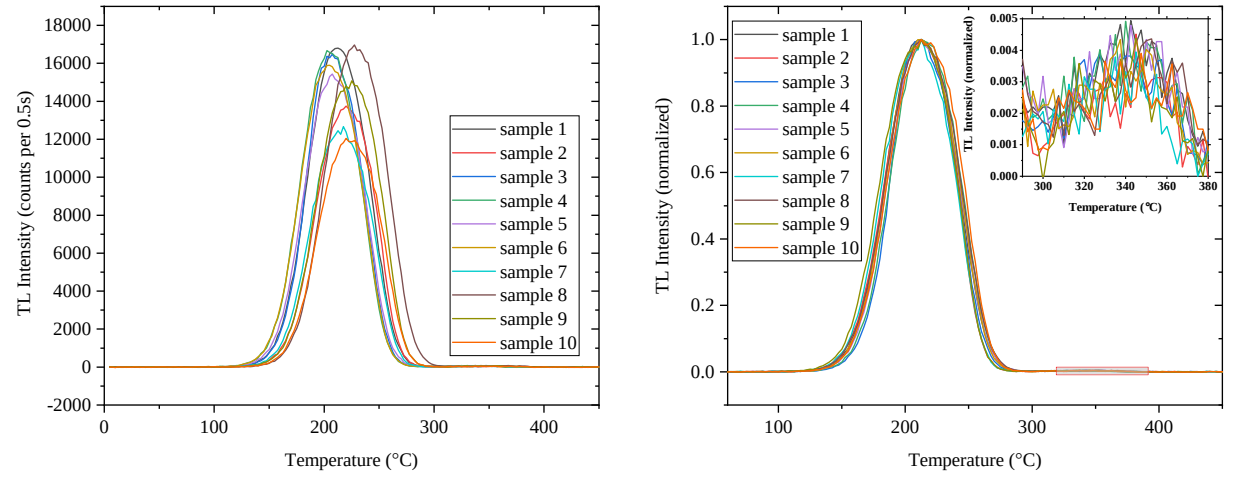

(a) (b)

Figure 5.9: Signal uniformity for 10 different Al_2O_3:C samples. a) TL curves. b) TL curves normalized to their peak values and shifted so that peak values occur at the same temperature. The inset shows the high temperature peak. Each sample was exposed to 500 seconds of α irradiation.

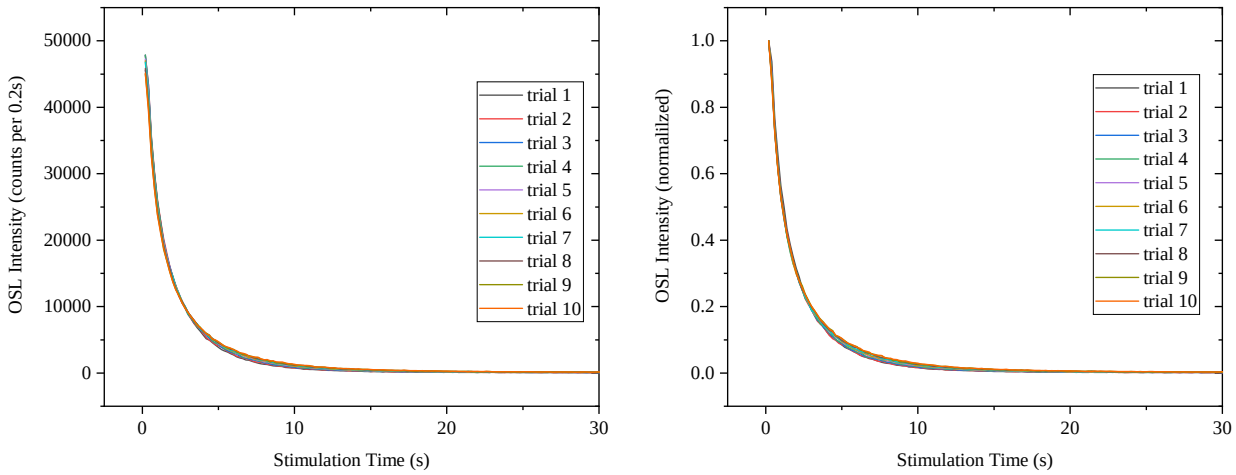

(a) (b)

Figure 5.10: (a) OSL curves of a single Al_2O_3:C sample exposed to repeated cycles of 500 s α irradiation followed by measurement. (b) OSL curves normalized to their initial intensity.

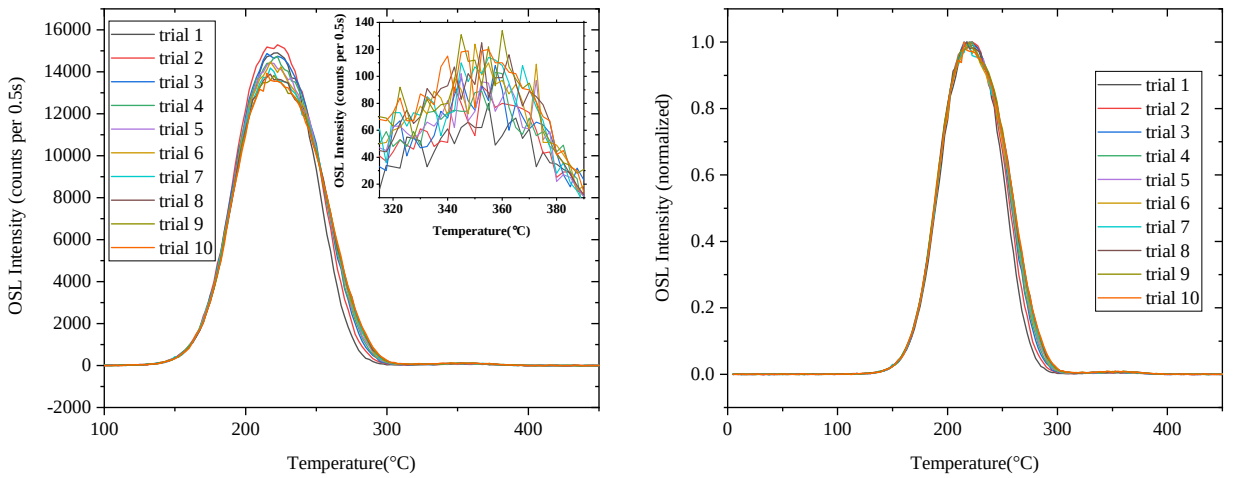

(a) (b)

Figure 5.11: (a) TL curves of a single sample exposed to repeated cycles of 500 s α irradiation followed by measurement. The inset shows the high temperature peak. (b) TL curves normalized to their peak height.

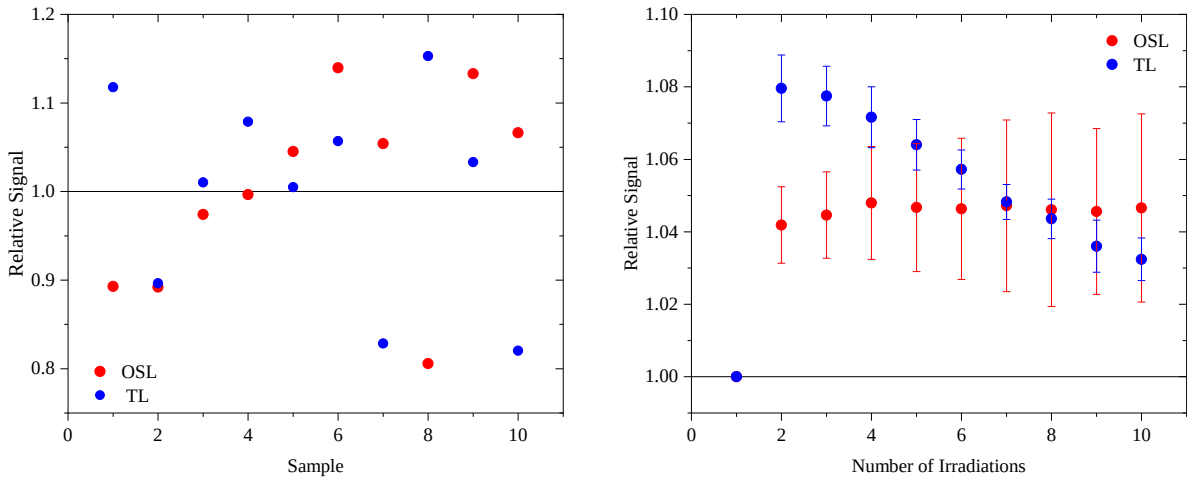

(a) (b)

Figure 5.12: (a) OSL and TL signals of 10 Al_2O_3:C dosimeters exposed to 500 s α. (b) Repeatability of 4 samples exposed to 500 s α 10 times. The data points represent the mean signal normalized to the initial signal. Error bars represent the standard deviation.

Dose response

The normalized OSL curves from α (figure 5.13a) have less shape change than β (figures 5.5a). This is consistent with previous OSL curve shape change results for Luxel dosimeters [60]. The largest shape change for α occurs at 10s and 20s, whereas the curves for 50s - 500s are nearly indistinguishable. It is important to make two comments here. Irradiation times for β and α sources are not directly comparable, since the two sources have different dose rates. Also, as discussed previously, track structure must be considered for larger particles such as α. It is believed that track overlap is one reason for OSL shape changes as HCP fluence increases [60]. Thus, it is likely that the normalized curves point to a relationship between OSL curve shape and LET. There is negligible normalized TL curve shape change with increasing α dose inside the range investigated (figure 5.13a).

Dose responses and their supralinearity values are shown in figure 5.14. Overall, the various responses are more similar than when exposed to β. The l_0 response is linear until higher doses and saturates later than both thermal responses when exposed to α. l_0 also

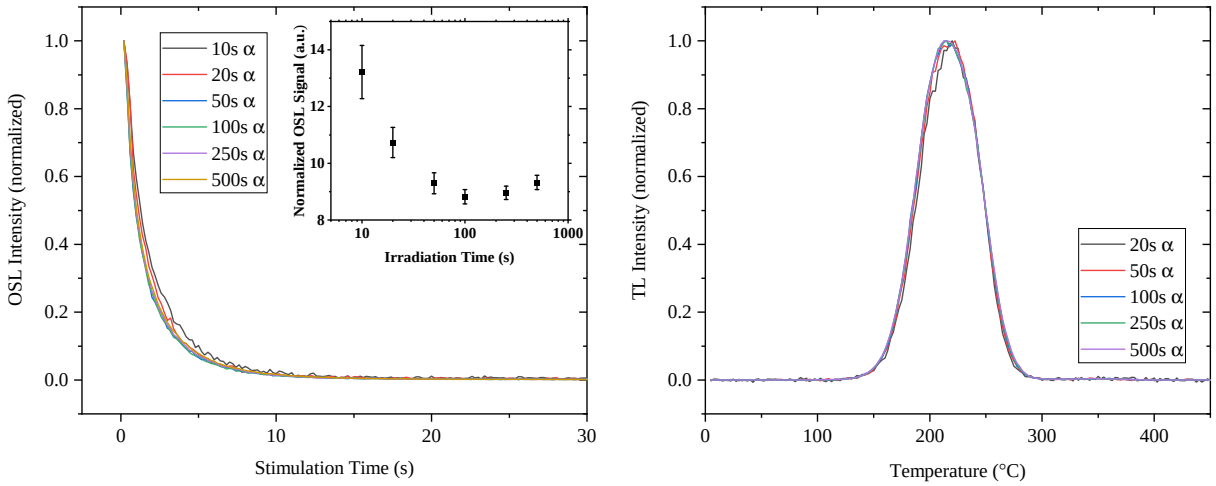

(a) (b)

Figure 5.13: (a) OSL curves of Al_2O_3:C after irradiation with increasing α doses, normalized to initial intensity values. The inset shows the area under the normalized curves. (b) TL curves normalized to their respective peak values.

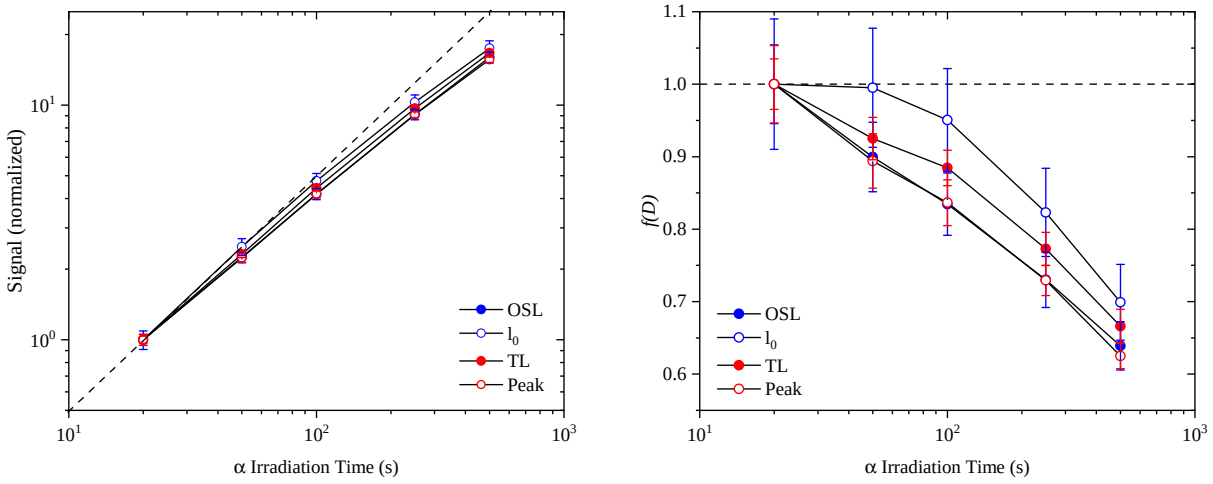

(a) (b)

Figure 5.14: (a) Al_2O_3:C dose responses after 20-500s α irradiation for the signals indicated in the legend. The dashed line indicates linearity. (b) Supralinearity function for the dose responses. Each point indicates the mean and standard deviation of three unique dosimeters.

has the largest signal variance along its domain, reaching values of nearly 10%. The OSL response follows closely with the peak response and is more sublinear than the TL response. Differences between beta radiation and the various ion irradiations will be discussed later in more detail.

5.2 BeO

5.2.1 β Source (^{90}Sr/^{90}Y) Irradiation

OSL uniformity and repeatability

Measurement sequences for BeO are similar to those used for Al_2O_3:C. However, adjustments had to be made due to the different nature of the materials. According to the literature BeO has deep traps that are emptied at lower temperatures than is the case for the synthesis of Al_2O_3:C used in this research. Also, BeO exhibits a slower signal decay under blue-light stimulation. Therefore, OSL uniformity characteristics of BeO dosimeters were investigated with the following procedure:

(i) annealing at 700 °C (15 minutes) in an external furnace

(ii) β dose equivalent to irradiation for 20s

(iii) OSL readout (120 seconds)

(iv) heating to 500 °C (at 2 °C/s)

(v) repeat steps (i)-(iv) for 9 other samples.

Results are shown in figure 5.15. Signals for 10 dosimeters exposed to 20s β varied in initial intensity and curve area (figure 5.15a) as well as curve shape (figure 5.15b). However, BeO OSL signal variance was less than Al_2O_3:C, with a σ_s value of 5.57%.

OSL repeatability characteristics of BeO dosimeters were investigated using the procedure outlined in the following sequence:

(i) annealing at 700 °C (15 minutes) in an external furnace

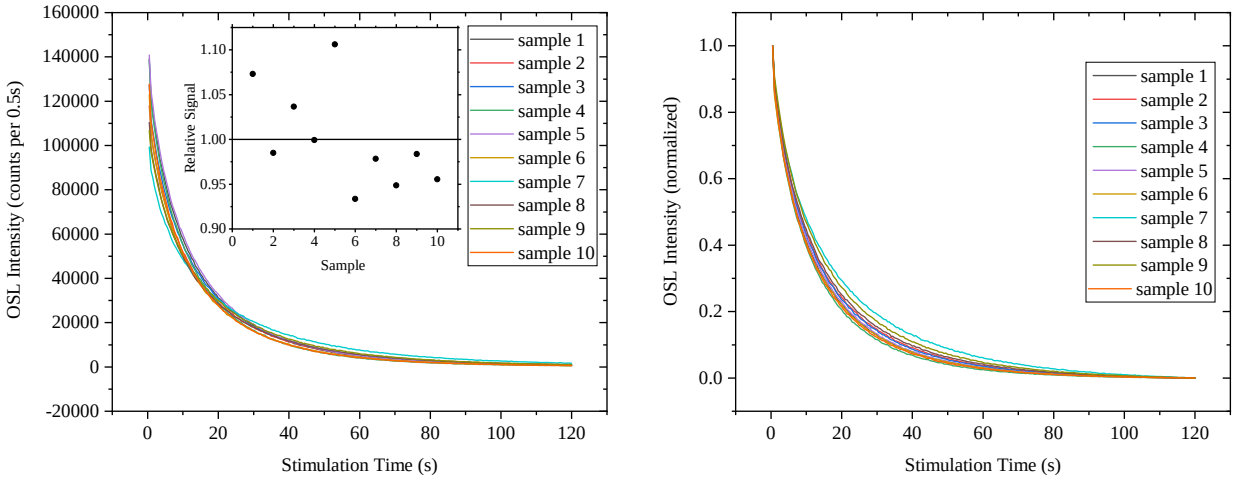

(a) (b)

Figure 5.15: Signal uniformity for 10 different BeO samples. a) OSL curves. The inset shows the integrated signal relative to the mean value of the 10 dosimeters. b) OSL curves normalized to their initial values. Each sample was exposed to 20 seconds of β irradiation.

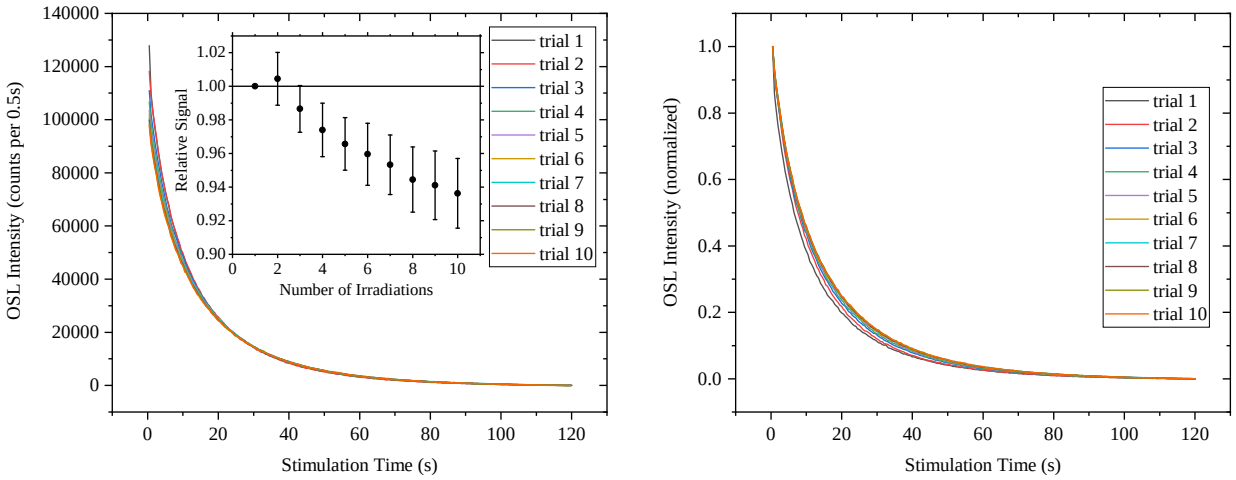

(a) (b)

Figure 5.16: Signal repeatability for 4 different BeO samples during 10 cycles of exposure to 20 seconds of β irradiation and measurement. a) OSL curves for one dosimeter. The inset shows the average signal of the 4 dosimeters relative to the signal measured in the first cycle as a function of number of irradiations. Error bars represent standard deviations. b) OSL curves normalized to their initial values.

(ii) β dose equivalent to irradiation for 20s

(iii) OSL readout (120 seconds)

(iv) heating to 500 °C (at 2 °C/s)

(v) repeat steps (ii)-(iv) 9 times for each sample.

(vi) repeat steps (i)-(v) for 3 more samples.

BeO OSL signals increased slightly from the first to second irradiation, followed by a decrease of about 1% per irradiation (figure 5.15a). Thus, BeO becomes desensitized upon repeated irradiations of the same magnitude, without annealing to 700 °C between each irradiation. This is consistent with previous results [121]. The signal decay also becomes slightly slower with successive irradiations (figure 5.15b).

TL uniformity and repeatability

All BeO TL tests were performed in the same manner as their OSL counterparts, with the exception that step (iii) is now a TL readout (0-500 °C at 2 °C/s). The signal uniformity test (figure 5.17) performed with 10 dosimeters exposed to 20 s of β has a TL signal deviation σ_s of 7.88%, fortifying the argument that TL variance should be higher than OSL variance due to inconsistent thermal contact (figure 5.17a). The high temperature peak location varies even after the main dosimetric peaks are centered, suggesting a larger dosimeter specific shape variance (figure 5.17b)) than is the case for Al_2O_3:C. The BeO optical and thermal signal σ_s values are lower than Al_2O_3:C for 20 s β.

While meaningful conclusions are hard to draw solely by analyzing the TL curves of a single dosimeter after repeated irradiation (figure 5.18a), the repeatability signals of BeO TL yield insight into the material's luminescence mechanisms. The total TL signal and the TL signal solely from the primary peak become slightly sensitized for the first 5 trials, followed by a plateau and even slight desensitization (figure 5.18b). However, the high temperature peak signal experiences significant desensitization, much like OSL. This reinforces the notion that the high temperature peak is primarily associated with the traps responsible for the

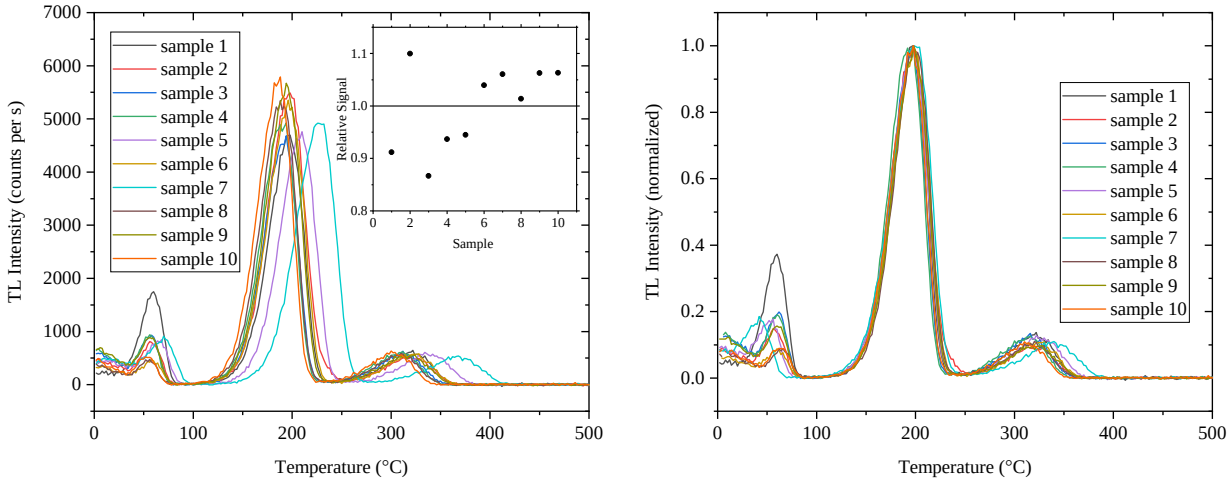

(a) (b)

Figure 5.17: Signal uniformity for 10 different BeO samples. a) TL curves. The inset shows the area under the main dosimetric peak signal relative to the mean value of the 10 dosimeters. b) TL curves normalized to their peak values and shifted so that peak values occur at the same temperature. Each sample was exposed to 20 seconds of β irradiation, then the luminescence was measured.

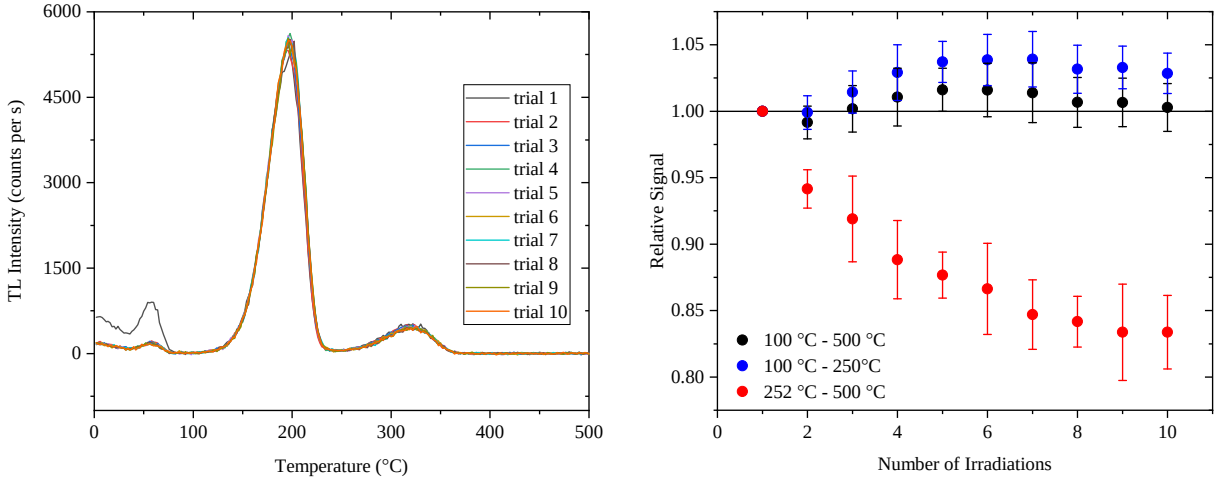

(a) (b)

Figure 5.18: TL repeatability. 4 dosimeters were exposed to repeated cycles of 20 seconds of β irradiation followed by measurement.(a) TL curves for a single BeO sample.(b) Average values for 4 dosimeters as a function of cycle number for the entire TL signal (black), as well as the TL area of the main domestic and high temperature peaks (blue abd red, respectively). Error bars represent the standard deviation.

OSL signal [108, 110].

The idea that the OSL signal is mostly derived from traps associated with the high temperature peak seems contrary to the results above, as the high temperature TL peak is much weaker than the primary dosimetric peak signal, much less the OSL signal. This is because BeO TL is prone to severe thermal signal quenching, i.e. temperature dependent signal suppression (see chapter 2). The efficiency of luminescence production decreases considerably with increasing temperature [25], meaning the measured TL curves are not truly representative of the charge distribution in the traps. Yukihara found the values necessary to correct measured TL curves for thermal quenching and obtain curves that are more representative of the actual charge distribution [107] by effectively solving the luminescence efficiency η [108] using the function previously derived in chapter 2 (equation (2.37)).

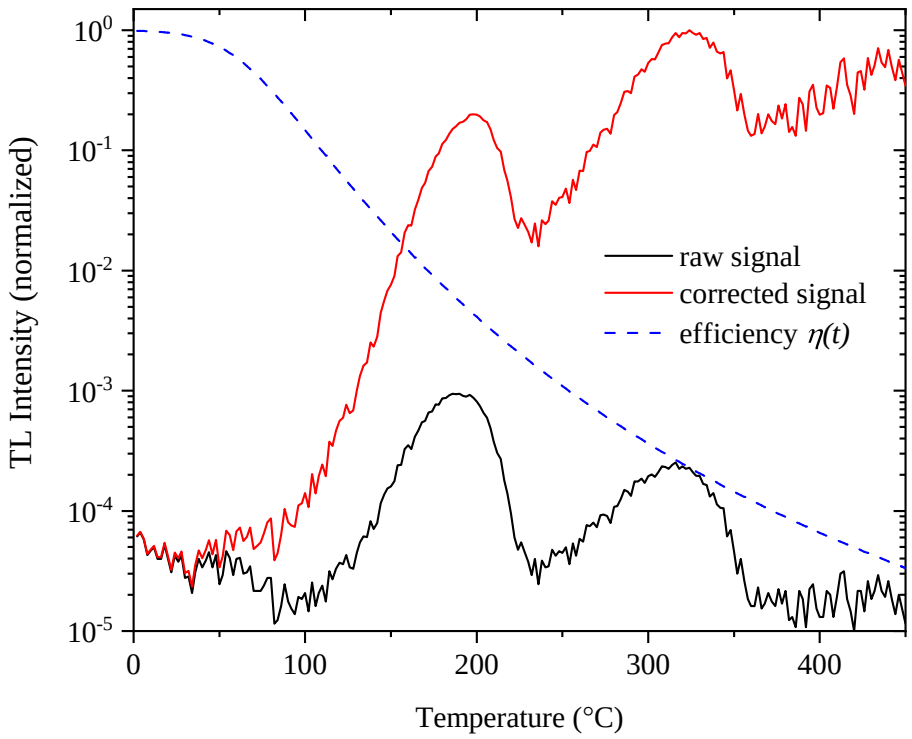

Figure 5.19: Depiction of the effect of thermal quenching on the TL signal of BeO. The corrected signal (red) can be obtained by dividing the raw signal (black) by the luminescence efficiency (blue dashed).

Figure 5.19 shows such a corrected BeO TL signal from 10 s β relative to the raw signal. For comparison, the luminescence efficiency as a function of temperature is shown as well. It is clear that the raw and corrected curves diverge as efficiency decreases. The corrected high temperature peak provides significantly more trapped charges than the low temperature and main dosimetric peaks, justifying the bright OSL signals derived primarily from charges associated with the high temperature peak. Luminescence is 73% efficient at 50 °C (OSL preheat temperature) and 0.025% efficient at 320 °C (high temperature peak center), equating to an OSL signal that is $\approx$ 2900 times more efficient than the high temperature peak based solely on temperature difference.

Dose response

The OSL dose response from BeO was investigated using the procedure outlined below:

(i) annealing at 700 °C (15 minutes) in an external furnace

(ii) beta dose #1

(iii) OSL readout (180 seconds)

(iv) heating to 500 °C (at 2 °C/s)

(v) repeat steps (ii)-(iv) for beta doses #2-6.

(vi) repeat steps (i)-(v) for 3 more samples.

The OSL readout in step (iii) was extended from 120s to 180s to increase signal collection for higher doses. Contrary to Al_2O_3:C, BeO OSL signals become slower with increasing dose between 2 and 100 s β (figure 5.20).

The central TL peak grows so rapidly with increasing dose that the uncorrected central peak from 100 s β dominates the TL curves for lower doses, to the point where they are not visible on the linear scale (figure 5.21a). Normalized and shifted curves (figure 5.21b) indicate that curve shape does not change significantly. The ratio of the high temperature peak signal to the main dosimetric peak signal, referred to as S_L, decreases as a function of dose.

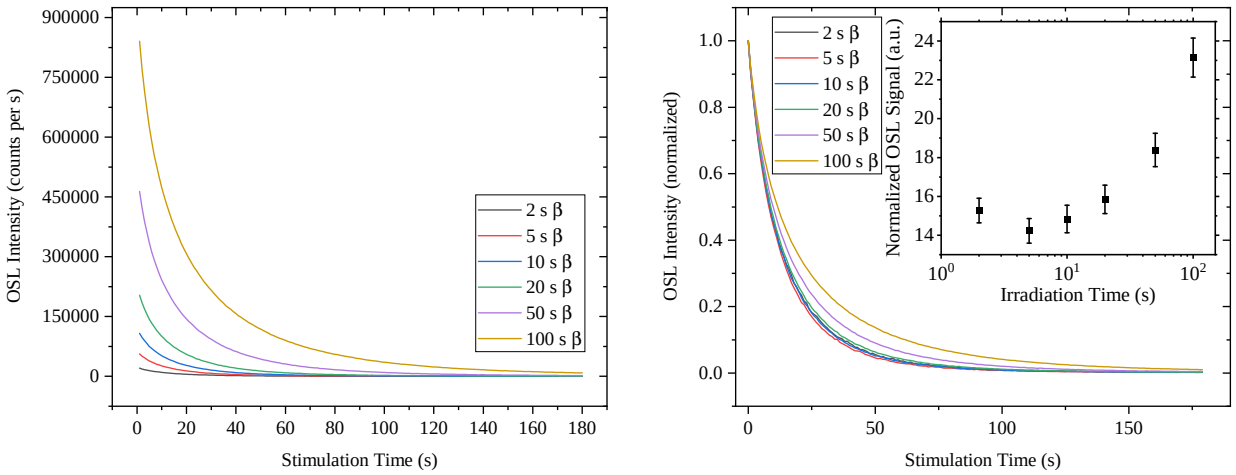

(a) (b)

Figure 5.20: OSL curves for a BeO dosimeter after irradiation with increasing beta doses (a) OSL curves as measured and (b) OSL curves normalized to their initial values. The inset shows the area under the normalized curves. Data points are mean values of four dosimeters, error bars indicate the standard deviation.

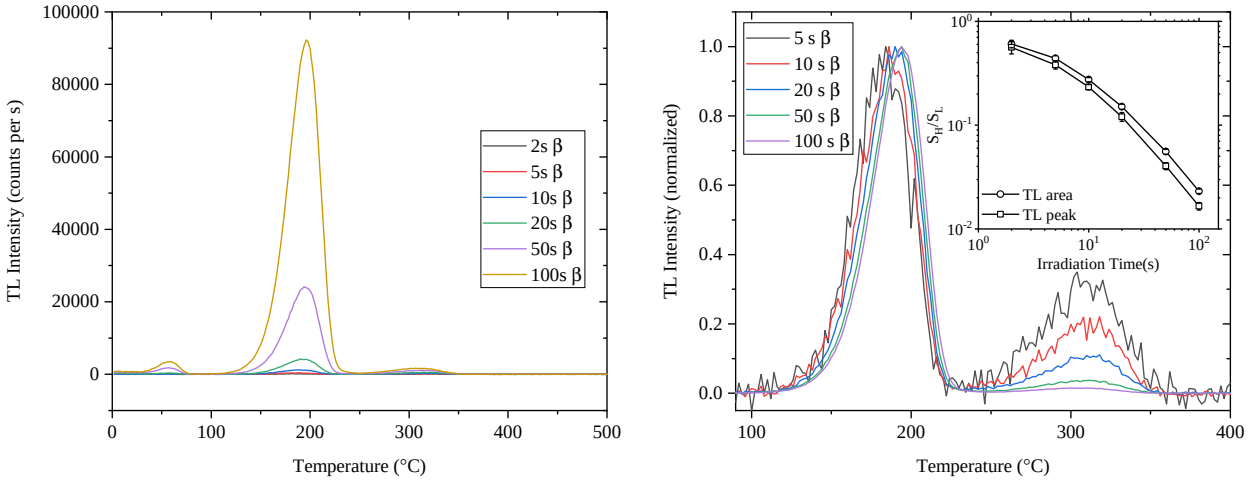

(a) (b)

Figure 5.21: (a) TL curves for a BeO dosimeter after irradiation with increasing beta doses. (b) TL curves normalized to their peak values. The inset shows the area and peak signal ratios of the high temperature peak to the main dosimetric peak (S_H/S_L) as a function of dose.

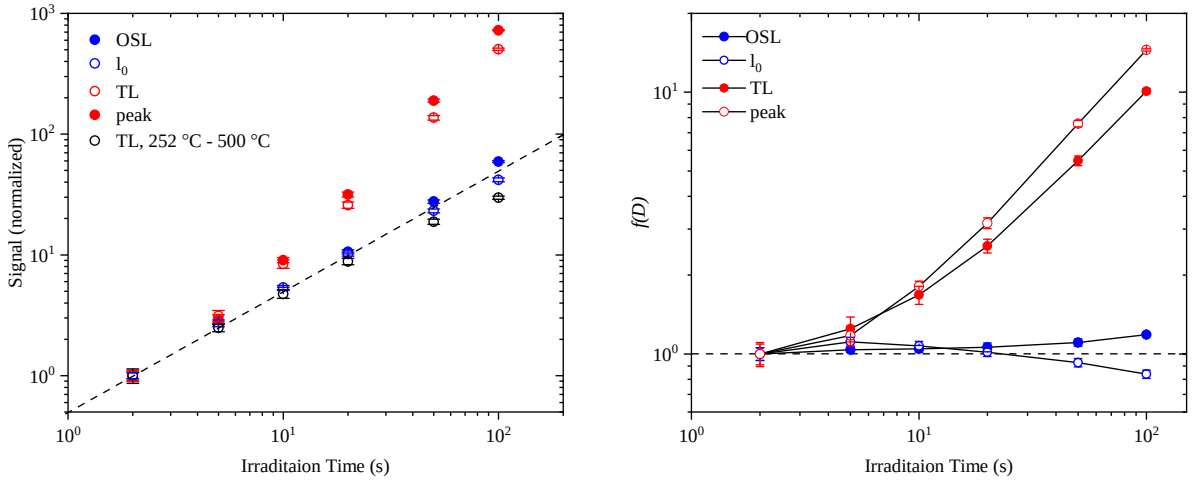

(a) (b)

Figure 5.22: (a) BeO dose responses from 2-100s β. Signals were calculated with the 4 methods indicated in the legend. Signals were normalized to the values obtained for the lowest dose point. The dashed line indicates a linear relationship. Each point indicates the mean and standard deviation of three unique dosimeters. (b) Supralinearity for the 4 dose responses. The dashed line at 1 indicates linearity.

The 4 analysis methods previously described are used to build BeO's response to β irradiation (figure 5.22). As an additional method, the TL area associated with the high temperature peak was determined. The OSL response is slightly supralinear and l_0 is linear/sublinear in the domain investigated (figure 5.22a). The qualitatively different behavior of the two methods indicates' the benefits of reporting both, although OSL appears to be the most linear method. Both thermal measurement techniques respond in a highly supralinear manner, with similar trends and only slight magnitude differences. However, the area of the high temperature peak has a sublinear response that most closely resembles the initial OSL intensity. This is in good agreement with the repeatability and quenching results already discussed. The supralinearity of the primary peak and sublinearity of the high temperature peak have been previously observed [106].

It is important to recognize a previous material observation because its effects are pertinent to the responses above; while repeated irradiations and measurements of the same

dose without annealing resulted in slight OSL desensitization (figure 5.16b), an increase in dose with subsequent irradiations cause sensitivity increase up to a value of ≈1.13 for 3.5 Gy [121]. These results and the repeatability results indicate the necessity for annealing samples to 700 °C between measurement and subsequent irradiation to reset the dosimeter. This also suggests that much of the OSL supralinearity above is due to lack of annealing. For example, the supralinearity value of OSL is 1.10 at a dose value of 3.76 Gy, or 50s (figure 5.22b). This is very similar to the increase in sensitivity expected based on Yukihara's findings. From this result it can also be speculated that l_0 would be even more sublinear were appropriate annealing procedures followed.

5.2.2 α Source (^{241}Am) Irradiation

Uniformity and repeatability

OSL and TL signal shape variance among different samples receiving the same α exposure (figures 5.23 and 5.24) is less than when exposed to β irradiation. This entails less variation in OSL decay time (figure 5.23b) and less thermal lag of the high temperature peak (figure 5.24b). The OSL and TL signal standard deviations σ_s of 10 chips exposed to 500 s α are 5.96% and 9.77%, respectively. Similar to the results obtained for β irradiation, OSL from BeO presents the most uniform signal compared to TL, and it is also more uniform than Al_2O_3:C when exposed to α.

The OSL signal decreases in initial intensity (figure 5.25a) and gets slower (figure 5.25b) when a single dosimeter is repeatedly exposed to the same α dose, then measured. This is consistent with observations from β irradiation. TL signals show minimal shape change under the same conditions (figure 5.26). During repeatability tests the OSL signal decreased significantly after each of the first 3 irradiations, followed by a slower desensitization for later irradiations (figure 5.27b). TL signals increased rapidly for the first few irradiations and then plateaued. Both of these trends are consistent with results from β.

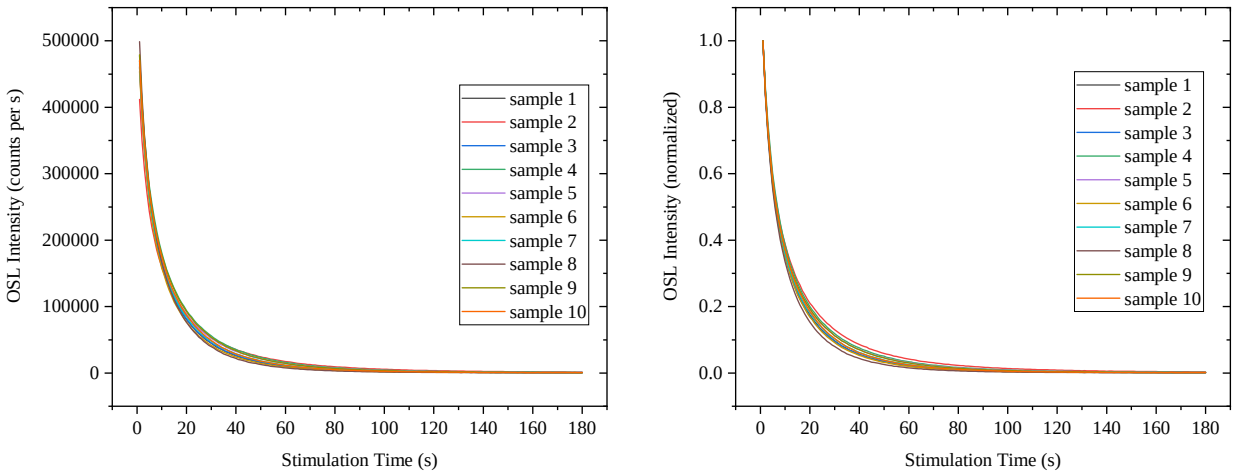

(a) (b)

Figure 5.23: Signal uniformity for 10 different BeO samples. a) OSL curves. b) OSL curves normalized to their initial values. Each sample was exposed to 500 seconds of α irradiation.

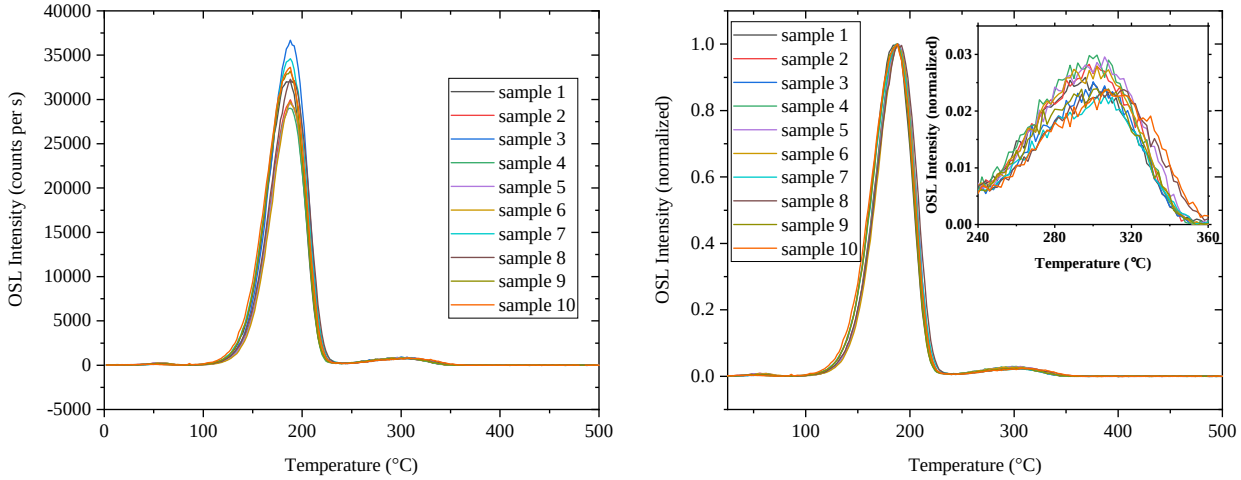

(a) (b)

Figure 5.24: Signal uniformity for 10 different BeO samples. a) TL curves. b) TL curves normalized to their peak values and shifted so that peak values occur at the same temperature. The inset shows the high temperature peak. Each sample was exposed to 500 seconds of α irradiation.

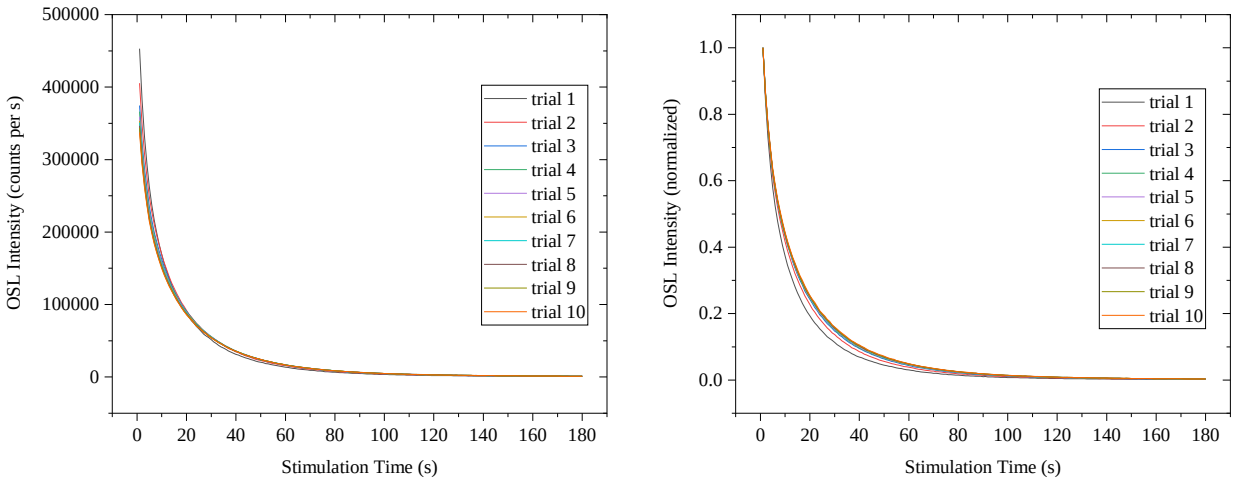

(a) (b)

Figure 5.25: (a) OSL curves of a single BeO sample exposed to repeated cycles of 500 s α irradiation followed by measurement. (b) OSL curves normalized to their initial intensity.

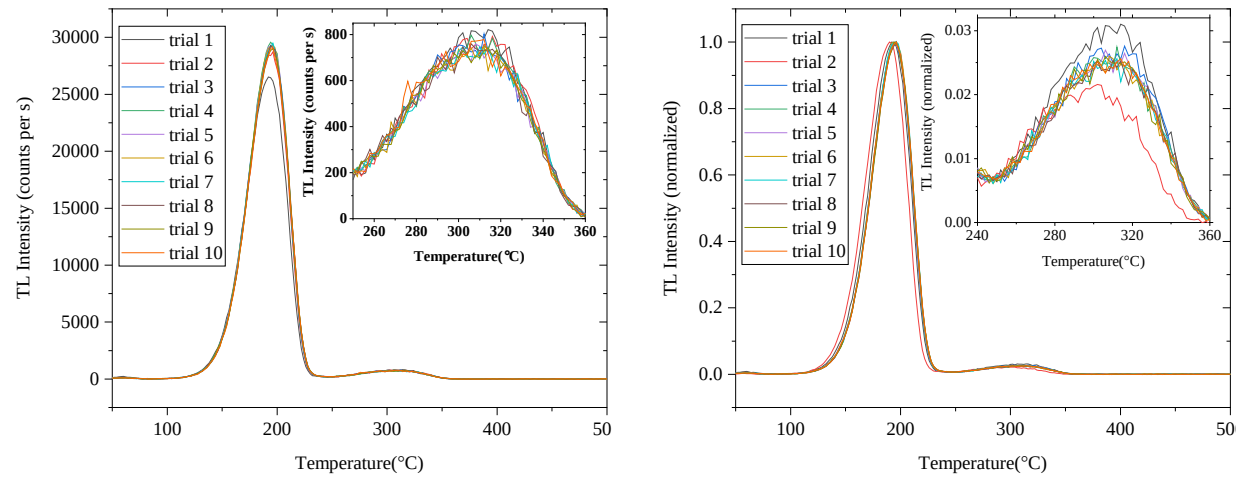

(a) (b)

Figure 5.26: (a) TL curves of a single BeO sample exposed to repeated cycles of 500 s α irradiation followed by measurement. (b) TL curves normalized to their peak height. The inset of both graphs show the high temperature peak.

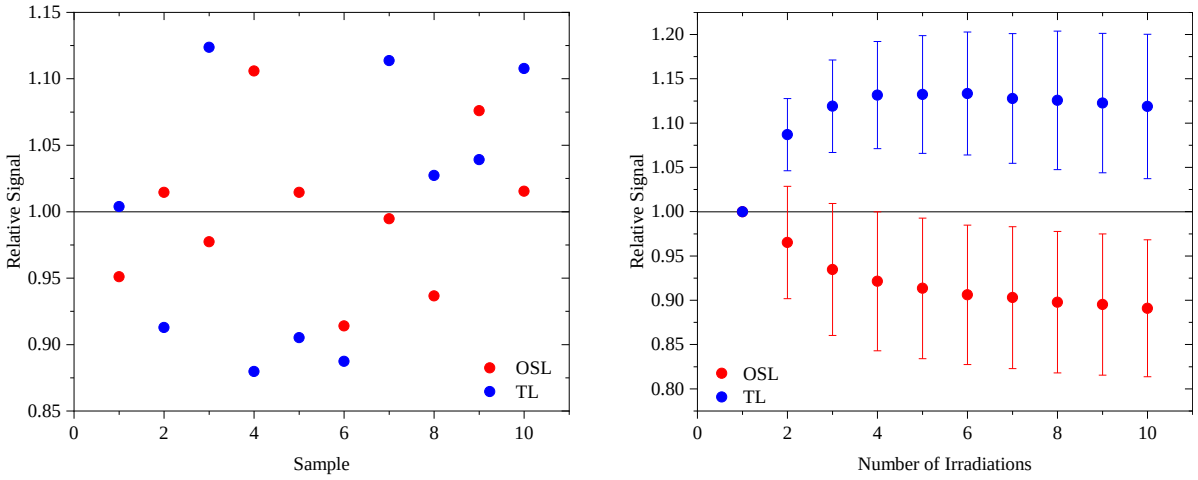

(a) (b)

Figure 5.27: (a) OSL and TL signals of 10 BeO dosimeters exposed to 500 s α. (b) Repeatability of 4 samples exposed to 500 s α 10 times. The data points represent the mean signal normalized to the initial signal. Error bars represent the standard deviation.

Dose response

The shapes of OSL curves with increasing α dose (figure 5.28) follow closely with the trend for β irradiation; the normalized signals decrease slightly for low doses, then the curves become flatter (slower decay) with increasing dose (figure 5.28a). Althought the exact dose rate of the α source is not known, one cannot help but speculate that the observations of Yasuda et al. apply here when looking at the discrepancy between relative high temperature peak heights between β (figure 5.21b) and α (figure 5.28b); that is, the ratio of the high temperature peak to main dosimetric peak S_H/S_H is LET dependent in this synthesis of BeO.

All 4 analysis methods yield a signal over-response when exposed to 10s α, relative to 20s - 500s α (figure 5.29). Beyond 10s the OSL response is slightly supralinear, the l_0 response is sublinear, and the TL area and peak responses are highly supralinear.

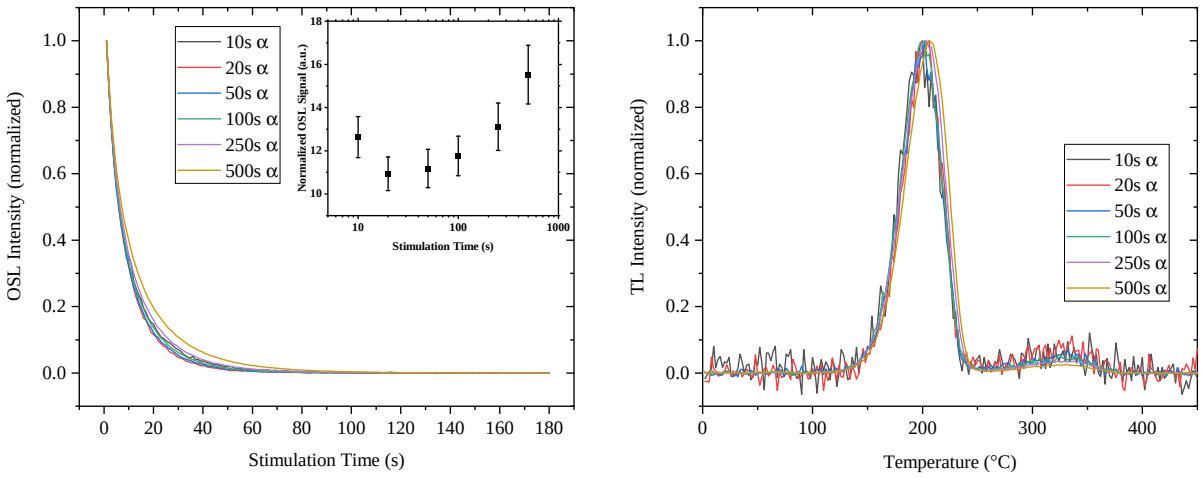

(a) (b)

Figure 5.28: (a) OSL curves of BeO after irradiation with increasing α doses, normalized to initial intensity values. The inset shows the area under the normalized curves. (b) TL curves normalized to their respective peak values.

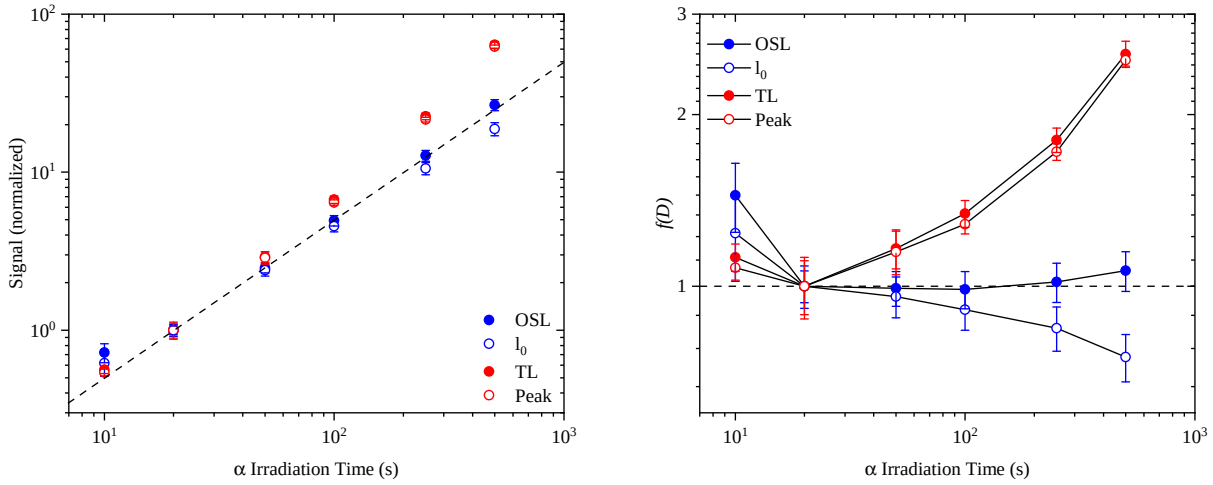

(a) (b)

Figure 5.29: (a) BeO dose responses after 10-500s α irradiation for the signals indicated in the legend. The dashed line indicates linearity. (b) Supralinearity function for the dose responses. Each point indicates the mean and standard deviation of three unique dosimeters.

5.3 Conclusions Relevant for Measurement of Accelerator Irradiated Dosimeters

Significant signal and shape non-uniformity among dosimeters given the same dose was observed for both materials and readout methods. It was also observed that individual dosimeters which are repeatedly given the same dose, then measured, display sensitization and desensitization, depending on the material and readout method. The 4 signal calculation method responses are nominally different for Al_2O_3:C and drastically different for BeO. Lastly, it was observed that BeO optical and thermal signals are subject to fading.

These observations lead to the following HCP experimental protocols: all dosimeters exposed to HCPs are first given a low-LET test dose to mitigate the dosimeter non-uniformity observed. The effectiveness of this method in correcting dosimeter variation will be shown later. Samples receive only a single test dose between annealing and exposure to HCPs to avoid significant repeatability effects. A fresh dosimeter will be irradiated for every data point to avoid issues with sensitivity changes.

Although it is not shown here, thermal fading of luminescence signals is known to be prolific in BeO. The term "fading" describes a time dependent loss of signal between irradiation and measurement. Thermal fading is caused when charges escape from shallow traps due to thermal stimulation at room temperature. Anomalous fading is used for any signal loss that cannot be explained through thermal influence. The origin of anomalous fading is often not well understood, and possibilities include localized tunneling and recombination of charges. Groppo and Caldas performed robust signal fading tests and determined that there is negligible OSL and TL fading beyond 1 day, and little fading beyond 6 hours for β and α [122]. Therefore, measurements are not performed on the same day as irradiation, ensuring that signals derive from stable traps at the time of measurement.

Chapter 6

Heavy Charged Particle Irradiation

It has already been discussed in Chapter 4 that while significant HCP research has been conducted for Al_2O_3:C and BeO, the response of the exact synthesis used in this study to heavy ions in the 1-8 MeV energy range has not been studied. The experiments and results presented in this chapter constitute the primary focus of this dissertation. They are constructed to systematically test the effects of a large HCP irradiation parameter space on Al_2O_3:C and BeO. Many of the methods used in similar publications will be utilized here, even if the materials are different. These include analyzing curve shape with increasing absorbed energy, absorbed energy signal response, and current-dependence of curve shape and signal. Additionally, curve shape differences among different ions will be investigated.

6.1 General experimental considerations

A summary of the investigated parameter space can be found in Table 1. For ion type, Hydrogen and Carbon were chosen because they yield prolific sputter source outputs. Ion energies are determined by terminal voltage and charge specie yields as discussed in chapter 3.1.3. Varying the energy absorbed by a dosimeter is equivalent to measuring a dose response. But while dose is a suitable concept for beta radiation which completely penetrates the dosimeters, a more suitable concept for HCPs is absorbed energy (see discussion in chapter

3.2.1).

The absorbed energies utilized were chosen because they compliment the ion source current and shutter speed. As mentioned in Chapter 3.2.5, shutter time uncertainty is the most significant source of error for low absorbed energy exposures. It is therefore desirable to obtain the lowest current possible so that timing error is minimized for a given absorbed energy. However, the ion source can only reach currents as low as $\approx$ 50-100 pA in the chamber Faraday cup before the beam is very noisy and unstable over time. The lowest fluence rate listed in Table 6.1 was deemed the minimal current required for uniform and stable beam, while the lowest absorbed energy listed was deemed the minimum value required to keep timing uncertainty below $\sim$15%. The remaining energy values were chosen so that the data is equidistant on the log scale and covers two orders of magnitude using only six dosimeters.

Parameter type	Experimental Choices
Material	Al_2O_3:C, BeO
Ion	Hydrogen, Carbon
Ion Energy (MeV)	H: 1, 2, 4 and C: 2, 4, 8
Absorbed Energy (J)	2E-5, 5E-5, 1E-4, 3E-4, 8E-4, 2E-3
Fluence Rate (ions $s^{-1}cm^{-1}$)	$\sim$4.3E6, $\sim$3.3E7, $\sim$2.0E8

Table 6.1: Parameter space investigated utilizing the particle accelerator.

Fluence Rate

Dosimeters are generally used to determine the dose (or energy) absorbed by a material. Absorbed energy is a function of irradiation time and fluence rate. The lower the number of ions impacting a target in a given time (i.e. the lower the dose rate), the longer the target has to be irradiated to achieve a given dose. In an ideal case the signal depends on the absorbed energy only, and not on the irradiation time.

Little dose rate research has been conducted compared to other parameters investigated in this work. Rahman et al. observed dose rate dependence in SiO_2 TL signal from therapeutic energy photons and electrons in the 100-1000 cGy/min dose rate range [123]. The Al_2O_3:C

signal on the other hand was found to be independent of dose rate for therapeutic range photon and electron beams in the dose range of 100-1000 cGy/min [124, 125]. To the authors knowledge, no HCP OSL or TL dose rate research has been conducted for Al_2O_3:C. This is potentially due to the experimental precision required to detect very small dose dependent changes, making therapeutic cyclotrons ideal candidates.

3 dosimeters were irradiated with 2E-3 J of energy from 4 MeV protons at three different fluence rates. The lowest fluence rate, 4.35E6 protons s^{-1} cm^{-1}, is the nominal dose rate utilized for all other HCP irradiations and corresponds to a chamber Faraday cup reading of about 80 pA. Very high currents result in problematic uncertainties due to very small exposure times. Thus, fluence rates higher than 2.00E8 protons s^{-1} cm^{-1} were not utilized. The resulting high fluence to low fluence ratio is ≈ 46. The highest absorbed energy from the dose response was chosen because it is the minimum value necessary to investigate currents well over an order of magnitude apart, while minimizing exposure time uncertainties.

LET

SRIM software was utilized to calculate the projected range of ions in water and each dosimeter material [63]. Water is calculated in addition to the dosimeter material because it is the standard way of presenting LET. An interesting dichotomy arises for the chosen ions and energies; the LET decreases with increasing proton energy, but increases with increasing carbon energy. The reason behind this is evident when Transport of Ions in Matter (TRIM) software[1] is utilized to calculate the energy lost to ionizations per unit path length and characteristic Bragg peaks are constructed [63].

Figure 6.1 shows the energy loss along the ions track for 1 MeV H, 4 MeV H, and 4 MeV C in Al_2O_3:C and BeO. Several conclusions can be drawn by comparing Bragg peaks pertinent to this work. First, projected range increases with increasing particle energy. For

[1] http://srim.org, last accessed on May 3, 2021.

Ion	Energy (keV)	LET_{H_2O} (keV/μm)	$LET_{Al_2O_3:C}$ (keV/μm)	LET_{BeO} (keV/μm)
H	1000	37.6	112	90.9
H	2000	26.0	77.5	61.9
H	4000	16.6	50.0	39.2
C	2000	471	1320	1090
C	4000	628	1660	1380
C	8000	748	1890	1590

Table 6.2: LET values for water, Al_2O_3:C, and BeO calculated via SRIM code for all ions utilized in this work [63].

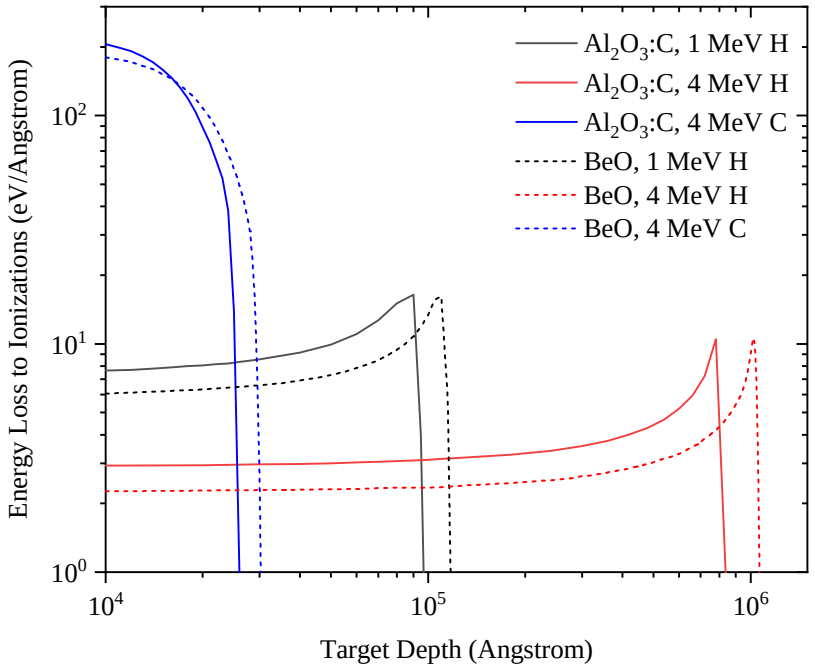

Figure 6.1: Bragg peaks of 1 MeV H, 4 MeV H, and 4 MeV C ions traversing Al_2O_3:C and BeO. The energy losses were calculated using TRIM (the Transport of Ions in Matter) software [63].

instance, 4 MeV protons travel almost 10 times the distance of 1 MeV protons. LET measures energy deposited per unit length. Thus, mean LET is smaller for high proton energies due to the low dose plateau preceding higher energy Bragg peaks. However the Bragg peak of Carbon is essentially directly below the surface, negating the effect of the low dose plateau on the mean LET. Next, increasing particle size drastically increases mean LET. 4 MeV carbon has a peak energy loss of over 200 eV/Angstrom in Al_2O_3:C, while 4 MeV H has a

peak loss of about 10 eV/Angstrom. Lastly, sample physical density affects projected range. The mean LET of any particle and energy in Al_2O_3:C is higher than BeO because it is about 38% more dense. All of these factors should be considered when comparing results presented in this work.

Measurement considerations

The ranges of low-energy ions in BeO and Al_2O_3:C are considerably shorter than the thickness of either dosimeter. Thus all of the ion energy is absorbed on the side of the dosimeter that faces the beam during irradiation. The Al_2O_3:C samples are opaque and the BeO samples are white (figure 4.9). Therefore, incoming light reduces in intensity as it passes through the samples, making consistent sample orientation paramount when measuring and irradiating samples [126].

Figure 6.2 shows a preliminary 2 MeV H dose response measured with OSL. The 1E-4 J and 3E-4 J samples were accidentally flipped 180 degrees after irradiation and before measurement. This resulted in signal measurements equalling approximately 13% of their expected values. The dosimeter self-attenuation is twofold: the LED light must pass through the dosimeter to reach the trapped charges, effectively reducing the stimulation light intensity, and the proportion of luminescence travelling back through the sample to the PMT is reduced as well.

Several previous HCP research experiments irradiated multiple dosimeters per dose to obtain an average and standard deviation [82]. Because of the scope of this dissertation, which included construction of the beamline, and constraints on available irradiation time, only one sample was irradiated per absorbed energy. This process was initially tested to ensure satisfactory results. It is known that HCP can change the dosimeter after exposure, thus it is not possible to provide an initial HCP test dose without potentially altering the sample. Thus all HCP responses are corrected with a low LET β test dose, known as reference dose S_R [82].

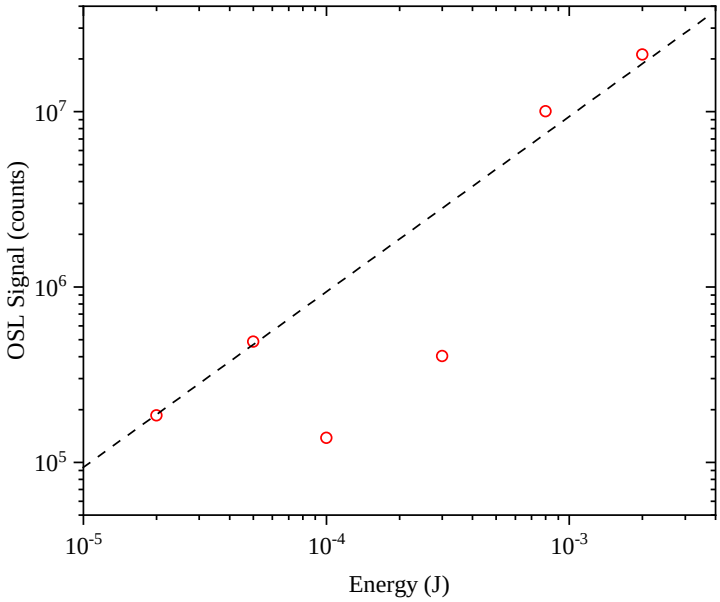

Figure 6.2: Relationship between sample orientation and signal.

The following experimental sequence was followed for each dosimeter:

(i) annealing in an external furnace

(ii) reference β dose

(iii) OSL or TL readout

(iv) heating to 450 °C or 500 °C using the Risø

(v) HCP irradiation

(vi) OSL or TL readout

(vii) heating to 450°C or 500 °C using the Risø

(viii) reference β dose

(ix) OSL or TL readout.

Two test doses were given (steps ii and viii), one before and one after HCP irradiation, to test for sensitivity changes after HCP irradiation. The resulting sensitivity differences were unclear and appeared random in nature. A definitive claim would require further investigation in which many dosimeters are given the same dose.

6.2 Al_2O_3:C

6.2.1 Hydrogen

Absorbed Energy Response

As stated above, the absorbed energy response is analog to a dose response for beta radiation. Representative OSL and TL curves for 1 proton energy are shown in figures 6.3 and 6.4. Curves for other ion energies are very similar besides signal magnitude differences. The initial OSL signal from 1 MeV protons increases until 8E-4 J, then decreases for 2E-3 J (figure 6.3a). The normalized signals from protons (figure 6.3b) are similar to those of α (figure 5.13a); curves initially decay faster with increasing absorbed energy, followed by slightly slower decays at higher absorbed energy. There is rather complicated TL signal growth with increasing absorbed energy from 4 MeV protons, with 3E-4 J and 8E-4 J displaying near maximum signal (figure 6.4a). It is not possible to determine how much of the peak temperature change is due to differing absorbed energy, mass and sensitivity differences, and inconsistent thermal contact. Normalized and temperature-shifted curves (figure 6.4b) show, that the TL curves get generally wider, although this trend is not entirely clear, especially on the high temperature side of the primary peak. The inset shows that the relative high temperature peak signal contribution from HCPs is very small for Al_2O_3:C in this absorbed energy domain.

Energy response curves are shown in figure 6.5. OSL, l_0, TL area, and TL peak measurement techniques all respond similarly when exposed to 1, 2, and 4 MeV protons; their signals are quickly saturating and even decrease with increasing absorbed energy beyond saturation, depending on the individual dosimeter's trap concentration. There is a clear LET signal-magnitude dependence as 4 MeV protons produce the highest signals and 1 MeV protons produce the smallest signal. This behaviour is similar to previous results for Al_2O_3:C TLD-500s and LiF:Mg,Ti [43, 127]. It can be attributed to the differences in ionization density and therefore dose deposition already discussed. To achieve the same value of absorbed

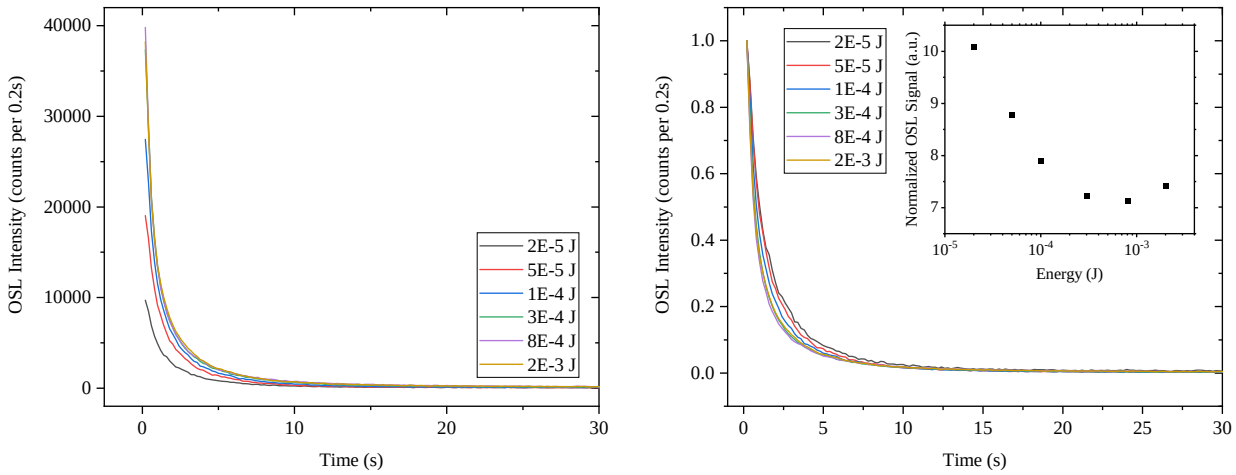

(a) (b)

Figure 6.3: Raw (a) and normalized (b) Al_2O_3:C OSL curves from 1 MeV protons. The inset shows the area under the normalized curves.

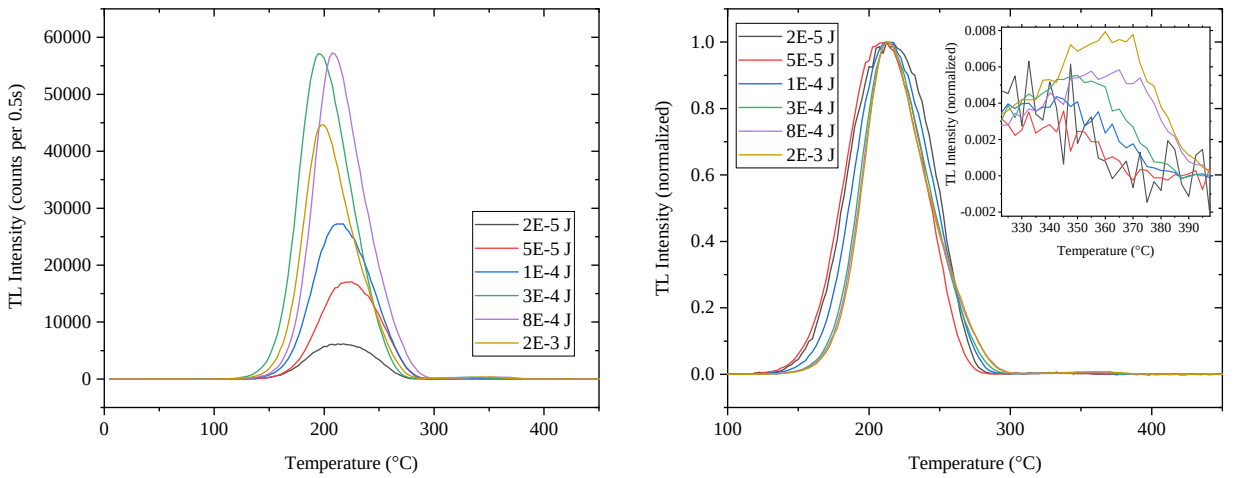

(a) (b)

Figure 6.4: Raw (a) and normalized (b) Al_2O_3:C TL curves from 4 MeV protons. The inset shows the high temperature peak only.

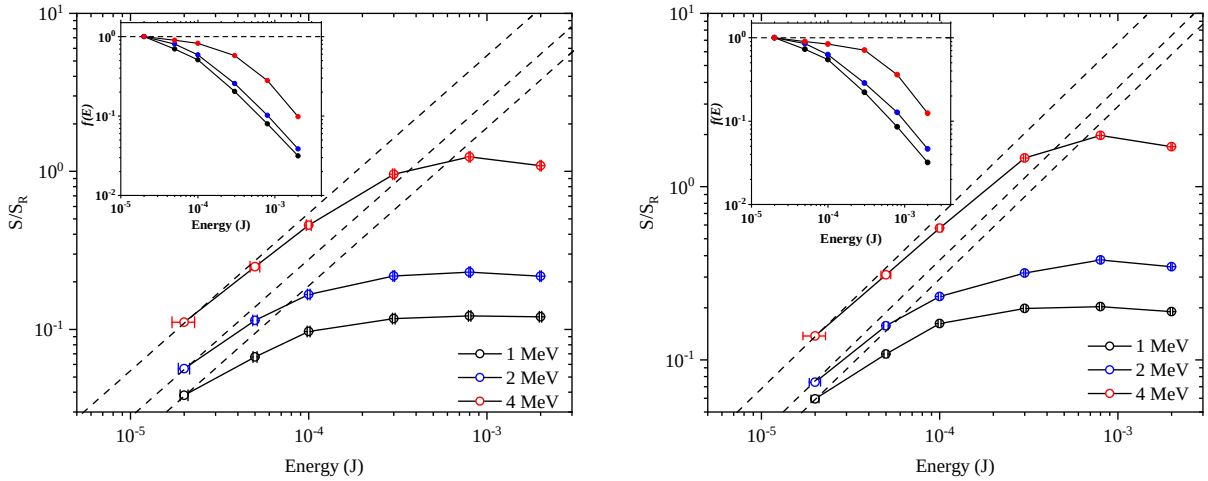

(a) (b)

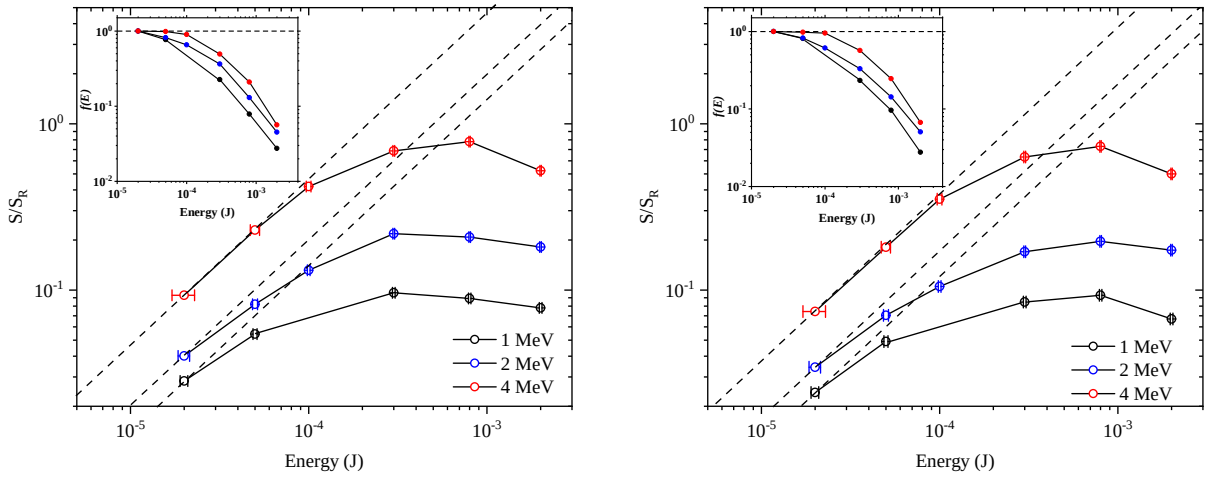

(c) (d)

Figure 6.5: Absorbed energy responses of Al_2O_3:C to 1, 2, and 4 MeV H^+: (a) OSL , (b) l_0, (c)TL, and (d) TL peak. All HCP signals are corrected with a 10s β test dose, and absorbed energy uncertainties are shown. Insets show the supralinearity factor as a function of absorbed energy E.

energy, a larger number of 1 MeV than 4 MeV protons is required, so that track overlap is more prevalent for lower energy protons. 4 MeV protons have the lowest ionization density and therefore produce more luminescence. The data suggests that there are only small difference between the 4 measurement and analysis methods.

Current

To test the impact of fluence rate (ion current) on measured signals, 3 dosimeters were irradiated with 2E-3 J of energy from 4 MeV protons at three different fluence rates. Results are shown in figures 6.6 and 6.7. Normalized TL and OSL curves indicate very small change in curve shape in the range of fluence rates investigated (figures 6.6a and 6.6a). The OSL curves appear to get slightly slower and the TL curves appear to become narrower. However, these differences are small enough that dosimeter shape non-uniformity could be responsible (see figures 5.8b and 5.9b). Furthermore, there are no OSL, l_0, TL area, or TL peak signal differences by current (figures 6.7a and 6.7b). However, it has to be taken into consideration that tests like these should ideally be performed in the linear response domain. Because Al_2O_3:C is already completely saturated at 2E-3 J, the results essentially display the spread in saturation signals of dosimeters at different dose rates. The results are shown for the sake of completeness. The absorbed energy uncertainties are 0.54%, 1.4%, and 11% (from low to high current, respectively), indicating the relative effect of fluence rate on exposure precision.

6.2.2 Carbon

Normalized OSL and TL curves for 4 MeV Carbon are shown in figure 6.8. The OSL curves get faster with increased absorbed energy in the same manner as protons. However, comparing the normalized signal reveals that the Carbon OSL curves (figure 6.8a) are slower than proton proton OSL curves (figure 6.3a) in the absorbed energy range investigated. The Al_2O_3:C signals from Carbon were much weaker than from protons, and especially β. As

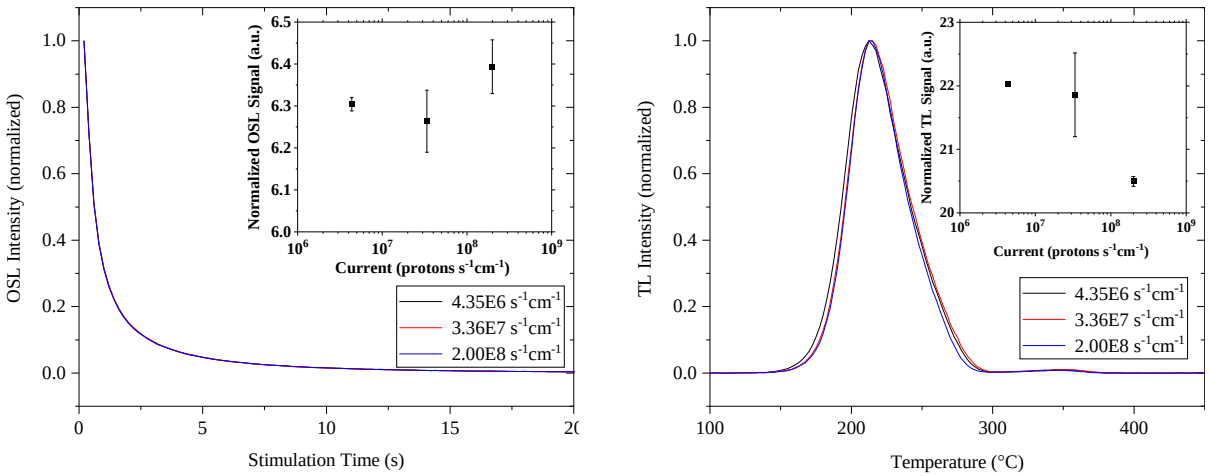

(a) (b)

Figure 6.6: Normalized Al_2O_3:C OSL (a) and TL curves (b) for different H^+ currents, each representing the average of three curves. Insets show the mean ± standard deviation of the normalized signal from three dosimeters.

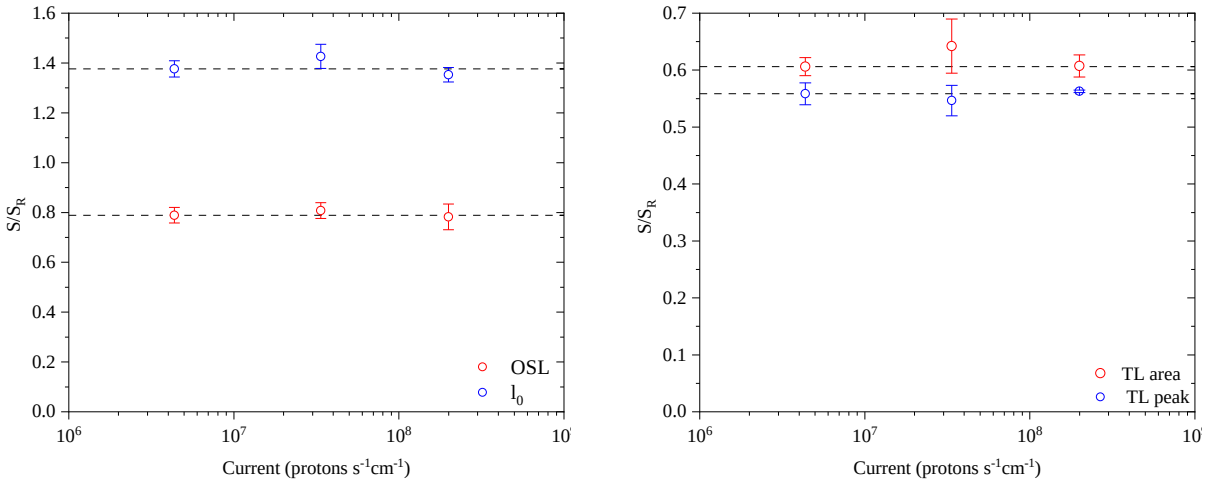

(a) (b)

Figure 6.7: Al_2O_3:C H^+ current dependence for both optical (a) and thermal (b) measurement methods. Points represent the mean ± standard deviation of the signal from three dosimeters normalized with a 10 s β reference dose. The dashed lines extrapolate the mean value of the lowest current.

seen in Table 3.4, Carbon signals were measured with no filters or apertures. This enabled a higher resolution view of the high temperature peak, which was very noisy for protons (see figure 6.4b) due to the filter attenuation necessary to protect the PMT. The relative Carbon signal contribution of the high temperature peak is significantly more pronounced than for protons (figure 6.8b). Even more remarkably, the high temperature peak deconvolves into two distinct high temperature peaks, which were thought to be a single peak until this point.

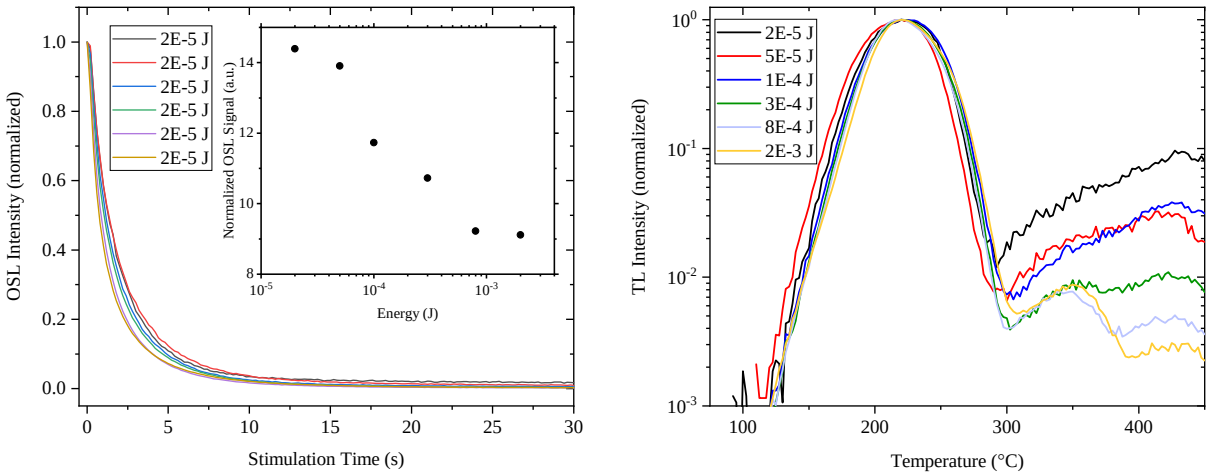

(a) (b)

Figure 6.8: Normalized Al_2O_3:C OSL curves (a) and TL curves (b) for different absorbed energies from 4 MeV Carbon. The inset shows the area under the normalized curve.

Absorbed energy responses are shown in figure 6.9. OSL, l_0, TL area, and TL peak measurement techniques all respond similarly when exposed to 2, 4, and 8 MeV Carbon. The insets of all responses show a sublinear supralinearity factor that quickly approaches zero. The increased saturation of the 2 MeV Carbon signal relative to the 4 and 8 MeV signals, due to higher fluence (see Chapter 2.5), is more pronounced than for protons. There are again observable signal magnitude differences by varying ion energy.

Based on the model presented signal magnitude is inversely correlated to LET (i.e., higher LET yields lower signal). The data for 8 MeV Carbon are not consistent with this model,

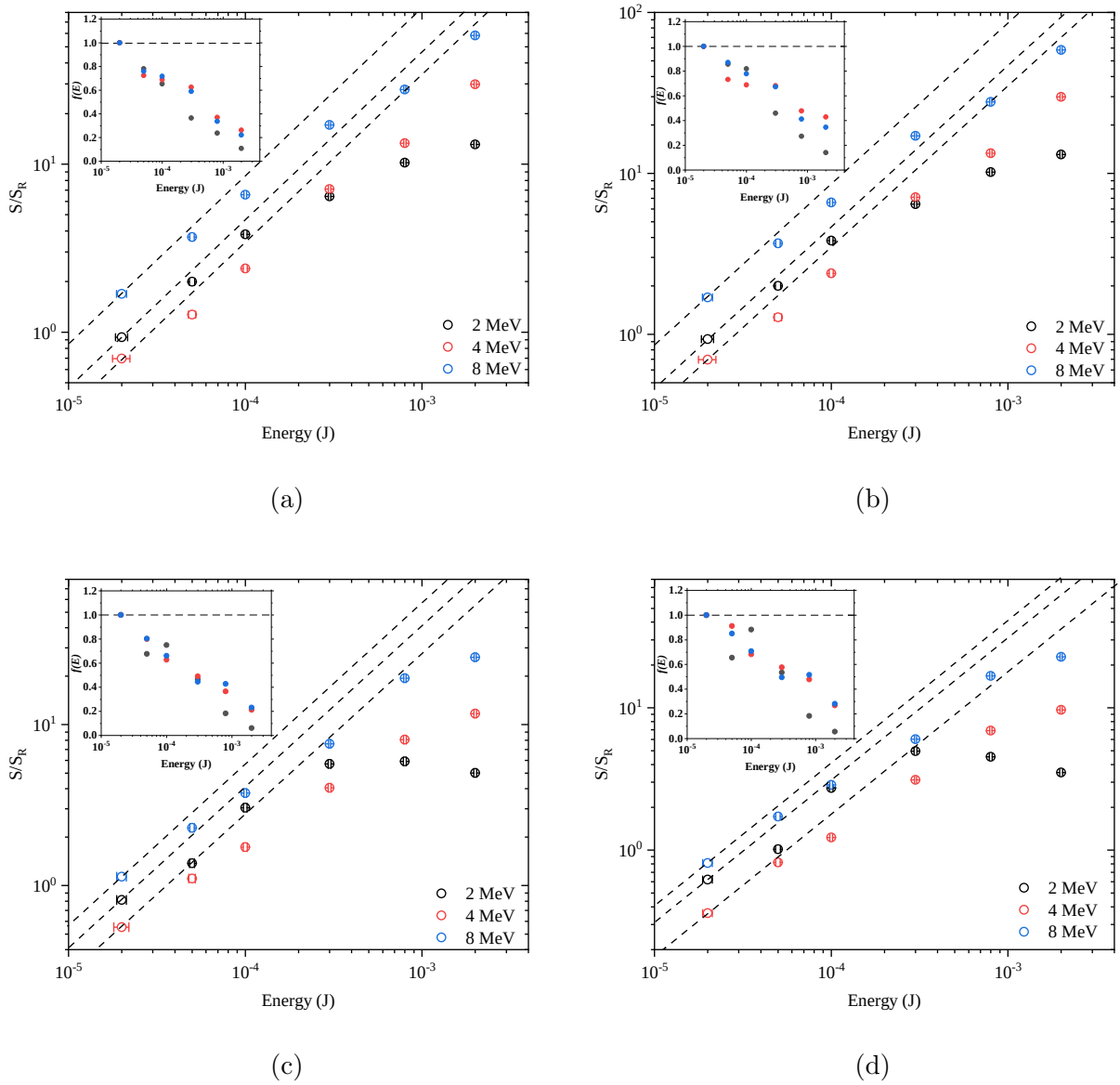

Figure 6.9: Absorbed energy responses of Al_2O_3:C to 2, 4, and 8 MeV Carbon: (a) OSL , (b) l_0, (c)TL, and (d) TL peak. All HCP signals are corrected with a 2s β test dose, and absorbed energy uncertainties are shown. Insets show the supralinearity factor as a function of absorbed energy E.

unlike the other 5 ions and energies used in this work (reference table 6.2). The author has no explanation for this discrepancy. The accelerator was experiencing vacuum and pressure gauge malfunctions when this data was collected. However, all of the equipment required to calculate absorbed energy were functioning normally, suggesting the experimental results are valid. Ideally the 8 MeV data collection process would be repeated; there simply was not adequate time. Thus, all 8 MeV results are still shown but should be considered questionable.

6.2.3 Comparison of H, C, α, and β

Normalized OSL and TL curves for 4 MeV H, 4 MeV C, ~5.49 MeV He (α), and β are shown in figure 6.10. The proton and Carbon data have the same ion energy, and therefore the same ion fluence for a given absorbed energy. Thus these two curves are best suited for investigating the effect of ion type alone on curve shape. Nevertheless, He and β curves are also shown. The He and β energies were chosen because they are closest to 2E-5 J, and were calculated using the absorbed energy rates and dose rates discussed in chapter 3.3.1. As a reminder, the α energy value is an estimation based on geometrical approximations whereas the other energies were obtained from measured values.

The OSL curves for this synthesis of Al_2O_3:C get slower with increasing ion LET (figure 6.10a); this completely opposes published results for TLD-500 single crystal dosimeters [43] and Luxel dosimeters [86], which get faster with increasing ion LET. The signal is shown on the log scale so it is easier to distinguish between differing decay speeds. The high temperature peak from Carbon irradiation is significantly more prevalent than any other ion. It is too noisy to distinguish between the relative high temperature peak heights of H, He, and β. There is also significant normalized width difference between ions on the high temperature side of the main dosimetric peak, although this could simply be due to dosimeter-specific shape variation.

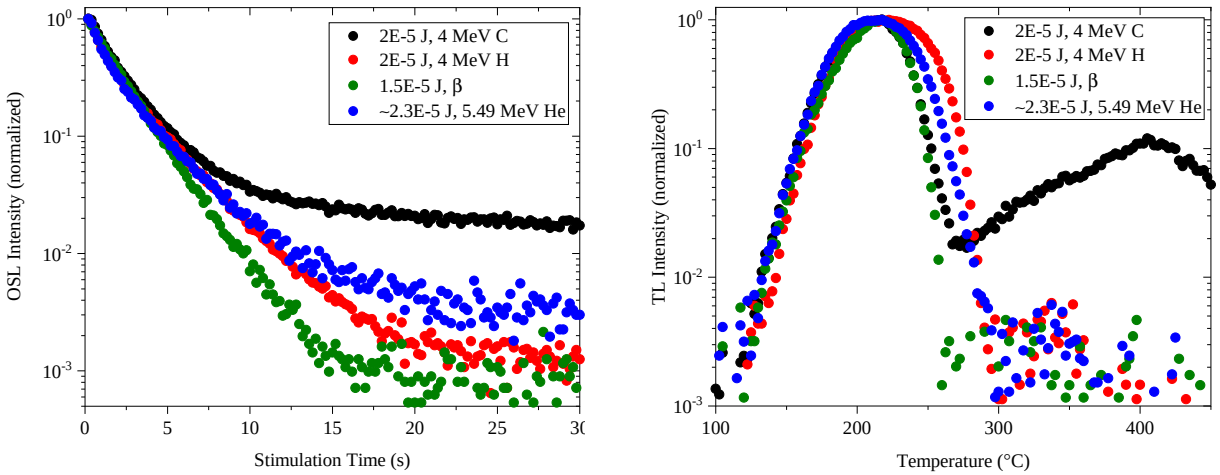

(a) (b)

Figure 6.10: Normalized Al_2O_3:C OSL (a) and TL (b) curves for 2E-5J 4 MeV H, 2E-5J 4 MeV C, ∼2.3E-5J 5.49 MeV He, and 1.5E-5J β.

6.3 BeO

6.3.1 Hydrogen

Absorbed Energy Response

OSL curves for different absorbed energies from 1 MeV protons are shown in figure 6.18. There is an initial decrease in area under normalized signal followed by an increase to a local maximum and further decrease. It is visibly evident that the curves initially decay slower, but then start to decay faster with increasing absorbed energies. TL curves from 4 MeV protons are shown in Figure 6.12. The 4 MeV curves have a relatively larger high temperature peak than curves for 1 and 2 MeV protons. Normalized signal is shown as a semi-log scatter plot to elucidate the relative contribution of the high temperature peak based on dose and the signal-to-noise ratio (SNR) associated with low doses. The width of the main peak increases as dose increases and the relative signal height of the high temperature peak decreases with absorbed energy. Low dose TL curves are exceptionally weak and noisy because of the of

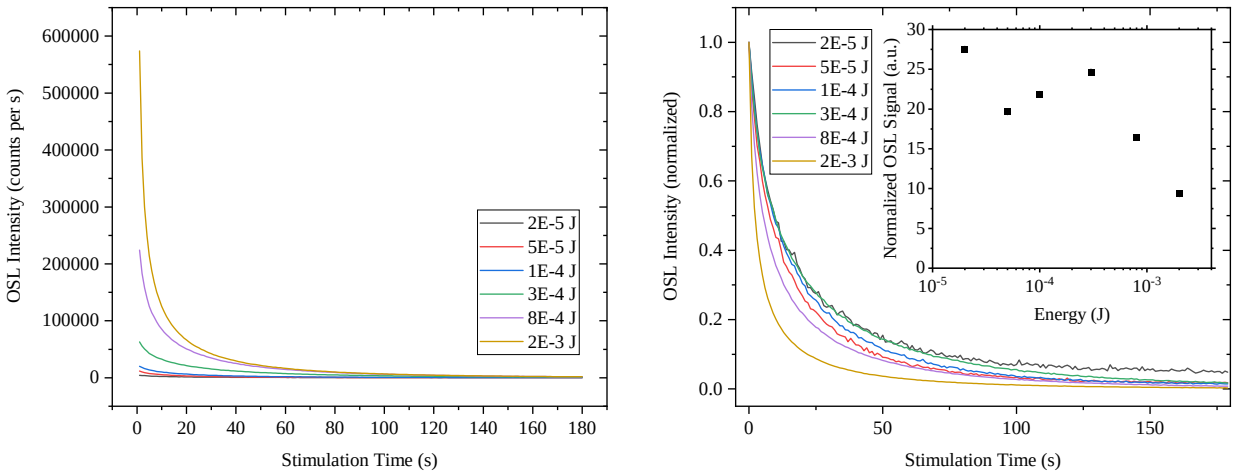

(a) (b)

Figure 6.11: Raw (a) and normalized (b) BeO OSL curves for different absorbed energies from 1 MeV protons. The inset shows the area under the normalized curves.

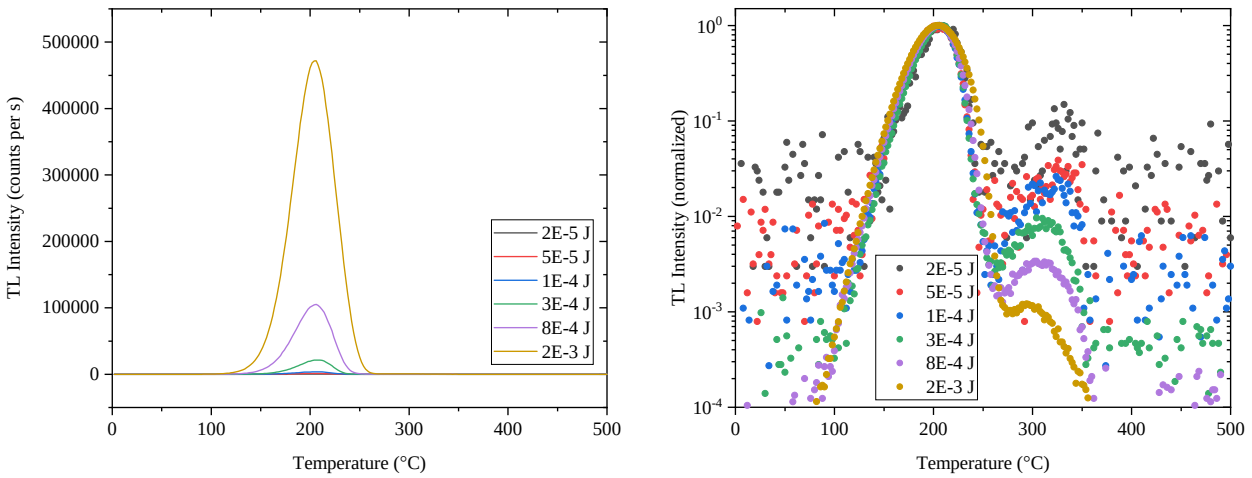

(a) (b)

Figure 6.12: Raw (a) and normalized (b) BeO TL curves from 4 MeV protons for different absorbed energies.

the neutral density filters required to prevent high doses from saturating the PMT.

Absorbed energy responses are shown in Figure 6.19. A systematic approach was taken to evaluate the response of BeO to 36 unique combinations of absorbed energy, proton energy, and data analysis method. The total OSL is close to linearity. It shows slight sublinearity from 2E-5 J to 1E-4 J, followed by supralinearity until apparent saturation effects kick in (figure 6.13a). Supralinearity increases with decreasing LET, and signal saturation occurs at lower absorbed energy for 1 and 2 MeV protons compared to 4 MeV protons. l_0 (figure 6.13b) is close to linearity as well. The initial signal becomes increasingly sublinear until the trend reverses and the initial intensity becomes supralinear. This sublinearity becomes more pronounced for increasing proton energy. For BeO, the optical signals are both nearly linear, but taking a closer look, the OSL area shows a different trend than l_0. This is unlike Al_2O_3:C where the two signals showed similar trends and were both approaching saturation. The intensities of both optical signals vary with proton energy. The same trend is observed in Al_2O_3:C TL; as proton energy increases, mean LET decreases, leading to increased signals.

TL area and peak responses exhibit strong supralinearity (figures 6.13c and 6.13d, respectively) similar to the observations for β and α (figures 5.22 and 5.29, respectively). The responses for the two signals are nearly identical apart from slight signal magnitude differences. Signal magnitudes from different energy protons are very similar for small absorbed energies, but diverge beyond 3E-4 J. Proton TL responses have negligible LET-dependent signal quenching due to saturation along the tracks up to 3E-4 J, whereas OSL signals are already quenched at 2E-5 J, leading the author to deduce that TL traps are significantly more populous than OSL traps.

No explanation has been offered thus far for the extreme TL supralinearity observed in BeO. Explanation of this phenomenon requires an understanding of trapping mechanisms. For BeO, there are at least four different deep traps [106] which do not contribute significantly to TL signal because they are either thermally quenched or are only activated above 500 °C.

However, these traps still compete for free charge carriers even though they do not

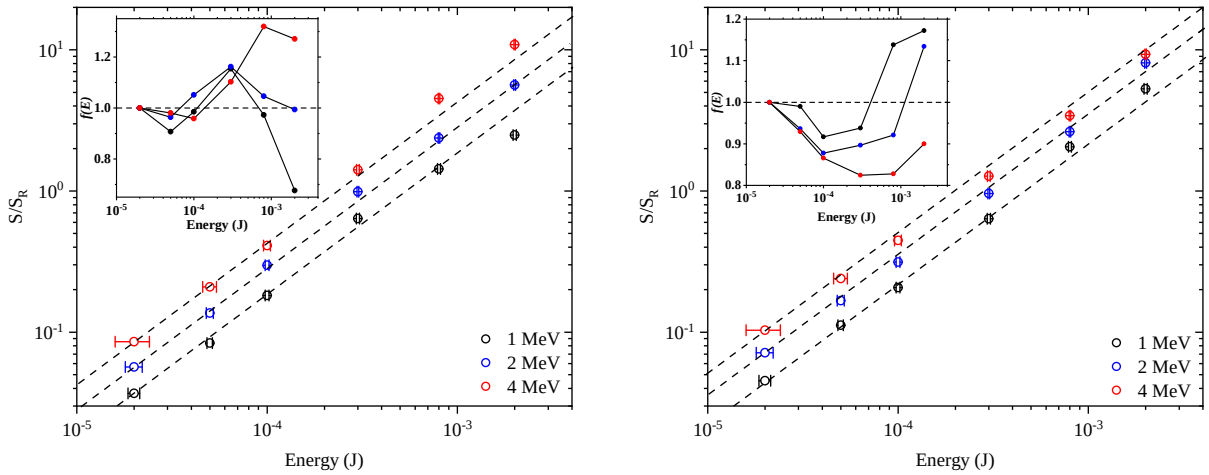

(a)

(b)

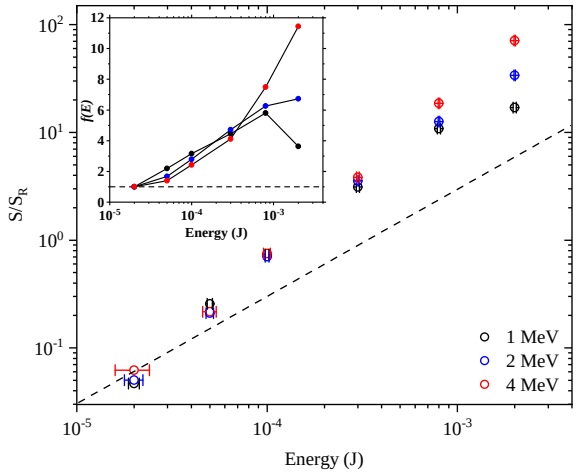

(c)

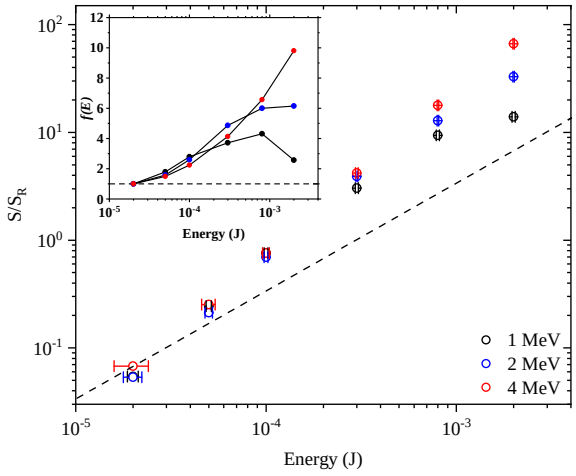

(d)

Figure 6.13: Absorbed energy responses of BeO to 1, 2, and 4 MeV H_+: (a) OSL , (b) l_0, (c)TL, and (d) TL peak. All HCP signals are corrected with a 50s β test dose, and absorbed energy uncertainties are shown. Insets show the supralinearity factor as a function of absorbed energy E.

contribute to signal [45]. For low doses, there are enough traps associated with the main dosimetric peak (peak 1) and high temperature peak (peak 2) such that the relative proportion of charges captured by these traps, compared to deep traps, is constant. Supposing that there is a higher concentration of peak 1 traps than deep traps, the ratio of available (unfilled) peak 1 traps to available deep traps will increase as dose increases; this results in a increased amount of peak 1 traps competing for charges migrating in the conduction band relative to deep traps, leading to supralinearity. By analogy, if there are less peak 2 traps than deep traps, the ratio of available peak 2 traps to available deep traps will decrease as dose increases; this will result in decreased competition among peak 2 traps for free electrons, leading to sublinearity followed by saturation.

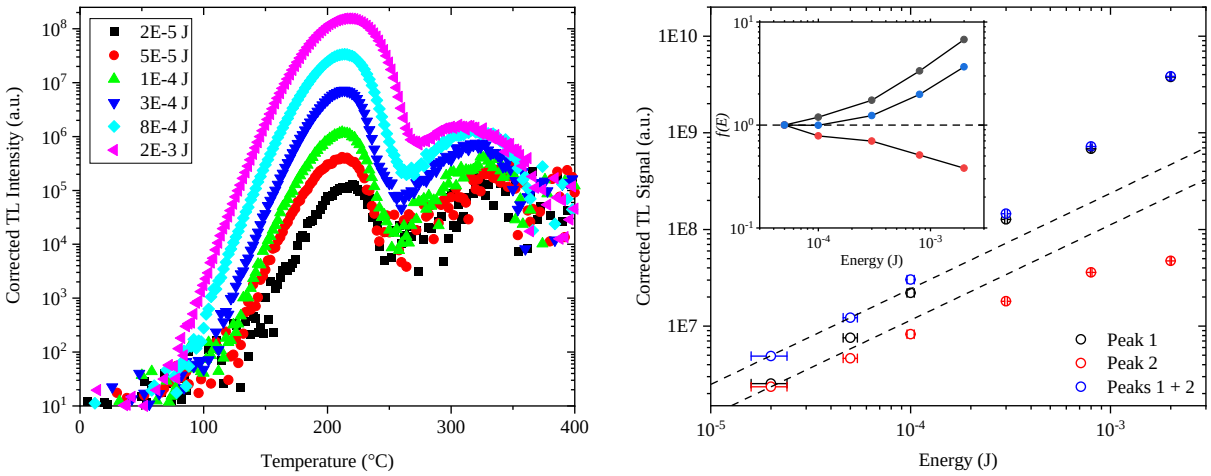

(a) (b)

Figure 6.14: TL intensities from 4 MeV protons corrected for thermal quenching (a). Energy responses from the low temperature peak (Peak 1), high temperature peak (Peak 2), and the sum of both peaks using the corrected signals (b).

To test whether the BeO TL response can be attributed to the trap competition explained above, peak 1 and peak 2 responses are compared. All TL curves for 4 MeV protons were corrected for signal quenching using the formalism outlined in Chapter 5.2, resulting in true relative signal magnitudes associated with each set of traps. Curves are shown in figure

6.14a. Responses and supralinearity curves were built for peak 1, peak 2, and the sum of both peaks from the corrected signal (figure 6.14b). As peak 1 becomes more supralinear, peak 2 becomes more sublinear. While the corrected peak 2 signal was greater than the peak 1 signal when BeO was exposed to a .75 Gy β dose (figure 5.19), it is clear that peak 2 saturates sooner than peak 1. It is not clear how the signal of peak 2 is higher than peak 1 for low doses, but saturates sooner; one explanation is that the traps associated with peak 2 have a larger interaction cross section, making them more likely to trap electrons.

Fluence Rate

BeO dose rate dependence is sparsely investigated, even less so than Al_2O_3:C. Polymeris et al. built dose responses of the primary and high temperature TL peaks, and the fast and medium OSL components when exposed to 2 Gy/hr and 31 Gy/hr of γ radiation. They found that the fast-decay and low temperature peak responses increased in supralinearity with increasing γ dose rate [128]. To the authors knowledge, no HCP OSL or TL dose rate research has been conducted for BeO.

BeO dosimeters were exposed to currents varying from 4.32E6 protons cm^{-1} s^{-1} to 2.00E8 protons cm^{-1} s^{-1}. Unlike Al_2O_3:C, BeO is still in the linear/supralinear range when exposed to 2E-3 J of 4 MeV protons. Thus, this experimental set-up provides a viable way to investigate dose rate effects. There is negligible OSL and TL curve shape change (figures 6.15a and 6.15b). There is no change in test dose corrected OSL signal with increasing fluence rate, ranging from an S/S_R value of 7.29 $\pm$ 0.31 at 4.35E6 protons cm^{-1} s^{-1} to 7.29 $\pm$ 0.12 at 2.00E8 protons cm^{-1} s^{-1} (figure 6.16a). Although l_0 decreased from an initial value of 6.34 $\pm$ 0.43 to 5.76 $\pm$ 0.23 at the highest fluence rate, the values have to be considered identical within error limits. The TL area (peak) signal decreases from 35.8 $\pm$ 0.6 (34.3 $\pm$ 0.6) at 4.35E6 protons cm^{-1} s^{-1} to 33.6 $\pm$ 1.0 (31.6 $\pm$ 0.7) at 2.00E8protons cm^{-1} s^{-1} (figure 6.16b). The associated absorbed energy uncertainties are 0.60%, 2.4%, and 14% (from low current to high current, respectively). It is important to note that the decrease in signal for

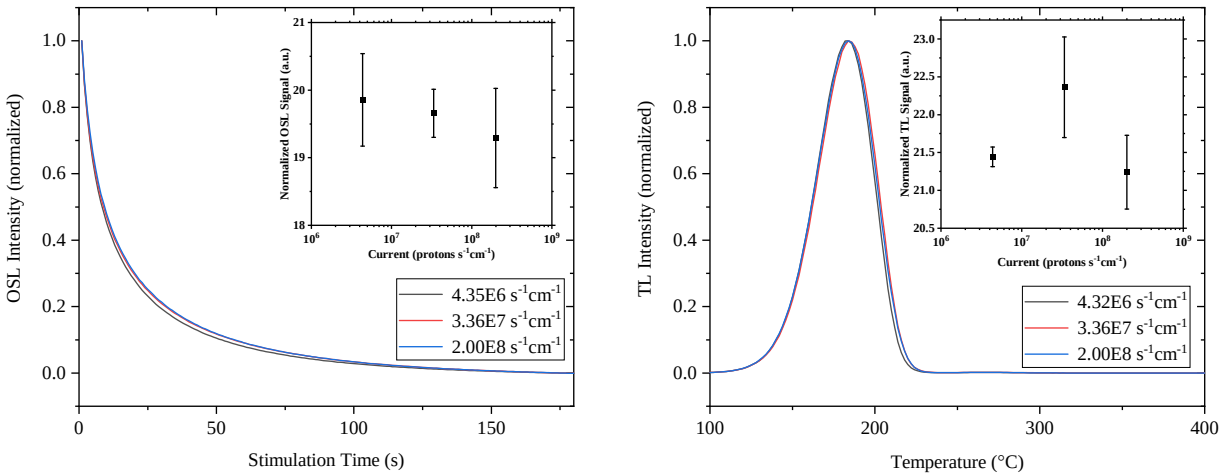

(a) (b)

Figure 6.15: Normalized BeO OSL (a) and TL curves (b) for different H^+ currents, each representing the average of three curves. Insets show the mean ± standard deviation of the normalized signal from three dosimeters.

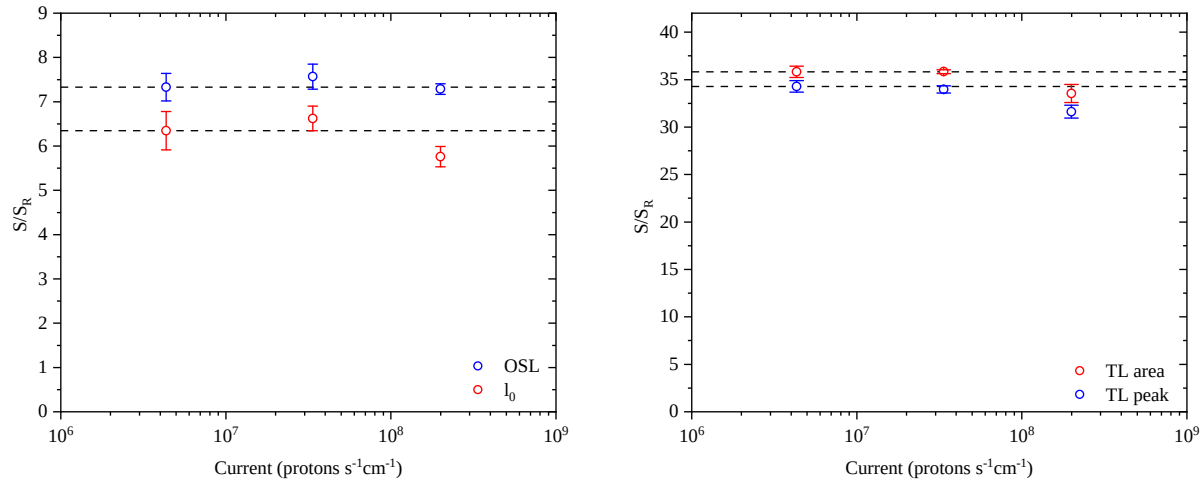

(a) (b)

Figure 6.16: BeO H^+ current dependence for both optical (a) and thermal (b) analysis methods. Points represent the mean ± standard deviation of the signal from three dosimeters corrected with a 50 s β reference dose. The dashed lines in the insets extrapolate the mean value of the lowest current.

the highest current is possibly attributed to the large uncertainty associated with a ∼0.7s exposure times using an air powered pneumatic Faraday cup as a shutter. A more precise shutter is necessary to validate this signal decrease.

6.3.2 Carbon

Normalized OSL curves of increasing absorbed energies from 4 MeV Carbon are shown in figure 6.17. The inset shows different variation in shape with increasing dose compared to protons (figure 6.11b). The curves get faster until 3E-4 J, then they slow down. Proton curves get slower from 5E-5 J to 3E-4 J, then speed up. Normalized TL curves from 4 MeV carbon (figure 6.18a) are very similar to those for protons; the ratio of the high temperature peak height to the main dosimetric peak height decreases with absorbed energy. The low energy data are again faint and noisy because of the 2.0 OD neutral density filters used for signal measurement. All filters were then removed and this process was repeated using the three lowest absorbed energies. Not only does the high temperature peak prominence decrease with increasing energy, but a deep electron trap peak that is centered around 400 °C decreases in prominence (figure 6.18b). This peak was not observed with resolution until now because of the apertures and filters required for all other proton and Carbon measurements.

All BeO Carbon energy responses are presented in figure 6.19. The OSL responses to Carbon (figure 6.19a) are drastically different than those of protons (figure 6.13a); they are initially extremely sublinear, then become supralinear beyond 3E-4 J, while the proton responses are linear followed by slight supralinearity. Remarkably, the Carbon l_0 responses are very linear (figure 6.19b), while the proton responses are sublinear then supralinear (figure 6.13b). The Carbon TL area and peak responses are still supralinear (figures 6.19c and 6.19d), but not to the extent of proton responses (figures 6.13c and 6.13d). For example, the $f(E)$ values for 2E-3 J from Carbon range from ∼2.5 to ∼4, while they range from ∼4 to ∼11 for protons, depending on energy. The signal discrepancy previously discussed for 8 MeV C ions is observed here as well.

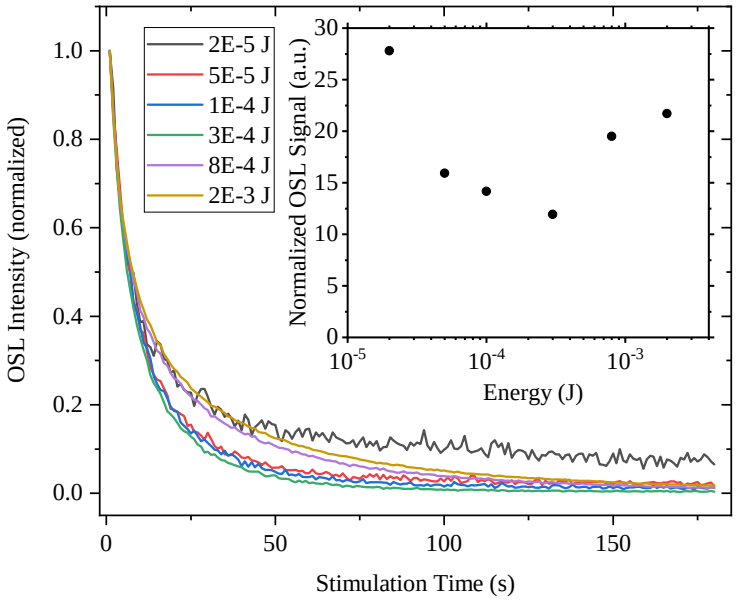

Figure 6.17: Normalized BeO OSL curves for different absorbed energies from 4 MeV Carbon. The inset shows the area under the normalized curve.

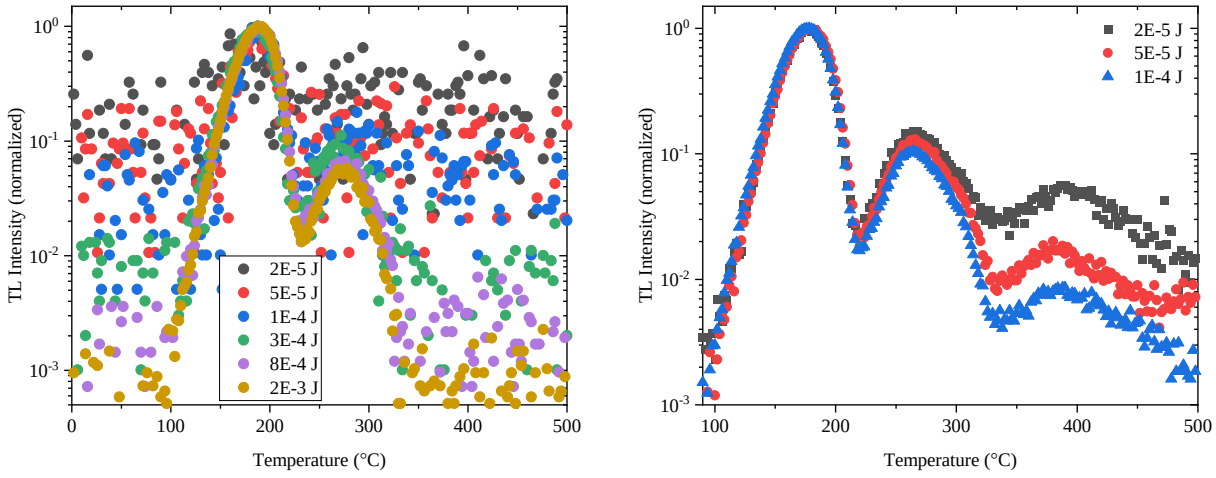

(a) (b)

Figure 6.18: Normalized BeO TL curves for different absorbed energies from 4 MeV Carbon measured with 2.0 OD neutral density filters (a) and no filters (b).

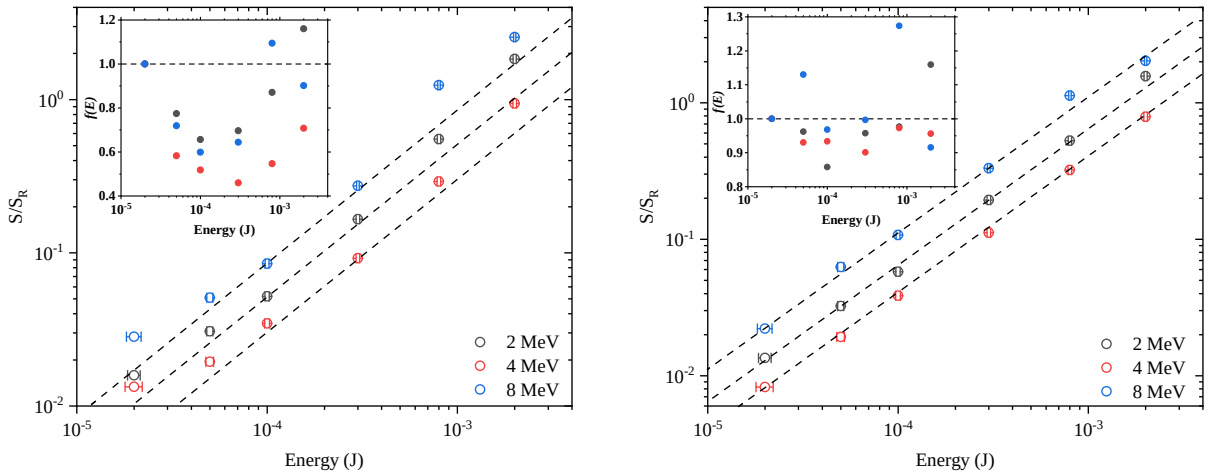

(a)

(b)

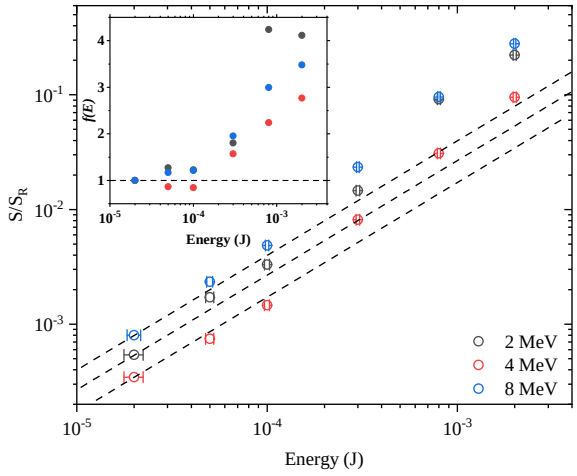

(c)

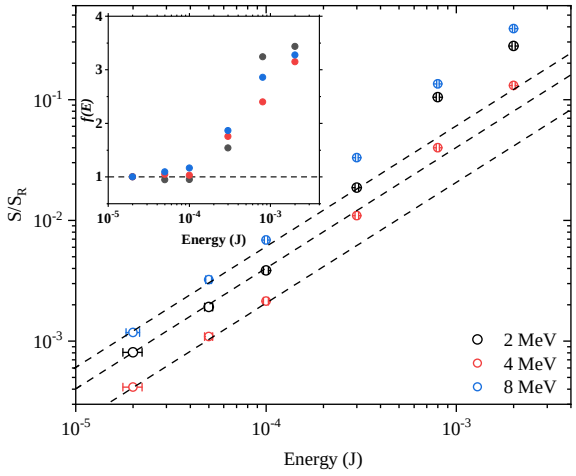

(d)

Figure 6.19: OSL (a), l_0 (b), TL (c), and TL peak (d) absorbed energy responses of BeO to 2, 4, and 8 MeV C. All HCP signals are corrected with a 5 s β test dose, and absorbed energy uncertainties are shown.

6.3.3 Comparison of H, C, α, and β

Normalized OSL and TL curves for 4 MeV H, 4 MeV C, ~5.49 MeV He, and β are shown in figure 6.20. Carbon irradiation results in a drastically slower decay than H, He, and β (figure 6.20a). The overall trend does not appear to follow a simple LET dependence, like Al_2O_3, once the He curve is observed relative to the H and β curves. This indicates complex ion and LET OSL curve shape dependence. It is not clear if the high temperature TL peak height is LET or ion dependent (figure 6.20b). It is likely that a clear trend can only be observed if many dosimeters are irradiated per ion type due to the high temperature peak height dosimeter non-uniformity relative to the main dosimetric peak (figure 5.17b), if one exists at all.

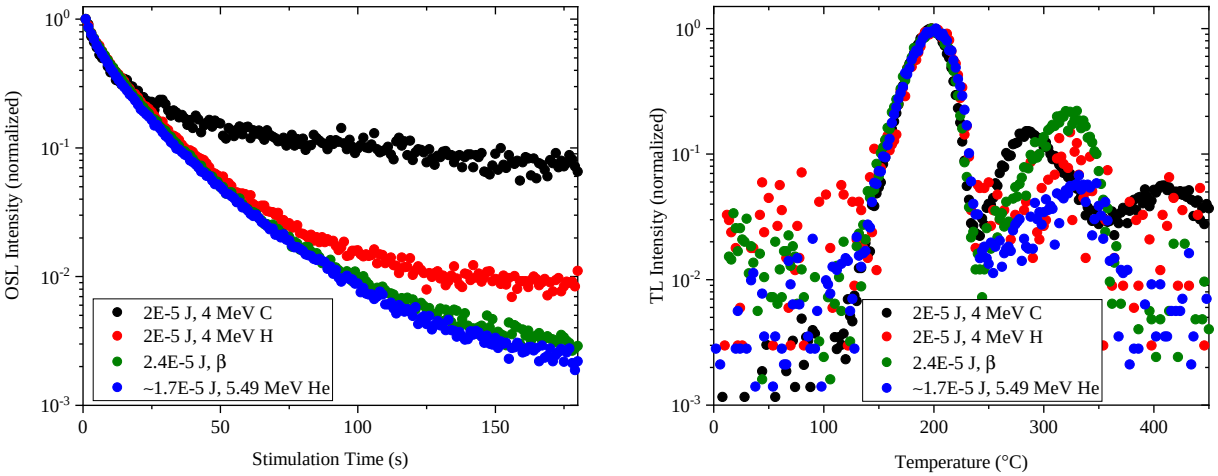

(a) (b)

Figure 6.20: Normalized BeO OSL (a) and TL (b) curves for 2E-5 J 4 MeV H, 2E-5 J 4 MeV C, ~1.7E-5 J 5.49 MeV He, and 2.4E-5 J β.

6.4 Summary

Al_2O_3:C OSL curves get faster with increasing absorbed energy and decreasing ion size. There is little β, H, and He high temperature peak signal contribution relative to Carbon.

The OSL, l_0, and TL area and peak responses saturate similarly when exposed to protons and Carbon, with only slight signal magnitude differences. The effect of fluence on absorbed energy necessary for saturation was observed for Carbon and proton responses. There is very slight OSL and TL curve shape change, and no signal variation, with increasing current for the absorbed energy and fluence rates investigated.

BeO OSL curves are complex, and change shape in a different manner when exposed to the same absorbed energies from protons and Carbon. Proton and Carbon TL curves trend in similar fashion when absorbed energy increases; the relative high temperature peak contribution decreases, but the SNR increases which leads to more robust TL curves. Neither OSL nor TL curves displayed a clear ion LET curve shape dependence. The OSL decay from Carbon was significantly slower than other ions, however. The OSL response to protons is linear followed by supralinear, whereas it is very sublinear followed by extreme supralinearity for Carbon. The l_0 response to protons is slightly sublinear followed by supralinearity, whereas it is very linear for Carbon. TL area and peak signals respond supralinearly to protons and Carbon, but differ in $f(E)$ values. The effect of fluence on saturation is also observed for BeO Carbon and proton responses. There is negligible OSL and TL shape change induced by increasing current, and small optical signal variations that are still within uncertainty limits. The TL area and peak signals decreased slightly at the highest current value for the absorbed energy investigated in this work.

Chapter 7

Shape Change of OSL Curves

OSL curves can be described by a superposition of exponential decays in the following form:

$$I(t) = C\sum_{i=1}^{n} A_{\mathrm{i}} exp(-t/\tau_{\mathrm{i}}), \tag{7.1}$$

where C is a constant, A_i and τ_i are the amplitude and decay times of the i^{th} component, respectively, and $\sum_{i=1}^{n} A_{\mathrm{i}} = 1$. This form is consistent with the first-order kinetics rate equation found in chapter 2 (equation 2.16). All distinguishable decays represents a separate trap or grouping of traps, each of which contribute signal at a different rate. Thus empirical quantization of decays enable one to deduce the number of OSL signal contributions without any knowledge of luminescence mechanisms. Decay times are dependent on the photon flux $\phi(\lambda)$ and the photoionization cross-section $\sigma(\lambda)$, both of which are wavelength dependent.

$$\tau = \frac{1}{\phi(\lambda)\sigma(\lambda)} \tag{7.2}$$

$\sigma(\lambda)$ typically decreases with increasing wavelength. Therefore, higher Risø LED power settings and lower wavelengths cause faster decay. Yukihara et al. observed that green LEDs produced a significantly slower BeO OSL decay than blue LEDs for this reason [121].

Additionally, an in-depth study on the differing effects of blue and green LEDs on the OSL of Al_2O_3:C has been conducted [85].

The purpose of this chapter is the following:

(i) determine the number of OSL signal contributions for a given material exposed to blue LEDs;

(ii) calculate the contribution growth and decay of individual components as a function of absorbed energy;

(iii) utilize the results of (ii) to explain change in shape of OSL curves, and optical dose response behavior.

Step (i) is accomplished by fitting OSL curves with a Levenberg Marquardt non-linear iterative algorithm to determine the number of superimposed decays [129]. This entails fitting all curves simultaneously for a given ion energy, and assigning the same decay times. The signal de-convolution method is well described [130, 119]. The quality of the fit for a given number of exponential decays is judged based on two factors:

1) Residual: difference between fit and raw data;

2) Autocorrelation: correlation of a given signal and a delayed copy of itself as a function of the magnitude of the delay [131].

Essentially the autocorrelation is sensitive to non-random distribution of data around the fit. Grinvald and Steinberg argued the merits of judging fits based on this method because wrong theoretical models do not always yield significantly high residuals, but will "betray themselves" with non-random residuals about the fit [132]. 1) and 2) will indicate if there are too few components in the fit, but will not indicate if there are too many. When an OSL curve is fit for too many components, one of two things happens: the fit fails to converge due to a mutual parameter dependency, or a negative amplitude is assigned to at least one component. If the amplitudes are set to be positive and the fit is still performed, there will be redundant decay times.

Component-specific growth and decay (Step ii) is calculated by multiplying the normal-

ized amplitudes from each fit by the total initial intensity, then correcting with a β test dose. Multiplying the normalized fit amplitudes by the initial intensity yields the relative initial intensity that can be attributed to each component, which then requires test dose correction due to initial intensity non-uniformity among dosimeters (see figure 5.8a). Direct comparison of dose responses with these results enable inferences to be made about how specific components contribute to response behavior (iii).

7.1 Al_2O_3:C

A two component fit for 2E-5 J from 1 MeV protons is shown in figure 7.1. The comparisons of the residual and normalized autocorrelation of this data to the single component exponential fit are seen in figures 7.2a and 7.2b , respectively. The residual from the two component fit is generally much smaller than the 1 component fit, especially beyond 10s of stimulation. Additionally, the autocorrelation of the two component fit is noisy and random throughout while the single component autocorrelation exhibits low frequency, non-random fluctuation. This suggests that this synthesis of Al_2O_3:C derives its OSL from two components, dubbed fast and slow.

To calculate the fast and slow component growth curves, all 1 MeV curves were simultaneously fit with shared parameters τ_1 and τ_2, resulting in τ_1= (0.514 $\pm$ 0.005) s and τ_2= (2.58 $\pm$ 0.02) s. The resulting amplitudes are listed in Table 7.1. A_1 increases, whereas A_2 decreases, indicating that the intensity of the fast component increases relative to the slow component. To construct the growth and supralinearity curves seen in figure 7.3, the amplitudes were multiplied by their respective initial intensities (parameter C in equation (7.1)) for each curve and normalized with a beta test dose. The growth curve for each component is well described by a saturating exponential, as seen by the R^2 values of 0.988 and 0.986 in the inset of figure 7.3a. This explains why the optical dose responses saturate when exposed to protons (figures 6.5a and 6.5b); both components are sublinear, and thus approaching sat-

uration from the beginning. This also elucidates that the shape change caused by increasing absorbed energy from 1 MeV protons occurs because the slow component saturates quicker than the fast component; hence the normalized curves get faster with increasing absorbed energy (figure 6.3a).

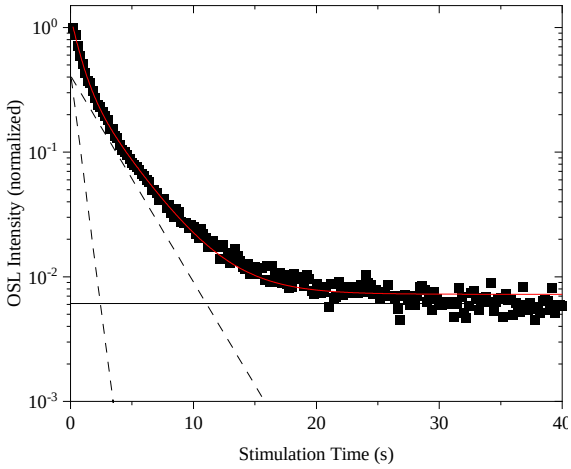

Figure 7.1: Two component fit for OSL curve of 2E-5 J from 1 MeV H^+. The black squares show experimental data and the red lines show the 2-component fit. Dashed lines represent the individual decay components and black lines show the value calculated for background.

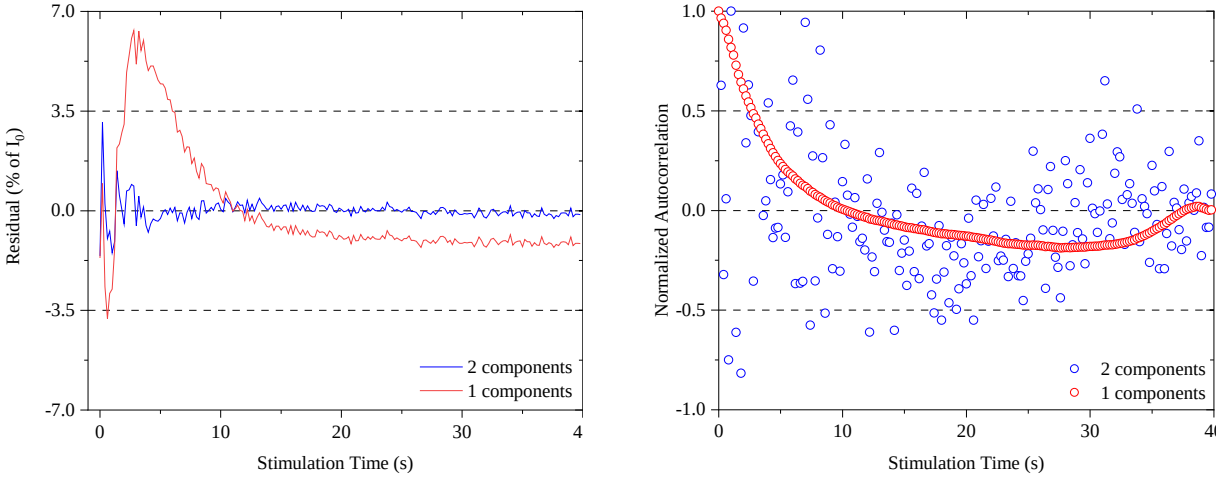

(a) (b)

Figure 7.2: Comparison of residual (a) and normalized autocorrelation (b) of 2E-5 J from 1 MeV H^+ for fits containing 1 and 2 decay components.

Absorbed Energy (J)	A_1	A_2
2E-5	0.50	0.50
5E-5	0.55	0.45
1E-4	0.63	0.37
3E-4	0.70	0.30
8E-4	0.73	0.27
2E-3	0.69	0.31

Table 7.1: Normalized amplitude contributions for various absorbed energies from 1 MeV protons. A_1 and A_2 indicate the normalized fast and slow component amplitudes, respectively. $\sum_{i=1}^{n} A_i = 1$.

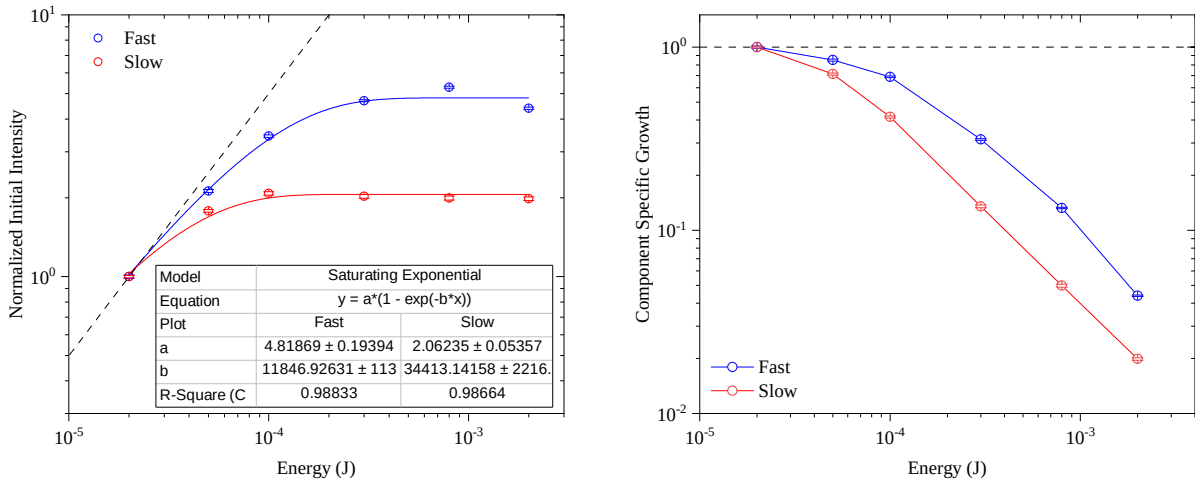

(a) (b)

Figure 7.3: Normalized initial intensity (a) and component growth (b) of the 2 decay components as a function of absorbed energy from protons. Errors were calculated using uncertainties of the fit amplitudes. Intensities were normalized with a β test dose. Dashed lines indicate linearity.

This process was repeated in Appendix C using the β source to investigate which, if any, of these results are induced by high LET.

7.2 BeO

The number of components contributing to BeO OSL signals is still being investigated, likely because of the complex shape change with increasing dose [133]. Several groups have fit OSL curves from small β doses with 2 superimposed decays [101, 118]. Additionally, Yukihara found a very fast component ($\tau = 64.2$ ms) that fades at room temperature within ten minutes, and is likely due to shallow traps [121]. It is important to mention a comparative statistical analysis was not performed by these groups to verify that 2 components provide the best fit.

7.2.1 Proton curve analysis

Two and three component fits for 2E-5 J and 2E-3 J from 1 MeV protons are shown in figure 7.4. The global fit resulted in values of $\tau_1 = (1.716 \pm 0.036)$ s, $\tau_2 = (9.464 \pm 0.186)$ s, and $\tau_3 = (37.10 \pm 0.47)$ s, and $R^2 = 0.9994$. Figure 7.4a shows how 2E-5 J from 1 MeV protons is well described by three components. The residual shows random fluctuation, and the % difference is small considering the initial intensity is 5600 counts/sec. However, the comparison of the residuals alone does not elucidate whether 2 or 3 components provide a better fit, as both fluctuate about 0 and have similar magnitudes. The normalized autocorrelation (figure 7.5a) of 3 components is random and noisy throughout, while the 2-component autocorrelation is nonrandom in parts. When the absorbed energy increases by two orders of magnitude (2E-3 J) the 3 component fit is just as effective, if not more so (Figure 7.4b). The highest residual beyond 25 seconds is 0.08% of the initial intensity, although some of this is due to the high initial signal (574,000), and therefore more favorable statistics. The inset again confirms that the global 3-component fit is far superior to a 2-component fit in terms of error magnitude. The 3 decay fit overestimates by ~0.06% of the initial intensity during the last 20 seconds for 2E-3 J. Autocorrelation analysis provides evidence that 3 components is far superior to two components for high doses (figure 7.5b).

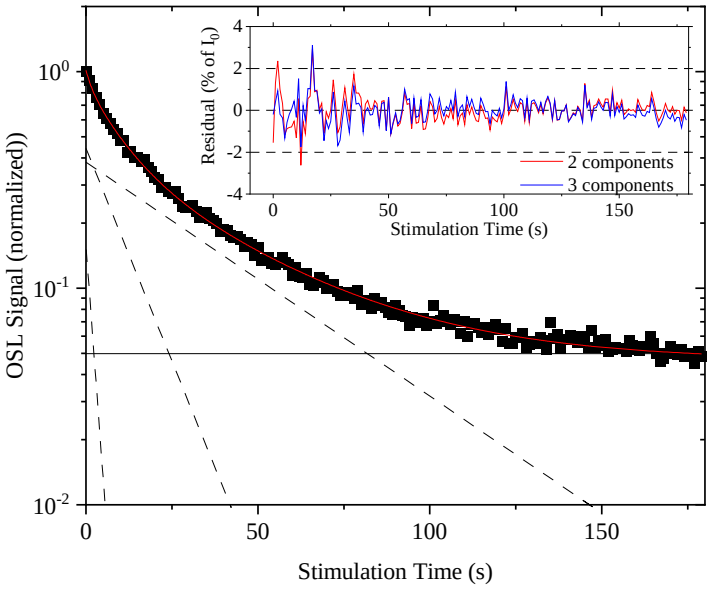

(a)

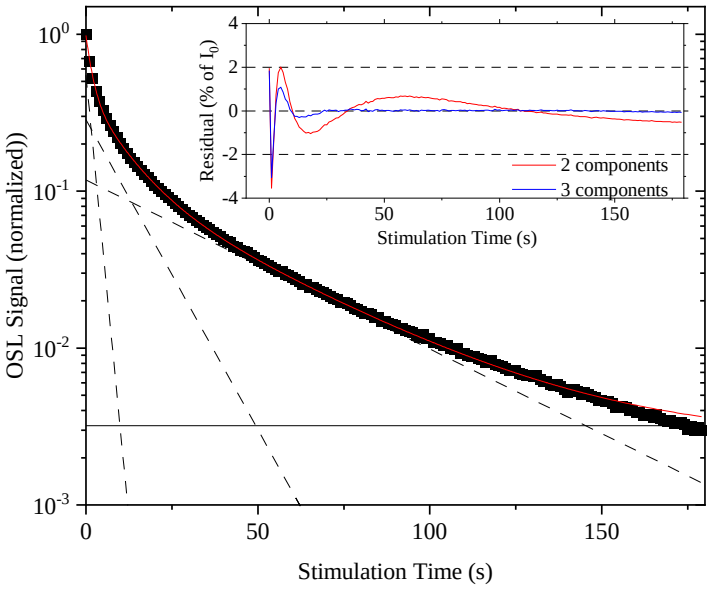

(b)

Figure 7.4: Three component fits for 2E-5 J (a) and 2E-3 J (b) from 1 MeV protons. The black squares show experimental data and the red lines show the 3-component fit. Dashed lines represent the individual decay components and solid black lines indicate the value used for background. The insets compare 2 and 3 component fit residuals, which are expressed in percent initial intensity.

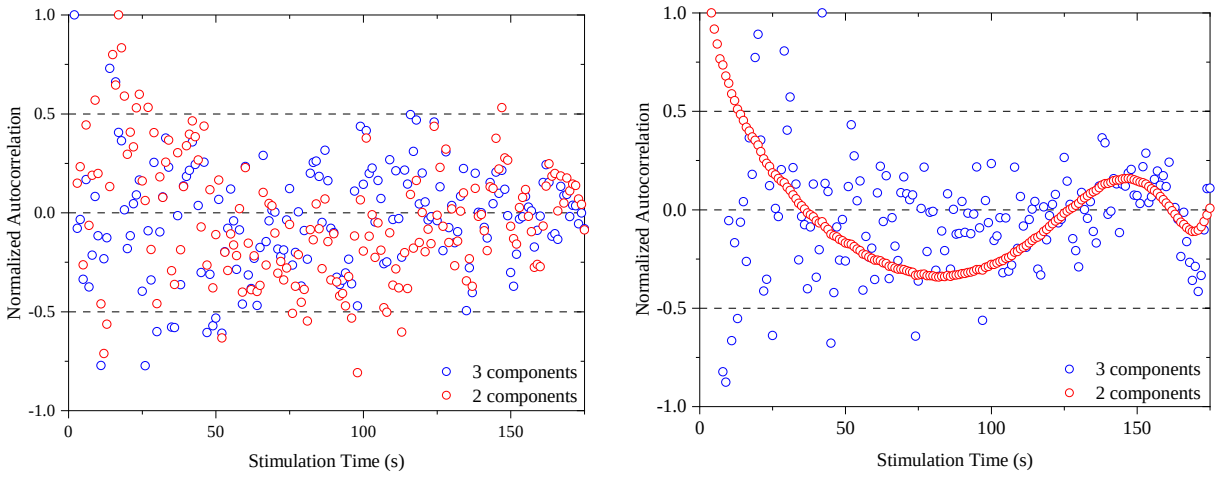

(a) (b)

Figure 7.5: Normalized autocorrelation comparison of 2 and 3 component fits for 2E-5 J (a) and 2E-3 J (b) from 1 MeV protons.

Fitting with 4 exponential decays resulted in mutual dependency among parameters (i.e. the 3rd and 4th components were assigned the same time constants), meaning the signal is indeed comprised of three components.

Table 7.2 shows the normalized amplitude utilized to construct component-specific growth (figure 7.6a) and linearity curves (figure 7.6b). Components are dubbed fast, medium and slow. The fast decay is initially linear, then becomes supralinear beyond 1E-4 J. The medium decay experiences approximately linear growth while the slow decay becomes sublinear beyond 8E-4 J (figure 6.11b). This explains why the area under the normalized OSL curves for 1 MeV protons begin to get faster beyond 3E-4 J; the slow component is decaying and the fast component is growing, eventually reaching supralinearity values of $\sim$0.4 and $\sim$5, respectively. It is important to remember that the initial intensities do not equate to total signal contribution. For that, the decay time and time constant τ must also be considered. It can be found that the total signal contributed by each component along the entire OSL curve (i.e., integrate equation (7.1) from 0 s to 180 s) is approximately equal to the initial amplitude multiplied by the decay constant $A_i\tau_i$. Thus, per unit of normalized amplitude,

Absorbed Energy (J)	A_1	A_2	A_3
2E-5	0.14	0.47	0.40
5E-5	0.15	0.52	0.33
1E-4	0.13	0.47	0.41
3E-4	0.18	0.35	0.47
8E-4	0.31	0.42	0.28
2E-3	0.57	0.30	0.13

Table 7.2: Normalized amplitude contributions for various absorbed energies from 1 MeV protons. A_1, A_2, and A_3 indicate the fast, medium, and slow component amplitudes, respectively. $\sum_{i=1}^{n} A_i = 1$.

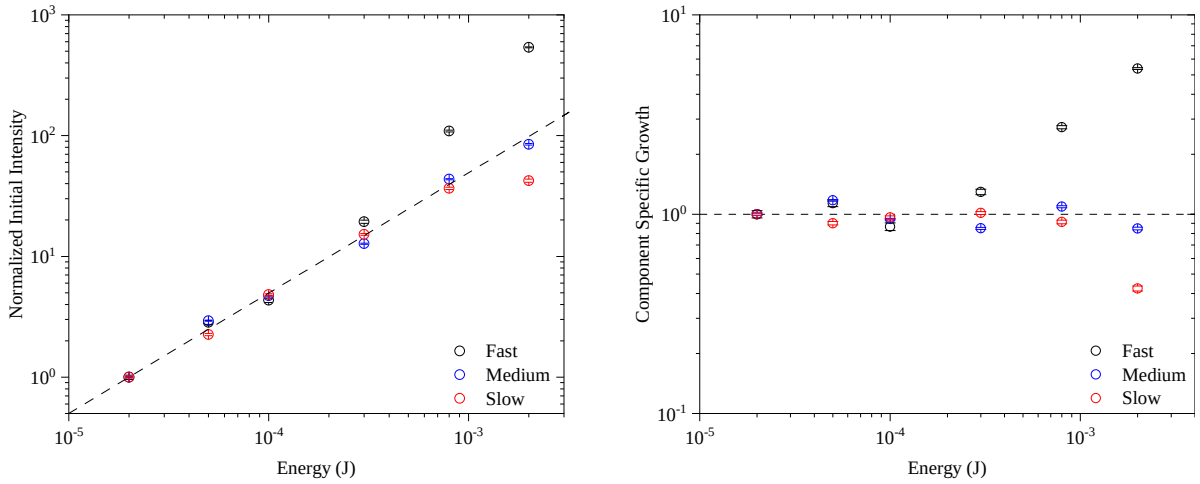

(a) (b)

Figure 7.6: Normalized initial intensity (a) and component growth (b) of the 2 decay components as a function of absorbed energy from 1 MeV protons. Errors were calculated using uncertainties of the fit amplitudes. Intensities were normalized with a β test dose. Dashed lines indicate linearity.

the slow decay contributes ~22 times as much OSL signal as the fast decay (τ_3/τ_1), and ~3.9 times as much signal as the medium decay (τ_3/τ_2). If the total contributions to the l_0 signal are calculated by integrating the first two seconds of intensity, the ratio of signal contributions of the slow decay to the fast decay is now only ~1.6.

Because the slow decay contributes the most signal per unit of amplitude, the saturation

of the 1 MeV proton integrated OSL response (figure 6.13a) can be primarily attributed to the slow component behavior. On the other hand, supralinearity of the l_0 response for high energies (figure 6.13b) is largely due to significant growth of the fast decay.

7.2.2 Carbon curve analysis

Because the optical responses to Carbon are so much different than those of protons, this process was repeated to elucidate how component growth and decay affected shape and signal. Table 8.3 lists the normalized amplitudes resulting from a simultaneous 3-component exponential fit. The resulting decay times are $\tau_1 = (3.287 \pm 0.013)$ s, $\tau_2 = (12.93 \pm 0.35)$ s, and $\tau_3 = (50.69 \pm 1.86)$ s. These amplitudes were used to construct the growth and linearity curves seen in figure 7.7.

Absorbed Energy (J)	A_1	A_2	A_3
2E-5	0.49	0.33	0.18
5E-5	0.37	0.56	0.07
1E-4	0.36	0.57	0.07
3E-4	0.39	0.55	0.06
8E-4	0.37	0.37	0.25
2E-3	0.38	0.33	0.30

Table 7.3: Normalized amplitude contributions for various absorbed energies from 4 MeV Carbon. A_1, A_2, and A_3 indicate the fast, medium, and slow component amplitudes, respectively. $\sum_{i=1}^{n} A_i = 1$.

The fast component decreases after the first energy value, but is almost perfectly linear beyond that. The trend of the medium decay is parabolic in nature. It is difficult to attribute this component to any shape or signal characteristics in this case. The normalized slow component intensity did not increase from the first energy to the second energy. It then grows linearly, followed by extreme supralinear growth. Comparing the inset of the normalized OSL curves (figure 6.17) to the slow component linearity suggests that the OSL curve gets much faster at 5E-5 J and then much slower again at 8E-4 primarily because of the decreasing

and then increasing relative contribution of the slow component. Additionally, the extreme sublinearity of the OSL response (figure 6.19a) at low doses can only be attributed to the slow decay, since the fast and medium components are linear and supralinear, respectively. Most remarkably, the l_0 response is very linear because the fast decay, which heavily contributes to the initial intensity, is exceptionally linear. Both of these trends present noteworthy contrast to protons.

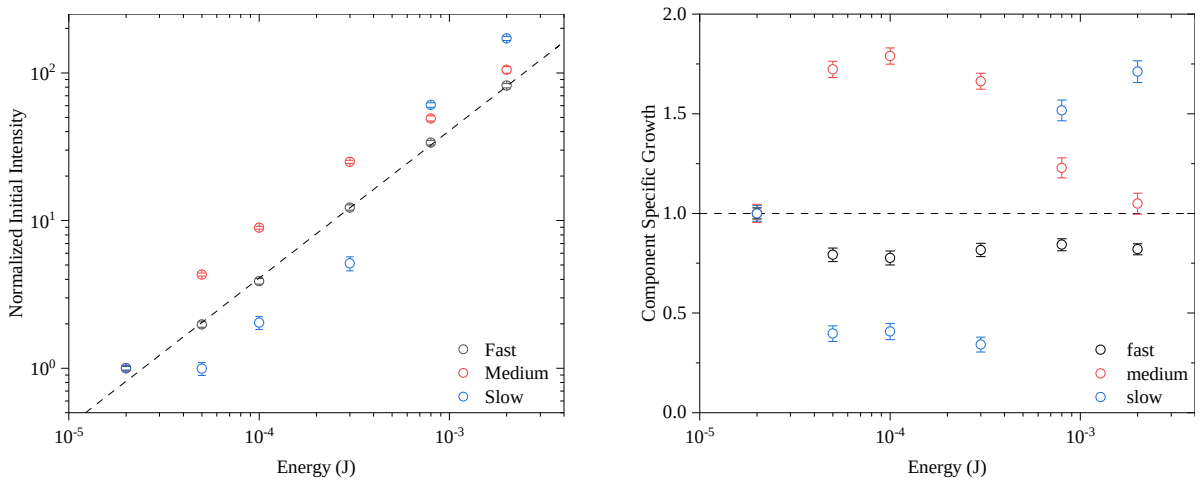

(a) (b)

Figure 7.7: Normalized initial intensity (a) and component growth (b) of the 3 decay components as a function of absorbed energy from 4 MeV C. Errors were calculated using uncertainties of the fit amplitudes. Intensities were normalized with a β test dose. Dashed lines indicate linearity.

Because the fitting of these curves suggests 3 OSL signal components while all other publications have used 2 components, this analysis was repeated with the ^{90}Sr β source (see Appendix C). This ensures that the results shown above are a material property which is not LET dependent. Additionally, results from over three orders of magnitude using the ^{241}Am α source are shown in Appendix C as well.

7.3 Summary

A robust method for resolving the number of OSL signal components has been presented here. Once resolved, the relative signal intensity and linearity associated with each component was plotted as a function of absorbed energy. It has been shown that these component-specific growth and linearity curves can be utilized to explain shape change in OSL curves, as well as OSL and l_0 absorbed energy response trends.

Chapter 8

Luminescence Efficiency

To determine a dose absorbed by a dosimeter, the luminescence signal is measured. This signal is then compared to a calibration curve (aka. dose response) to infer the dose that is equivalent to the signal. For experimental reasons, calibration doses are constructed by irradiating the dosimeters with known doses of beta or gamma radiation. This approach is valid as long as the dose to be measured and the calibration curve stem from the same type of radiation. In this case the same dose is expected to result in the same signal. However, as discussed in chapter 2.5, this is not true for ion-radiation. For a given value of absorbed energy, ion radiation will result in a lower signal than gamma radiation, i.e. ion irradiation has a smaller "efficiency." Comparing such a signal to a gamma-calibration curve would result in an underestimation of the dose value. On the other hand, if the efficiency is known and the signal is corrected for its efficiency, using a gamma dose response is still a valid approach and will result in a correct dose value.

Knowing efficiency values is therefore crucial whenever luminescence dosimeters are to be used for HCP radiation fields. Efficiency values vary with ion type, ion energy and dosimetric material. The purpose of this chapter is to determine efficiency values for the ion types, energies, and dosimeters used in this dissertation. The first part explains how efficiency values were determined. The second part shows results for Al_2O_3:C and BeO.

8.1 Methodology

8.1.1 Definition of efficiency

Luminescence efficiency η is defined as the sensitivity z of a dosimeter to HCP radiation of LET L relative to its sensitivity to gamma radiation, where sensitivity is the signal S per unit absorbed energy E [16].

$$\eta_L = \frac{z_L}{z_\gamma} = \frac{S_L/E_L}{S_\gamma/E_\gamma} \tag{8.1}$$

Instead of absorbed energy E_γ it is common to use dose D_γ:

$$\eta_L = \frac{S_L/E_L}{S_\gamma/(D_\gamma m_\gamma)}, \tag{8.2}$$

where m_γ is the mass penetrated by γ radiation (i.e, the entire dosimeter).

It is possible to define a corrected HCP signal $S_{L,corr}$:

$$S_{L,corr} = \frac{S_L}{S_\gamma/D_\gamma} \tag{8.3}$$

$S_{L,corr}$ has units of dose and signifies the γ dose that would result in the same signal as S_L, i.e. the "γ-equivalent absorbed dose" [43]. $S_{L,corr}m_\gamma$ has units of energy and is termed the "γ-equivalent absorbed energy". Combining equations (8.2) and (8.3) allows the efficiency to be defined simply as the ratio of signal of the γ-equivalent absorbed energy $S_{L,corr}m_\gamma$ to the absorbed energy from HCPs.

$$\eta_L = \frac{S_{L,corr}m_\gamma}{E_L} \tag{8.4}$$

Dosimeter mass and E_L, the energy from ion radiation absorbed by the dosimeter, are well known for the work presented here. The main task of efficiency calculation is therefore to determine the corrected HCP signal $S_{L,corr}$. From equation (8.3) it can be seen that

this requires (i) measurement of the luminescence signal S_L resulting from ion irradiation (as measured with the Riso reader) and (ii) a calibration curve that correlates S_γ and D_γ. Comparing S_L to this curve enables inferring the γ-equivalent absorbed dose $S_{L,corr}$.

8.1.2 Calibration curves

Calibration curves are obtained by exposing dosimeters to known doses with the built-in β source of the Risø reader and measuring the signal. The β source has been calibrated against a γ source so that the dose values are in terms of D_γ. The curves are built by necessity from a limited number of points. As observed in Chapter 5, Al_2O_3:C and BeO display non-linear responses to β irradiation in the dose range investigated. To correlate signals S_L with equivalent gamma doses requires interpolation, it is therefore necessary to outline a robust and precise method for evaluating signal associated with γ-equivalent dose, and vice versa.

Calibration curves and ion signals must be measured under the same conditions to ensure that "apples are compared to apples". Thus an individual calibration curve must be measured for every filter combination used. Also, separate curves must be measured for TL and OSL and for each material. This does not correct variation between individual dosimeters, however. Yukihara et al. proposed correcting for inconsistencies by dividing the measured signal S by the signal from a small β test dose S_R [134]. Variations in dosimeter sensitivity are reflected in this signal and will thus be eliminated. The calibration curve is constructed such that the units of the y-axis are S/S_R. It has been shown that precision greatly increases utilizing this method.

The measured points S/S_R are plotted versus their respective doses D_γ and are then fit with a response function. As suggested by Sawakuchi et al. [135], the following function was used to fit the calibration curves:

$$\frac{S}{S_R} = A_1\left(1 - e^{-aD_\gamma}\right) - A_2\left(1 - e^{-bD_\gamma}\right)^c \tag{8.5}$$

The first term is a saturating exponential function which accounts for linear-sublinear-saturation behavior while the second term allows for supralinearity, which is dictated by the magnitude of parameter c [16]. Therefore, this function enables fitting both, the saturating responses of Al_2O_3:C and the supralinear responses of BeO.

Figure 8.1a shows the calibration curve used to evaluate D_γ for all proton OSL signals for BeO, giving an idea of the precision achievable utilizing this method. The function has 5 fitting parameters and was fit to 8 points. Nevertheless, the R^2 of the fit equals 1 to five significant figures, meaning essentially all of the data variation can be explained by the shape of the curve. Additionally, the residual of the fit $\pm$ standard deviation is shown in figure 8.1b. Of the 8 data points used to construct the curve, 7 have residuals of less than 0.5% and 6 have standard deviations of 1% or less.

In addition to the S/S_R procedure being precise, equation (8.4) is robust enough to account for many types of responses. Figure 8.2a presents the complex and highly-supralinear BeO TL area and peak responses while figure 8.2b presents the saturating TL responses of Al_2O_3:C. Only the first term in (8.4) is required to describe all Al_2O_3:C responses, since the material does not display significant supralinearity. It is apparent that each fit excellently describe the data, and can therefore be confidently utilized to quantify D_γ.

In the next step the signal S_L resulting from ion exposure is measured and compared to the calibration curve to determine the gamma dose D_γ that would result in the same signal, i.e. $S_{L,corr}$. It is important to note that this cannot be solved through traditional analytical methods. The use of numerical methods or interpolation of a high resolution calibration curve is necessary to evaluate D_γ ($= S_{L,corr}$) for a given S/S_R from HCPs. With known $S_{L,corr}$, equation (8.3) can be used to calculate the efficiency η for a given value of E_L.

8.1.3 Efficiency calculation

In this work several dosimeters were irradiated with the same type and energy of ion (e.g. 4 MeV H) but irradiation times and thus absorbed energies E_L were increased. Efficiency

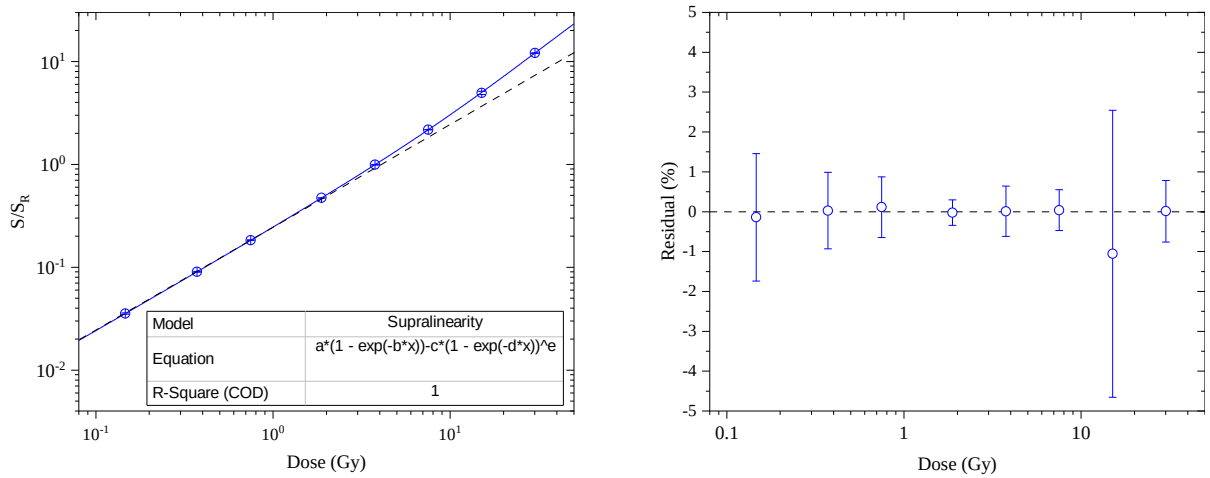

(a) (b)

Figure 8.1: (a) BeO OSL calibration curve used to evaluate D_γ for all proton signals. The data points were fit with equation (8.5) and indicate the mean ± standard deviation of three unique dosimeters. (b) Residual of the parametrized fit. $R^2 = 1.00000$.

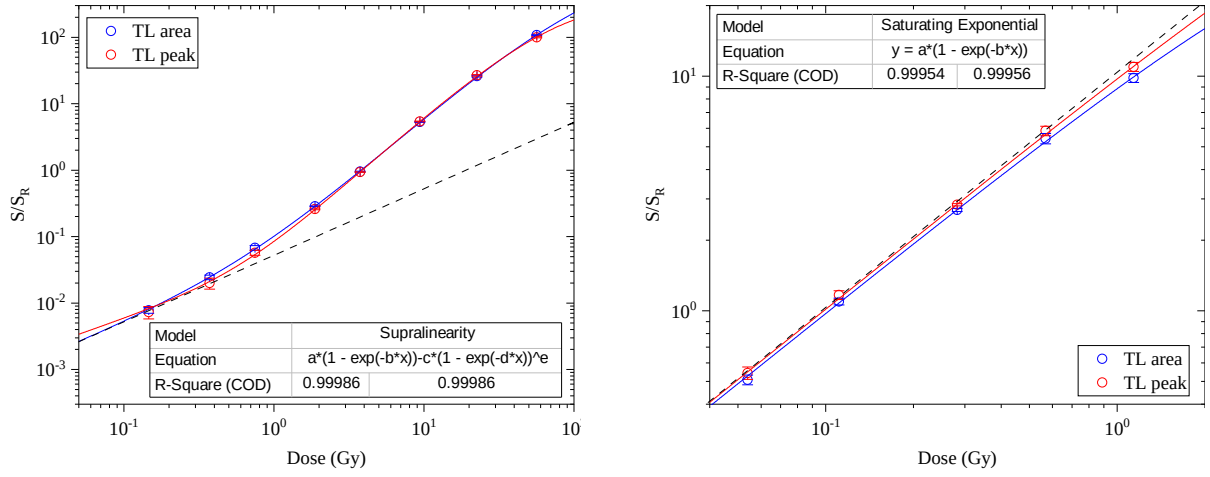

(a) (b)

Figure 8.2: (a) BeO TL area and peak calibration curve used to evaluate D_γ for all proton signals. The data points were fit with equation (8.5) and indicate the mean ± standard deviation of three unique dosimeters. $R^2 = 0.99986$ for the TL area and peak fits. (b) Al_2O_3:C TL area and peak calibration curves used to evaluate D_γ for all proton signals. The data points were fit with first term in equation (8.5) and indicate the mean ± standard deviation of three unique dosimeters. $R^2 = 0.99954$ and $R^2 = 0.99956$ for TL area and peak fits, respectively.

values are defined for a certain ion type and energy. The ratio of $S_{L,corr}m_\gamma$ and E_L is expected to be constant for the same type of ion, even as the total number of absorbed ions and thus E_L increases. A plot of $S_{L,corr}$ versus E_L is therefore expected to be a straight line and the slope reflects the efficiency η. However, when the results are plotted (see e.g. figure 8.3 for Al_2O_3:C) the plots are not linear as expected. Instead, the slope, and thus the efficiency for a given ion, vary with total absorbed energy. This behavior can be explained with saturation effects. The measured signals are not only influenced by the ion-versus-gamma efficiency, they are also impacted by saturation due to high absorbed energies (see chapter 6.2). The saturation effects increase with increasing absorbed energy. Gaza et al. [43, 136] suggested the following approach to determine a representative efficiency value in such a case. The non-linear $S_{L,corr}m_\gamma$ versus E_L plots are fit with a function. Efficiency is directly correlated with the slope of this function, if the slope is calculated for small energies, which are expected to be in the linear dose range. The details of the procedure are explained in the following.

The relationship between $S_{L,corr}m_\gamma$ and E_L for Al_2O_3:C is best-defined by a saturating exponential for all signal calculation methods.

$$S_{L,corr}m_\gamma(E_L) = a\left(1 - e^{-bE_L}\right) \tag{8.6}$$

This has also been suggested by Gaza et al. [43, 136]. Some curves are highly supralinear and can only be approximated by an exponential growth function (equation (8.6)), whereas other responses are well-described by a linear relationship (equation (8.8)).

$$S_{L,corr}m_\gamma(E_L) = ae^{E_L/b} + (S_{L,corr}m)_0 \tag{8.7}$$

$$S_{L,corr}m_\gamma(E_L) = aE_L + (S_{L,corr}m)_0 \tag{8.8}$$

Calculating the slope (i.e. taking the derivative) of equations (8.6)-(8.8) at low energy values allows evaluating efficiencies of non-linear responses:

$$\eta_{L,Eq.(8.6)} = \lim_{E_L \to 0} \frac{\mathrm{d}S_{L,corr} m_\gamma(E_L)}{\mathrm{d}E_L} = ab \tag{8.9}$$

$$\eta_{L,Eq.(8.7)} = \lim_{E_L \to 0} \frac{\mathrm{d}S_{L,corr} m_\gamma(E_L)}{\mathrm{d}E_L} = \frac{a}{b} \tag{8.10}$$

$$\eta_{L,Eq.(8.8)} = \lim_{E_L \to 0} \frac{\mathrm{d}S_{L,corr} m_\gamma(E_L)}{\mathrm{d}E_L} = a \tag{8.11}$$

Note that equations (8.8) and (8.11) reduce to the initial approach from equation (8.4).

Efficiency values are typically standardized to water, because many linear accelerator beams are calibrated to absorbed dose to water. According to [16, 19] the ratio of the efficiency in water to the efficiency of a detector material η_L^w/η_L^{det} can be approximated using relative energy absorption coefficients μ_{en}/ρ and mass stopping powers L/ρ, assuming the dosimeter is large with respect to the secondary electron range.

$$\eta_L^w = \eta_L^{det} \frac{D_\gamma^w}{D_\gamma^{det}} \cdot \frac{D_L^{det}}{D_L^w} = \eta_L^{det} \left(\frac{\mu_{en}}{\rho}\right)_{det}^{w} \left(\frac{L}{\rho}\right)_{w}^{det} \tag{8.12}$$

Simply put, a detector will absorb a different amount of energy than water when exposed to the same HCP or γ fluence. Thus equation (8.12) is not a measured efficiency to water in the traditional sense, but the relative response of absorbed dose to water for a non-reference field (i.e., HCPs) to the absorbed dose to water of a reference field times the measured efficiency of the detector [16].

8.1.4 Summary of the procedure

In summary, the steps required to calculate η_L^w are as follows:

(i) create calibration curves (figure 8.1a, for example) for all filter and test dose combinations used in chapter 6;

(ii) evaluate γ-equivalent absorbed energy values $S_{L,corr}m$ for all S/S_R signals from chap-

ter 6 using these calibration curves;

(iii) plot $S_{L,corr}m_\gamma$ versus E_L;

(iv) Calculate the efficiency of the detector η_L^{det} using the linear response domain (equation (8.3)) or by taking the limit of the associated function (equations (8.6)-(8.8));

(v) calculate the efficiency to water η_L^w using the η_L^{det} values from (iv) and equation (8.12).

8.2 Results

Calibration curves were measured and calculated for all dosimeters and filter combinations used. γ-equivalent absorbed energies ($S_{L,corr}m_\gamma$ in units J) were calculated for all combinations of ion types and energies (1, 2, and 4 MeV H; 2, 4, and 8 MeV C), absorbed energies (2E-5 J to 2E-3 J), dosimetric materials (BeO and Al_2O_3:C) and readout and analysis techniques (OSL, l_0, TL area and peak). Resulting efficiencies are presented in the following sections.

8.2.1 Al_2O_3:C

Figure 8.3 shows the γ-equivalent absorbed energies ($S_{L,corr}m_\gamma$ in units J) plotted versus total absorbed energy for Al_2O_3:C. Results are shown for the 6 different ion and energy combinations and all 4 signal calculation methods. The proton responses have a much higher γ-equivalent energy than the Carbon responses. With the exception of 8 MeV Carbon, the magnitude of the responses follow the proposed LET-dependent model (i.e., higher LET leads to more signal saturation within the track and thus a lower efficiency). The dashed line in the top left-hand corner represents the $\eta_L^{det} = 1$ response. Anything below the line has $\eta_L^{det} < 1$, effectively requiring more absorbed energy from HCPs than γ to obtain the same signal. It can be seen that the γ-equivalent responses saturate from the first energy value, preventing equation (8.3) from being used to quantify η_L^{det}. Therefore, Al_2O_3:C efficiency values can only be calculated using equation (8.8).

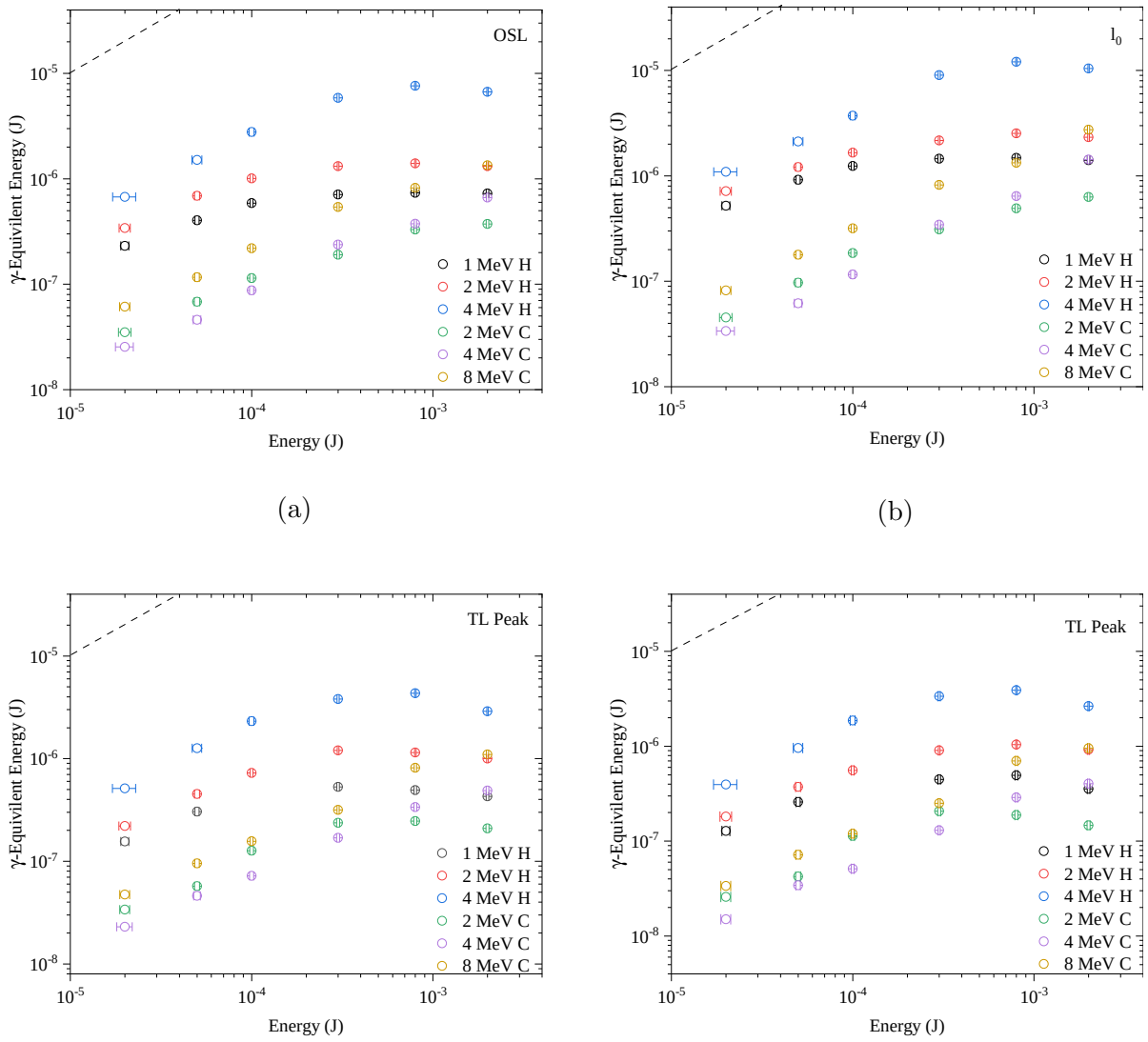

Experimer

Figure 8.3: γ-equivalent absorbed energy responses of Al_2O_3:C to 6 different particle and energy combinations (1, 2, and 4 MeV H; 2, 4, and 8 MeV C): (a) OSL area, (b) l_0 , (c) TL area, and (d) TL peak. Dashed lines represent $\eta_L^{det} = 1$.

Table 7.1 displays the approximated η_L^{det} values and uncertainties for each particle/energy combination and signal calculation method. The efficiencies are on the order of 1-5% for protons and 0.05-0.2% for Carbon. l_0 has the highest efficiency for most ions and energies, while the other signals typically yield similar efficiencies to one another. Although the OSL is often slightly higher than TL area and peak, they can be considered the same within error limits. The fast decay was observed to saturate slower than the slow decay in Chapter 7.1. The larger η^{det} values here also suggest that the fast signal is less affected by intra-track saturation than the slow signal. Many of the errors are very large due to the uncertainty associated with extrapolating an extremely saturated signal to the linear range (i.e. $E_L \rightarrow 0$). This indicates that the preferred calculation method is utilizing data inside the linear response range, which does not exist for this material.

Ion	OSL	l_0	TL area	TL peak
1 MeV H	$(1.23\pm0.06)\cdot10^{-2}$	$(2.97\pm0.16)\cdot10^{-2}$	$(9.59\pm2.05)\cdot10^{-3}$	$(7.85\pm2.61)\cdot10^{-3}$
2 MeV H	$(1.90\pm0.10)\cdot10^{-2}$	$(3.25\pm0.46)\cdot10^{-2}$	$(1.23\pm0.23)\cdot10^{-2}$	$(1.08\pm0.10)\cdot10^{-2}$
4 MeV H	$(3.78\pm0.53)\cdot10^{-2}$	$(5.38\pm0.95)\cdot10^{-2}$	$(3.53\pm1.22)\cdot10^{-2}$	$(2.75\pm0.94)\cdot10^{-2}$
2 MeV C	$(1.05\pm0.16)\cdot10^{-3}$	$(1.53\pm0.27)\cdot10^{-3}$	$(1.56\pm0.20)\cdot10^{-3}$	$(1.68\pm0.63)\cdot10^{-3}$
4 MeV C	$(7.49\pm1.76)\cdot10^{-4}$	$(9.82\pm4.02)\cdot10^{-4}$	$(6.89\pm0.50)\cdot10^{-4}$	$(5.61\pm0.40)\cdot10^{-4}$
8 MeV C	$(1.84\pm0.40)\cdot10^{-3}$	$(2.34\pm0.88)\cdot10^{-3}$	$(1.80\pm0.11)\cdot10^{-3}$	$(1.25\pm0.23)\cdot10^{-3}$

Table 8.1: $\eta_L^{Al_2O_3:C}$ values calculated using equation (8.9). The errors were calculated using the uncertainties of fitting parameters a and b.

Table 8.5 lists η_L^w values obtained from Table 8.4 and equation (8.12). In all cases the efficiencies decreased because $\eta_L^w/\eta_L^{det} < 1$. $\left(\frac{\mu_{en}}{\rho}\right)_{det}^{w} = 1.015$ for all data because the same low-LET source was used for all irradiatons. However, $\left(\frac{L}{\rho}\right)_{w}^{det}$ varies because the relative LET in water versus Al_2O_3:C varies with ion and energy. For clarity, the conversion from η_L^{det} to η_L^w for 4 MeV protons is shown.

$$\begin{aligned}\frac{\eta_L^w}{\eta_L^{det}} &= \frac{D_\gamma^w}{D_\gamma^{det}} \cdot \frac{D_L^{det}}{D_L^w} \\ &= \left(\frac{\mu_{en}}{\rho}\right)_{det}^{w} \left(\frac{L}{\rho}\right)_{w}^{det} \\ &= \left(\frac{2.935 \cdot 10^{-2} \frac{cm^2}{g}}{2.892 \cdot 10^{-2} \frac{cm^2}{g}}\right)\left(\frac{49.69 \frac{keV}{\mu m} / 3.97 \frac{g}{cm^3}}{16.59 \frac{keV}{\mu m} / 1.00 \frac{g}{cm^3}}\right) \\ &= 0.765\end{aligned} \tag{8.13}$$

Ion	OSL	l_0	TL area	TL peak
1 MeV H	$(9.39\pm0.44)\cdot10^{-3}$	$(2.27\pm0.12)\cdot10^{-2}$	$(7.31\pm1.56)\cdot10^{-3}$	$(5.98\pm1.99)\cdot10^{-3}$
2 MeV H	$(1.45\pm0.08)\cdot10^{-2}$	$(2.48\pm0.35)\cdot10^{-2}$	$(1.45\pm0.08)\cdot10^{-2}$	$(8.27\pm0.76)\cdot10^{-3}$
4 MeV H	$(2.89\pm0.40)\cdot10^{-2}$	$(4.12\pm0.73)\cdot10^{-2}$	$(2.89\pm0.40)\cdot10^{-2}$	$(2.11\pm0.72)\cdot10^{-2}$
2 MeV C	$(7.56\pm1.17)\cdot10^{-4}$	$(1.10\pm0.20)\cdot10^{-3}$	$(1.12\pm0.14)\cdot10^{-3}$	$(1.21\pm0.46)\cdot10^{-3}$
4 MeV C	$(5.06\pm1.19)\cdot10^{-4}$	$(6.64\pm2.72)\cdot10^{-4}$	$(4.66\pm0.34)\cdot10^{-4}$	$(3.79\pm0.27)\cdot10^{-4}$
8 MeV C	$(1.19\pm0.26)\cdot10^{-3}$	$(1.51\pm0.57)\cdot10^{-3}$	$(1.16\pm0.07)\cdot10^{-3}$	$(8.06\pm1.48)\cdot10^{-4}$

Table 8.2: η_L^w values calculated using table 7.1 and equation (8.12).

Figure 8.4 shows the OSL η_L^w values plotted versus LET in water. The results support the LET efficiency dependence discussed previously, excluding 8 MeV Carbon. Although the ECU particle accelerator cannot achieve high enough energies to create protons and Carbon of similar LET, it would be interesting to investigate whether η_L^w depends on ion type for this material synthesis, not only LET. Efficiency differences for differing ions of similar LET have been previously observed for Luxel Al_2O_3:C dosimeters [135] and TLD-500 single crystal Al_2O_3:C dosimeters [136].

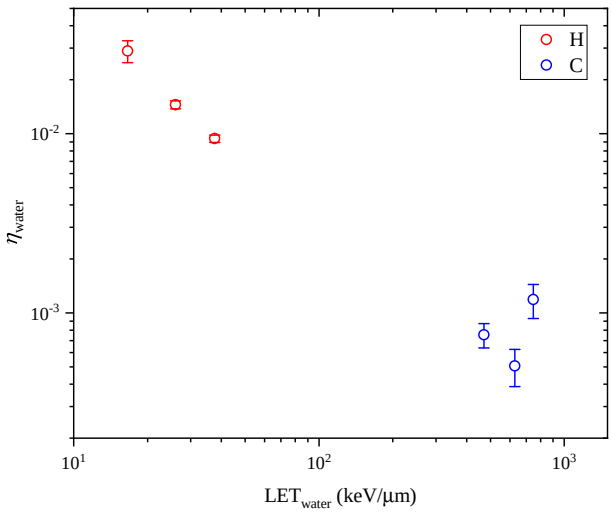

Figure 8.4: Proton and Carbon OSL η_L^w values calculated for Al_2O_3:C.

8.2.2 BeO

Figure 8.5 shows the γ-equivalent absorbed energy responses of BeO to 6 different ion and energy combinations for all 4 signal calculation methods. The discrepancy between proton and carbon signals is observed again. Additionally, both thermal signals are higher than optical signals relative to γ. The merits of this procedure are apparent based on the TL area and peak responses. It is not possible to calculate BeO TL efficiency in the traditional manner due to the extreme response supralinearity observed in chapter 6 (see figure 6.19). However, when the TL signals are converted to γ-equivalent absorbed energy, the responses follow a linear-sublinear-saturation model. This enables the efficiency to be calculated in two ways: in the linear region, and by taking the limit of the saturating exponential function. This allows a direct efficiency comparison between optical and thermal signal calculation methods. All optical signal magnitudes depend on ion and energy and have $\eta_L^{det} < 1$. The TL area and peak responses are each close to unity for protons ($\eta_L^{det} \approx 1$), i.e. close to the values for β and γ radiation. This indicates that intra-track saturation has little impact on the traps responsible for the TL signal, and that they can trap significantly more electrons

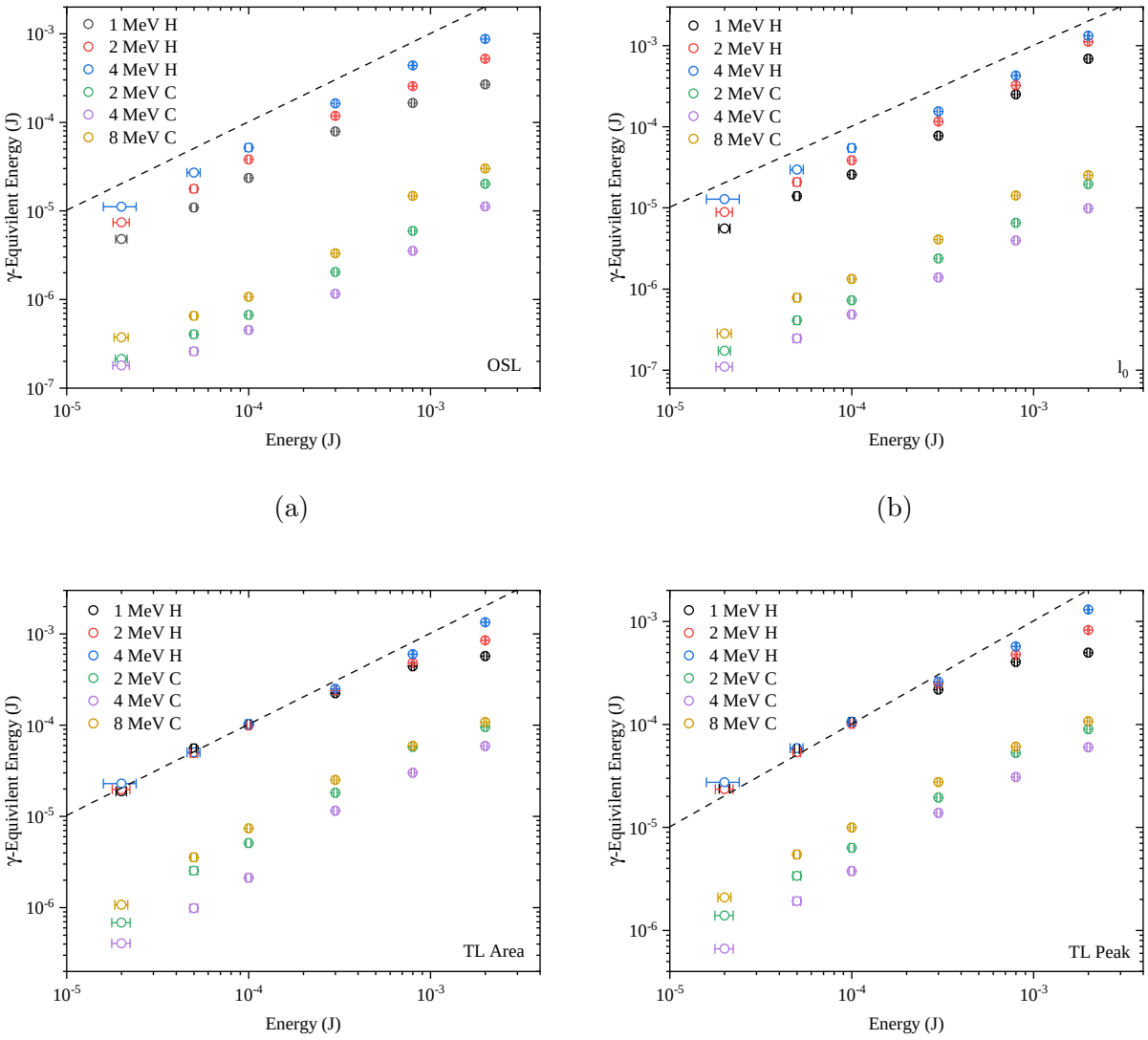

Figure 8.5: γ-equivalent absorbed energy responses of BeO to 6 different particle and energy combinations (1, 2, and 4 MeV H; 2, 4, and 8 MeV C): (a) OSL area, (b) l_0 , (c) TL area, and (d) TL peak. Dashed lines represent $\eta_L^{det} = 1$.

than OSL. For carbon ions, however, $\eta_L^{det} < 1$. Table 8.6 shows η_L^{BeO} values calculated using the linear region of all BeO responses. The Carbon OSL responses cannot be used because they are highly supralinear along the entire domain investigated in this work. Optical efficiencies decreased with increasing LET, excluding 8 MeV C. They range between approximately 24% and 55% for protons, and approximately 0.8% and 1.4% for Carbon. The l_0 efficiencies are slightly higher than those of OSL, but generally within error limits. All TL area proton efficiencies are equal to 1 within their uncertainties, with the exception of 2 MeV H due to its very small error. However, the proton TL peak efficiencies are slightly greater than 1. Because the integrated TL signal stays the same but the peak height increases, it is concluded that the higher LET protons induce a relatively taller TL peak signal compared to signals from low LET radiation. TL area and peak η_L^{BeO} values range from approximately 2.0% to 10% for Carbon.

Ion	OSL	l_0	TL area	TL peak
1 MeV H	$(2.39\pm0.19)\cdot10^{-1}$	$(2.68\pm0.12)\cdot10^{-1}$	1.022 ± 0.085	1.132 ± 0.069
2 MeV H	$(3.75\pm0.17)\cdot10^{-1}$	$(3.98\pm0.14)\cdot10^{-1}$	$(9.88\pm0.01)\cdot10^{-1}$	1.085 ± 0.084
4 MeV H	$(5.41\pm0.14)\cdot10^{-1}$	$(5.48\pm0.33)\cdot10^{-1}$	1.058 ± 0.074	1.201 ± 0.158
2 MeV C	-	$(8.04\pm0.51)\cdot10^{-3}$	$(5.41\pm0.54)\cdot10^{-2}$	$(6.63\pm0.24)\cdot10^{-2}$
4 MeV C	-	$(4.96\pm0.29)\cdot10^{-3}$	$(2.04\pm0.08)\cdot10^{-2}$	$(3.88\pm0.46)\cdot10^{-2}$
8 MeV C	-	$(1.45\pm0.19)\cdot10^{-2}$	$(7.57\pm0.54)\cdot10^{-2}$	$(1.01\pm0.07)\cdot10^{-1}$

Table 8.3: η_L^{BeO} values calculated using equation (8.4). The errors were calculated using the standard deviation of the data in the linear domain.

Table 7.4 shows η_L^{BeO} values calculated using equations (8.9)-(8.11). The carbon OSL responses can only be approximated by an exponential growth function, whereas the Carbon l_0 responses are well-described by a linear function. η_L^{BeO} values calculated using equations (8.9)-(8.11) follow more or less the same trend described above, but there are magnitude differences. For example, while 1 MeV TL area and peak efficiencies are very similar to previous values, the 2 and 4 MeV efficiencies decrease by $\approx 20\%$. Additionally, the uncertainties of some data are very large, likely attributed to the same reasons previously discussed for

Al_2O_3:C. Although the cause is unknown, the TL area response for 4 MeV Carbon was not well described by a saturating exponential, resulting in an uncertainty larger than the efficiency value itself. This data point is therefore discarded.

Ion	OSL	l_0	TL area	TL peak
1 MeV H	$(2.91\pm0.14)\cdot10^{-1}$	$(2.85\pm0.87)\cdot10^{-1}$	$(9.97\pm0.53)\cdot10^{-1}$	1.013 ± 0.072
2 MeV H	$(3.86\pm0.45)\cdot10^{-1}$	$(3.38\pm0.26)\cdot10^{-1}$	$(8.40\pm1.06)\cdot10^{-1}$	$(8.66\pm1.36)\cdot10^{-1}$
4 MeV H	$(6.15\pm0.73)\cdot10^{-1}$	$(4.73\pm0.46)\cdot10^{-1}$	$(8.33\pm2.32)\cdot10^{-1}$	$(8.14\pm4.49)\cdot10^{-1}$
2 MeV C	$(6.01\pm0.19)\cdot10^{-3}$	$(9.83\pm0.34)\cdot10^{-3}$	$(6.72\pm1.09)\cdot10^{-2}$	$(8.16\pm1.24)\cdot10^{-2}$
4 MeV C	$(3.62\pm0.37)\cdot10^{-3}$	$(4.95\pm0.03)\cdot10^{-3}$	-	$(4.68\pm0.46)\cdot10^{-2}$
8 MeV C	$(9.93\pm1.25)\cdot10^{-3}$	$(1.29\pm0.11)\cdot10^{-2}$	$(9.15\pm0.69)\cdot10^{-2}$	$(1.00\pm0.03)\cdot10^{-1}$

Table 8.4: η_L^{BeO} values calculated using equations (8.9)-(8.11). Carbon OSL responses were fit with equation (8.10), Carbon l_0 responses were fit with equation (8.11), and all other responses were fit with equation (8.9). The errors were calculated using the uncertainty of the fitting parameters.

Tables 7.5 and 7.6 present the η_L^w data using the linear method and the function approximation method, respectively. As with Al_2O_3:C, $\eta_L^w/\eta_L^{det} < 1$ due to the large discrepancy between stopping powers in water and BeO in this LET range. For 4 MeV protons,

$$\begin{aligned}\frac{\eta_L^w}{\eta_L^{det}} &= \frac{D_\gamma^w}{D_\gamma^{det}} \cdot \frac{D_L^{det}}{D_L^w} \\ &= \left(\frac{\mu_{en}}{\rho}\right)_{det}^{w} \left(\frac{L}{\rho}\right)_{w}^{det} \\ &= \left(\frac{2.935 \cdot 10^{-2}\frac{cm^2}{g}}{2.772 \cdot 10^{-2}\frac{cm^2}{g}}\right)\left(\frac{39.22\frac{keV}{\mu m}/2.85\frac{g}{cm^3}}{16.59\frac{keV}{\mu m}/1.00\frac{g}{cm^3}}\right) \\ &= 0.878.\end{aligned} \tag{8.14}$$

There is no published efficiency data concerning the Al_2O_3:C synthesis utilized in this work, which would allow results comparison. However, a comparison of η_L^w values in this work to previously published values for Materion Thermolox® 995 BeO dosimeters allows the effectiveness of the beamline constructed as part of this research to be evaluated. Sadel

et al. evaluated the efficiency to water of BeO for 58.7, 27, and 6.5 MeV protons using a 60 MeV cyclotron and Poly(methyl methacrylate) (PMMA) to slow down the beam [116]. Figure 8.6 compares the OSL proton efficiencies calculated in this work using equation (8.3) to those presented in Radiation Protection Dosimetry by Sadel et al. The data is in excellent agreement. Therefore it is argued that the beamline adequately delivers a measurable amount of absorbed energy from charged particles, and can be used to calculate efficiencies for other ions and dosimeter materials. Sadel et al. did not go through the extra steps required to build calibration curves. They instead gave a known dose with protons and γ, and compared the signals. However, this method does not correct for mass and sensitivity differences between dosimeters, and is likely responsible for the larger uncertainties.

Ion	OSL	l_0	TL area	TL peak
1 MeV H	$(2.14\pm0.17)\cdot10^{-1}$	$(2.41\pm0.11)\cdot10^{-1}$	$(9.18\pm0.76)\cdot10^{-1}$	1.017 ± 0.062
2 MeV H	$(3.31\pm0.15)\cdot10^{-1}$	$(3.52\pm0.12)\cdot10^{-1}$	$(8.74\pm0.01)\cdot10^{-1}$	$(9.60\pm0.74)\cdot10^{-1}$
4 MeV H	$(4.75\pm0.13)\cdot10^{-1}$	$(4.81\pm0.29)\cdot10^{-1}$	$(9.29\pm0.65)\cdot10^{-1}$	1.054 ± 0.139
2 MeV C	-	$(6.90\pm0.44)\cdot10^{-3}$	$(4.64\pm0.47)\cdot10^{-2}$	$(5.69\pm0.21)\cdot10^{-2}$
4 MeV C	-	$(4.06\pm0.24)\cdot10^{-3}$	$(1.67\pm0.06)\cdot10^{-2}$	$(3.18\pm0.38)\cdot10^{-2}$
8 MeV C	-	$(1.15\pm0.15)\cdot10^{-2}$	$(5.99\pm0.43)\cdot10^{-2}$	$(8.02\pm0.59)\cdot10^{-2}$

Table 8.5: η_L^w values calculated for BeO using table 7.3 and equation (8.12).

Ion	OSL	l_0	TL area	TL peak
1 MeV H	$(2.61\pm0.13)\cdot10^{-1}$	$(2.56\pm0.78)\cdot10^{-1}$	$(8.96\pm0.48)\cdot10^{-1}$	$(9.10\pm0.65)\cdot10^{-1}$
2 MeV H	$(3.41\pm0.40)\cdot10^{-1}$	$(2.99\pm0.23)\cdot10^{-1}$	$(7.43\pm0.94)\cdot10^{-1}$	$(7.66\pm1.21)\cdot10^{-1}$
4 MeV H	$(5.40\pm0.64)\cdot10^{-1}$	$(4.15\pm0.40)\cdot10^{-1}$	$(7.31\pm2.04)\cdot10^{-1}$	$(7.15\pm3.94)\cdot10^{-1}$
2 MeV C	$(5.16\pm0.16)\cdot10^{-3}$	$(8.44\pm0.29)\cdot10^{-3}$	$(5.77\pm0.93)\cdot10^{-2}$	$(7.00\pm1.07)\cdot10^{-2}$
4 MeV C	$(2.96\pm0.30)\cdot10^{-3}$	$(4.05\pm0.02)\cdot10^{-3}$	-	$(3.83\pm0.37)\cdot10^{-2}$
8 MeV C	$(7.86\pm0.99)\cdot10^{-3}$	$(1.02\pm0.08)\cdot10^{-2}$	$(7.25\pm0.55)\cdot10^{-2}$	$(7.95\pm0.21)\cdot10^{-2}$

Table 8.6: η_L^w values calculated for BeO using table 7.4 and equation (8.12).

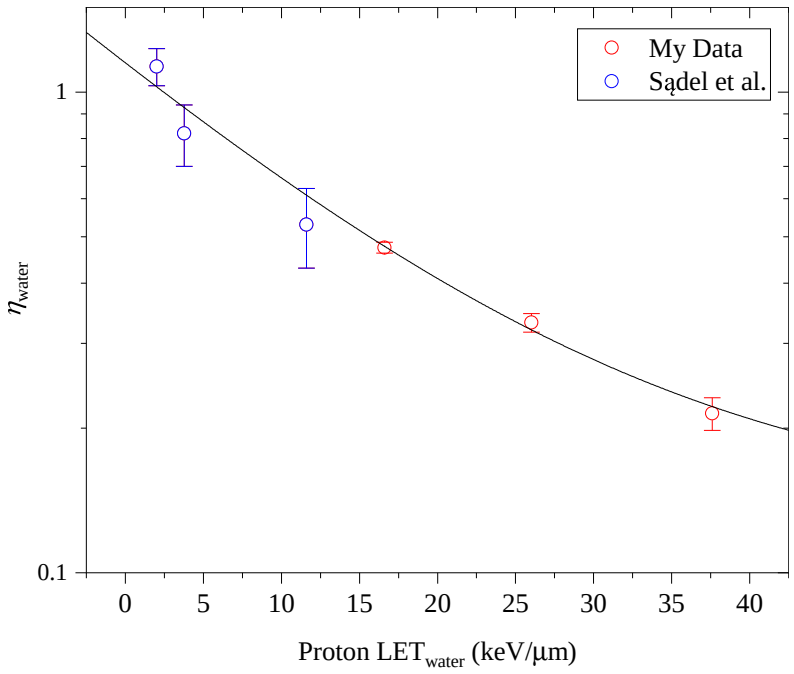

Figure 8.6: Comparison of proton η_L^w values determined by Sadel et al. [116]. and those calculated in this work. The corresponding proton energies, from left to right, are 58.7, 27, 6.5, 4, 2, and 1 MeV. The data has been arbitrarily fit with an exponential decay to show a continuous trend, and is not intended as a theoretical model.

Chapter 9

Conclusions and Future Directions

9.1 Conclusions

The goal of this dissertation was to investigate the effects of low-energy HCPs on the optically and thermally stimulated luminescence signals of Al_2O_3:C and BeO single crystal dosimeters. Chapter 3 presented the luminescence beamline built as a significant portion of this dissertation, including a description of the utility of every important component; it took about two years to design, construct, and test.

Several dosimeter specific qualities were characterized in Chapter 5, the results of which were used to inform our HCP measurement procedure; these qualities include signal and shape uniformity, repeatability, and dose response. Significant signal and shape non-uniformity between individual dosimeterswas observed for OSL and TL for both material. Individual dosimeters repeatedly given the same dose, followed by measurement, display increased or decreased sensitization, depending on which dosimeter and readout method was utilized. The OSL, l_0, Tl area, and TL peak responses vary slightly for Al_2O_3:C, but are drastically different for BeO. The Al_2O_3:C responses follow the linear-sublinear-satuation response model, while the BeO responses follow the linear-supralinear-saturation model.

The effects of ion, ion energy, total absorbed energy, and current were investigated for

both materials in Chapter 6. Al_2O_3:C OSL curves decay more quickly as absorbed energy increases and ion size decreases. The high temperature peak was significantly more prominent in Carbon signals compared to all other lower LET ions. All 4 signal calculation methods yield similar responses that saturate when exposed to protons and Carbon, with small signal differences. Fluence-derived saturation effects were observed for Carbon and proton responses. Increasing HCP current induced slight OSL and TL curve shape change, but no signal variation for any calculation method.

Generally speaking, the response of BeO to differing experimental parameters was richer, but also more complex. The area under normalized OSL curves trends differently when exposed to the same absorbed energies from protons and Carbon. The relative TL high temperature peak contribution decreased and the SNR increased with increasing absorbed energy for protons and Carbon. Unlike Al_2O_3:C, the dependence of curve shape on ion type and LET is not clear. The OSL and l_0 responses are ion dependent; OSL is linear followed by supralinear for protons, and very sublinear then extremely supralinear for Carbon. l_0 is slightly sublinear followed by supralinearity for protons, but is exceptionally linear when exposed to Carbon. TL area and peak signals both respond supralinearly to protons and Carbon; however the supralinearity factor $f(E)$ decreases with increasing LET for a given absorbed energy. BeO Carbon and proton responses experience fluence related saturation effects, just like Al_2O_3:C. OSL and TL curves do not change shape to a significant degree when exposed to differing HCP currents. Optical signals obtained using different currents are within error of each other, but thermal signals decrease at the highest fluence rate utilized.

In Chapter 7 it was shown that OSL signals can be resolved as sums of exponential functions. The number of components comprising an OSL signal can be robustly determined by a direct comparison of the residuals of the fit and autocorrelation function of the residuals. The β-corrected contributions of these components were then plotted against absorbed energy to elucidate component-specific growth and decay. OSL curves from the synthesis of Al_2O_3:C studied in this dissertation are comprised of a fast and slow component. The slow compo-

nent saturates sooner than the fast component, leading to faster OSL decay with increasing absorbed energy. Because the dose responses of both components are well described by a saturating exponential, the OSL response is sublinear until saturation. This study found that BeO OSL curves are comprised of a fast, medium, and slow decay; this claim opposes results from several other researchers. The fast decay was supralinear, the medium decay was approximately linear, and the slow decay became very sublinear at high absorbed energies from protons. However, Carbon irradiation induced an exceptionally linear fast component, an extremely supralinear then sublinear medium component, and an extremely sublinear then supralinear slow component. These component growth curves were used to elucidate the difference between proton and Carbon OSL curve shape change observed in Chapter 6. These results also indicate that new growth curves must necessarily be constructed every time varying OSL shape is interpreted using complex dosimeters.

Chapter 8 defines luminescence efficiency, outlines a previously utilized, precise methodology for evaluating γ-equivalent dose, explains how to obtain efficiency from the γ-equivalent response relative to HCPs, and presents efficiency data for all readout methods and ions and energies used in this work. The Al_2O_3:C data are not linear for any ion or energy, thus efficiencies were calculated by taking evaluating the slope of the response as absorbed energy from HCPs approaches zero. Al_2O_3:C is very inefficient, with OSL values ranging from $\sim$ .04 for 4 MeV protons, to $\sim$ .0007 for 4 MeV Carbon. OSL and TL area and peak signal efficiencies are generally within error, while l_0 is higher for most ions and energies. The expected LET dependence of efficiency was observed for all ions and energies excluding 8 MeV C.

BeO efficiency values are significantly higher than those of Al_2O_3:C, with TL η_L^{det} values ranging from $\sim$1 for 4 MeV protons to $\sim$0.02 for 4 MeV C. All BeO γ-equivalent responses, except for Carbon OSL responses, were linear; this allowed the efficiency to be calculated using the linear domain, as well as the method used for Al_2O_3:C. Both thermal efficiencies are significantly higher than either optical efficiency for all ions and energies, suggesting the

hard-to-bleach traps associated with the high temperature TL peak are significant in number. The TL area efficiencies for 1, 2, and 4 MeV protons are all ∼1 while the corresponding OSL efficiencies range from ∼0.2 to ∼0.5; this suggests the traps contributing to TL signal have not experienced saturation effects for an LET_{H_2O} of 37.6 keV/μm, whereas traps contributing to the OSL signal are already saturating at an LET_{H_2O} of 16.6 keV/μm. The TL peak efficiencies are slightly higher than TL area values, meaning HCP TL curves get taller relative to γ, for a given absorbed energy. As with Al_2O_3:C, the relationship between η_L^{det} and LET was observed for all ions and energies excluding 8 MeV C. Lastly, a comparison of η_L^w proton values calculated in this work are in good agreement with previously published results.

The consistency of BeO proton efficiencies with previous results strongly suggest that the beamline constructed as part of this dissertation can be effectively utilized to irradiate other dosimeters with known absorbed energies from HCPs. Should very thin dosimeters be used, the energy departing the dosimeter will also require consideration, making the absorbed energy calculation method more complex.

9.2 Future Directions

There are several beamline modifications that could improve the current experimental process, and even offer different research prospects altogether. Not all luminescence beamline chamber ports are currently occupied by equipment; it is therefore possible that additional equipment can be integrated into the beamline which would enable luminescence measurement during irradiation (i.e. phosphorescence). It was observed that while the YAG crystal was well-suited to monitor proton fluence, it became heavily doped and thus unusable when exposed to Carbon. Thin quartz was used to monitor Carbon, but this is not a long-term solution; quartz crystals become doped as well, the effects are just noticeable at a much slower rate than for the YAG crystal. Additionally the spatial resolution of quartz is lower than YAG, and the current required to obtain bright scintillation is much higher. All of these

factors suggest it is well worth investigating an alternative method for monitoring fluence. Lastly, the beamline would benefit from a more precise shutter with a known uncertainty. This would enable verification of the high dose rate results from this work, as well as precise delivery of very low absorbed energies or very high currents. The alternative approach to increasing precision is using Rutherford scattering to lower HCP current upstream of the analyzing magnet. However, this method is more complex and adds geometric and experimental uncertainties. It is the author's opinion that a faster shutter is simpler, and likely more precise.

There are many valuable experiments that can be performed without modification to the beamline. To start, all 8 MeV C tests should be repeated to verify the results presented in this dissertation. It would also be beneficial to irradiate the dosimeters in this work with other ions, such as Lithium. If two ions of similar size are utilized, it might allow one to investigate whether η_L^{det} is ion dependent. More precise responses can be built by irradiating multiple dosimeters per absorbed energy value, if it is required. This procedure is much more time consuming, but will pay dividends when utilizing samples which saturate very quickly. The effects of HCPs on the sensitivity of dosimeters used in this work was unclear. There were sensitivity changes observed between the test doses from before and after HCP irradiation, but they appeared random. It is likely that sensitivity changes, if they exist at all, are quite small and require irradiation of many dosimeters under the same conditions. Sensitivity changes are the result of doping a material's band gap with previously nonexistent traps and are therefore assumed to be dosimeter specific. It could also be the case that higher absorbed energies from HCPs are required to measure significant sensitivity change. Lastly, it was observed that pure quartz did not sensitize when exposed to protons. If the lattice structure is not altered by irradiation, electrons will immediately recombine and the sample cannot store any signal. It is therefore worth investigating whether heavier ions can increase quartz luminescence properties where protons could not. After all, Carbon affected the YAG crystal and protons did not.

As mentioned before, there are many scientists in the luminescence/dating community that would benefit from using the Risø's internal ^{241}Am α source. In dating applications the source is used to give a known dose with alpha and compare the signal to that from a beta dose of equal magnitude to determine the unknown efficiency of a material. However, this requires knowing the dose rate of the alpha source, which in turn must be calibrated with a material of known luminescence efficiency. The major issue is that no suitable materials of known alpha efficiency are available. As a result, many labs have uncalibrated (and thus useless) sources. However, were there a He ion source installed in the ECU accelerator lab, creation of 5.49 MeV α particles is possible; this would enable ^{241}Am α source calibration by calculating the efficiency. If this experiment is performed with a dosimeter available to anybody, such as the Thermolox® 995 BeO single crystal dosimeters used in this work, then anybody with a calibrated γ or β source can calibrate their own α source using standard methods.

References

[1] E Becquerel. Effects produced on bodies by the sun's rays. In *Annals of chemistry and physics*, volume 9, pages 257–322, 1843.

[2] AH Becquerel. Maxima and minima of excitinction of al phosphorescence under the influence of infra-red radiation. *Accounts Rendered*, 96:1853–1856, 1883.

[3] EL Nichols and E Merritt. Carnegie institution of washington, s. *Studies in luminescence*, 9:1912–225, 1912.

[4] Humboldt W Leverenz. Luminescent solids (phosphors). *Science*, 109(2826):183–195, 1949.

[5] Wallack Stanley. Dosimeter, September 1 1959. US Patent 2,902,605.

[6] John F Fowler. Solid state dosimetry. *Physics in Medicine & Biology*, 8(1):1, 1963.

[7] E Tochilin, N Goldstein, and WG Miller. Beryllium oxide as a thermoluminescent dosimeter. *Health physics*, 16(1):1–7, 1969.

[8] CR Rhyner and WG Miller. Radiation dosimetry by optically-stimulated luminescence of beo. *Health Physics*, 18(6):681–684, 1970.

[9] R Bernhardt. Radiation dosimetry by optically stimulated phosphorescence of caf2:mn. Technical report, Technische Univ., 1974.

[10] SAHAI AMBIKA, AMBIKA SAHAI PRADHAN, et al. Radiation dosimetry by photostimulated luminescence of caso:dy. 1977.

[11] AS Pradhan and RC Bhatt. Photo-stimulated luminescence and thermoluminescence in caso4:dy. *physica status solidi (a)*, 68(2):405–411, 1981.

[12] RC Yoder. A dosimetry system based on delayed optically stimulated luminescence. *Health Phys.*, 72:S18–S19, 1997.

[13] David J Huntley, Dorothy I Godfrey-Smith, and Michael LW Thewalt. Optical dating of sediments. *Nature*, 313(5998):105–107, 1985.

[14] Martin Jim Aitken. *Introduction to optical dating: the dating of Quaternary sediments by the use of photon-stimulated luminescence*. Clarendon Press, 1998.

[15] Lars Bøtter-Jensen, Stephen WS McKeever, and Ann G Wintle. *Optically stimulated luminescence dosimetry*. Elsevier, 2003.

[16] Eduardo G Yukihara and Stephen WS McKeever. *Optically stimulated luminescence: fundamentals and applications*. John Wiley & Sons, 2011.

[17] Kazuhiro Terasawa and Tadayoshi Doke. Operational radiation safety program for astronauts in low-earth orbit: A basic framework, ncrp report no. 142: Recommendations of the national council on radiation protection and measurements, november 30, 2002, 168pp, isbn 0-929600-75-4, national council on radiation protection and measurements, us 40. *Journal of radiation research*, 44(4):367–368, 2003.

[18] MC Thorne. Icrp publication 60: 1990 recommendations of the international commission on radiological protection: Annals of the icrp, 21 (1–3), 1991, 1992.

[19] Gabriel Oliveir Sawakuchi. *Characterization and modeling of relative luminescence efficiency of optically stimulated luminescence detectors exposed to heavy charged particles*. PhD thesis, Oklahoma State University, 2007.

[20] D Zhou, E Semones, R Gaza, and M Weyland. Radiation measured with passive dosimeters in low earth orbit. *Advances in Space Research*, 40(11):1575–1579, 2007.

[21] D Zhou, E Semones, R Gaza, S Johnson, N Zapp, and M Weyland. Radiation measured for iss-expedition 12 with different dosimeters. *Nuclear Instruments and Methods in Physics Research Section A: Accelerators, Spectrometers, Detectors and Associated Equipment*, 580(3):1283–1289, 2007.

[22] JH Fremlin and F Abu Jarad. Alpha-emitters in the environment i: Natural sources. *Nuclear Instruments and Methods*, 173(1):197–200, 1980.

[23] MS Akselrod and VS Kortov. Thermoluminescent and exoemission properties of new high-sensitivity tld -al_2o_3:c crystals. *Radiation Protection Dosimetry*, 33(1-4):123–126, 1990.

[24] BG Markey, LE Colyott, and SWS McKeever. Time-resolved optically stimulated luminescence from α-al_2o_3:c. *Radiation Measurements*, 24(4):457–463, 1995.

[25] E Bulur and HY Göksu. Osl from beo ceramics: new observations from an old material. *Radiation measurements*, 29(6):639–650, 1998.

[26] AS Pradhan, JI Lee, and JL Kim. Recent developments of optically stimulated luminescence materials and techniques for radiation dosimetry and clinical applications. *Journal of medical physics/Association of Medical Physicists of India*, 33(3):85, 2008.

[27] Alexandre M Caraça Santos, Mohammad Mohammadi, Johan Asp, Tanya M Monro, and Shahraam Afshar. Characterisation of a real-time fibre-coupled beryllium oxide (beo) luminescence dosimeter in x-ray beams. *Radiation measurements*, 53:1–7, 2013.

[28] Alexandre M Caraça Santos, Mohammad Mohammadi, and Shahraam Afshar. Investigation of a fibre-coupled beryllium oxide (beo) ceramic luminescence dosimetry system. *Radiation measurements*, 70:52–58, 2014.

[29] Alexandre M Caraça Santos, Mohammad Mohammadi, and Shahraam Afshar. Energy dependency of a water-equivalent fibre-coupled beryllium oxide (beo) dosimetry system. *Radiation Measurements*, 73:1–6, 2015.

[30] Alexandre M Caraça Santos, Raghu Gowda, Eva Bezak, and Shahraam Afshar. Evaluation of a real-time optically stimulated luminescence beryllium oxide (beo) fibre-coupled dosimetry system with a superficial 140 kvp x-ray beam. *Physica Medica*, 65:167–171, 2019.

[31] Erwin Schrödinger. Quantisierung als eigenwertproblem. *Annalen der physik*, 385(13):437–490, 1926.

[32] Felix Bloch. Über die quantenmechanik der elektronen in kristallgittern. *Zeitschrift für physik*, 52(7-8):555–600, 1929.

[33] Charles Kittel and Paul McEuen. *Introduction to solid state physics*, volume 8. Wiley New York, 1976.

[34] Neil W Ashcroft, N David Mermin, et al. Solid state physics [by] neil w. ashcroft [and] n. david mermin., 1976.

[35] R de L Kronig and William George Penney. Quantum mechanics of electrons in crystal lattices. *Proceedings of the Royal Society of London. Series A, Containing Papers of a Mathematical and Physical Character*, 130(814):499–513, 1931.

[36] Rolf E Hummel. *Electronic properties of materials*. Springer Science & Business Media, 2011.

[37] Benjamin Kollmitzer and Peter Hadley. Thermodynamic properties of separable square-wave potentials. *Physica B: Condensed Matter*, 406(23):4373–4380, 2011.

[38] Otfried Madelung. *Introduction to solid-state theory*, volume 2. Springer Science & Business Media, 2012.

[39] Rolf Enderlein and Norman JM Horing. *Fundamentals of semiconductor physics and devices*. World Scientific, 1997.

[40] Robert Swendsen. *An introduction to statistical mechanics and thermodynamics*. Oxford University Press, USA, 2020.

[41] VP Gribkovskii. Theory of luminescence. In *Luminescence of Solids*, pages 1–43. Springer, 1998.

[42] SWS McKeever. Thermoluminescence of solids, cambridge uni. *Press, Cambridge*, 1985.

[43] Ramona Gaza. *Space radiation dosimetry: An optically stimulated luminescence radiation detector for low-Earth orbit*. PhD thesis, Oklahoma State University, 2004.

[44] P Bräunlich, P Kelly, and J-P Fillard. Thermally stimulated luminescence and conductivity. In *Thermally stimulated relaxation in solids*, pages 35–92. Springer, 1979.

[45] Reuven Chen and Stephen WS McKeever. *Theory of thermoluminescence and related phenomena*. World Scientific, 1997.

[46] Stephen WS McKeever. *Thermoluminescence of solids*, volume 3. Cambridge University Press, 1988.

[47] John Turton Randall and Maurice Hugh Frederick Wilkins. Phosphorescence and electron traps-i. the study of trap distributions. *Proceedings of the Royal Society of London. Series A. Mathematical and Physical Sciences*, 184(999):365–389, 1945.

[48] SWS McKeever and R Chen. Luminescence models. *Radiation Measurements*, 27(5-6):625–661, 1997.

[49] GFJ Garlick and AF Gibson. The electron trap mechanism of luminescence in sulphide and silicate phosphors. *Proceedings of the physical society*, 60(6):574, 1948.

[50] CE May and JA Partridge. Thermoluminescent kinetics of alpha-irradiated alkali halides. *The Journal of Chemical Physics*, 40(5):1401–1409, 1964.

[51] JA Partridge and CE May. Anomalous thermoluminescent kinetics of irradiated alkali halides. *The Journal of Chemical Physics*, 42(2):797–798, 1965.

[52] Baldassare Di Bartolo. Optical interactions in solids. 1968.

[53] RW Gurney and NF Mott. Luminescence in solids. *Transactions of the Faraday Society*, 35:69–73, 1939.

[54] AG Wintle. Thermal quenching of thermoluminescence in quartz. *Geophysical Journal International*, 41(1):107–113, 1975.

[55] NF Mott. and 'gurney rw. *Electronic Processes in lonic Crystals*, 1940.

[56] George Blasse and BC Grabmaier. A general introduction to luminescent materials. In *Luminescent materials*, pages 1–9. Springer, 1994.

[57] LUTZ Nasdala, JENS Götze, JOHN M Hanchar, MICHAEL Gaft, MATTHIAS R Krbetschek, A Beran, and E Libowitzky. Luminescence techniques in earth sciences. *Spectroscopic methods in mineralogy*, 6:43–91, 2004.

[58] YS Horowitz. The theoretical and microdosimetric basis of thermoluminescence and applications to dosimetry. *Physics in Medicine & Biology*, 26(5):765, 1981.

[59] FH Attix. Introduction to radiological physics and radiation dosimetry (willey, 1986.

[60] Gabriel Oliveira Sawakuchi, EG Yukihara, SWS McKeever, and ER Benton. Overlap of heavy charged particle tracks and the change in shape of optically stimulated luminescence curves of al_2o_3:c dosimeters. *Radiation measurements*, 43(2-6):194–198, 2008.

[61] Linear Energy Transfer ICRU. Report no. 16. *International Commission on Radiation Units and Measurements, Washington, DC*, 1970.

[62] Roy Middleton. A negative ion cookbook. *University of Pennsylvania, unpublished*, 1989.

[63] JF Ziegler, U Littmark, and JP Biersack. Calculation using the stopping and range of ions in matter (srim) code, 2008.

[64] TL RISØ and OSL User Manual. Guide to "the risø tl/osl reader". *RISØ DTU. Denmark*, 2010.

[65] HH Hansen. Measurement of the beta-ray spectra of 90sr-90y. *The International Journal Of Applied Radiation And Isotopes*, 34(8):1241–1247, 1983.

[66] DC Kocher. Nuclear data sheets for a= 90. *Nuclear Data Sheets*, 16(1):55–105, 1975.

[67] MS Akselrod, VS Kortov, DJ Kravetsky, and VI Gotlib. Highly sensitive thermoluminescent anion-defective alpha-al_2o_3:c single crystal detectors. *Radiation Protection Dosimetry*, 32(1):15–20, 1990.

[68] SWS McKeever, MS Akselrod, and BG Markey. Pulsed optically stimulated luminescence dosimetry using alpha-al_2o_3:c. *Radiation Protection Dosimetry*, 65(1-4):267–272, 1996.

[69] SJ Zinkle, VA Skuratov, and DT Hoelzer. On the conflicting roles of ionizing radiation in ceramics. *Nuclear Instruments and Methods in Physics Research section B: Beam Interactions with Materials and Atoms*, 191(1-4):758–766, 2002.

[70] MS Akselrod, Lars Bøtter-Jensen, and SWS McKeever. Optically stimulated luminescence and its use in medical dosimetry. *Radiation Measurements*, 41:S78–S99, 2006.

[71] Bruce D Evans. A review of the optical properties of anion lattice vacancies, and electrical conduction in α-al_2o_3: their relation to radiation-induced electrical degradation. *Journal of nuclear materials*, 219:202–223, 1995.

[72] Kuo-Hua Lee and JH Crawford Jr. Luminescence of the f center in sapphire. *Physical review B*, 19(6):3217, 1979.

[73] BG Markey, L Bøtter-Jensen, and GAT Duller. A new flexible system for measuring thermally and optically stimulated luminescence. *Radiation Measurements*, 27(2):83–89, 1997.

[74] GP Summers. Thermoluminescence in single crystal alpha-al_2o_3. *Radiation protection dosimetry*, 8(1-2):69–80, 1984.

[75] Eduardo G Yukihara and Stephen WS McKeever. Ionisation density dependence of the optically and thermally stimulated luminescence from al_2o_3:c. *Radiation protection dosimetry*, 119(1-4):206–217, 2006.

[76] SWS McKeever, MS Akselrod, LE Colyott, N Agersnap Larsen, JC Polf, and V Whitley. Characterisation of al_2o_3 for use in thermally and optically stimulated luminescence dosimetry. *Radiation Protection Dosimetry*, 84(1-4):163–166, 1999.

[77] M Springis, P Kulis, A Veispals, V Tale, and I Tale. Origin of the 430 k tl peak in thermochemically reduced alpha-al_2o_3. *Radiation protection dosimetry*, 65(1-4):231–234, 1996.

[78] Gabor Molnar, Eric Papin, Philippe Grosseau, Bernard Guilhot, J Borossay, M Benabdesselam, P Iacconi, and Dominique Lapraz. Thermally stimulated luminescence and exoelectron emission mechanism of the 430 k (d') dosimetric peak of a-al_2o_3. *Radiation protection dosimetry*, 84(1-4):253–256, 1999.

[79] MS Akselrod and EA Gorelova. Deep traps in highly sensitive α-al_2o_3:c tld crystals. *Nuclear Tracks and Radiation Measurements*, 21(1):143–146, 1993.

[80] EG Yukihara, VH Whitley, JC Polf, DM Klein, SWS McKeever, AE Akselrod, and MS Akselrod. The effects of deep trap population on the thermoluminescence of al_2o_3:c. *Radiation measurements*, 37(6):627–638, 2003.

[81] EG Yukihara, VH Whitley, SWS McKeever, AE Akselrod, and MS Akselrod. Effect of high-dose irradiation on the optically stimulated luminescence of al_2o_3:c. *Radiation measurements*, 38(3):317–330, 2004.

[82] EG Yukihara, R Gaza, SWS McKeever, and CG Soares. Optically stimulated luminescence and thermoluminescence efficiencies for high-energy heavy charged particle irradiation in al_2o_3:c. *Radiation measurements*, 38(1):59–70, 2004.

[83] R Chen, V Pagonis, and JL Lawless. The nonmonotonic dose dependence of optically stimulated luminescence in al_2o_3:c analytical and numerical simulation results. *Journal of Applied Physics*, 99(3):033511, 2006.

[84] V Pagonis, R Chen, and JL Lawless. Nonmonotonic dose dependence of osl intensity due to competition during irradiation and readout. *Radiation measurements*, 41(7-8):903–909, 2006.

[85] Nancy K Umisedo, Elisabeth M Yoshimura, Patricia BR Gasparian, and EG Yukihara. Comparison between blue and green stimulated luminescence of al_2o_3:c. *Radiation Measurements*, 45(2):151–156, 2010.

[86] R Gaza, EG Yukihara, and SWS McKeever. The response of thermally and optically stimulated luminescence from al_2o_3:c to high-energy heavy charged particles. *Radiation measurements*, 38(4-6):417–420, 2004.

[87] EG Yukihara, Gabriel Oliveira Sawakuchi, S Guduru, SWS McKeever, R Gaza, ER Benton, N Yasuda, Y Uchihori, and H Kitamura. Application of the optically stimulated luminescence (osl) technique in space dosimetry. *Radiation measurements*, 41(9-10):1126–1135, 2006.

[88] O Avila, I Gamboa-deBuen, and ME Brandan. Study of the energy deposition in lif by heavy charged particle irradiation and its relation to the thermoluminescent efficiency of the material. *Journal of Physics D: Applied Physics*, 32(10):1175, 1999.

[89] HO Albrecht and CE Mandeville. Storage of energy in beryllium oxide. *Physical Review*, 101(4):1250, 1956.

[90] G Scarpa. The dosimetric use of beryllium oxide as a thermoluminescent material: A preliminary study. *Physics in Medicine & Biology*, 15(4):667, 1970.

[91] AJJ Bos. High sensitivity thermoluminescence dosimetry. *Nuclear Instruments and Methods in Physics Research Section B: Beam Interactions with Materials and Atoms*, 184(1-2):3–28, 2001.

[92] Eduardo G Yukihara, Stephen WS McKeever, and Mark S Akselrod. State of art: Optically stimulated luminescence dosimetry–frontiers of future research. *Radiation Measurements*, 71:15–24, 2014.

[93] Gilberto Busuoli, Ivo Sermenghi, Otello Rimondi, and Giulia Vicini. Tl personnel dosimeter with beo. *Nuclear Instruments and Methods*, 140(2):385–388, 1977.

[94] G Busuoli, L Lembo, R Nanni, and I Sermenghi. Use of beo in routine personnel dosimetry. *Radiation Protection Dosimetry*, 6(1-4):317–320, 1983.

[95] Stephen WS McKeever, Marko Moscovitch, and Peter David Townsend. Thermoluminescence dosimetry materials: properties and uses. 1995.

[96] M Sommer and J Henniger. Investigation of a beo-based optically stimulated luminescence dosemeter. *Radiation protection dosimetry*, 119(1-4):394–397, 2006.

[97] Marian Sommer, Robert Freudenberg, and Jürgen Henniger. New aspects of a beo-based optically stimulated luminescence dosimeter. *Radiation Measurements*, 42(4-5):617–620, 2007.

[98] M Sommer, A Jahn, and J Henniger. Beryllium oxide as optically stimulated luminescence dosimeter. *Radiation Measurements*, 43(2-6):353–356, 2008.

[99] E Bulur, L Bøtter-Jensen, and AS Murray. Frequency modulated pulsed stimulation in optically stimulated luminescence. *Nuclear Instruments and Methods in Physics Research Section B: Beam Interactions With Materials and Atoms*, 179(1):151–159, 2001.

[100] E Bulur, L Bøtter-Jensen, and AS Murray. Lm-osl signals from some insulators: an analysis of the dependency of the detrapping probability on stimulation light intensity. *Radiation Measurements*, 33(5):715–719, 2001.

[101] Enver Bulur and Aydan Yeltik. Optically stimulated luminescence from beo ceramics: An lm-osl study. *Radiation measurements*, 45(1):29–34, 2010.

[102] A Jahn, M Sommer, and J Henniger. 2d-osl-dosimetry with beryllium oxide. *Radiation measurements*, 45(3-6):674–676, 2010.

[103] A Jahn, M Sommer, M Liebmann, and J Henniger. Progress in 2d-osl-dosimetry with beryllium oxide. *Radiation measurements*, 46(12):1908–1911, 2011.

[104] Materion. Ceramics materials properties chart, 2020.

[105] Sıtkı Duman, A Sütlü, S Bağcı, HM Tütüncü, and GP Srivastava. Structural, elastic, electronic, and phonon properties of zinc-blende and wurtzite beo. *Journal of Applied Physics*, 105(3):033719, 2009.

[106] Enver Bulur. Photo-transferred luminescence from beo ceramics. *Radiation measurements*, 42(3):334–340, 2007.

[107] Eduardo G Yukihara. Luminescence properties of beo optically stimulated luminescence (osl) detectors. *Radiation measurements*, 46(6-7):580–587, 2011.

[108] EG Yukihara. A review on the osl of beo in light of recent discoveries: The missing piece of the puzzle? *Radiation Measurements*, page 106291, 2020.

[109] VA Pustovarov, V Yu Ivanov, M Kirm, AV Korotaev, AV Kruzhalov, G Zimmerer, and EI Zinin. Time-resolved luminescent vuv spectroscopy of f-and f+-centres in single beo crystals. *Nuclear Instruments and Methods in Physics Research Section A: Accelerators, Spectrometers, Detectors and Associated Equipment*, 470(1-2):353–357, 2001.

[110] Shigueo Watanabe, TK Gundu Rao, PS Page, and BC Bhatt. Tl, osl and esr studies on beryllium oxide. *Journal of Luminescence*, 130(11):2146–2152, 2010.

[111] Enver Bulur. More on the tr-osl signal from beo ceramics. *Radiation measurements*, 66:12–20, 2014.

[112] Klaus Becker, JS Cheka, and M Oberhofer. Thermally stimulated exoelectron emission, thermoluminescence, and impurities in lif and beo. *Health physics*, 19(3):391–403, 1970.

[113] H Yasuda and K Fujitaka. Glow curves from beryllium oxide exposed to high energy heavy ions. *Radiation protection dosimetry*, 87(3):203–206, 2000.

[114] B Voss, M Rebisz, and M Sommer. Investigations on beo as a dosimeter material for hadron therapy.

[115] Hiroshi Yasuda. Responses of a direct ion storage dosimeter (dis-1) to heavy charged particles. *Radiation research*, 156(6):805–808, 2001.

[116] Michał Sadel, Paweł Bilski, and Jan Swakoń. Relative tl and osl efficiency to protons of various dosimetric materials. *Radiation protection dosimetry*, 161(1-4):112–115, 2014.

[117] T Teichmann, MJ Gonzalez Torres, MJ van Goethem, ER van der Graaf, J Henniger, A Jahn, HH Kiewiet, M Sommer, W Ullrich, C Weinhold, et al. Dose and dose rate measurements in proton beams using the luminescence of beryllium oxide. *Journal of Instrumentation*, 13(10):P10015, 2018.

[118] Engin Aşlar, Niyazi Meriç, Eren Şahiner, Onur Erdem, George Kitis, and George S Polymeris. A correlation study on the tl, osl and esr signals in commercial beo dosimeters yielding intense transfer effects. *Journal of Luminescence*, 214:116533, 2019.

[119] RH Biswas, MK Murari, and AK Singhvi. Dose-dependent change in the optically stimulated luminescence decay of al_2o_3:c. *Radiation measurements*, 44(5-6):543–547, 2009.

[120] FD Walker, LE Colyott, N Agersnap Larsen, and SWS McKeever. The wavelength dependence of light-induced fading of thermoluminescence from α-al_2o_3:c. *Radiation measurements*, 26(5):711–718, 1996.

[121] EG Yukihara, AB Andrade, and S Eller. Beo optically stimulated luminescence dosimetry using automated research readers. *Radiation Measurements*, 94:27–34, 2016.

[122] Daniela P Groppo and Linda VE Caldas. Luminescent response from beo exposed to alpha, beta and x radiations. *Radiation measurements*, 71:81–85, 2014.

[123] AT Abdul Rahman, A Nisbet, and DA Bradley. Dose-rate and the reciprocity law: Tl response of ge-doped sio2 optical fibers at therapeutic radiation doses. *Nuclear Instruments and Methods in Physics Research Section A: Accelerators, Spectrometers, Detectors and Associated Equipment*, 652(1):891–895, 2011.

[124] A Viamonte, LAR Da Rosa, LA Buckley, A Cherpak, and JE Cygler. Radiotherapy dosimetry using a commercial osl system. *Medical physics*, 35(4):1261–1266, 2008.

[125] EG Yukihara and SWS McKeever. Optically stimulated luminescence (osl) dosimetry in medicine. *Physics in Medicine & Biology*, 53(20):R351, 2008.

[126] L Lembo, M Pimpinella, and B Mukherjee. Self optical attenuation coefficient of tl glow in beo detectors. *Radiation Protection Dosimetry*, 33(1-4):43–45, 1990.

[127] I Gamboa-deBuen, P Avilés, M Rodrıguez-Villafuerte, AE Buenfil, C Ruiz-Trejo, and ME Brandan. Supralinear response and efficiency of lif: Mg, ti to 0.7, 1.5 and 3 mev protons. *Nuclear Instruments and Methods in Physics Research Section B: Beam Interactions with Materials and Atoms*, 183(3-4):487–496, 2001.

[128] George S Polymeris, Miray Başdoğan, Gaye Ö Çakal, Engin Aşlar, and Niyazi Meriç. Gamma dose rate effects in luminescence signals of various artificial, well established dosimetric phosphors. *Radiation Measurements*, 133:106282, 2020.

[129] Kenneth Levenberg. A method for the solution of certain non-linear problems in least squares. *Quarterly of applied mathematics*, 2(2):164–168, 1944.

[130] MK Murari. Component specific luminescence of natural minerals and their application to dosimetry of natural radiation environment. *Mohanlal Sukhadia University, Udaipur, 141p*, 2008.

[131] John A Gubner. *Probability and random processes for electrical and computer engineers*. Cambridge University Press, 2006.

[132] Amiram Grinvald and Izchak Z Steinberg. On the analysis of fluorescence decay kinetics by the method of least-squares. *Analytical biochemistry*, 59(2):583–598, 1974.

[133] A Jahn, M Sommer, W Ullrich, M Wickert, and J Henniger. The beomax system–dosimetry using osl of beo for several applications. *Radiation measurements*, 56:324–327, 2013.

[134] EG Yukihara, EM Yoshimura, TD Lindstrom, S Ahmad, KK Taylor, and G Mardirossian. High-precision dosimetry for radiotherapy using the optically stimulated luminescence technique and thin al_2o_3:c dosimeters. *Physics in Medicine & Biology*, 50(23):5619, 2005.

[135] Gabriel O Sawakuchi, EG Yukihara, SWS McKeever, ER Benton, R Gaza, Y Uchihori, N Yasuda, and H Kitamura. Relative optically stimulated luminescence and thermoluminescence efficiencies of al_2o_3:c dosimeters to heavy charged particles with energies relevant to space and radiotherapy dosimetry. *Journal of Applied Physics*, 104(12):124903, 2008.

[136] Ramona Gaza, Eduardo G Yukihara, Stephen WS McKeever, Olga Ávila, Ana-Elena Buenfil, Isabel Gamboa-deBuen, Mercedes Rodríguez-Villafuerte, César Ruiz-Trejo, and María-Ester Brandan. Ionisation density dependence of the optically stimulated luminescence dose-response of al_2o_3:c to low-energy charged particles. *Radiation protection dosimetry*, 119(1-4):375–379, 2006.

[137] ICRP. Recommendations of the international radiological commission on radiological protection. *International Commission on Radiological Protection*, Publication 60, 1991.

[138] SB Scarboro and Stephen F Kry. Characterisation of energy response of al_2o_3:c optically stimulated luminescent dosemeters (oslds) using cavity theory. *Radiation protection dosimetry*, 153(1):23–31, 2013.

[139] Saveta Miljanic and Maria Ranogajec-Komor. Application of cavity theory to the response of various tlds to gammas degraded in water. *Physics in Medicine & Biology*, 42(7):1335, 1997.

[140] Paul Mobit, Ephraim Agyingi, and George Sandison. Comparison of the energy-response factor of lif and al2o3 in radiotherapy beams. *Radiation protection dosimetry*, 119(1-4):497–499, 2006.

[141] A Janssens, G Eggermont, R Jacobs, and G Thielens. Spectrum perturbation and energy deposition models for stopping power ratio calculations in general cavity theory. *Physics in Medicine & Biology*, 19(5):619, 1974.

[142] Sunil Dutt Sharma, Sudhir Kumar, Panchapakesan Srinivasan, and G Chourasiya. Establishment of air kerma reference standard for low dose rate cs-137 brachytherapy sources. *Journal of applied clinical medical physics*, 12(4):275–285, 2011.

Appendix A: ^{90}Sr/^{90}Y β Source Calibration

The ^{90}Sr/^{90}Y β source inside the Risø was calibrated against a 662 keV ^{137}Cs gamma source at an undisclosed location. The dose from the gamma source at a measured distance was determined via multiple ion chambers calibrated to equivalent dose to dry air. Because the chips cannot be exposed to light and because charged particle equilibrium needs to be established, they were placed inside alumina vials (LSP Industrial Ceramics, Inc.) and any remaining gaps were filled with fine powder. The powders were selected to match the mass absorption coefficients of the dosimeters. The objective of this section is to describe the methods used to calculate the ratio of dose in the cavity (either Al_2O_3:C or BeO) to the dose in dry air. This is done by utilizing Burlin cavity theory with the added recommendations of Scarboro and Fry [138], and Sharma et al. [142].

Burlin cavity theory was chosen because the cavity is of "medium" size; this simply means the dose is comprised of photon and electron contributions, and neither should be neglected for precise dosimetry [139]. Cavities are typically assumed to be spheres, while the vials used to hold the dosimeters are cylinders. Two approximations are therefore used to define cavity shape: a sphere with surface *area* equal to that of the cylinder, and a sphere with *volume* equal to that of the cylinder. Based on these considerations, the ratio of the dose in the cavity to the dose of the alumina vial D_{cav}/D_{al} can be defined [59].

$$\frac{D_{cav}}{D_{al}} = d\left(\frac{\bar{S}}{\rho}\right)_{al}^{cav} + (1-d)\left(\frac{\bar{\mu_{en}}}{\rho}\right)_{al}^{cav} \tag{1}$$

$(\bar{S}/\rho)$ is the mean stopping power of the Compton recoil electron spectrum produced from a 662 keV photon. This was found by first calculating the mean electron energy $\bar{T}$ arising from a photon of energy $h\nu$ using the Klein-Nishina cross section ${}_e\sigma$ and energy-transfer cross section ${}_e\sigma_{tr}$, which were obtained in the appendix in Attix [59].

$$\bar{T} = h\nu \frac{{}_e\sigma_{tr}}{{}_e\sigma} \tag{2}$$

$(\bar{S}/\rho)$ can be obtained using the NIST ESTAR (stopping-power and range tables for electrons) data[1] once $\bar{T}$ is calculated. Mobit et al. found that the contribution of carbon is insignificant when calculating $(\bar{S}/\rho)$ for Al_2O_3:C [140]. (μ_{en}/ρ) is the mass energy absorption coefficient, calculated by atomic weight for each material using NIST Standard Reference Database 126[2]. d is a function that considers the relationship between mean electron fluence arising in the cavity wall $\bar{\Phi}_w$ and the initial electron fluence Φ_w^e [59].

$$d = \frac{\bar{\Phi}_w}{\Phi_w^e} = \frac{1 - e^{-\beta L}}{\beta L} \tag{3}$$

L considers the specific geometry of the chamber and is equal to the mean chord length, or 4 times the volume divided by the surface area. Burlin cavity theory approaches small (large) cavity theory as $d \to 0$ ($d \to 1$). β accounts for the build-up and decay of electron fluence with increasing cavity distance [141].

$$\beta = -\frac{ln(0.04)}{t_{max}} \tag{4}$$

Here t_{max} is the maximum depth of electron penetration.

Because we are interested in D_{cav}/D_{air} but only have D_{air}/D_{al}, we substitute the following relationship between the dose to air and the dose to the alumina vial D_{air}/D_{al} [142].

$$\frac{D_{air}}{D_{al}} = \left(\frac{\bar{\mu_{en}}}{\rho}\right)_{al}^{air} A_w \tag{5}$$

A_w is a chamber wall correction factor that accounts for attenuation and scattering due to the 2 mm alumina chamber, and is equal to the following:

$$A_w = 1 - \rho_{al} t \left(\frac{\mu_{en}}{\rho}\right)_{al}, \tag{6}$$

where ρ_{al} and t are the density and thickness of the alumina vial, respectively [59]. This

[1] https://physics.nist.gov/PhysRefData/Star/Text/ESTAR.html, last accessed on May 4, 2021.
[2] https://www.nist.gov/pml/x-ray-mass-attenuation-coefficients, last accessed on May 4, 2021.

enables the ratio of the dose in the cavity to the dose to air to be calculated by combining equations (1) and (5) [142].

$$\frac{D_{cav}}{D_{air}} = \left(\frac{D_{cav}}{D_{al}}\right)\left(\frac{D_{al}}{D_{air}}\right) = \frac{d\left(\frac{\bar{S}}{\rho}\right)_{al}^{cav} + (1-d)\left(\frac{\bar{\mu_{en}}}{\rho}\right)_{al}^{cav}}{\left(\frac{\bar{\mu_{en}}}{\rho}\right)_{al}^{air}\left(1-\rho_{al}t\left(\frac{\mu_{en}}{\rho}\right)_{al}\right)} \tag{7}$$

Table A1 presents the parameters needed to calculate D_{cav}/D_{air}. $D_{Al_2O_3:C}/D_{air}$ was found to be 1.010 and D_{BeO}/D_{air} was found to be 0.968. No difference was observed between the volume and surface area approximations for either material.

	Dry Air	Al_2O_3:C	BeO
${}_e\sigma$ (cm^2/e)	-	$2.561{\cdot}10^{-25}$	$2.561{\cdot}10^{-25}$
${}_e\sigma_{tr}$ (cm^2/e)	-	$9.775{\cdot}10^{-26}$	$9.775{\cdot}10^{-26}$
$\bar{S}/\rho$ (MeV cm^2/g)	2.233	2.051	1.989
μ_{en}/ρ (cm^2/g)	$2.931{\cdot}10^{-2}$	$2.892{\cdot}10^{-2}$	$2.772{\cdot}10^{-2}$
t_{max} (mm)	-	0.515	0.693

Table A1: Parameters needed to calculate D_{cav}/D_{air}.

Several dosimeters were exposed to the ^{137}Cs source for a known time and dose rates were measured with ionization chambers. Absorbed doses in the dosimeters were calculated with the formalism described above. Resulting signals were then measured from 6 dosimeters to obtain a mean and standard error. A precise calibration curve was obtained by irradiating separate dosimeters with the Risø beta source for increasing times, giving each sample utilized to build the dose response a test dose, then accounting for previously determined shutter lag, (0.055 ± 0.026) s. Correcting for this small time lag is critical because the dose delivered is on the order of 1 second of irradiation time. All signals were testdose corrected. The irradiation time equivalent to the absorbed dose was determined by comparing the measured signals to the calibration curve. The dose rate and uncertainty delivered by the Risø simply equals the known dose from the gamma source divided by the exposure time and associated error obtained from the calibration curve. The previous Al_2O_3:C NIST calibration value (May

2015) was corrected for the Risø's ^{90}Sr source half-life decay, then compared to the current dose rate obtained using this procedure. They are less than 1% different.

Appendix B: Standard Operating Procedure: Accelerator and Luminescence Beamline

It takes approximately three to four hours to get uniform and steady beam on target from the time the ion source is turned on. However, the engineer handles heating the ion source whenever an experimenter runs beam. This procedure covers therefore only the standard protocol required to get beam on target after the source is heated up. This can take anywhere from one and a half to three hours, depending on the required beam and how many optimization iterations are performed. It should first be noted that the ion source and luminescence beamline were engineered entirely in-house while the tandem particle accelerator was manufactured by National Electrostatics Corp. The process of getting beam on target can be broken into four main steps: optimizing beam that enters the LE (low energy) Faraday cup, optimizing beam that enters the HE (high energy) Faraday cup, optimizing beam that enters the beamline Faraday cup, and finally optimizing beam that enters the chamber Faraday cup.

Getting beam on target

To begin, the pen recorder and run time options are selected at the accelerator control booth using the built in NEC software. These options enable real time graphs of many accelerator parameters, such as central terminal voltage and SF_6 concentration, and allow visual monitoring to ensure critical parameters stay within their allowed domains. For example, if the SF_6 concentration spikes too high, an alarm will sound and the engineer will be notified. Next, the left blower is turned on, followed by the power supply to the accelerator turbo pump, and finally the belt power supply. The charging belt power supply is set to a small voltage (approximately 1 KV) after being turned on so that the central regulator can build up charge. Now the central regulator is turned on, enabling the experimenter to set a stable central terminal voltage.

The HE cup is then assigned to the first readout. This allows the experimenter to see

how the HE current fluctuates as accelerator parameters change. Next, the Quad magnet 'strength' and 'balance' are assigned to controls 1 and 2, respectively, followed by the up/down and switching magnets being assigned to control 3 and 4. Finally, the beamline cup can be assigned to readout 2. All controls and readouts needed to get beam on target are now set.

The LE column gate valve is opened so that the accelerator and ion source reach approximately equal vacuum and so that ions can enter the accelerator. The LE current can now be maximized by varying the source voltage, the source Einzel lens voltage, and the cathode voltage. It is assumed that beam is on target (i.e. centered) when the current is maximized. An Einzel lens is a charged particle electrostatic lens that has the ability to focus and defocus the beam without altering beam energy. These parameters should each be adjusted, one at a time, until the current is maximized. Several iterations of setting adjustments must be completed to obtain a true maximum LE cup current. One must remember that the beam has several periodic Gaussian peaks, and the central peak corresponds to the highest current. This means that having an understanding of the source output can indicate whether the central peak or a peripheral peak constitutes the current. Before moving on to the HE cup, it is pertinent that the experimenter fill out the lab log, which entails specifying the LE cup reading and all parameter settings adjusted to obtain this reading.

Once the current has been maximized to the LE cup, the chains should be powered on so the central terminal can charge up. To do this, the voltage on the power supply must be increased until the terminal voltage builds to a value slightly higher than the desired central terminal value. After the terminal voltage is slightly higher than the desired voltage, the terminal control mode can be switched from manual to automatic so the voltage remains constant while running. At this point, the beam is considered monoenergetic. To determine the central terminal voltage setting (V) required to obtain a given particle energy (E), the following equation must be used:

$$V = \frac{E - V_s - V_c - 30kV}{n+1} \tag{8}$$

where n is the charge state of the particle measured in the chamber Faraday cup. This equation arises because particles will be accelerated five separate times before exiting the accelerator: once due to the source voltage (V_s), once due to the cathode voltage (V_c), once from a 30 kV linear acceleration between the source and the accelerator, and twice from 'tandem' accelerations of magnitude $q \cdot V$ in the accelerator itself. N_2 stripper gas is injected into the central terminal now that the central terminal is at constant voltage. The stripper gas is responsible for removing electrons from particles entering the central terminal so that they will flip polarity, repell away from the positively charged central terminal, and accelerate a second time. For this reason, beam quality is significantly affected by the central terminal stripper gas pressure. The pressure is slowly increased until a steady value of at least 1.2 μTorr is obtained. While this pressure tends to fluctuate over time, it is critical that it never gets close to 10 μTorr, which results in an alarm and the engineer being notified.

After the stripper gas has reached a quasi-steady value, the LE cup is placed in the "out" position so that the HE cup upstream of the accelerator measures beam current. The inflection magnet current, source up/down magnet current, LE Einzel lens voltage, and electrostatic steerer current should all be adjusted in the same manner prescribed previously, until the HE cup current is maximized. The Inflection and source up/down magnets steer the beam horizontally and vertically, respectively, from the ion source to the accelerator. The LE Einzel lens and electrostatic steerers focus and center the beam before entering the accelerator. On a good day, there will be 40 to 50 percent throughput from the LE cup to the HE cup. Protocol dictates that the electrostatic steerers be adjusted after the other three parameters are adjusted, as these magnets are only used for fine tuning in the x and y directions. After current is satisfactory, a new column in the lab data log is filled out to reflect new or changed parameters.

The last steps neccessary to get beam on target include optimizing beam in the primary

beamline cup and then the chamber. The R30 beamline gate valve is opened and pressures are monitored. If there is a spike or drop in the HE or beamline vacuum, the valve is immediately closed to identify the source of the leak. Once the HE cup is placed "out" and the beamline cup is placed "in", the switching magnet is used to steer the beam 30 degrees right. The up/down magnet is then utilized to center the beam vertically. Finally, the quad magnet's strength and balance settings spread out the beam and adjust magnet weighting, respectively. A beam profile monitor, located before the beamline cup, enables beam visualization along the x and y axes. Because uniform beam is desired, the strength and balance are adjusted until the beam is visually uniform on the oscilloscope. This drastically reduces the flux, sometimes to the point where the oscilloscope reads indeterminate signal, even with high gain. When this happens, the beam should be centered with the oscilloscope while uniformity can be visualized using the camera and YAG scintillator. If the current is too low for the oscilloscope to detect, light intensity from the YAG crystal can be analyzed in real time using ThorCam imaging software, providing horizontal and vertical beam profiles. ThorCam software gain and light collection frequency settings enable the camera to monitor very low currents (pAs). Alternatively, a narrow beam can be created by lowering the magnet strength.

Obtaining uniform beam in the x and y directions is often a tedious and time consuming process which requires many iterations of quad magnet strength and balance setting adjustments. A 3-dimensional light intensity plot (figure A1) can then be used to verify that the beam is uniform along both axes once the experimenter is ready to proceed. The collimators are used to attenuate any outer portion of the beam that is not uniform. While the beam is similar in size from day to day, collimators still require small adjustments. The goal is to obtain the largest uniform beam possible.

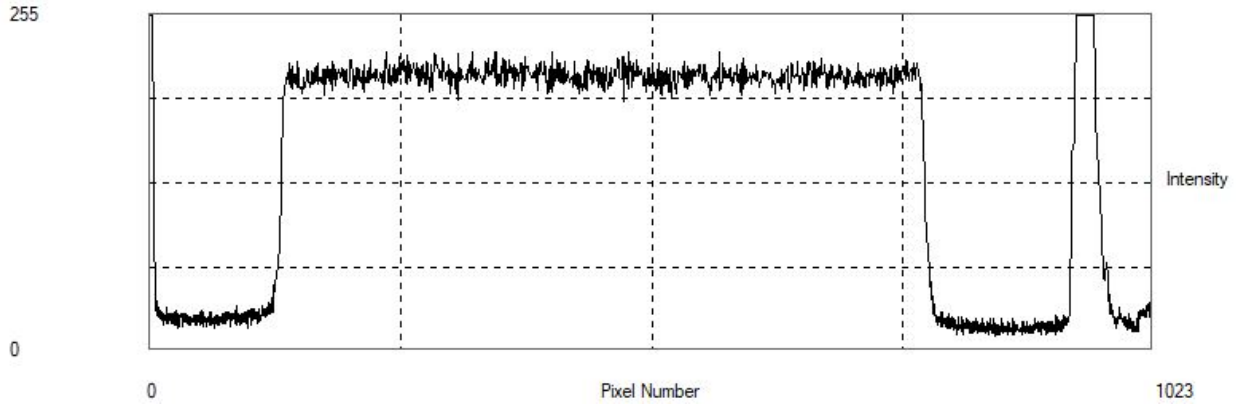

(a)

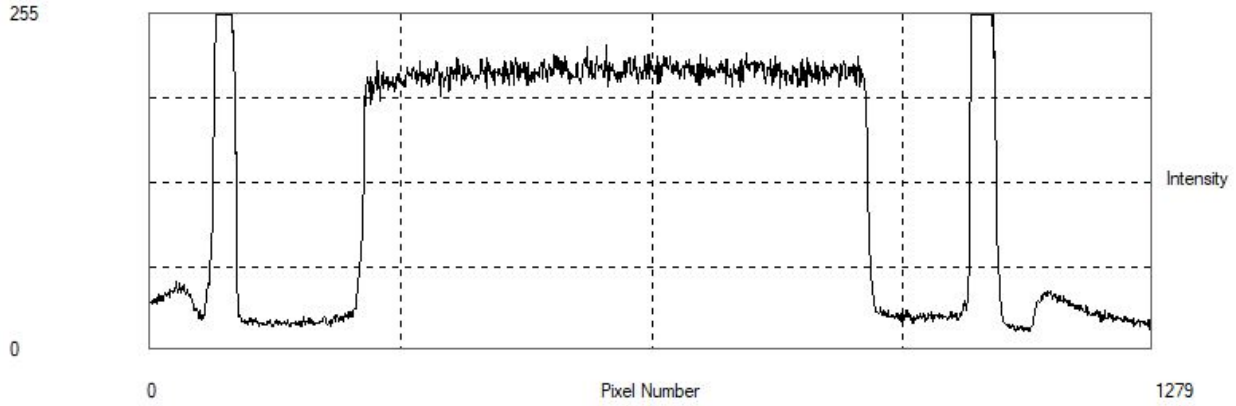

(b)

Figure A1: X (a) and y (b) profiles for a 4 MeV/u H^+ beam, created via ThorCam imaging software. Once beam is in the chamber the analyzing and steering magnets are utilized to centralize the beam on the YAG crystal. Then the quad magnet strength and balance are adjusted until beam is as uniform as possible in the x and y directions. The intensity spikes on the sides of each profile represent the edges of the YAG crystal. The profile plots above correspond to a beam of about 400,000 pixels with a light intensity signal standard deviation of approximately 3.5 percent. This fluctuation arises from the mechanics of the sputter source and the lower currents used in this research.

Loading samples

After uniform beam is in the chamber, samples can be loaded. Photos of the beamline with labels of all pertinent parts are shown in figures A2 and A3. The chamber and actuator port are isolated using the manual gate valve, then brought up to atmospheric pressure. The chamber turbo pump must be turned off and the chamber rough pump must be isolated using the pneumatic fore line valve before air can be slowly leaked into the volume

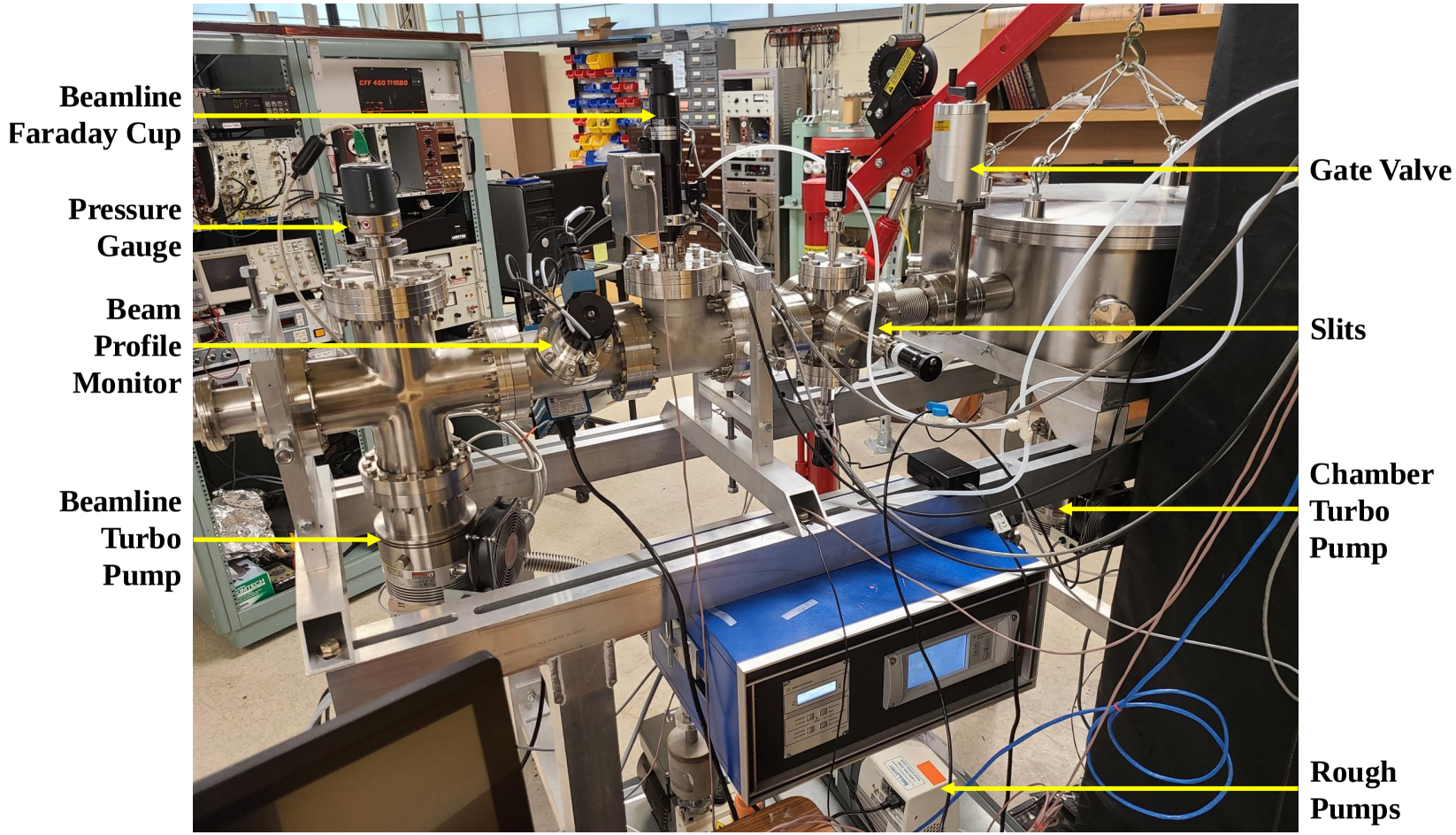

Figure A2: Picture of the primary beamline.

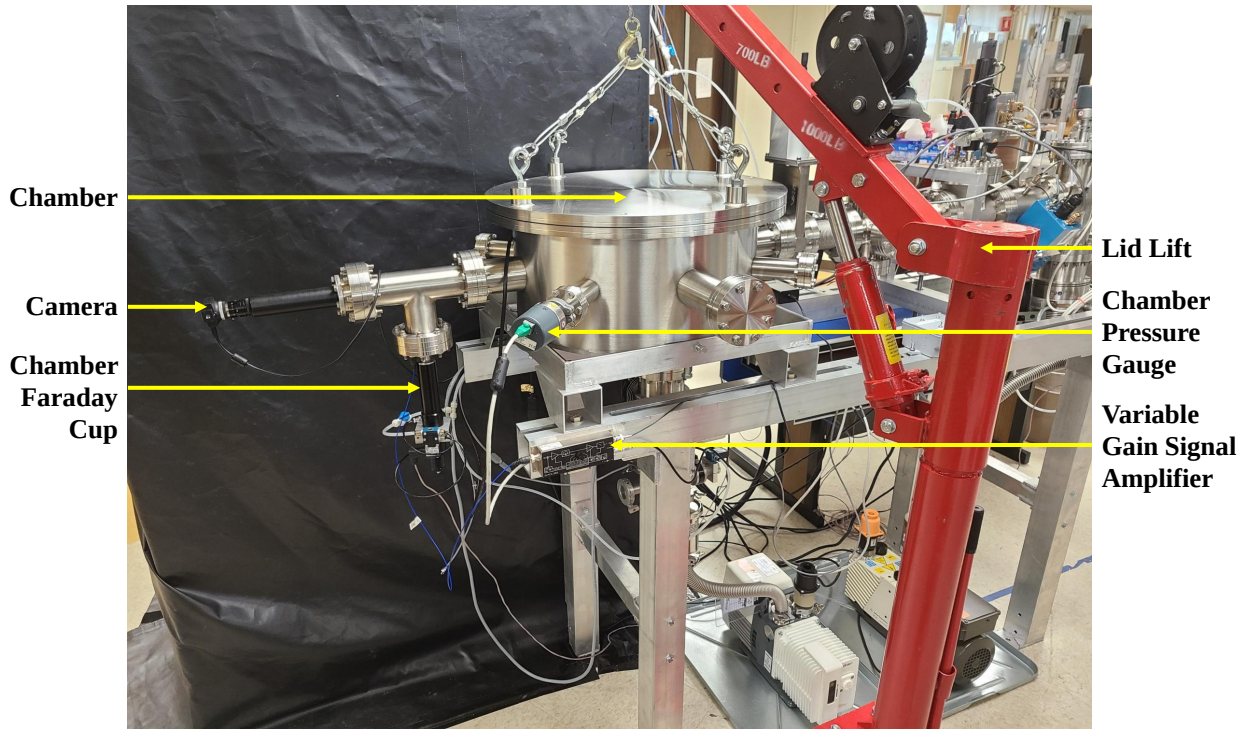

(a)

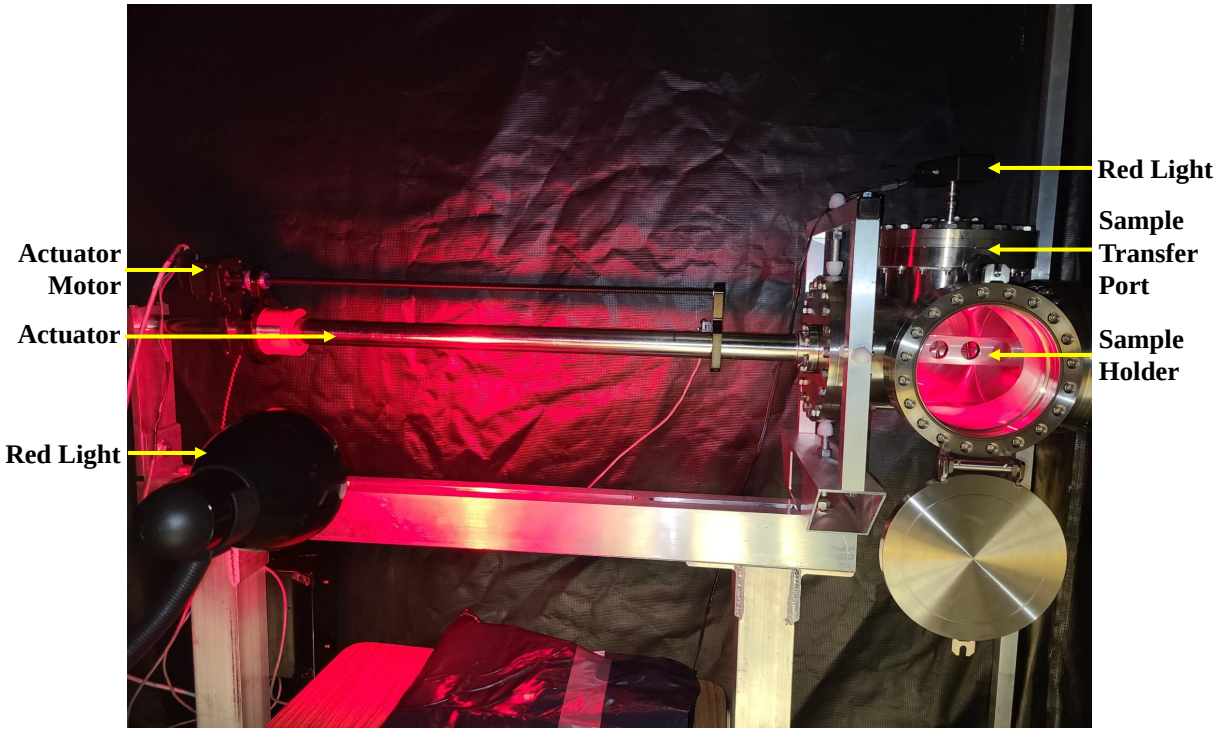

(b)

Figure A3: Pictures of the rear-view of the chamber (a) and view from inside the light-tight infrastructure (b).

using the adjustment knob on the turbo pump. It is important that the knob is turned very slowly, and that the experimenter stops opening the knob after air flow is audible. The turbines are spinning at several thousand RPM and a drastic change in vacuum will jolt and even damage the pump. As the turbo pump audibly winds down, air can be allowed in at a faster rate. Once the chamber pressure reaches atmosphere (this typically takes about 5-10 minutes) and the actuator port is opened, samples are loaded onto the ladder, which is then tightened onto the end of the actuator. The fore line valve is opened once the actuator port door is tightly closed, exposing the chamber and actuator to the rough pump. The turbo pump is powered on after the chamber pressure reaches $\sim 10^{-1}$ Torr. The manual chamber valve is opened and irradiation may begin once chamber pressure approximates beamline pressure. The process of raising pressure to atmosphere and dropping pressure to vacuum must be repeated every time new samples are loaded.

All beam parameters are recorded into excel immediately prior to irradiating samples, because many of these characteristics vary slightly over time. These parameters include current, energy per elementary charge, and beam surface area. Sample size and charge state are input beforehand to reduce time between current measurement and irradiation. From here, simple algebra yields the exposure time required to obtain a specific absorbed energy (see Chapter 3.2.1). The actuator is controlled using LabVIEW, allowing each mounted sample to be centered precisely in the beam. Multiple calibrations were performed to ensure that the precision is within 0.25mm. Operating the actuator is trivial once the samples are loaded; it only requires the experimenter to input desired exposure time.

Shutting down

It is very important that proper shutdown procedures are followed once all samples are irradiated. To begin, all Faraday cups are placed "in". The switching magnet current is turned to zero so that the beam is no longer steered into the R30 line. Now the gate valve is closed and pressures are monitored in the same manner as before. Both chains are turned off.

The central terminal and charging station are set to zero, followed by closing the N_2 stripper gas intake. The left blower and accelerator turbo pump power supply are then turned off. The LE gate valve can now be closed. The oven Watts and LE Einzel voltage are set to zero at the ion source control center. Finally, the central terminal is turned off. Auto Shutdown is selected if no one is running the following day. However, a warm shutdown is completed if beam will be used the following day. This entails setting the ionizer to 15 A once the oven temperature cools below 50 degrees.

Appendix C: OSL Curve Shape Change from β and α

This section is an extension of Chapter 7, and includes low LET radiation results for both materials. The same procedure outlined in the beginning of Chapter 7 to decompose the OSL curves (see figure A4) and compare residuals and autocorrelation signals (see figure A5) is followed here. Additionally, component intensity and linearity is plotted as a function of β-dose for Al_2O_3:C (see figure A6) and a function of irradiation time for BeO (see figure A10).

Al_2O_3:C

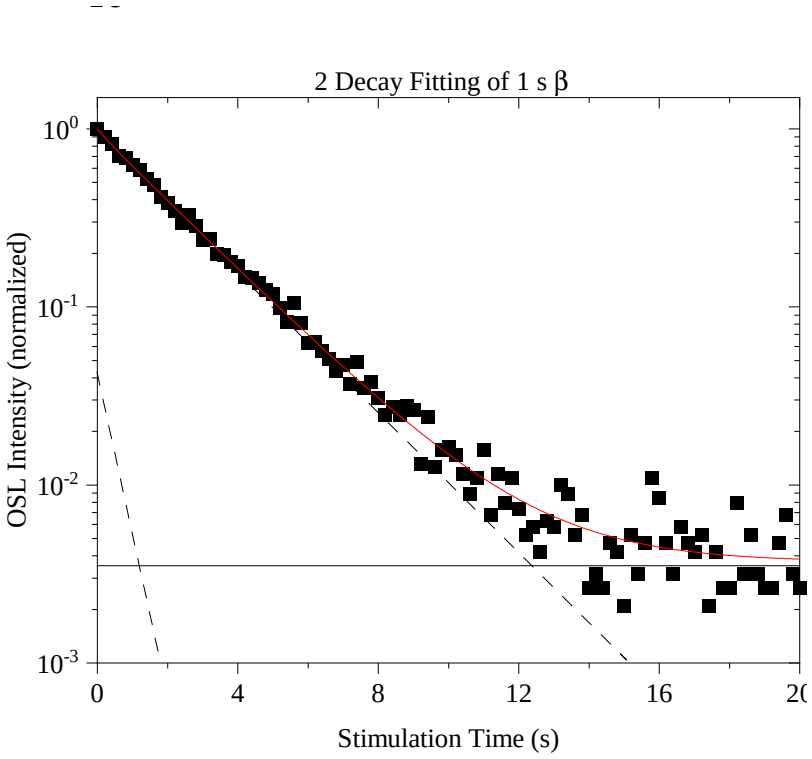

Figure A4: Two component fit for OSL curve after 2 s β. The black squares show experimental data and the red lines show the 2-component fit. Dashed lines represent the individual decay components and black lines show the value used for background.

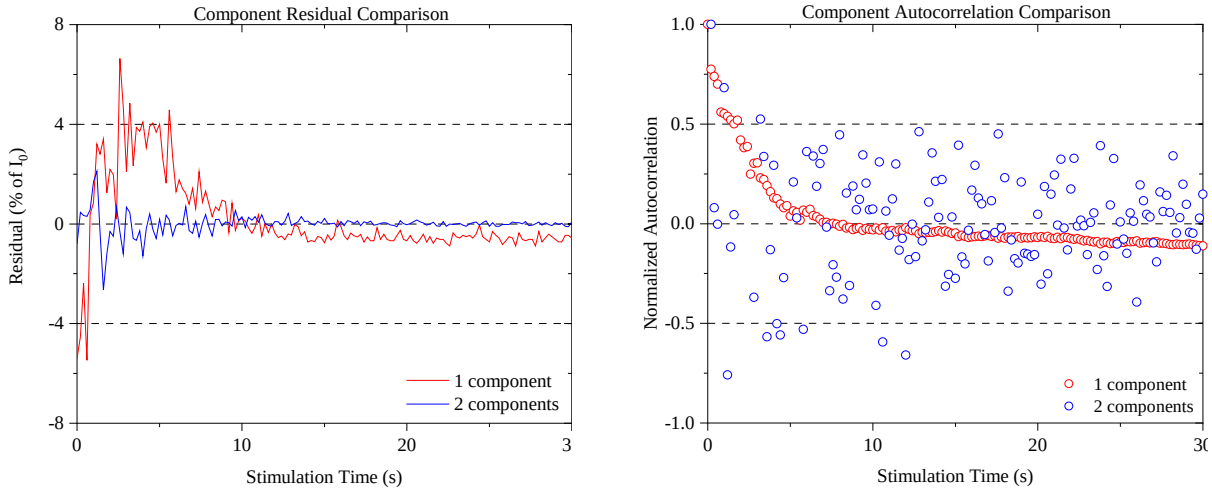

(a) (b)

Figure A5: Comparison of residual (a) and normalized autocorrelation (b) for fits containing 1 and 2 decay components.

β dose (s)	A_1	A_2
1	0.04	0.95
2	0.10	0.91
5	0.14	0.86
10	0.16	0.85
20	0.22	0.79
50	0.35	0.66
100	0.46	0.54
200	0.55	0.44
500	0.61	0.38

Table A2: Normalized amplitude contributions for various β doses. A_1 and A_2 indicate the fast and slow component amplitudes, respectively.

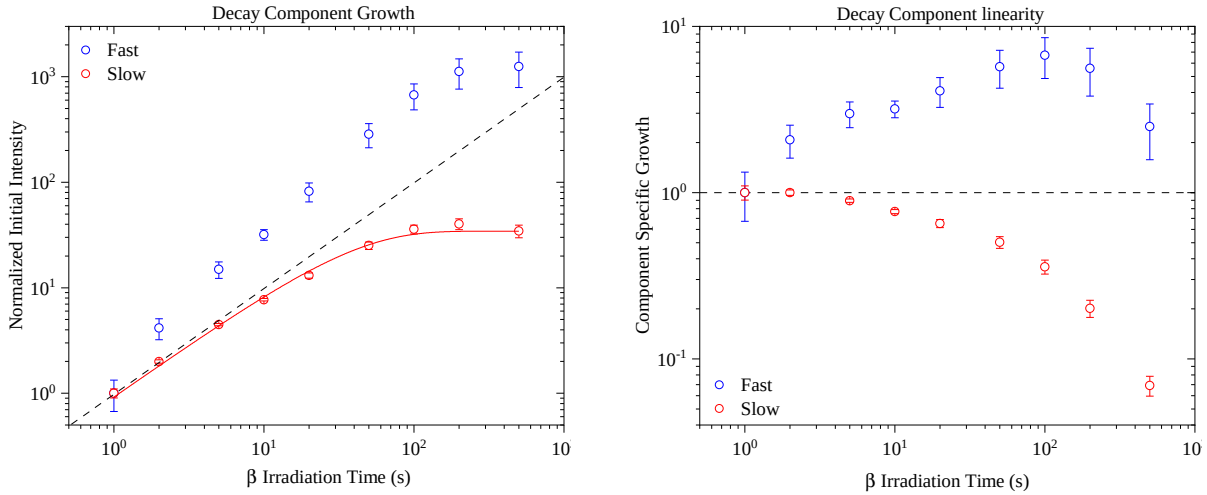

(a) (b)

Figure A6: Growth curves(a) and linearity (b) of the 2 decay components as a function of β dose. Points represent the mean and standard deviation of 3 dosimeters. Intensities were normalized via S/S_R. Dashed lines indicate linearity

BeO

β irradiation

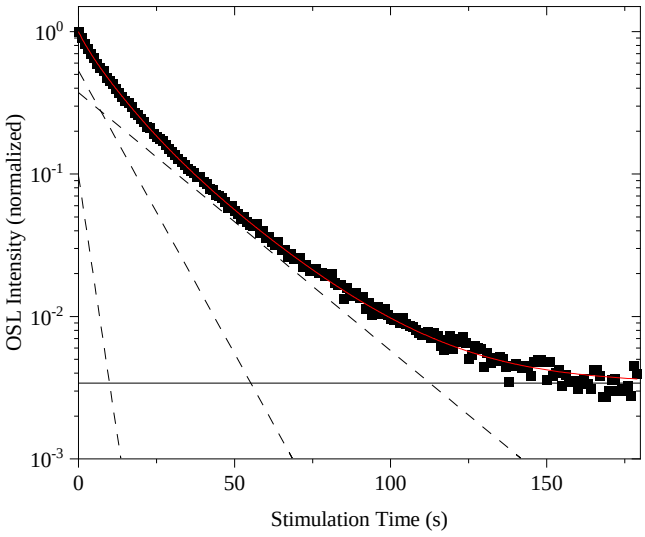

Figure A7: Three component fit for OSL curve of BeO exposed to 2 s β. The black squares show experimental data and the red lines show the 2-component fit. Dashed lines represent the individual decay components and black lines show the value used for background.

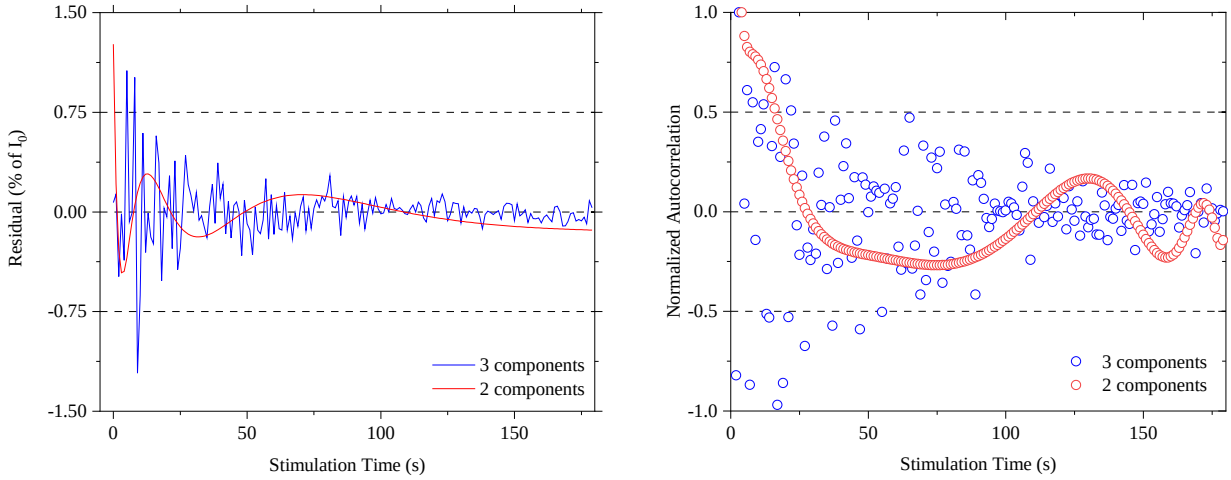

(a) (b)

Figure A8: Comparison of residual (a) and normalized autocorrelation (b) for fits containing 2 and 3 decay components.

α irradiation

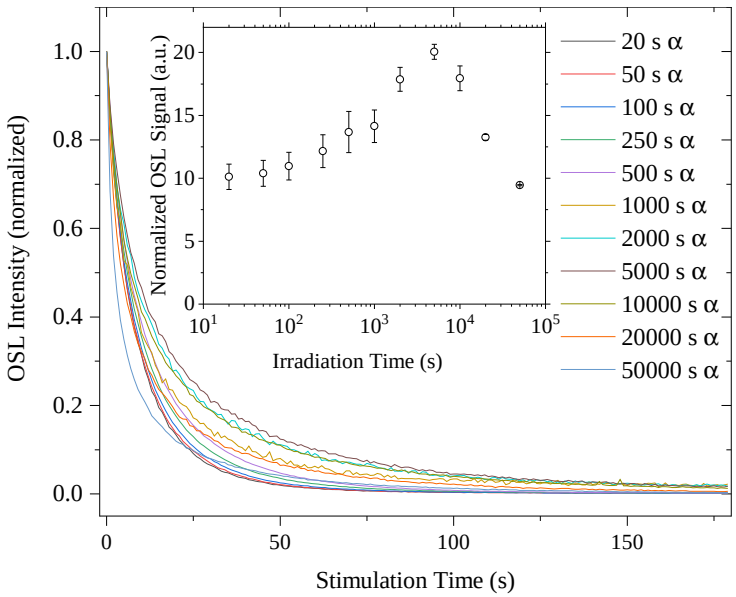

Figure A 9: OSL curves of BeO after irradiation with increasing α doses, normalized to initial intensity values. The inset shows the mean $\pm$ standard deviation of the area under the normalized curves of multiple dosimeters.

α dose (s)	A_1	A_2	A_3
20	0.22	0.75	0.04
50	0.22	0.73	0.06
100	0.21	0.72	0.08
250	0.18	0.70	0.12
500	0.18	0.66	0.17
1000	0.17	0.60	0.23
2000	0.17	0.49	0.33
5000	0.19	0.44	0.37
10000	0.25	0.42	0.32
20000	0.39	0.39	0.21
50000	0.57	0.30	0.14

Table A3: Normalized amplitude contributions for various doses from ^{241}Am. A_1, A_2, and A_3 indicate the fast, medium, and slow component amplitudes, respectively. $\sum_{i=1}^{n} A_{\mathrm{i}} = 1$.

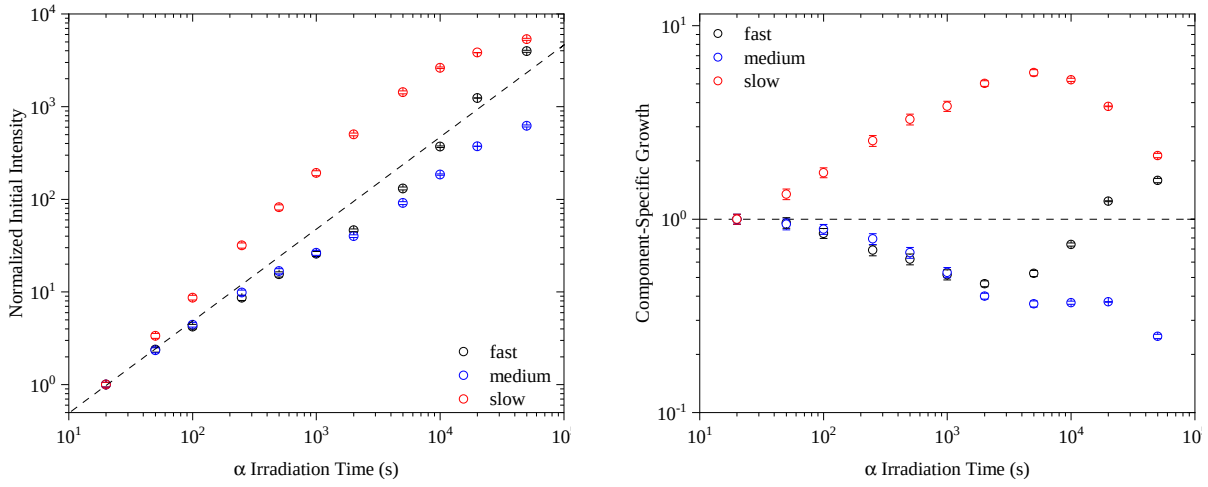

(a) (b)

Figure A 10: Normalized initial intensity (a) and component growth (b) of the 3 decay components as a function of dose from ^{241}Am. Points represent the mean and standard deviation of 3 dosimeters. Intensities were normalized with a test dose. Dashed lines indicate linearity.